TABLE 12.1 COMPOSITION OF 1 KILOGRAM OF SEAWATER

Species	Grams
Na^+	10.7822
Mg^{2+}	1.2837
Ca^{2+}	0.4121
K^+	0.3991
Sr^+	0.0079
Cl^-	19.3529
SO_4^{2-}	2.7124
HCO_3^-	0.1135
Br^-	0.0672
CO_3^{2-}	0.0116
$B(OH)_4^-$	0.0013
F^-	0.0010
$B(OH)_3$	0.0203
Total	35.1709

Notes:

(1) The contributions of the borate and carbonate systems are approximately given at surface water pH.

(2) For many years the salinity of sea water was measured by titration of the chloride ion with a silver nitrate solution. This formed the international standard of measurement, and it is often reported as the "chlorinity." The ratio is salinity = 1.80655 × chlorinity. Chlorinity = 19.374 grams per kilogram.

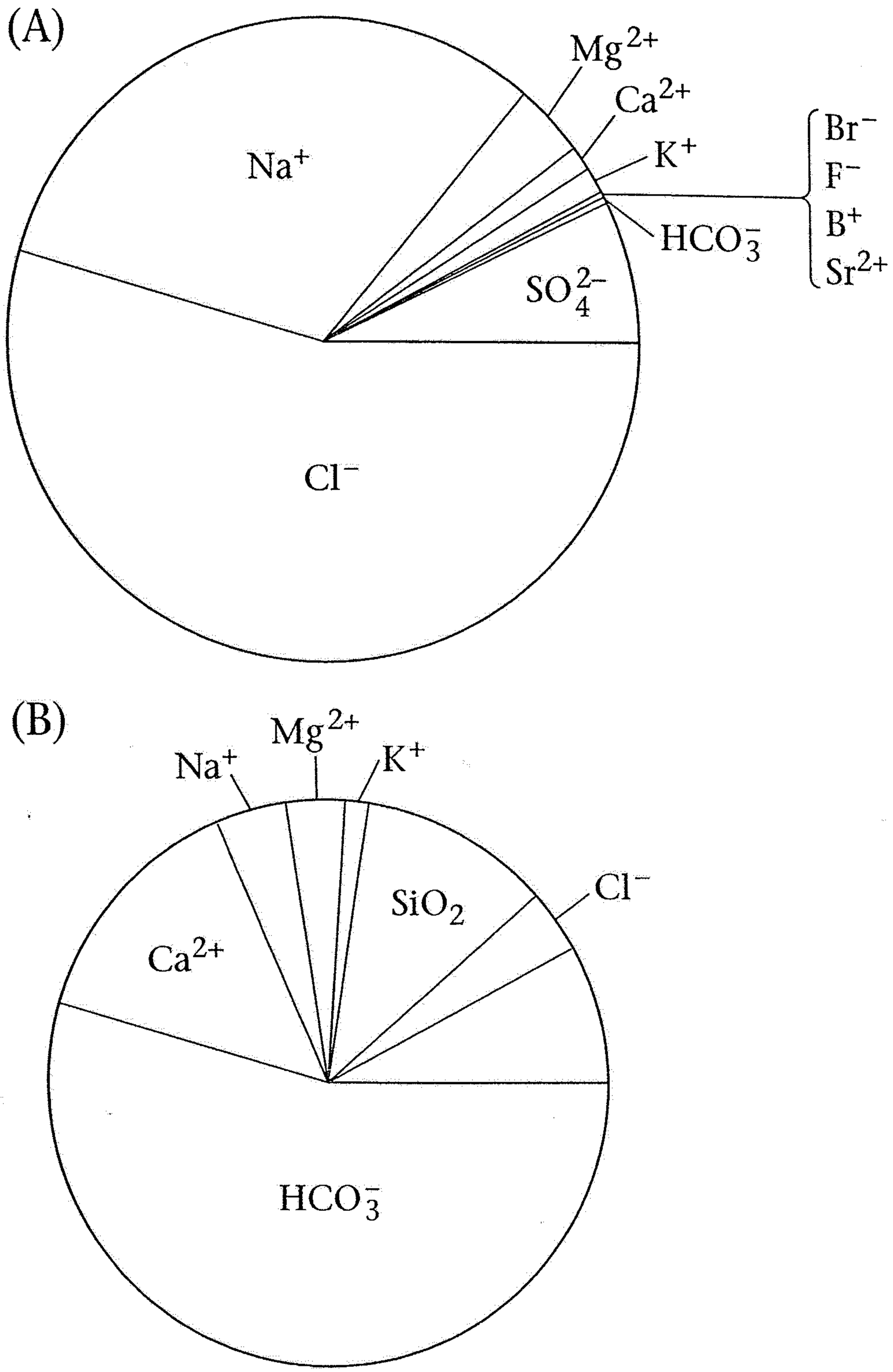

Figure 12.3. Average proportion of dissolved ions in (A) seawater and (B) river water.

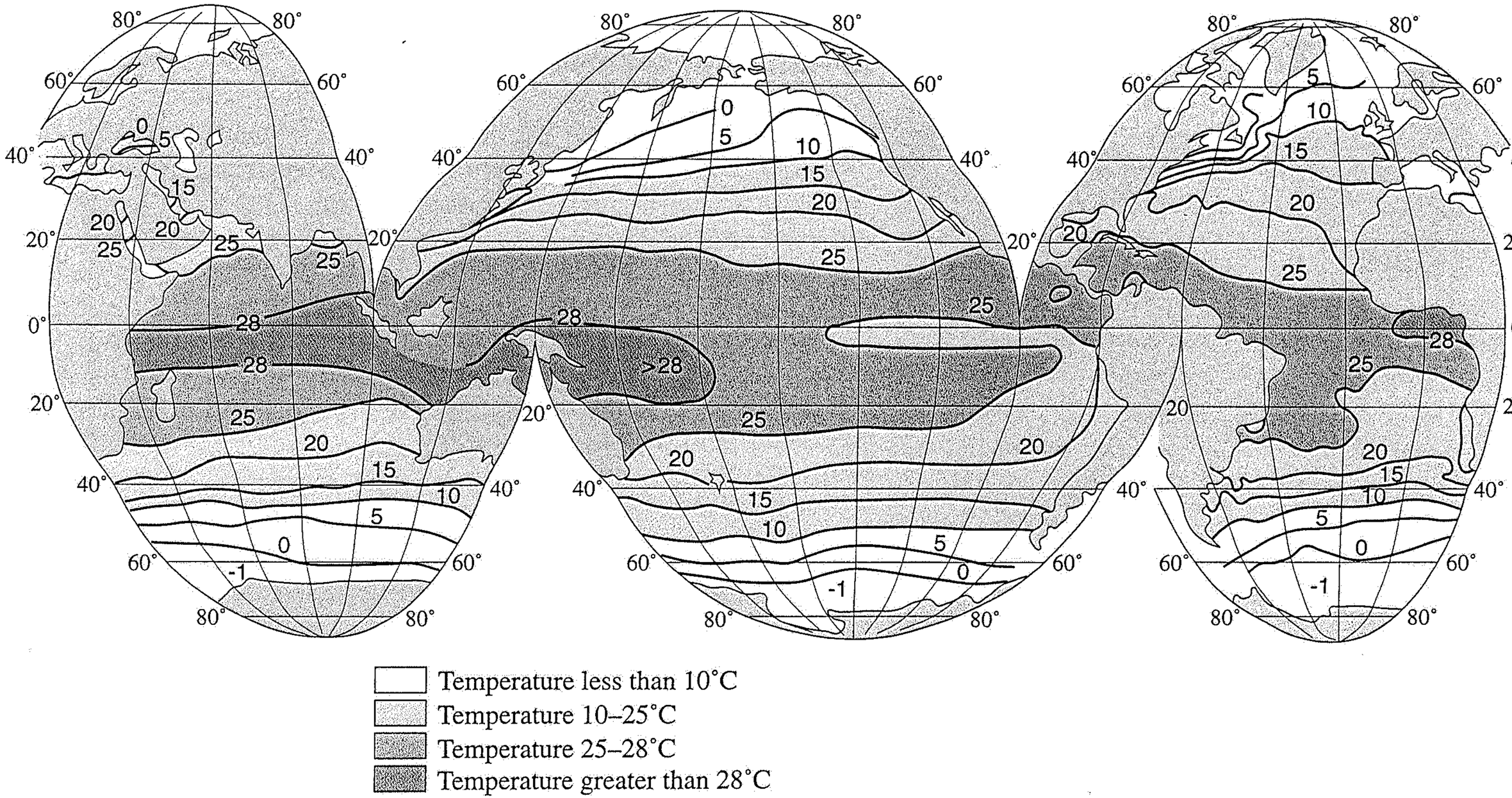

Figure 2.13 Average temperature at the sea surface in February (from Gross[6]; the values are derived from Sverdrup *et al.*[20] and from later sources).

3.1

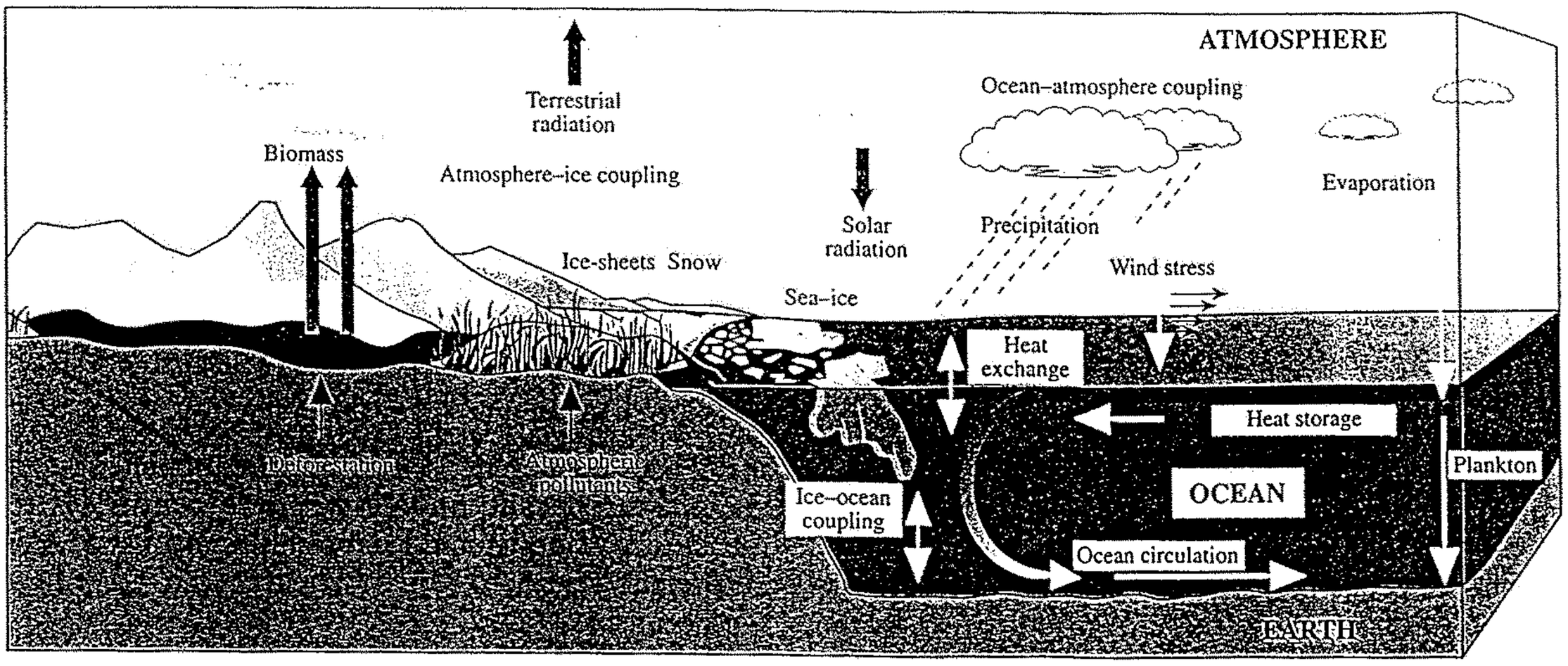

Figure 3.1 A schematic view of the Earth's climate system showing the roles of land, atmosphere, oceans, and sea ice.

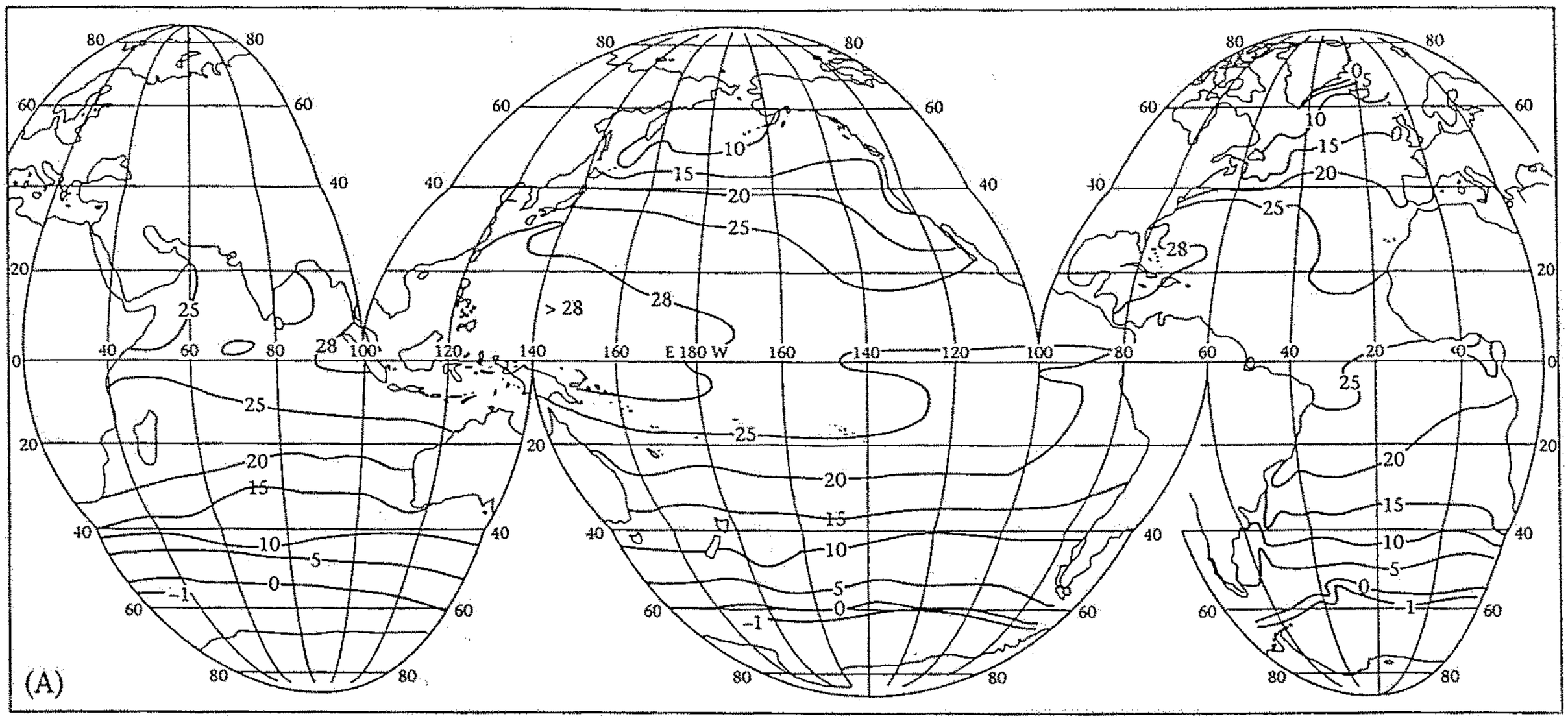

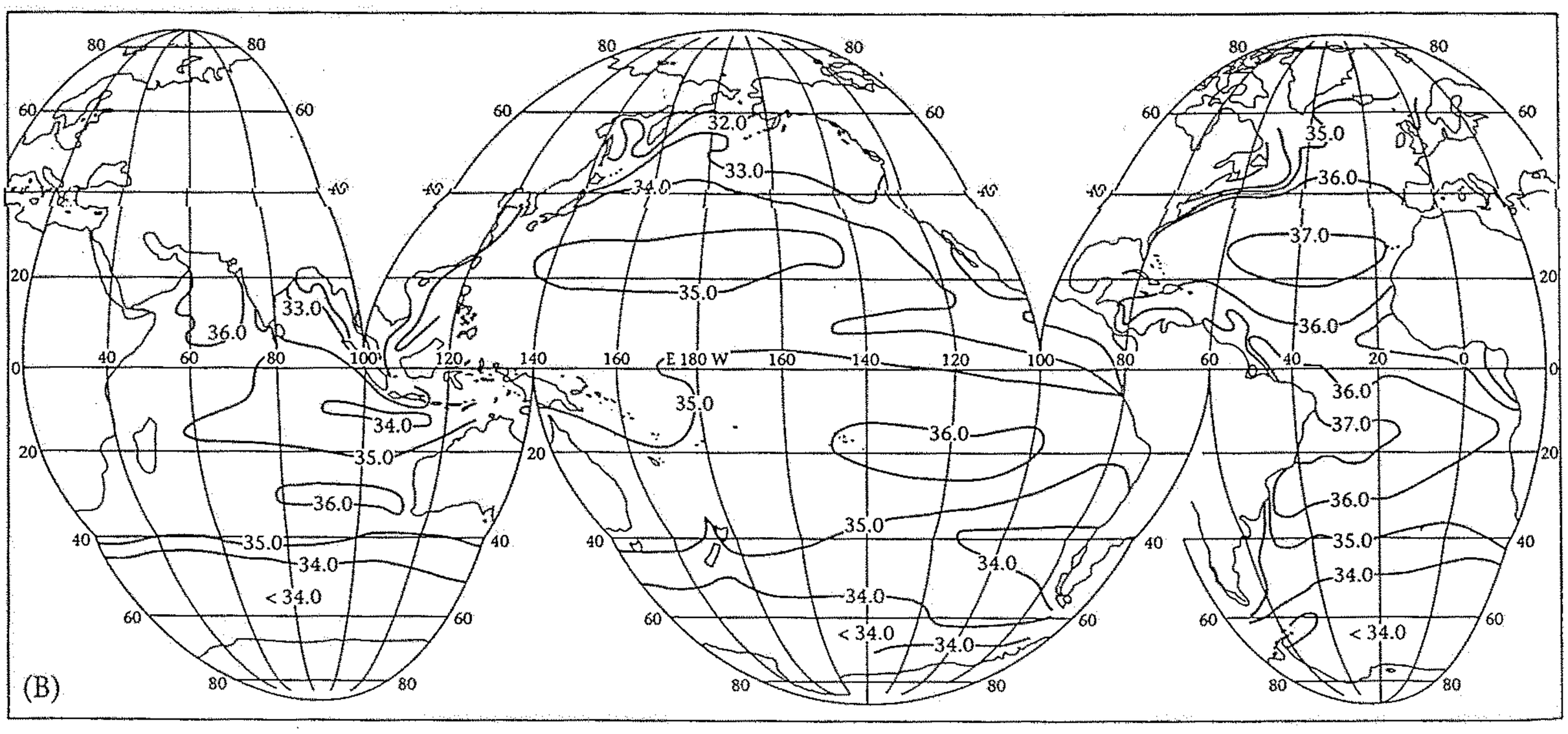

Figure 10.5. Generalized patterns of ocean surface (A) temperatures and (B)salinities in August (Northern Hemisphere summer). Lines of equal temperature (isotherms) and equal salinity (isohalines) tend to parallel latitude in the open ocean. Alternatively, isotherms are torqued north and south along continental margins, reflecting displacement by surface currents in these regions. (*Source:* Goode Base Maps, courtesy University of Chicago.)

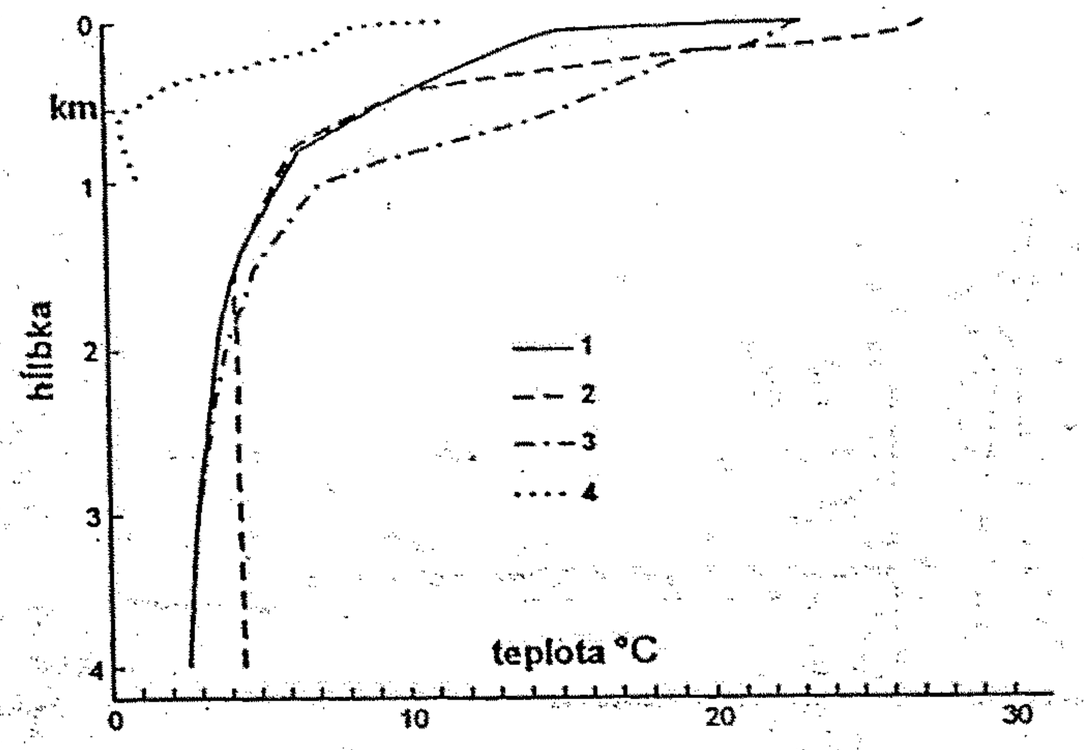

obr. 18.8. Zmena teploty morskej vody s hĺbkou. Rýchly pokles teploty siaha do hĺbky 1 až 2 km, hlbšie je teplota takmer konštantná. Krivky 1 a 2 sú z Atlantiku na 12. a 14. st. sev. zem. šírky, krivka 3 z Indického oceánu (22. st. sev. zem. šírky). Krivka 4 je z Biskajského zálivu.

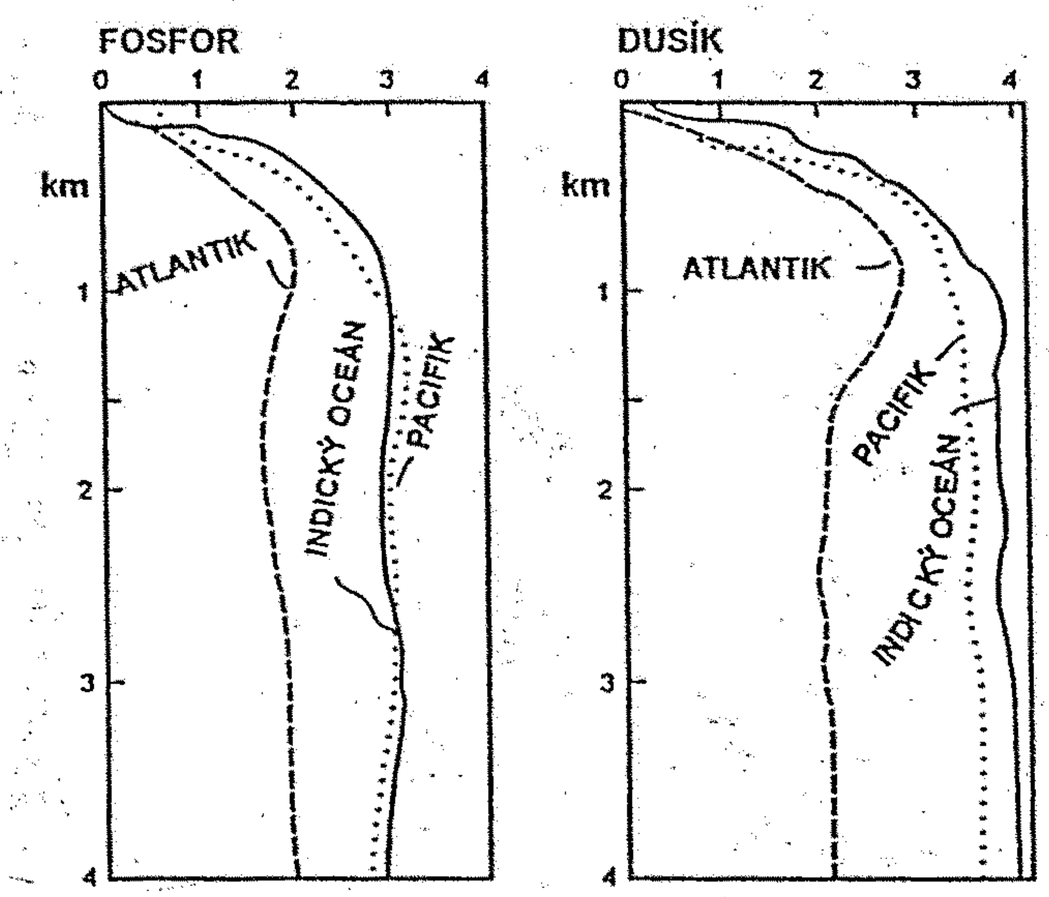

obr. 18.6. Prudký úbytok najdôležitejších živín od hĺbky 1 km k hladine je tiež dôsledok ich odčerpania organizmami z morskej vody. Hodnoty sú v mg/m^3.

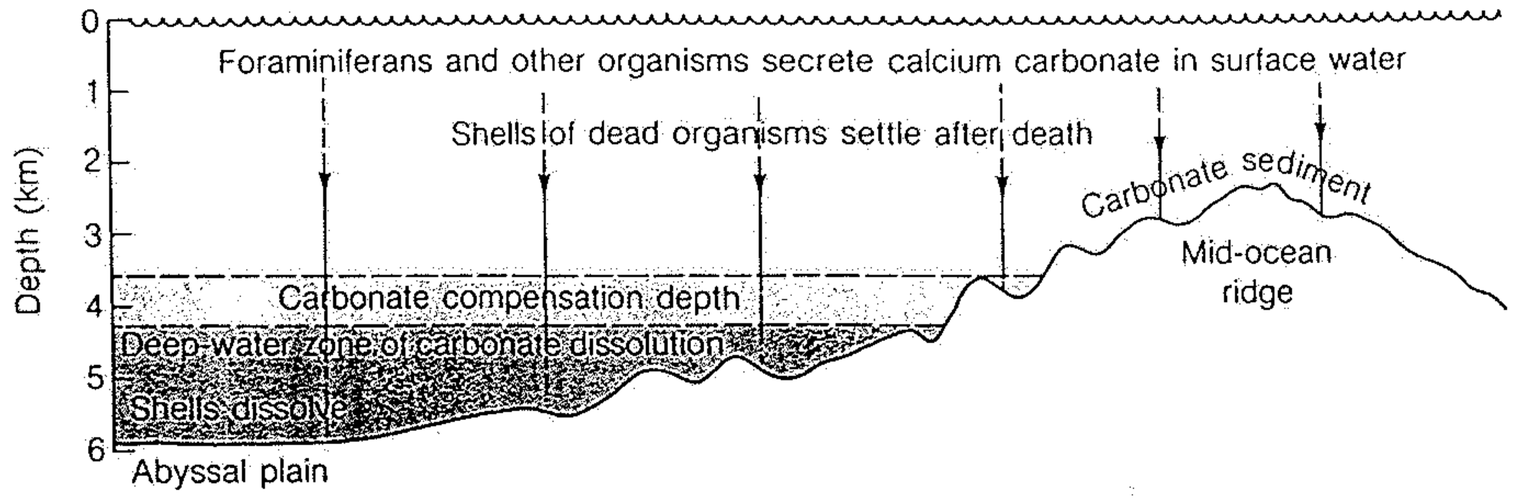

Figure 11-51

The calcium carbonate compensation depth is the level in an ocean below which the calcium carbonate of foraminifera and other shelled organisms that have settled from surface water dissolve. The depth, which is a zone rather than a sharp boundary, varies some from ocean to ocean.

Figure 11-52

As a site of sedimentation is transported away from a mid-ocean ridge by plate movement, plate subsidence moves the site downward with respect to sea level, eventually below the calcium carbonate compensation depth. At that point, carbonate sediment is succeeded by noncarbonate deposits.

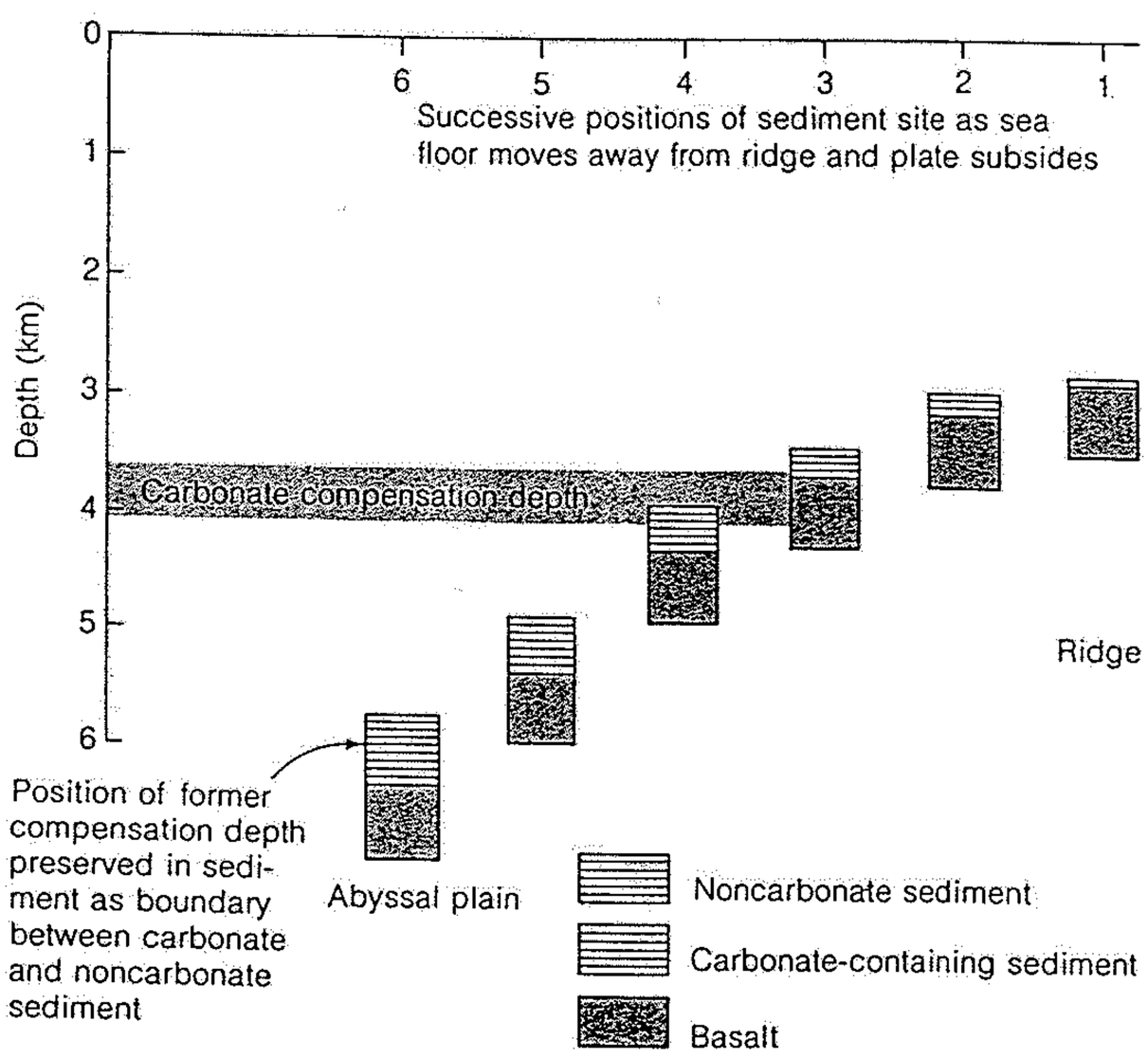

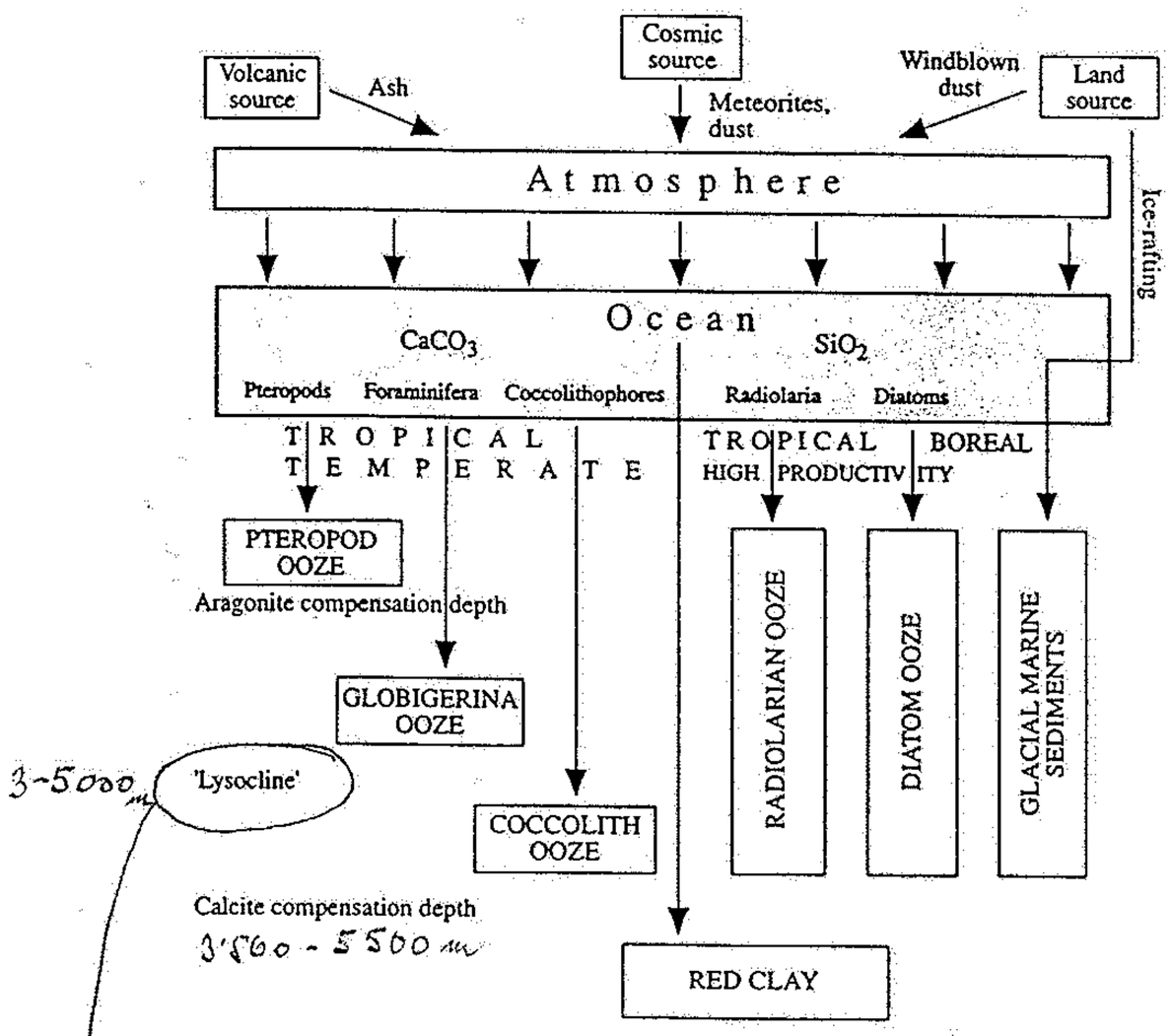

Figure 8.23 Sources and pathways of pelagic sedimentation in the oceans (after Hay[17]).

Figure 3.2 Poleward transfer of heat by: (a) ocean and atmosphere together (T_A+T_O), (b) atmosphere alone (T_A), and (c) ocean alone (T_O). The total heat transfer (a) is derived from satellite measurements at the top of the atmosphere, that of the atmosphere alone (b) is obtained from measurements of the atmosphere, and (c) is calculated as the difference between (a) and (b) (1 PW = 10^{15} W). (Based on Carrissimo *et al.*[7]; results from other investigations are added for comparison.)

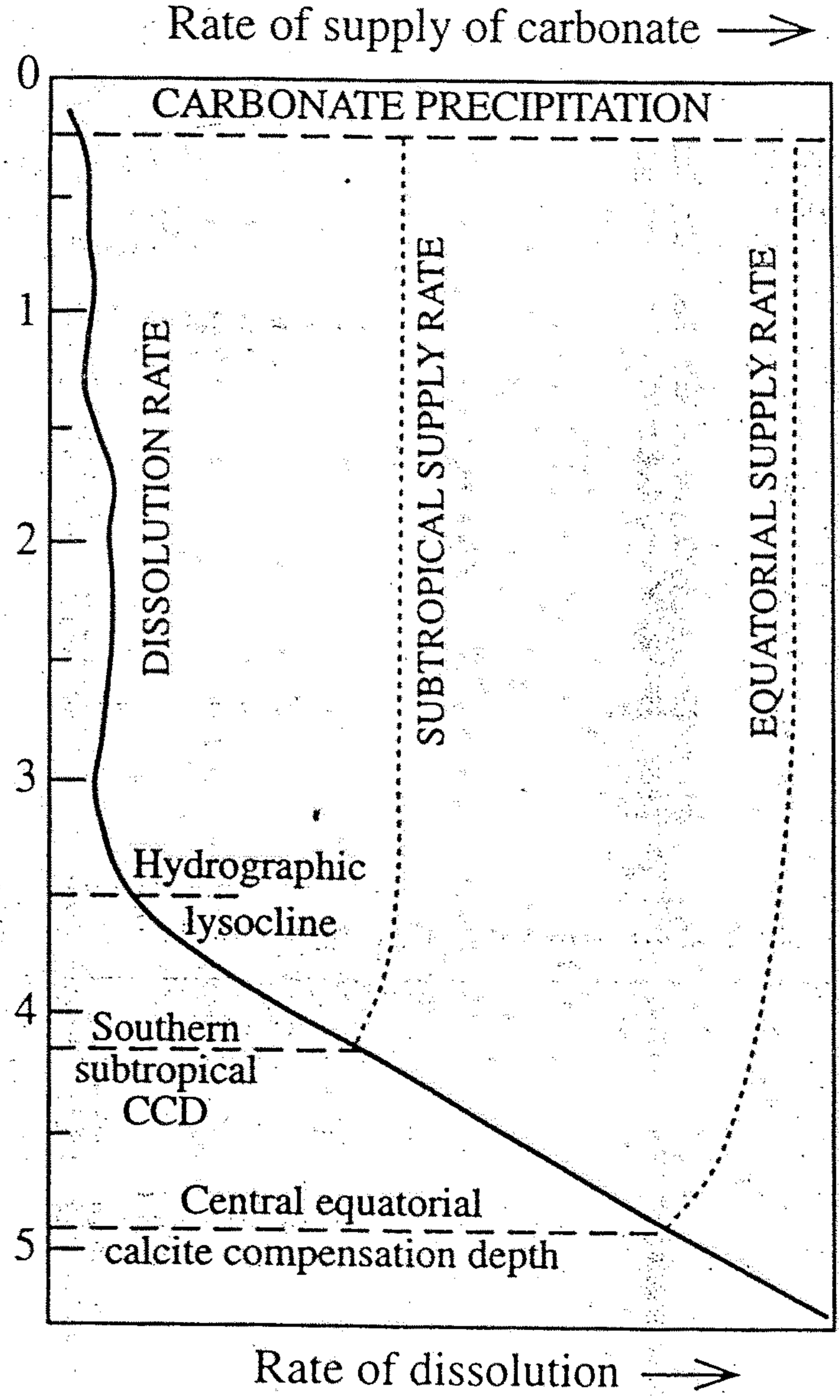

Figure 8.24 Conceptual model for calcite dissolution rate in the ocean, showing the relationship between the calcite compensation depth (CCD) and the lysocline. Increased carbonate supply at the equator depresses the CCD (*Figure 11* from Berger *et al.*[3]; © American Geophysical Union).

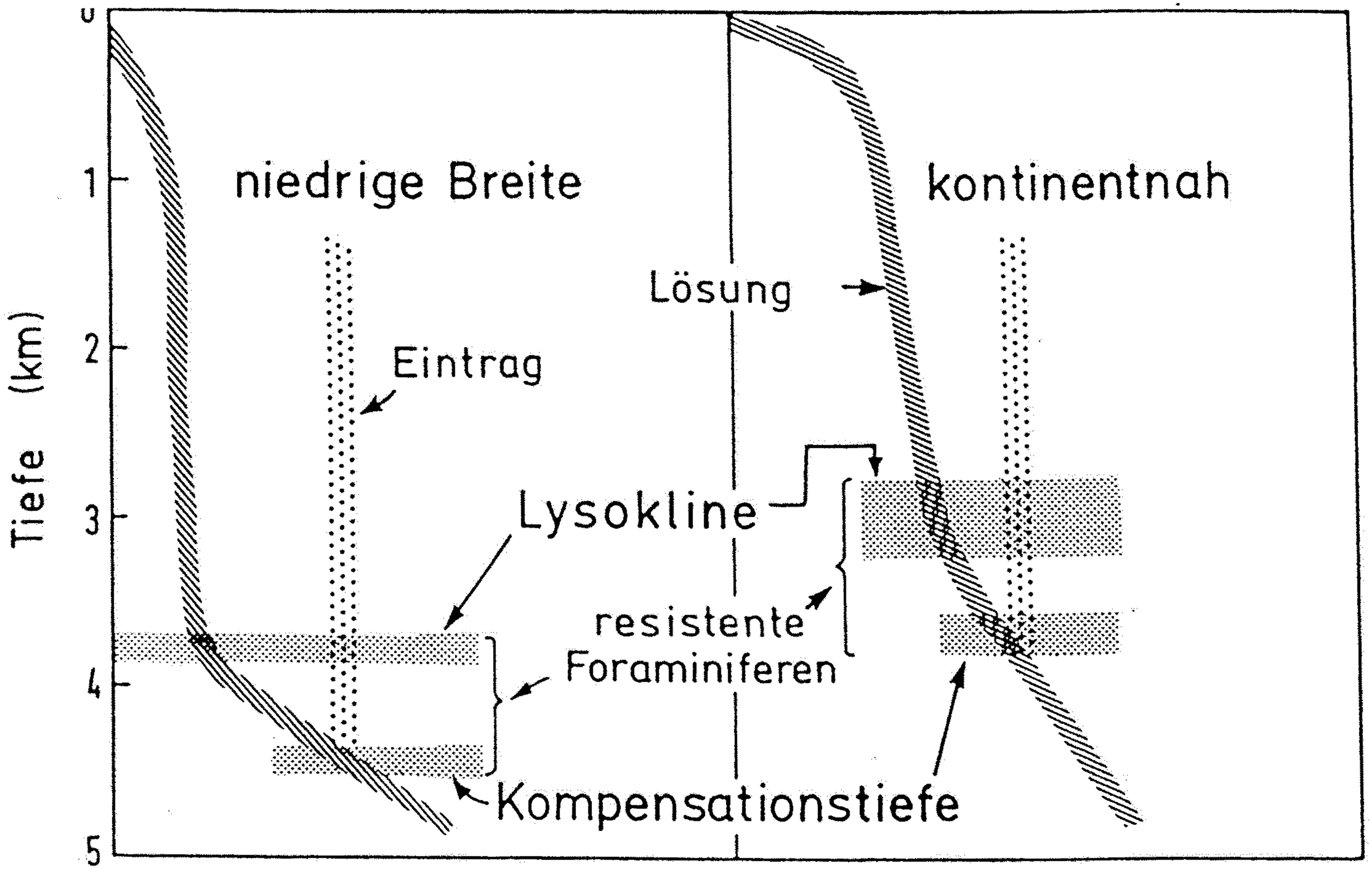

Steigende Rate von Eintrag und von Lösung

Schema der Beziehung zwischen der pelagischen Sedimentation von karbonatischen Skelettfragmenten, z.B. von Foraminiferen und Coccolithen, und der Karbonatlösung in größeren Tiefen des südöstlichen Pazifik (nach JENKYNS, 1986).

12.6

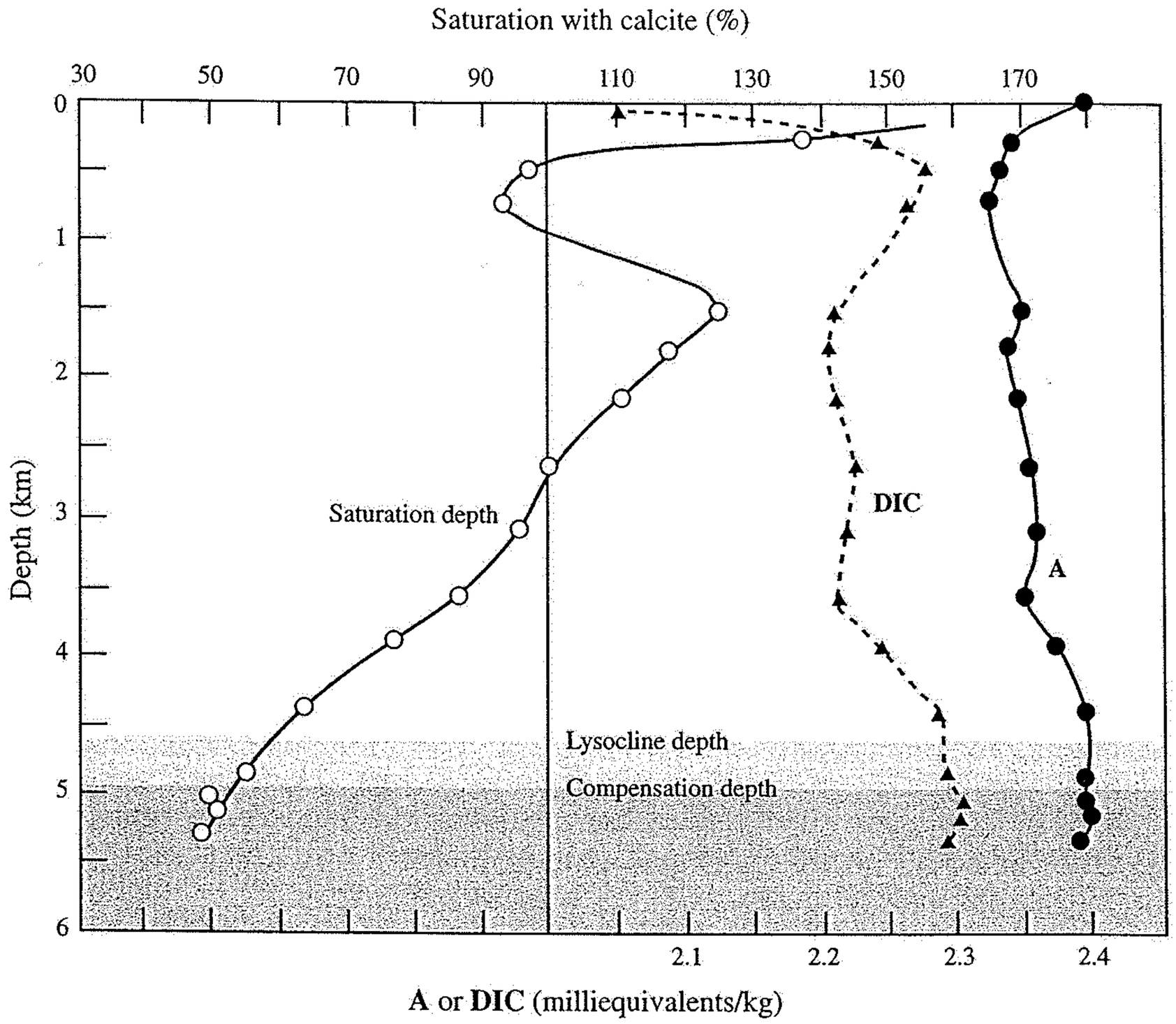

Figure 12.6 Total alkalinity, *A*, total dissolved inorganic carbon (*DIC*) concentration, and degree of calcite saturation as a function of depth in the equatorial Atlantic. Also indicated are the lysocline (see Chapter 11) at approximately 4600 m depth, where there is a perceptible amount of calcium carbonate dissolution, and the compensation depth at approximately 4900 m, below which all calcium carbonate should be dissolved. Since calcite dissolves at deeper depths than it should according to the calcite saturation index, this implies that plant and animal remains (which contain calcite) sink faster than they can be dissolved. (Adapted from Edmond and Gieskes[3].)

12.7

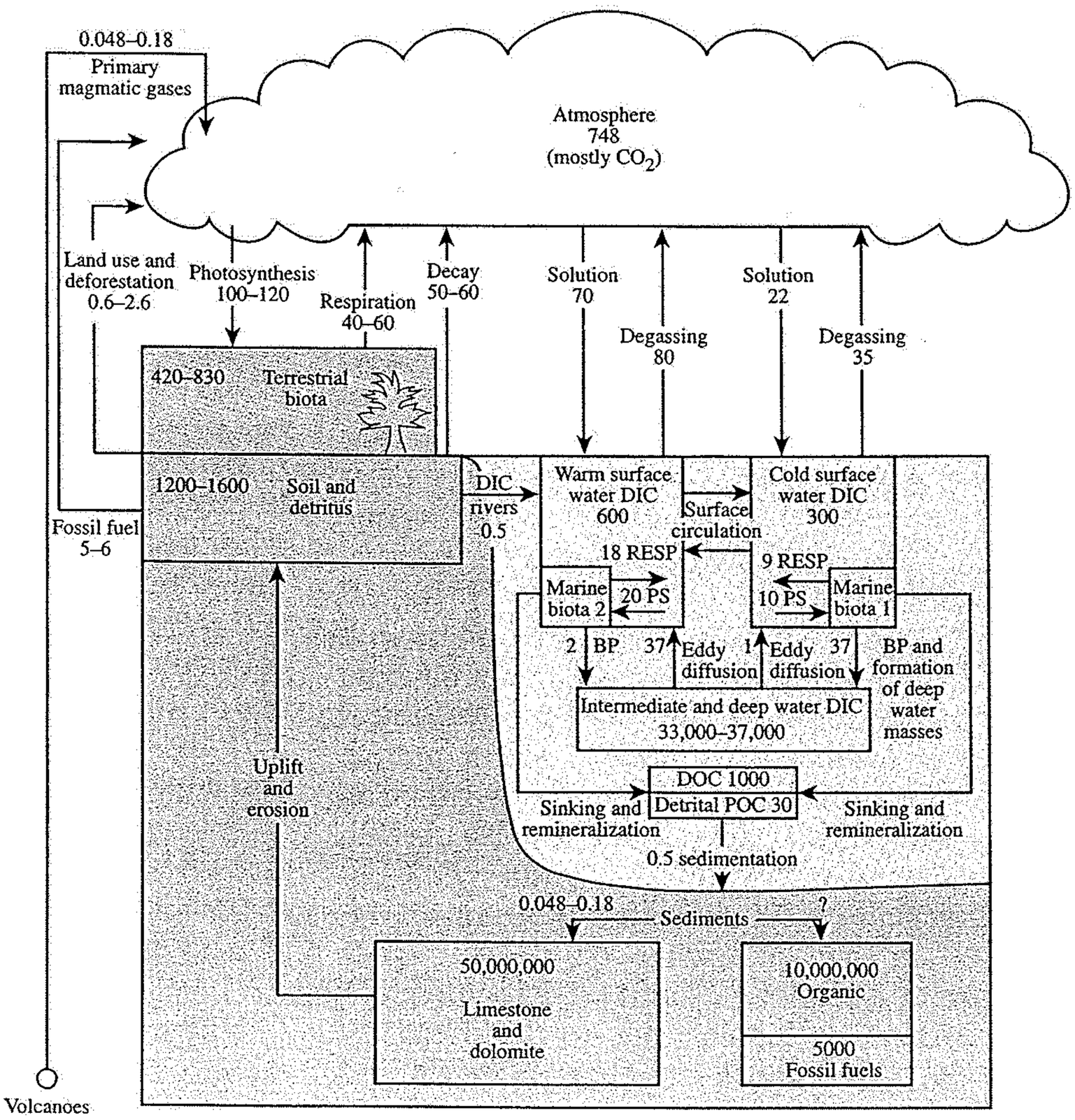

Figure 12.7 The biogeochemical cycle of carbon. The numbers show the current estimates of the major reservoirs (in units of 10^{15} gC) and fluxes (in units of 10^{15} gC/yr). BP = transport of carbon to the deep sea by the 'biological pump'; PS = conversion of dissolved inorganic carbon (*DIC*) into particulate organic carbon (*POC*) by photosynthesis; *DOC* = dissolved organic carbon; RESP = conversion of organic carbon into *DIC* by respiration. (Adapted from Post *et al.*[8] and Moore and Bolin[7].)

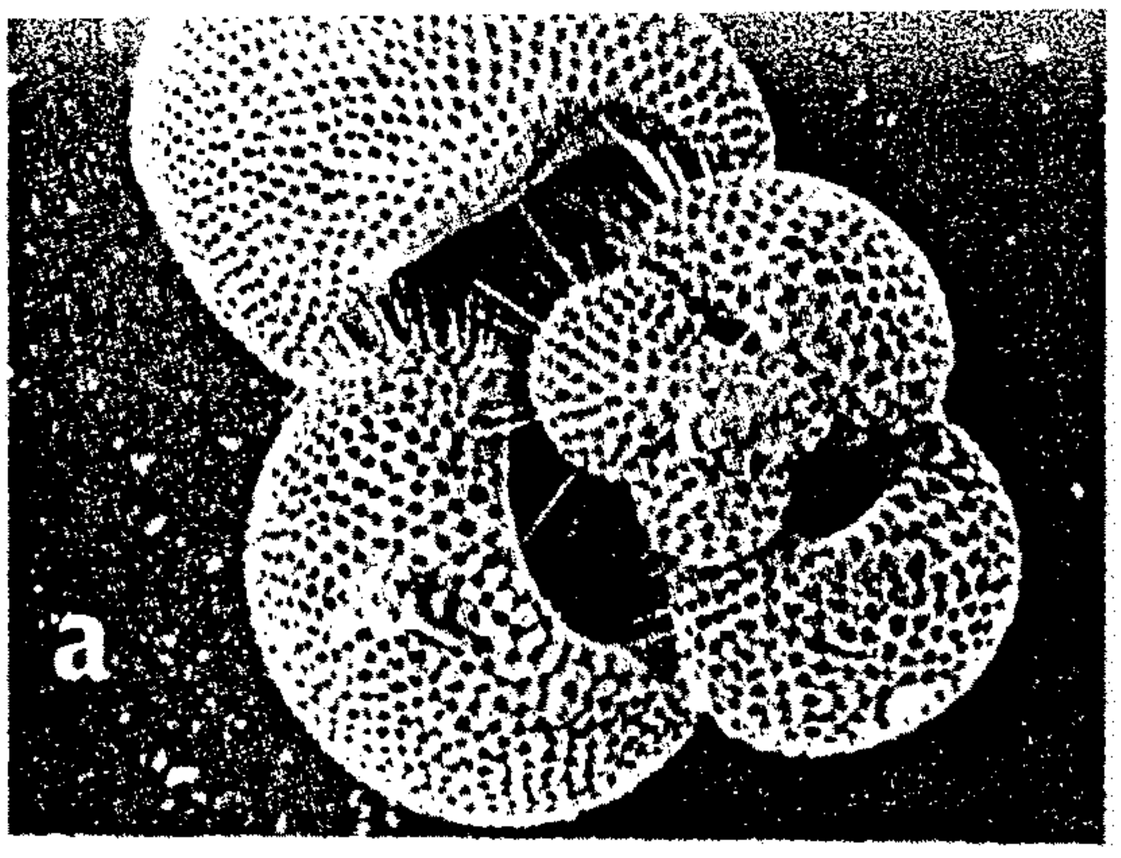

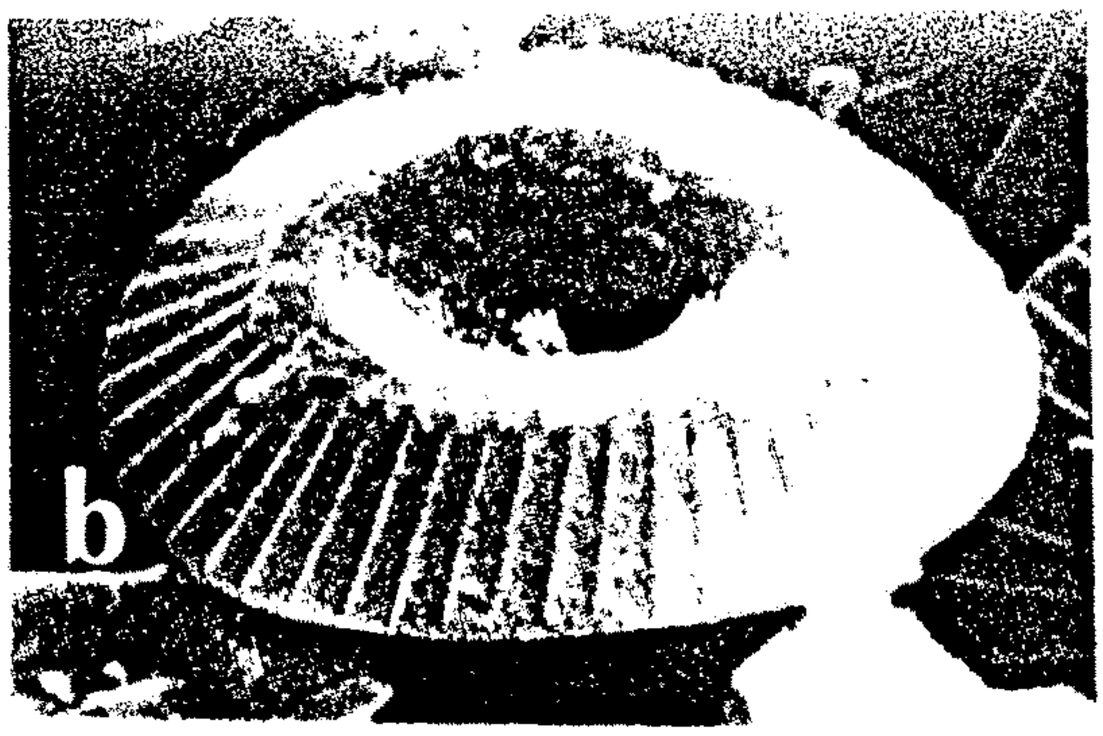

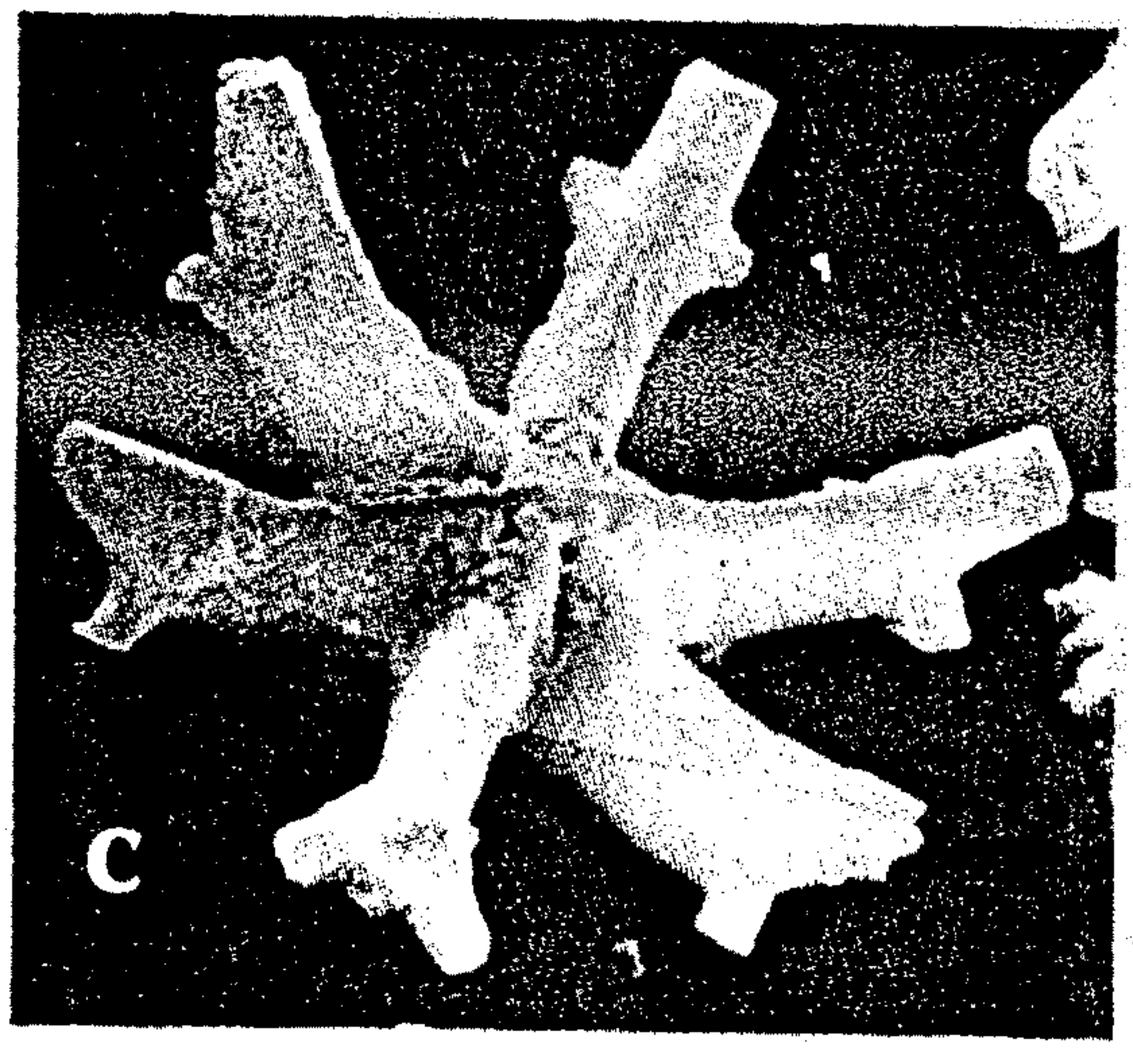

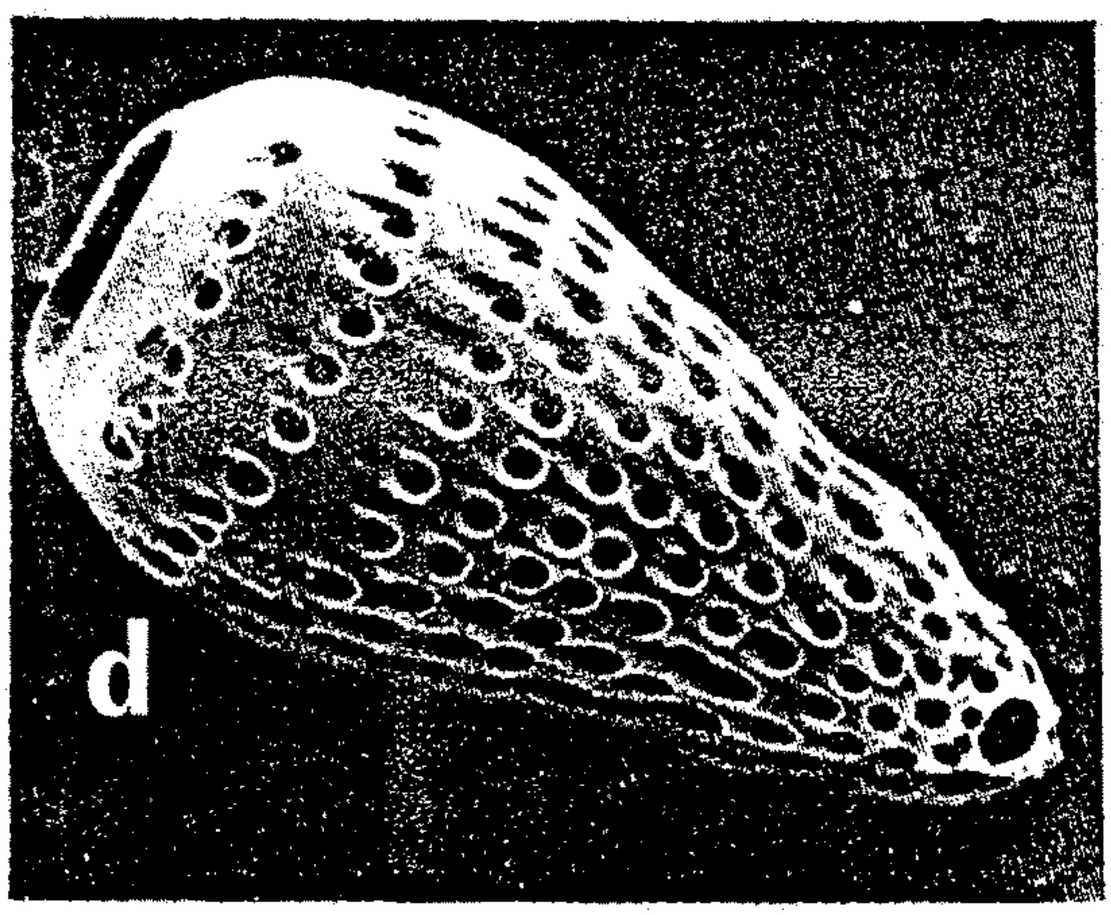

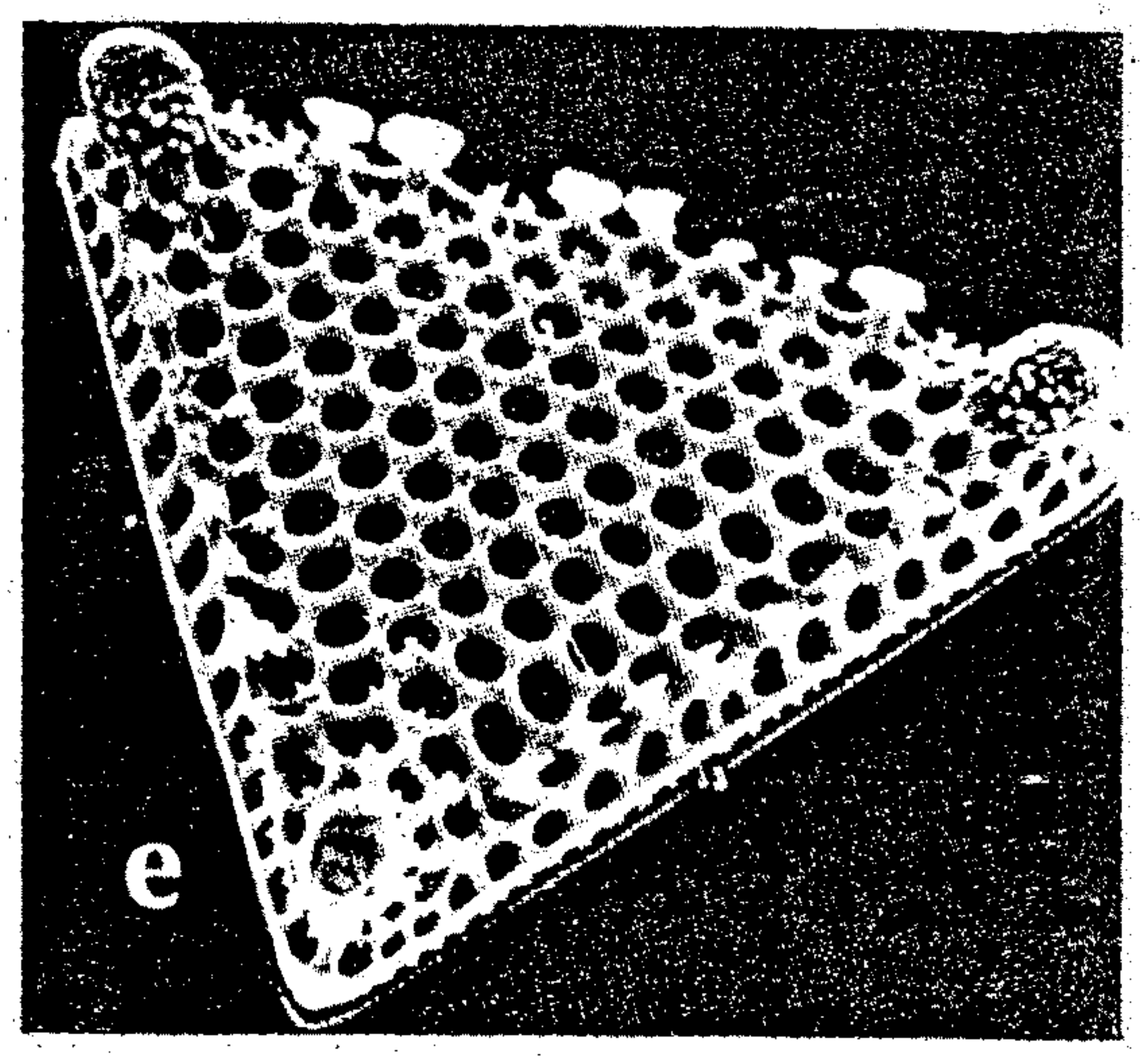

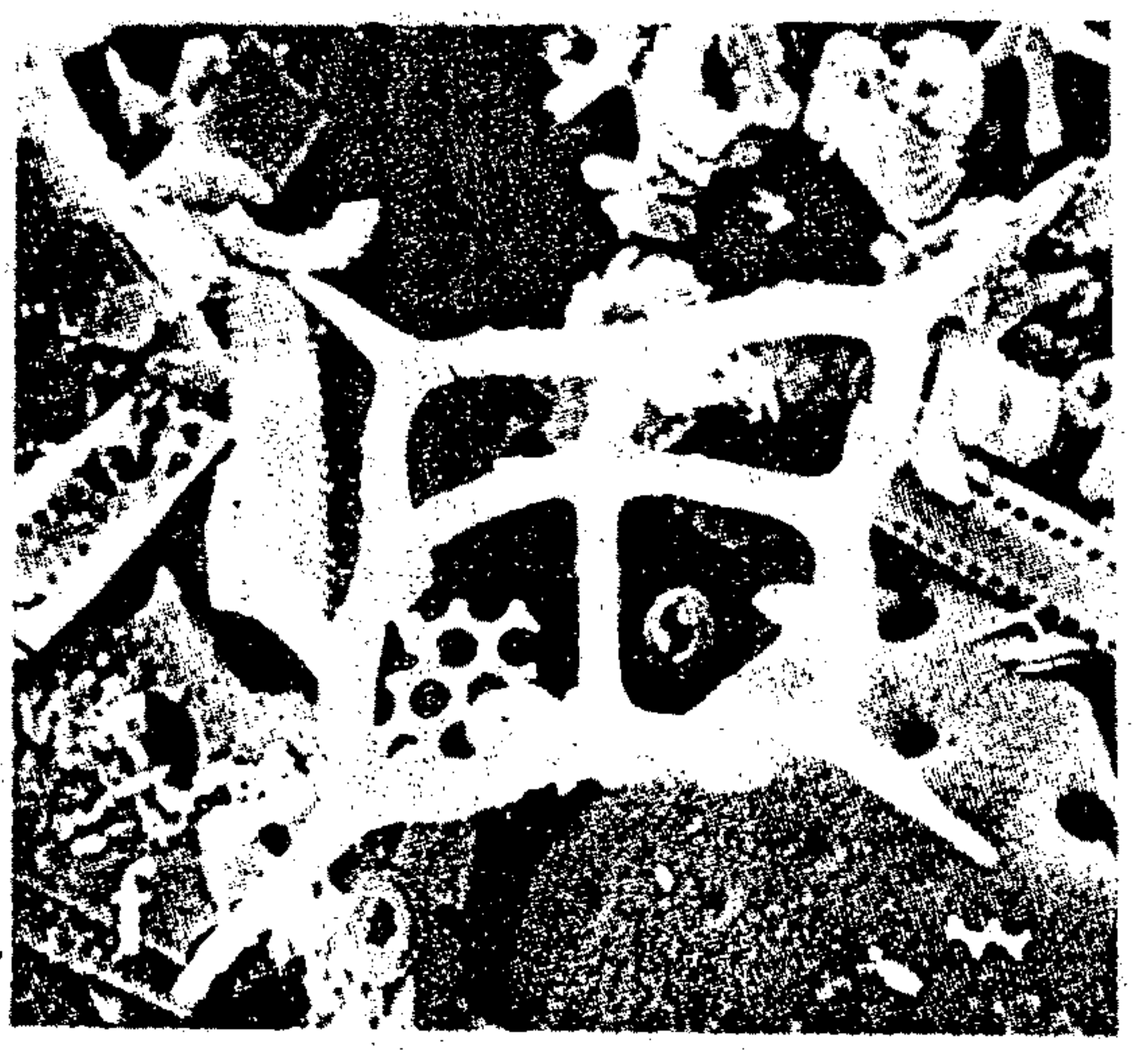

Figure 11.6 Skeletons of planktonic organisms constitut a major part of the sediments over extensive areas of th deep sea. The photographs, obtained from oceanic ooze with a scanning electron microscope, show calcareou [(a) foraminiferan, x 53; (b) coccolith, x 4000; (c) dis coaster, x 2700] and siliceous [(d) radiolarian, x 440; (e diatom, x 440; (f) silicoflagellate, x 970] planktoni remains (*Figure 7.7* from Kempe[9], with permission fror the Natural History Museum, London).

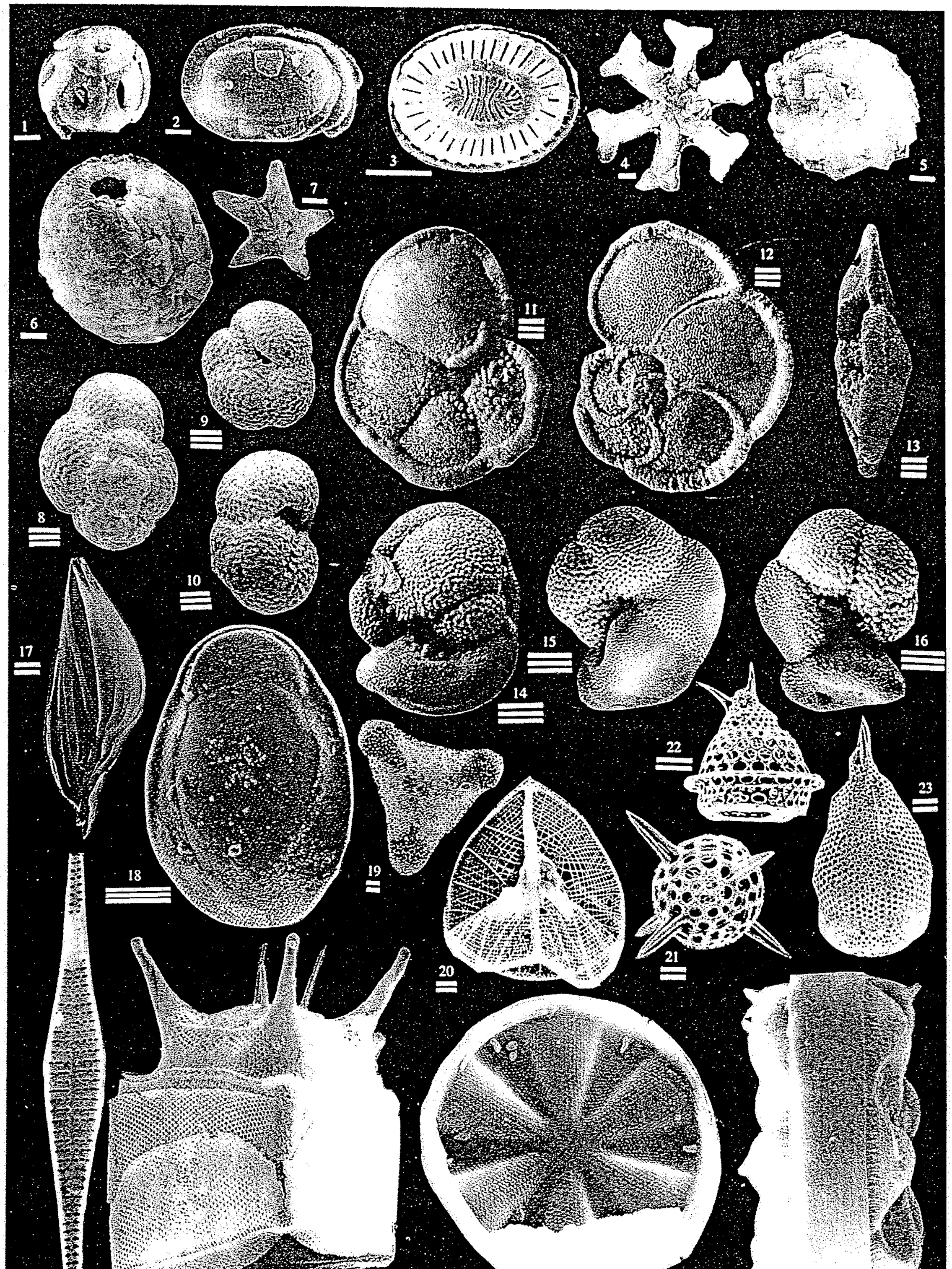

Fig. 54 Exemples d'espèces des principaux taxons impliqués dans la sédimentation biogène océanique.
C = Coccolithophoridés; D = Diatomées; Fb = Foraminifères benthiques; Fp = Foraminifères planctoniques; P = Ptéropodes; R = Radiolaires; L'échelle (trait blanc) est égale à 1 (–), 20 (=) et 100 (≡) µm.

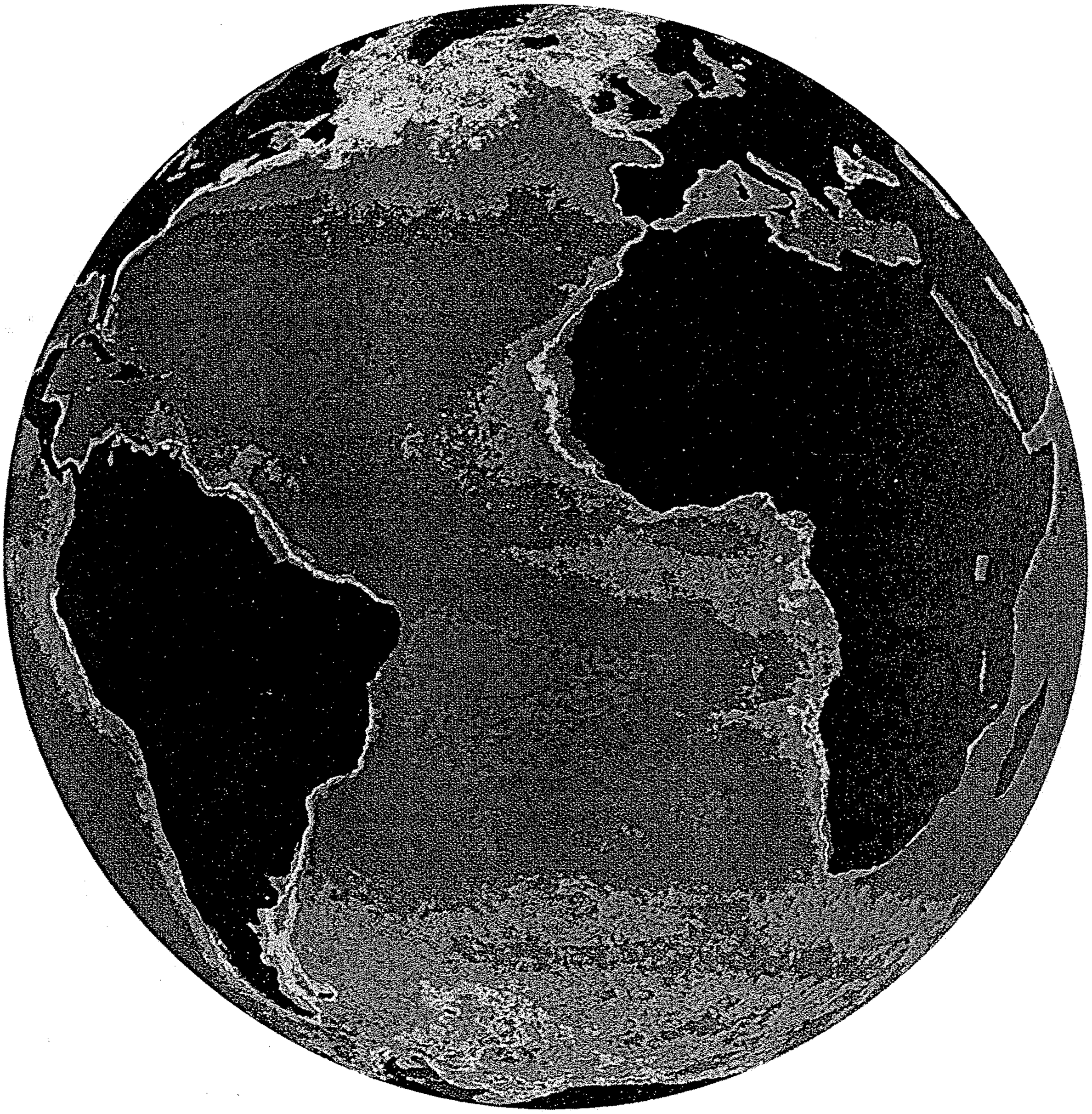

Figure 12.2. Distribution of phytoplankton in the ocean. Produced by scientists at the NASA Goddard Space Flight Center from data taken by the Coastal Zone Color Scanner on the *NIMBUS 7* satellite, the image is an ensemble of data from different seasons. Red, yellow: high concentrations; blue, purple: low concentrations. (*Source:* Courtesy of NASA.)

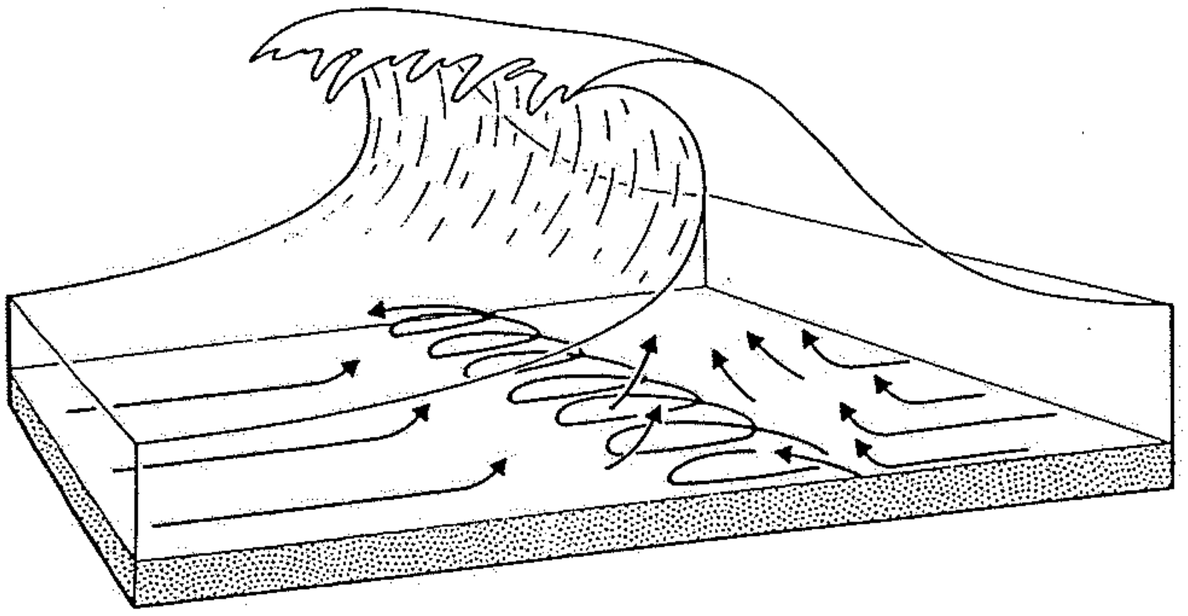

Fig. 7.5. Sediment transport associated with a breaking wave: coarse-grained sediment moves as bedload in a series of elliptical paths parallel to the coast, whilst finer sediment is suspended (modified after Ingle, 1966).

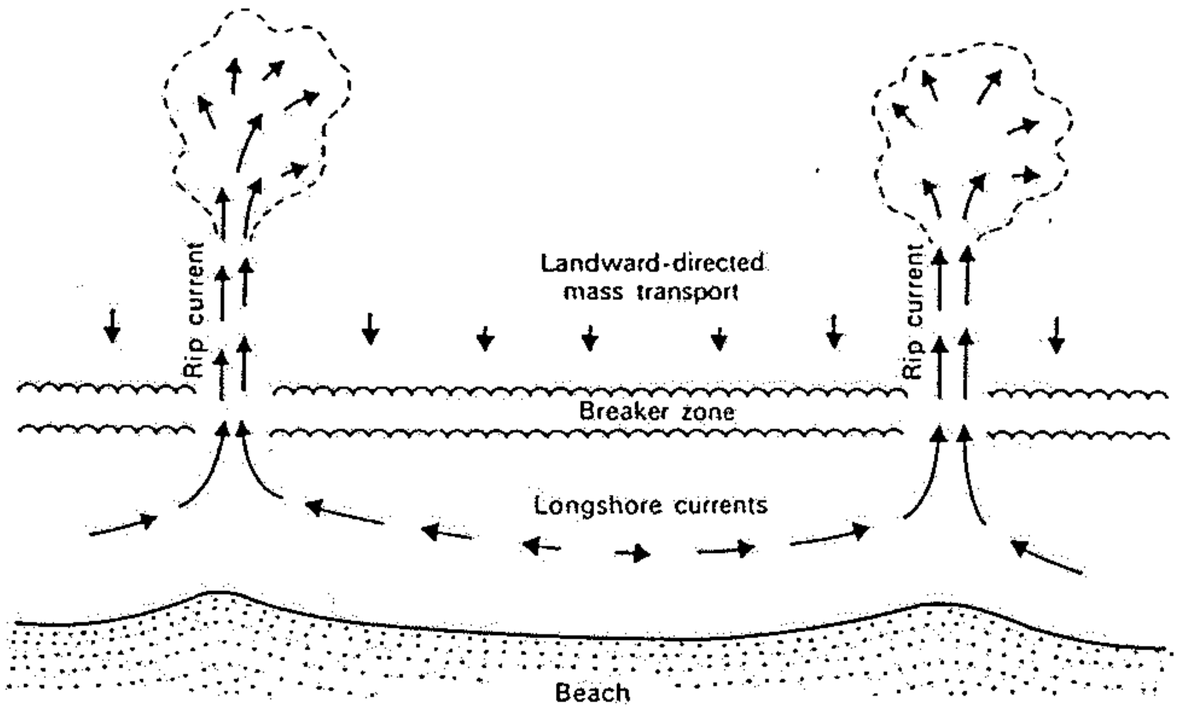

Fig. 7.6. Wave-induced nearshore circulation system (after Shepard and Inman, 1950).

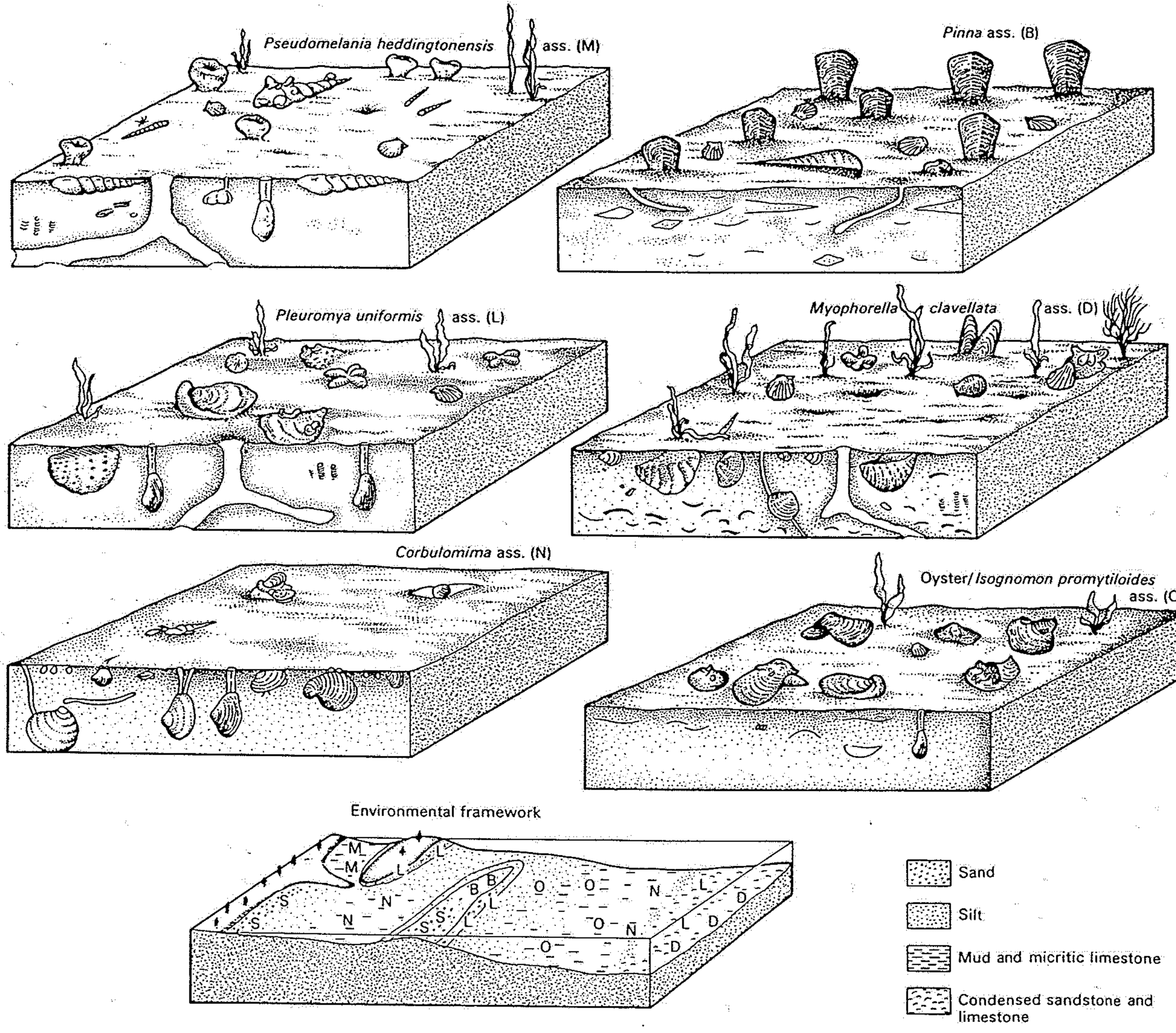

Fig. 9.27. Reconstruction of the Corallian (Jurassic) sublittoral environment (central block), in southern England and northern France, in terms of sediment type and benthic faunal associations. Attempted reconstructions of six faunal associations illustrate some fauna-substrate relationships and the inferred life habitats of some of the characteristic marine benthic faunas (from Fürsich, 1977).

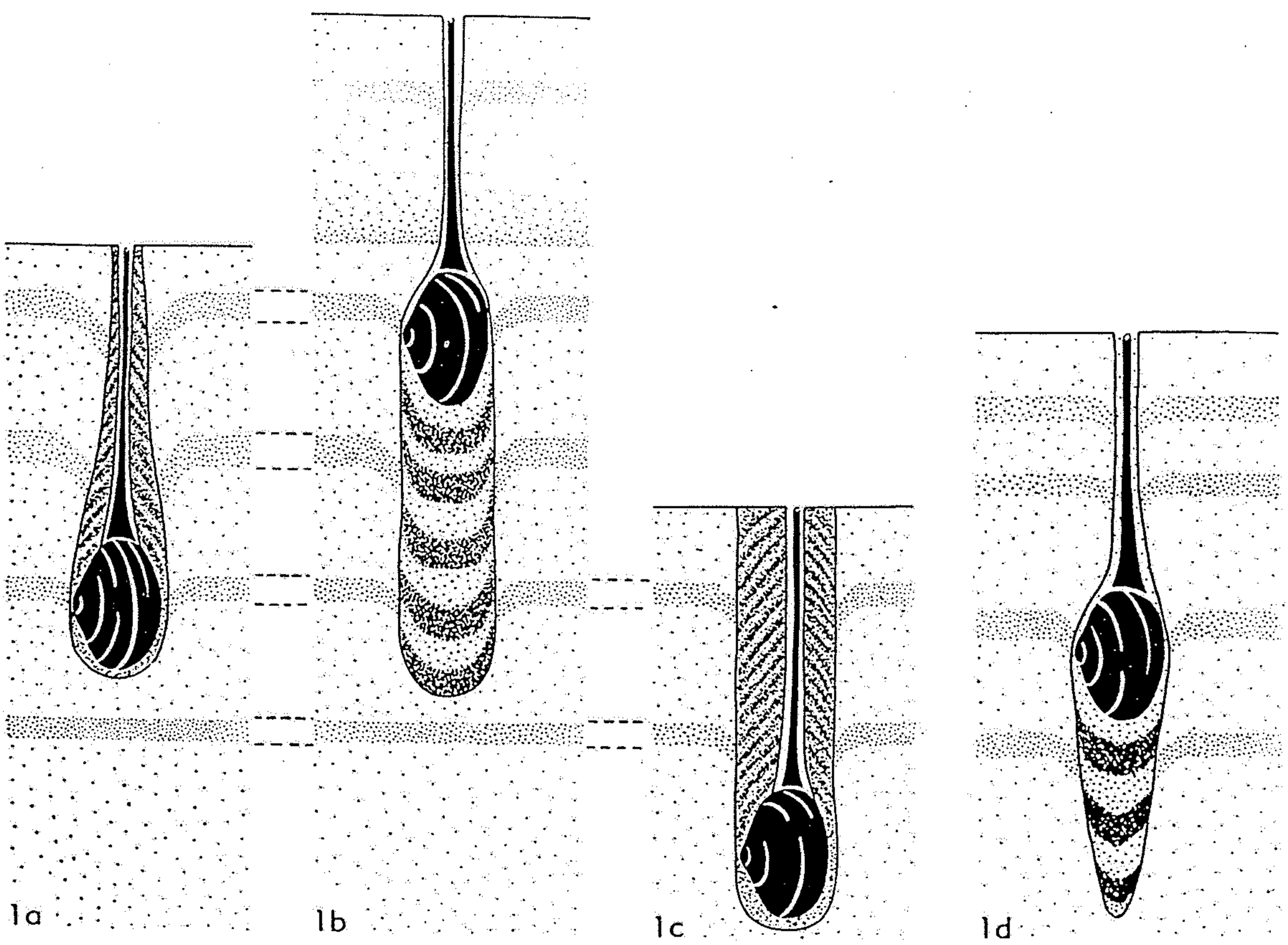

FIG. 14. Relationships of burrowing structures of unisiphonal pelecypods to rates of sedimentation (Reineck, 1958a).——*1a.* No sedimentation: a conical burrow forms above a growing pelecypod.——*1b.* Rapid sedimentation: as the animal moves upward through the sediment, a burrow is formed below equal to the animal's width.——*1c.* Erosion: animal migrates downward in sediment producing a burrow above it equal to its width.——*1d.* Very slow sedimentation: a growing pelecypod follows the accumulation of sediment upward creating a conical burrow beneath it.

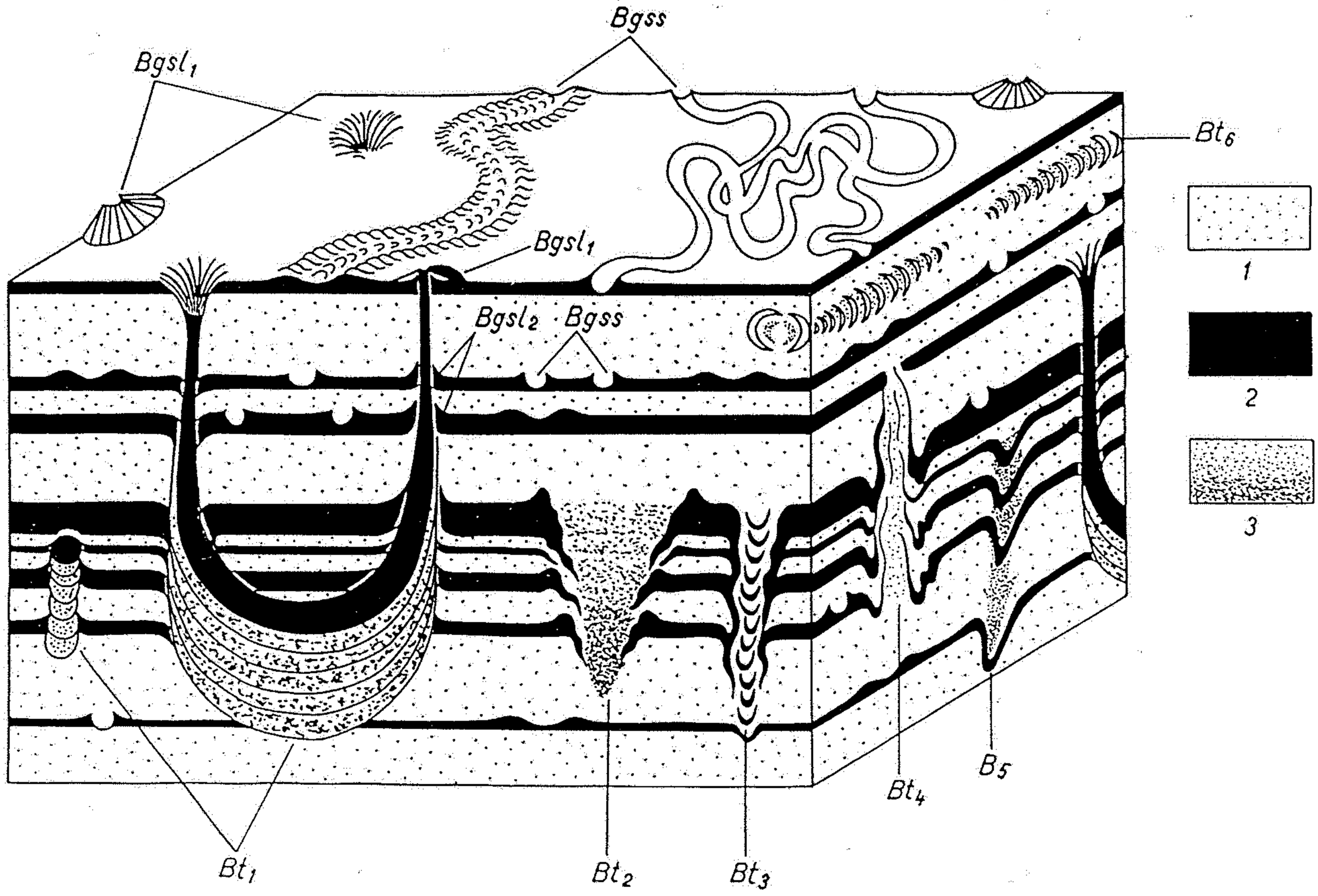

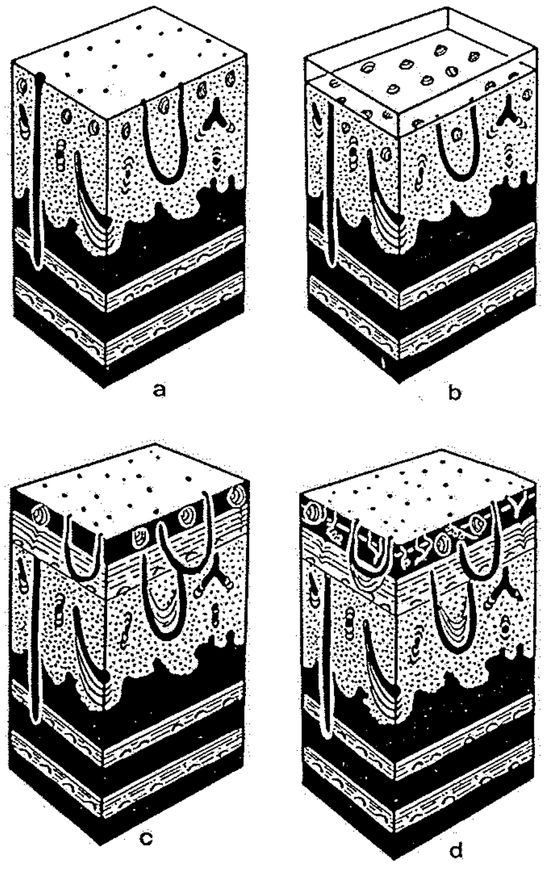

Fig. 550. Schematic representation of the genesis of storm sand layers, and associated features in the muddy shelf region under conditions of continuous mud deposition. a Situation before the heavy storm; dense population and intensive bioturbation. b Beginning of the heavy storm conditions, causing erosion and sedimentation of eroded shells. c Deposition of sand brought in from the coastal region. Mud is deposited quickly on the top as the waves of the storm die out. Molluscs move quickly through the newly deposited sediment and produce escape traces. Organisms living in the burrows extend or shift their burrows upwards. d Additional continuous deposition of mud brought in as mud-suspension by the rivers. There is an increase in animal population and bioturbation activity in the topmost newly deposited sediment layer. (After Reineck et al. 1968)

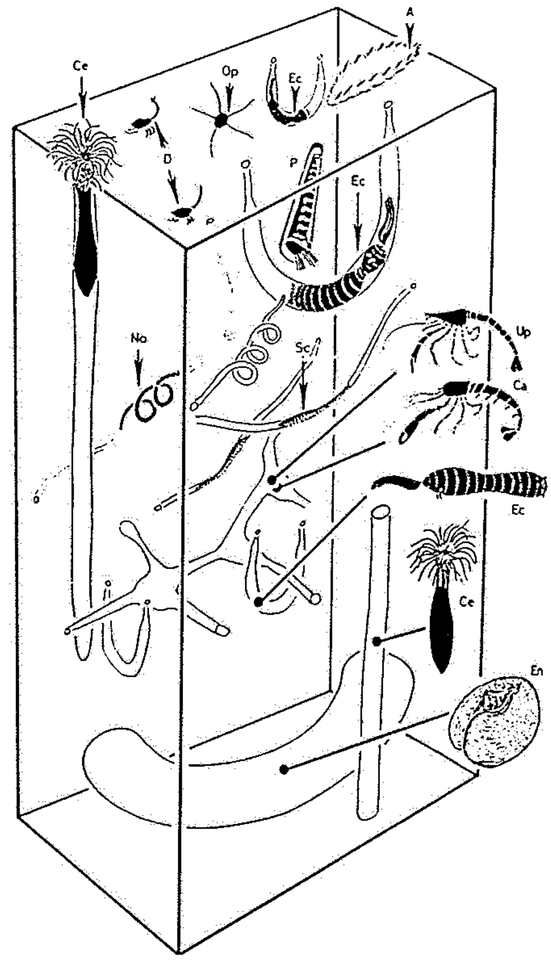

Fig. 551. Three-dimensional diagrammatic representation of some more important bioturbating animals. German Bay, southern North Sea. In the uppermost part of the diagram animals are shown in living position. Bioturbation patterns of some organisms along with their producer are figured. D = *Diastylis rathkei* (Cumacea), P = *Pectinaria koreni* or *P. auricoma*; En = *Echinocardium cordatum*, Ec = *Echiurus echiurus*; Ca = *Callianassa subterranea* and *C. helgolandica*; Up = *Upogebia deltaura*; and Ce = *Cerianthus lloydii*. Relative sizes of various animals are highly exaggerated, and the living depth is out of scale. (After Reineck et al. 1967)

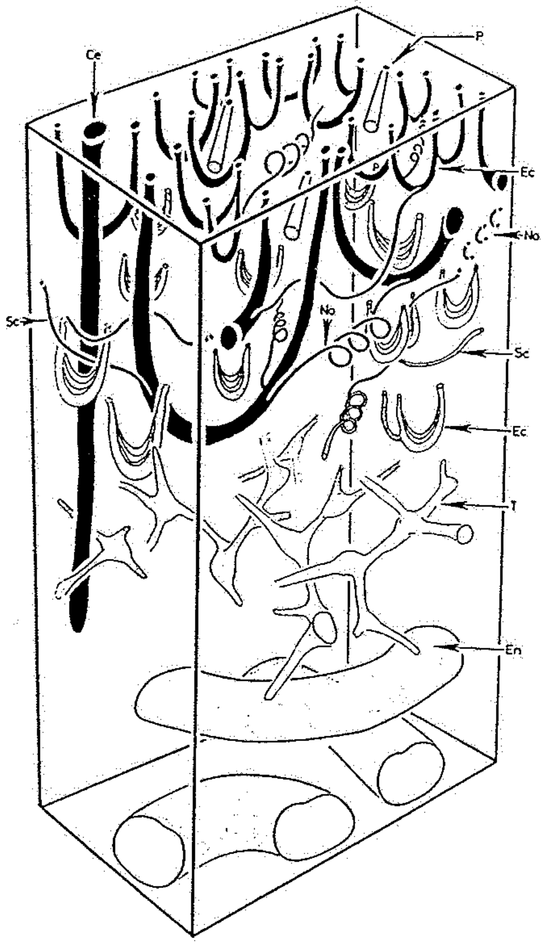

Fig. 552. Three-dimensional diagrammatic representation of burrows found in box-corer samples, German Bay, North Sea. Black burrows are occupied by living animals at the time of sampling. Ec = *Echiurus echiurus*; Sc = *Scalibregma inflatum*; No = *Notomastus latericeus*; Ce = *Cerianthus lloydii*; P = *Pectinaria koreni* and *P. auricoma*. White abandoned burrows are in the lower part of the section. T = *Upogebia deltaura* and/or *Callianassa subterranea* and *C. helgolandica*; No = *Notomastus latericeus*; *Echinocardium cordatum* (En). (After Reineck et al. 1967)

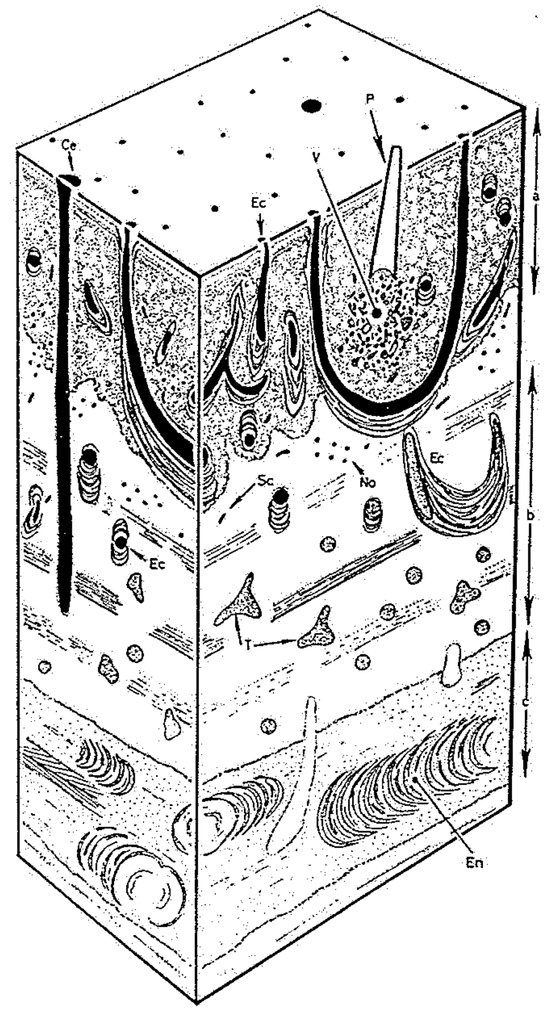

Fig. 553. Schematic block diagram of box-corer samples from the muddy sediments, south of Heligoland. The topmost layer (a) shows primary bedding completely destroyed by *Echiurus*. Below it another layer (b) shows a lower degree of bioturbation, produced by other benthic organisms (burrows of Thalassinidae). Thick sand layer (c) with bioturbation structures of *Echinocardium cordatum* (En). Multi-walled, U-shaped burrows of *Echiurus* (Ec); shell nests (V) by *Pectinaria* (P); burrows of *Cerianthus lloydii* (Ce) and *Notomastus latericeus*. (After Reineck et al. 1967)

schen mittlerer Hochwasserlinie (MTHWL) und mittlerer Niedrigwasserlinie (MTNWL). Das Hauptvorkommen der Tierarten liegt jeweils im Bereich der ausgezogenen schwarzen Linien; geringere Populationsdichten oder sporadische Funde sind durch nicht eingegrenzte weiße Felder angedeutet.
Population zones of important macrobenthic animals in a intertidal flat located in a bay. The main occurrence of individual species is shown by the area between the black lines; thin population and sporadic occurrences are shown by the white areas (borders are not marked by black lines).

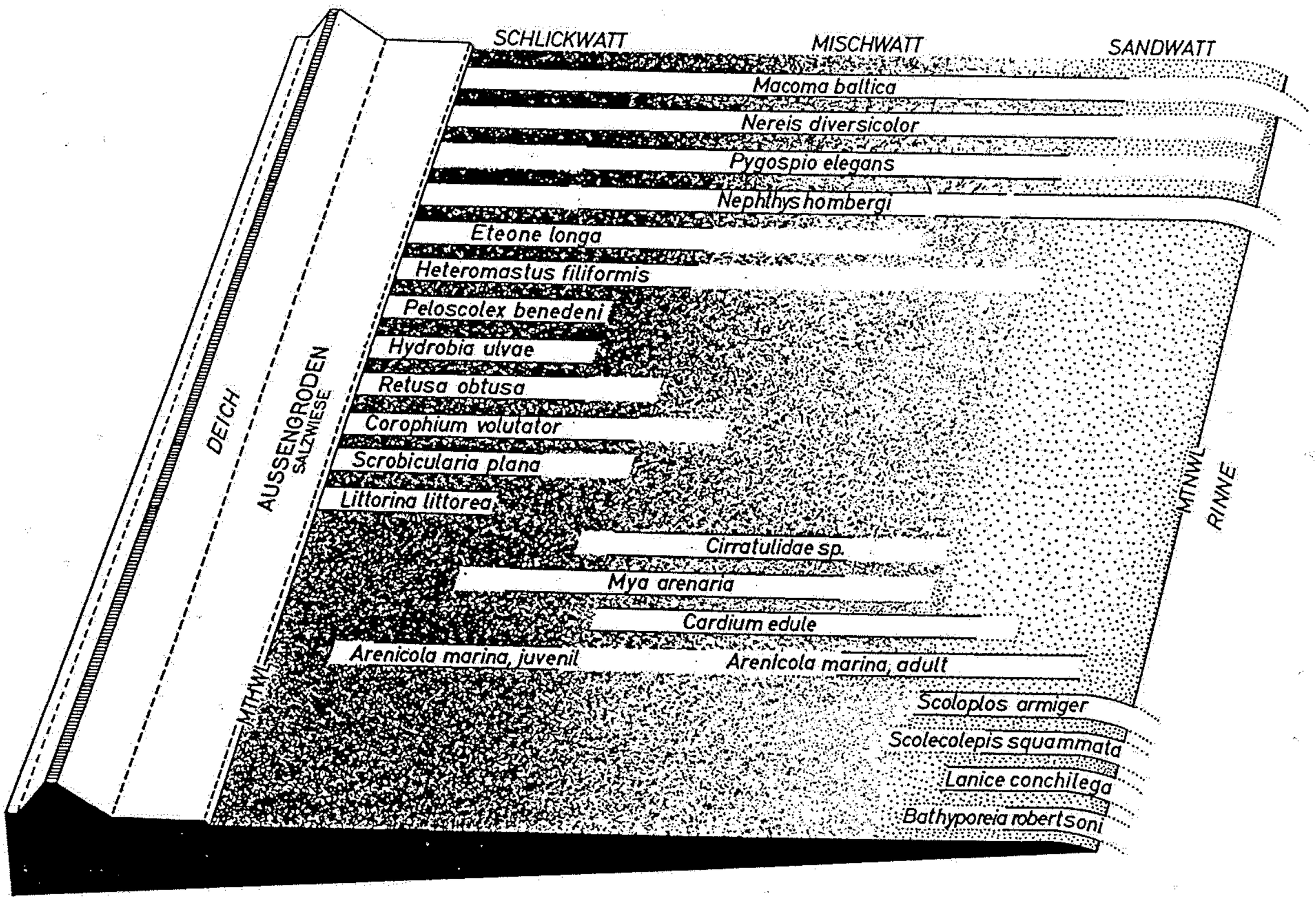

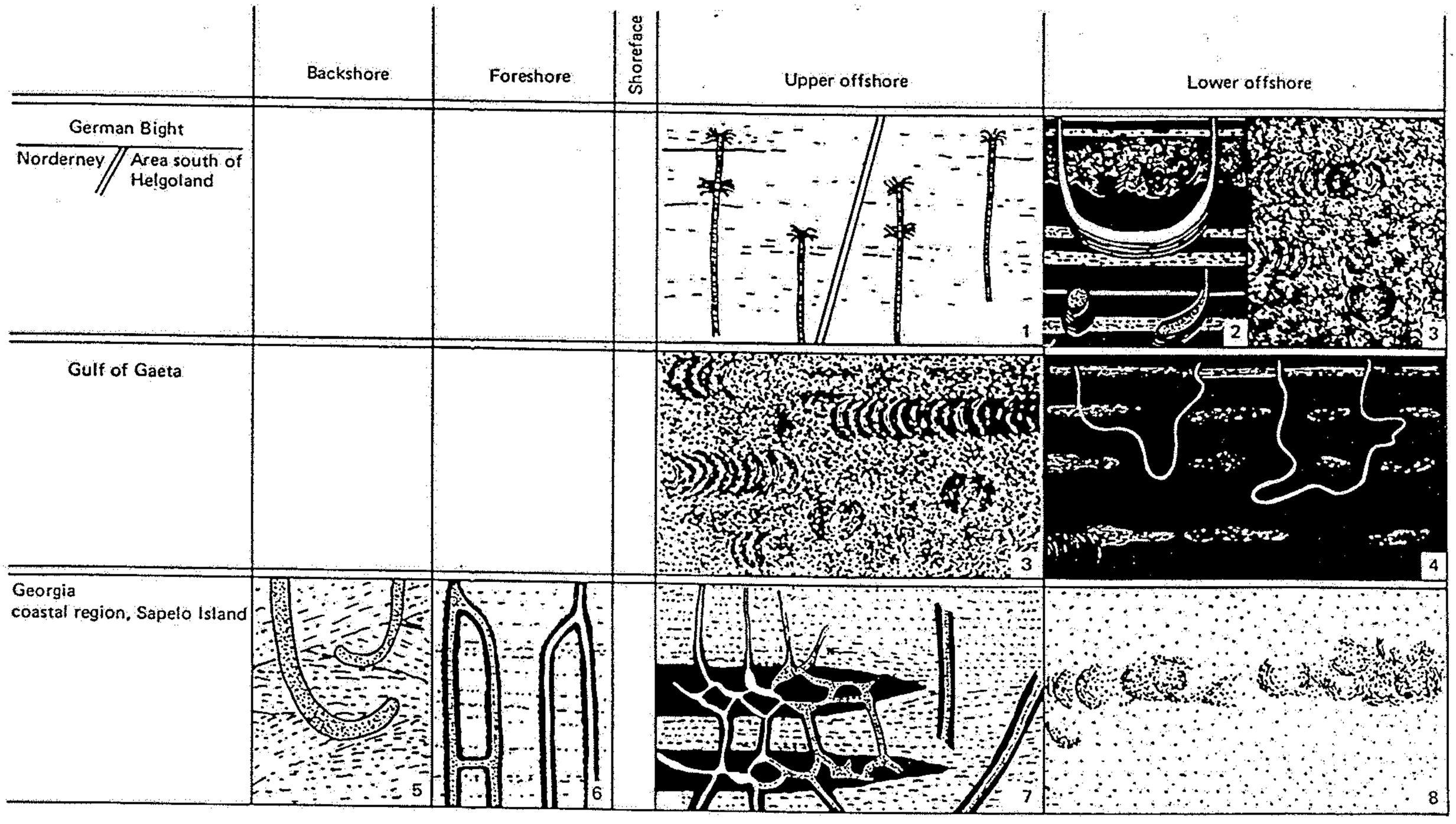

Fig. 20.6 Zonation of ichnofacies in shallow nearshore environments of the German Bight, Gulf of Gaeta, and Georgia coastal region. 1, *Lanice conchilega* ichnofacies. 2, *Echiurus echiurus* ichnofacies. 3, areas dominated by *Echinocardium cordatum* traces. 4, *Nephthys hombergi* ichnofacies. 5, *Ocypode quadrata* ichnofacies. 6, *Callianassa major* ichnofacies. 7, *Callianassa biformis* ichnofacies. 8, *Moira atropos* ichnofacies.

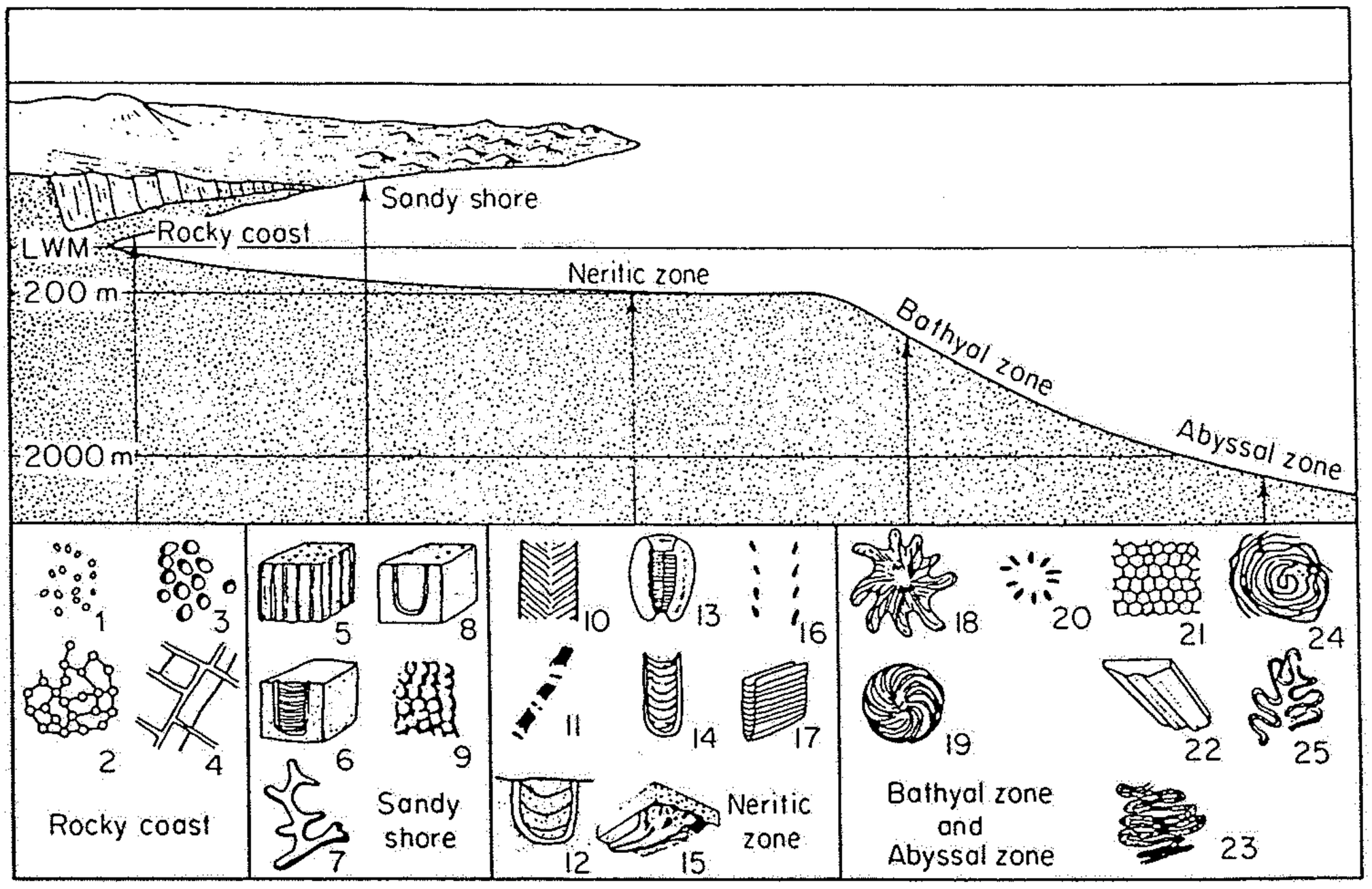

Fig. 5-30 Summary diagram of the most common marine facies and depth-related trace fossils. 1–4 all borings; 5 *Skolithus*, 6 *Diplocraterion*, 7, 8 other deep burrows, 9 detail of wall of *Ophiomorpha* burrow; 10 *Cruziana*; 11, 13, 16 other trilobite traces; 12, 14, 15 and 17 feeding burrows, with web-like "spreiten" between the vertical parts of the U tubes; 18 *Zoophycus*; 19 another complex feeding burrow; 20 a radiating trace; 21 *Paleodictyon*, 23, 24, 25 typical meandering or spiral surface traces; 22 enlarged portion of one section of a meandering bilobate grazing trail, preserved as a sole mark. (From Crimes in Frey, *The Study of Trace Fossils: a Synthesis of Principles, Problems, and Procedures in Ichnology*, 1975, Springer-Verlag, p. 118.)

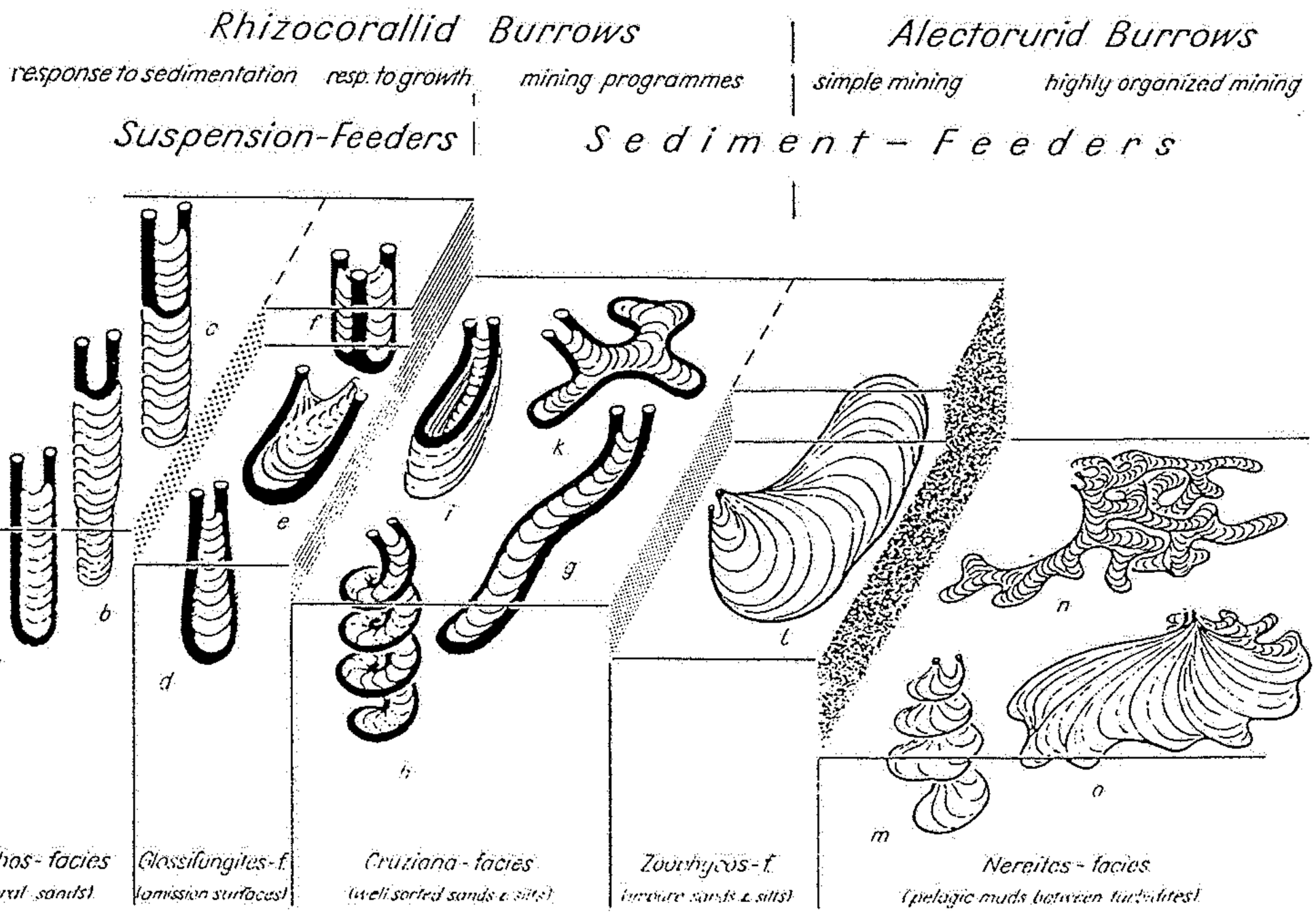

Fig. 247. Bathimetric zonation of trace fossils with spreites. There is a general gradation from vertical burrows in shallow-water deposits to increasingly patterned and horizontal burrows of deep water deposits. (After Seilacher 1967)

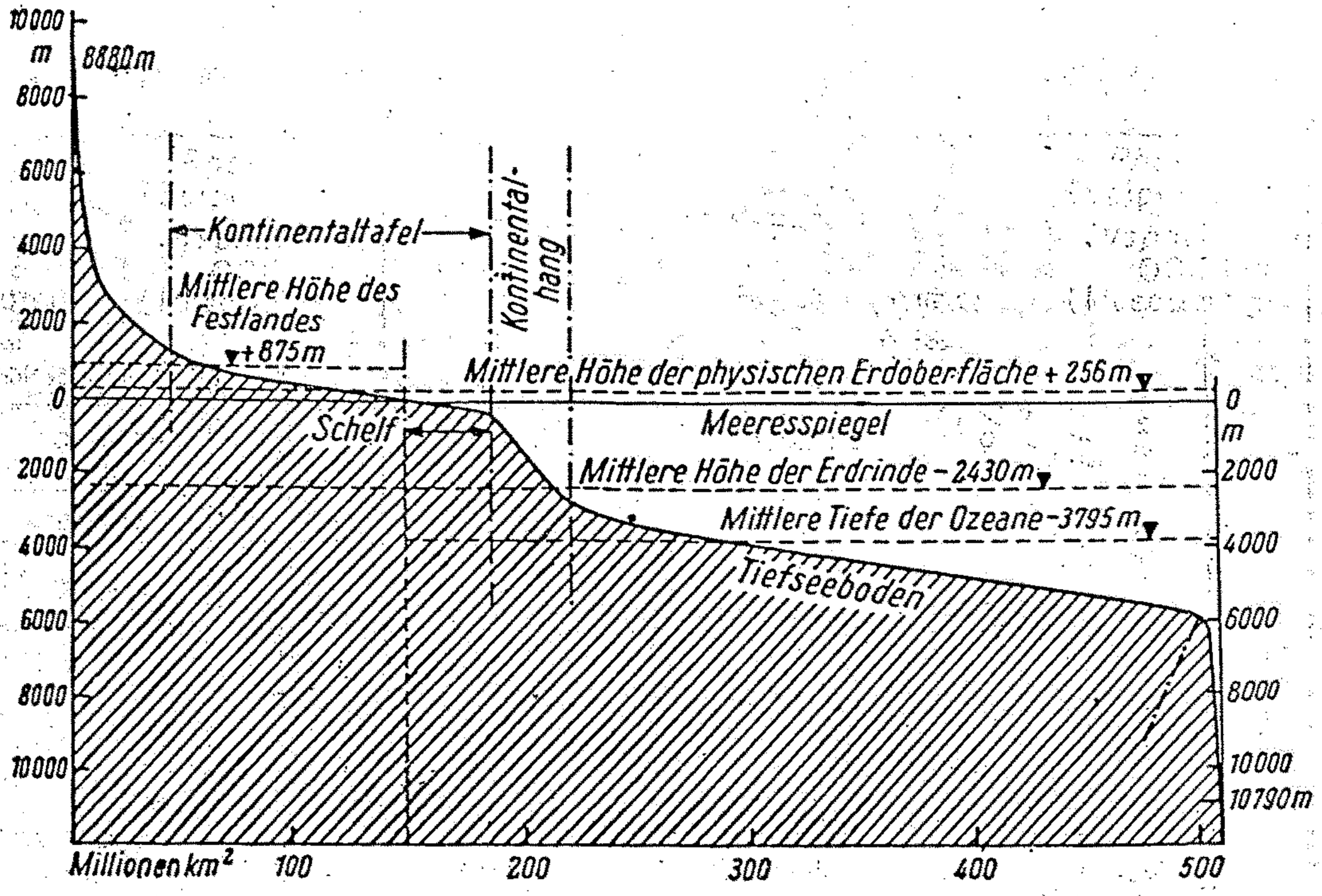

Abb. 2. Hypsographische Kurve der Erdkruste. (Nach E. Kossina.)

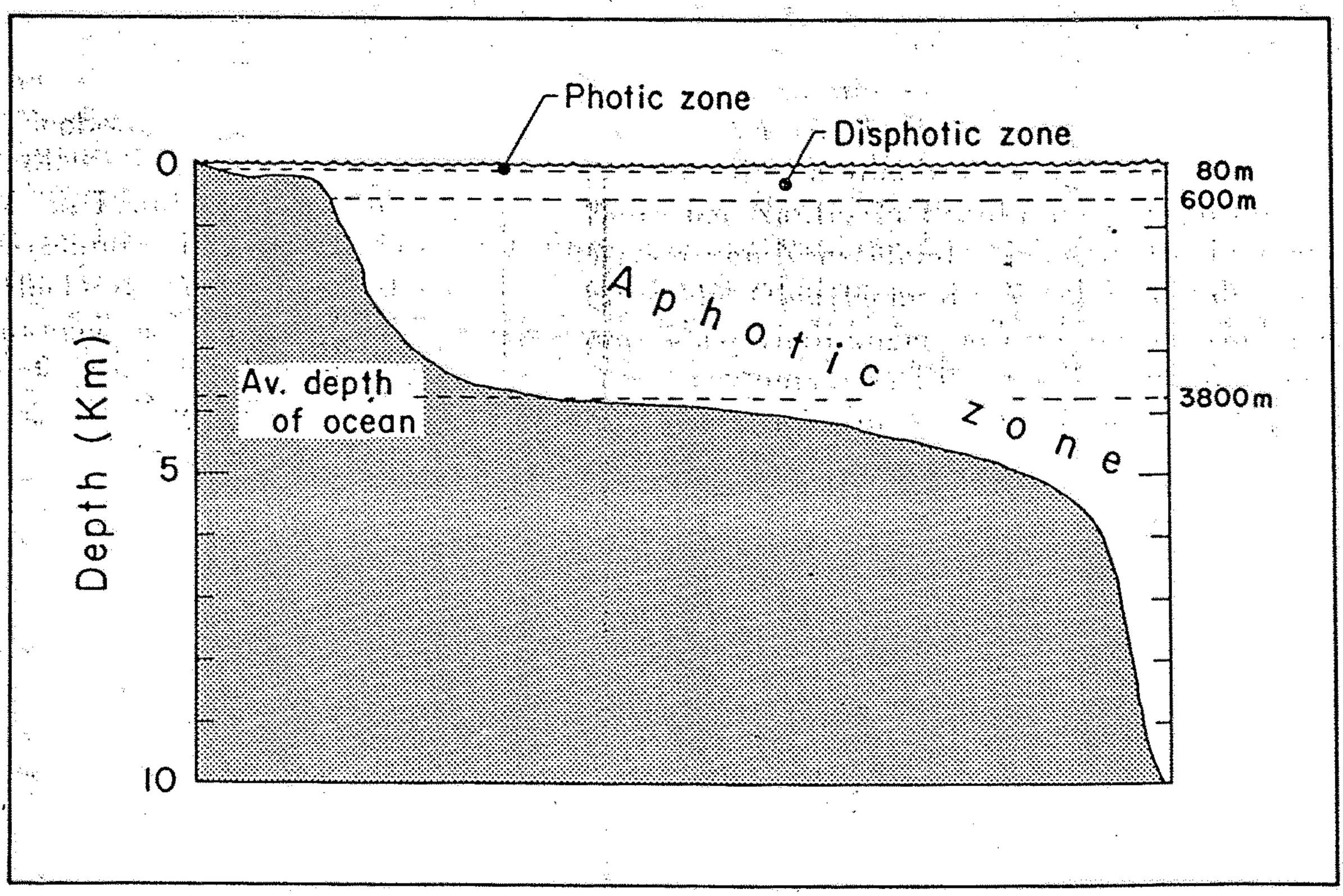

Figure 12-3 *Relationships of three major depth zones in the oceans based on light penetration compared with schematic profile of ocean depths. Text defines terms. (After J. W. Hedgpeth, 1957a, Fig. 3, p. 22.)*

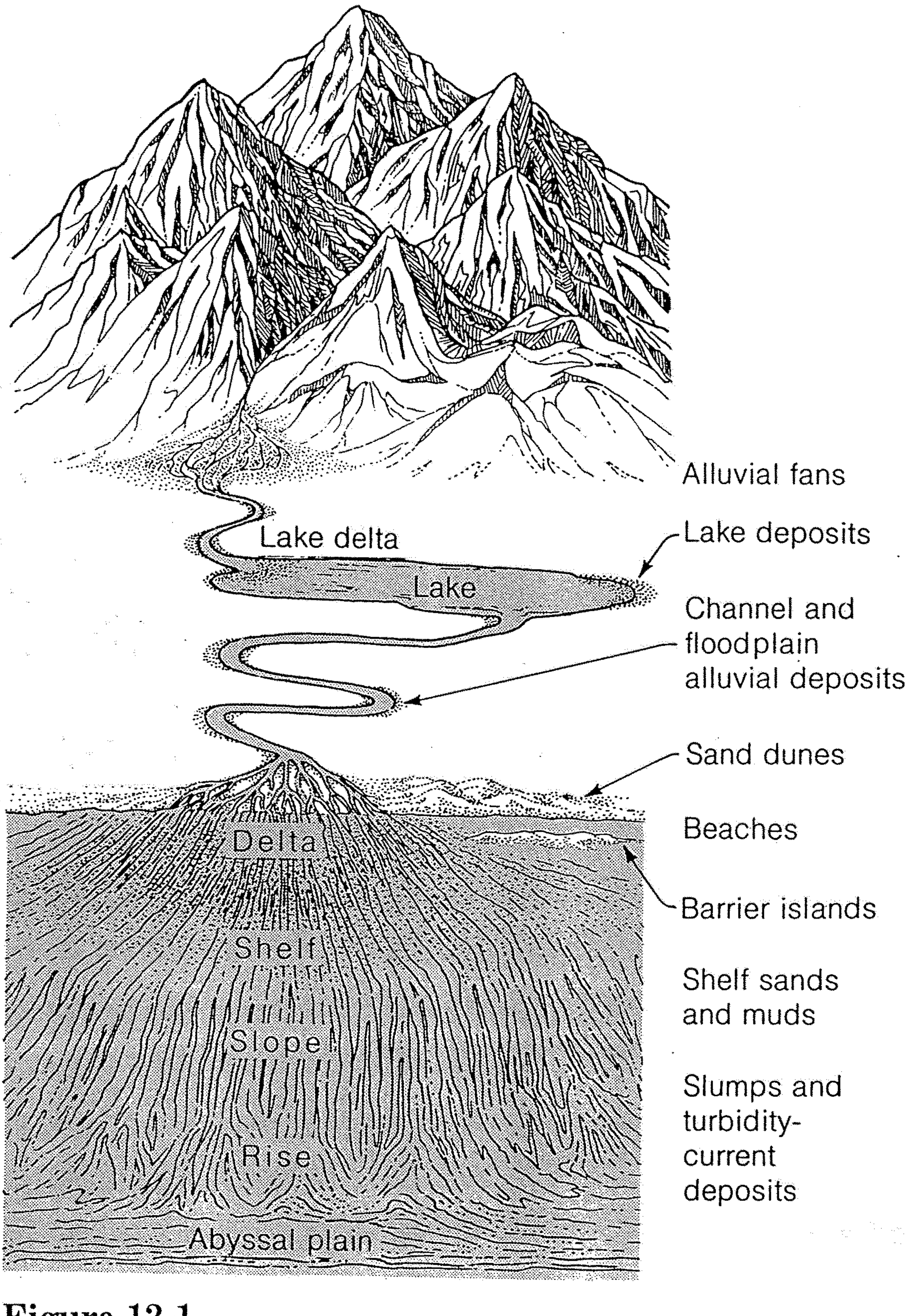

Figure 12-1

The downhill path of transportation and deposition takes solid particles from the heights of mountains to the depths of the oceans, many different sedimentary environments of physical deposition being encountered along the way.

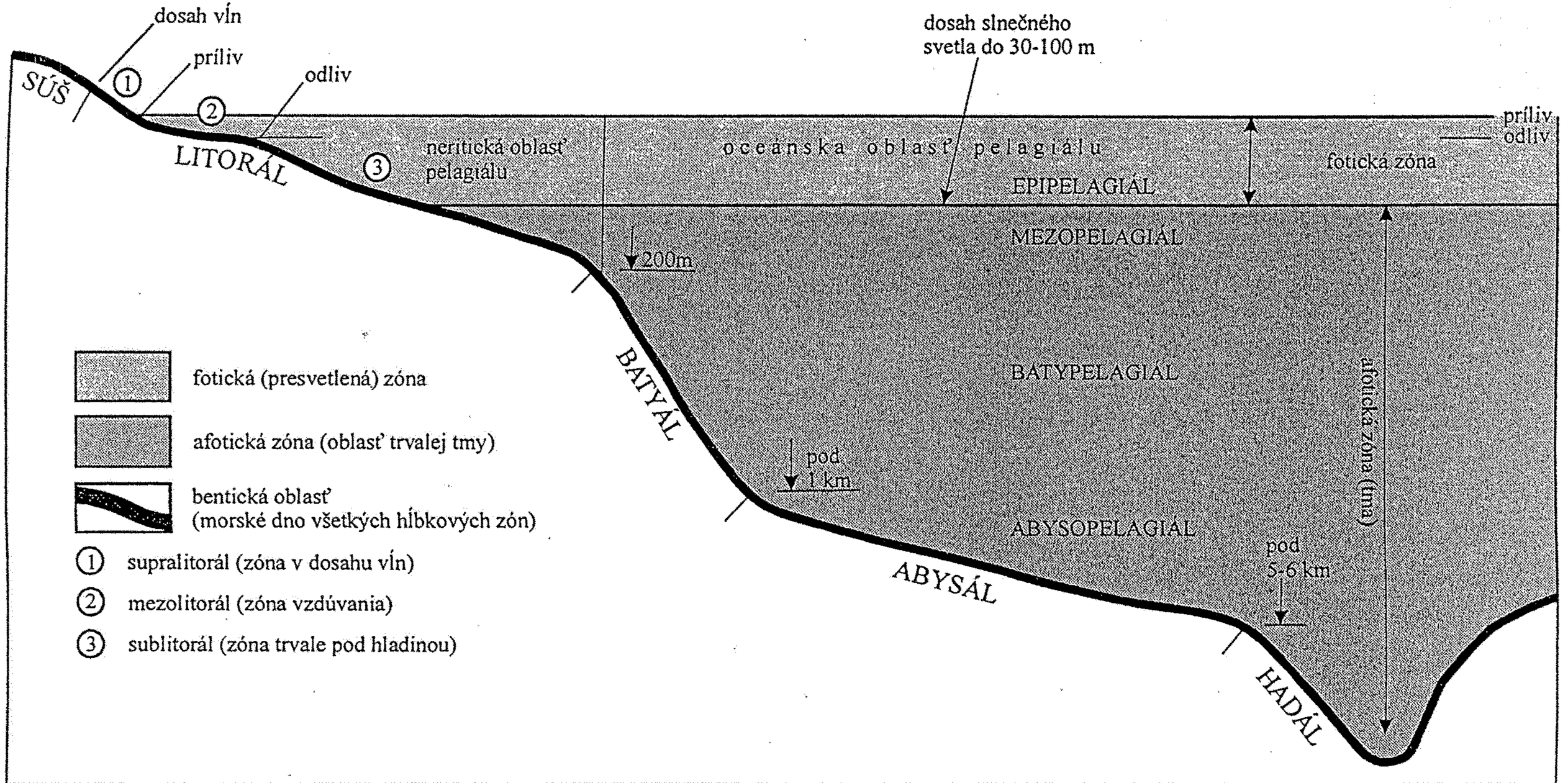

Obr. 18.9. Členenie životného prostredia morských organizmov pri zohľadnenní hĺbky. (upravené podľa Tardenta 1979 ex Hensela 1983)

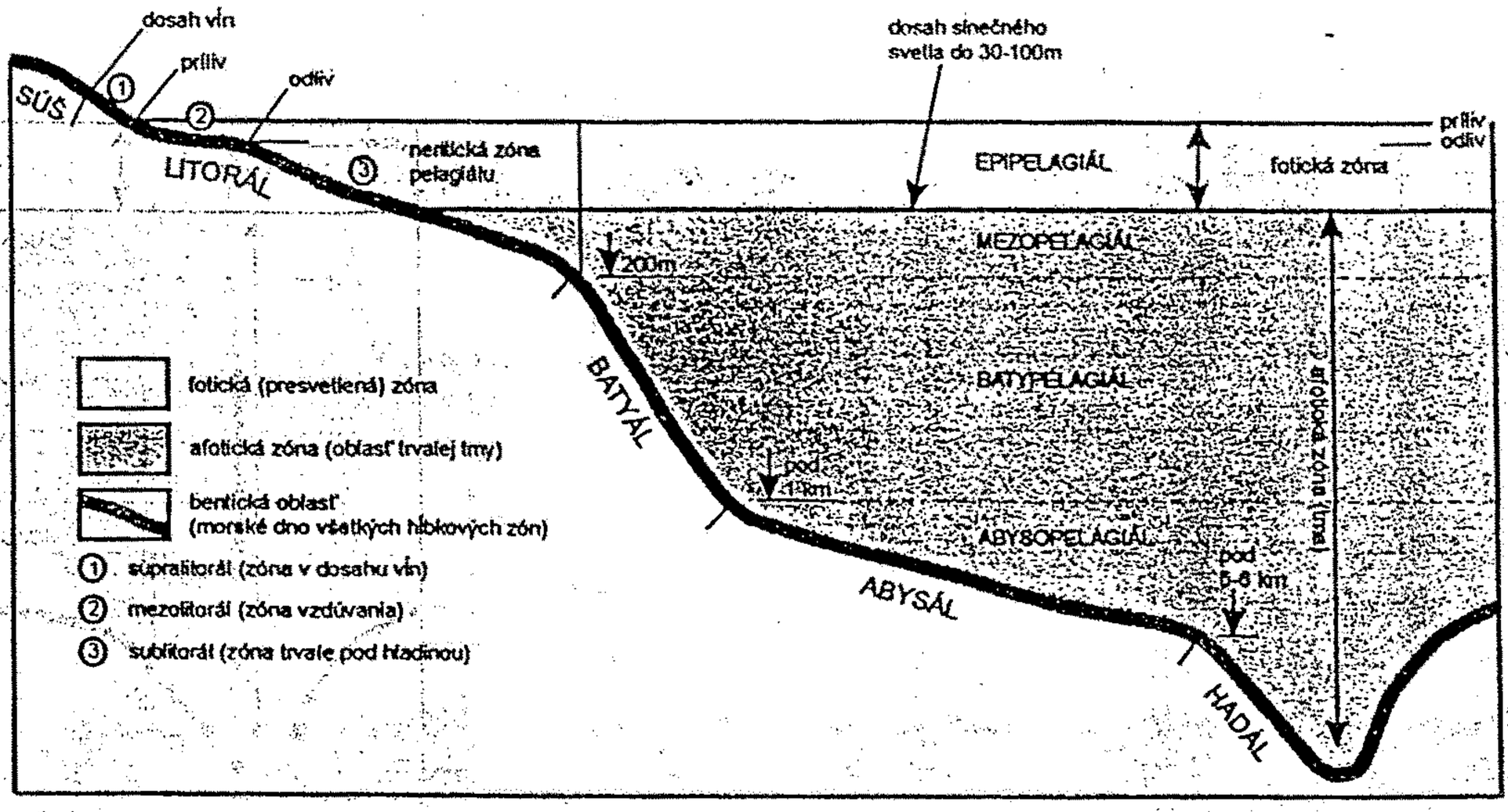

obr. 18.9. Základné členenie morských ekosystémov zohľadňujúcich hĺbku. Hadál zaberá oblasť trenčov, oblasť bentická je dnový ekosys-

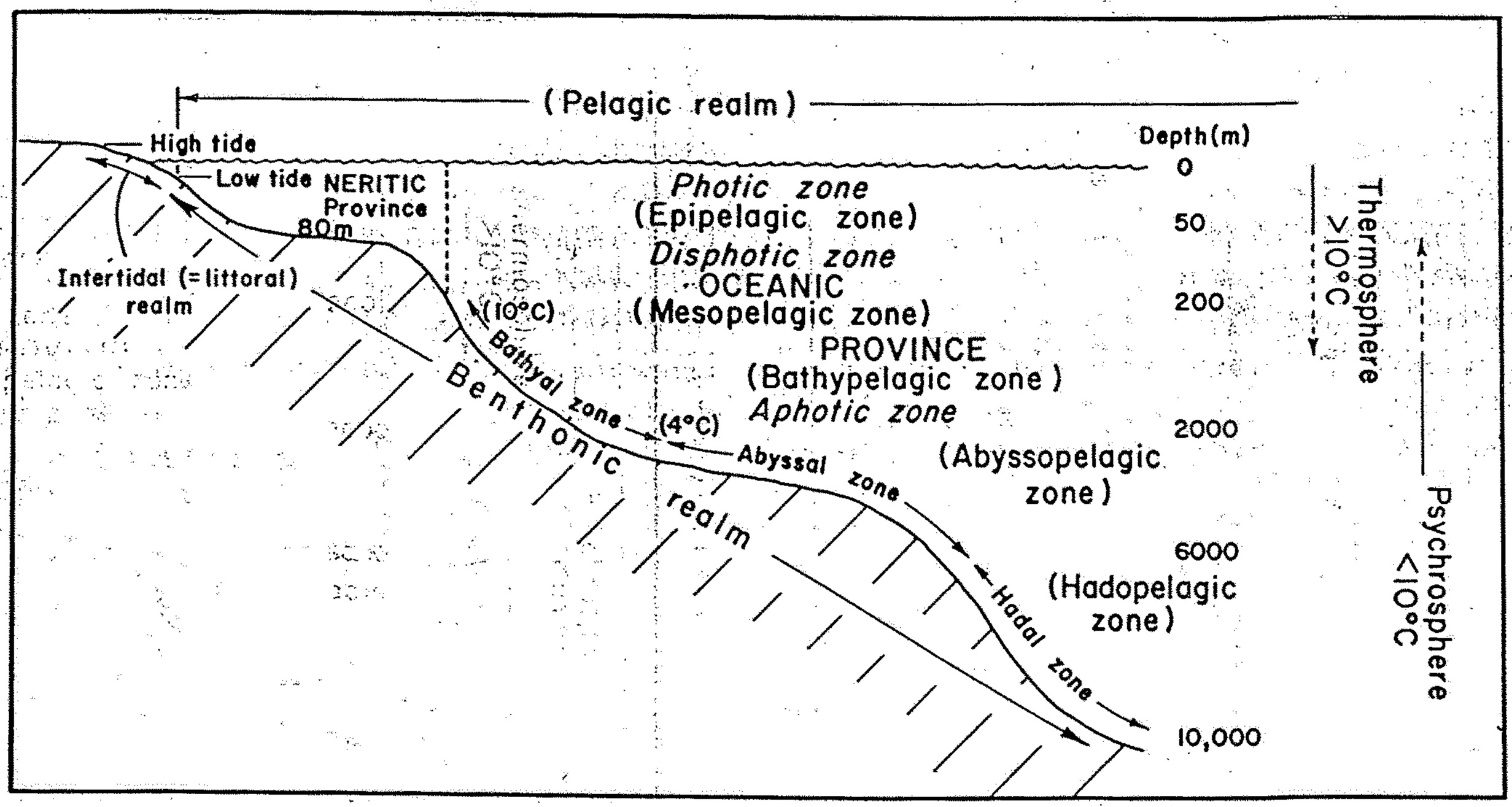

Figure 12-5 *Schematic profile through ocean showing ecologic subdivisions of bottom and of water. Important boundaries are based on depth of penetration of sunlight, depth where water temperature becomes 10°C (100 to 700 m), and depth below which water temperature is always 4°C or colder (about 2000 m in Atlantic Ocean; 1000 to 1500 m in Pacific and Indian Oceans). (Based on J. W. Hedgpeth, 1957a, Fig. 1, p. 18, and A. F. Bruun, 1957, p. 641–645, and Fig. 1, p. 642.)*

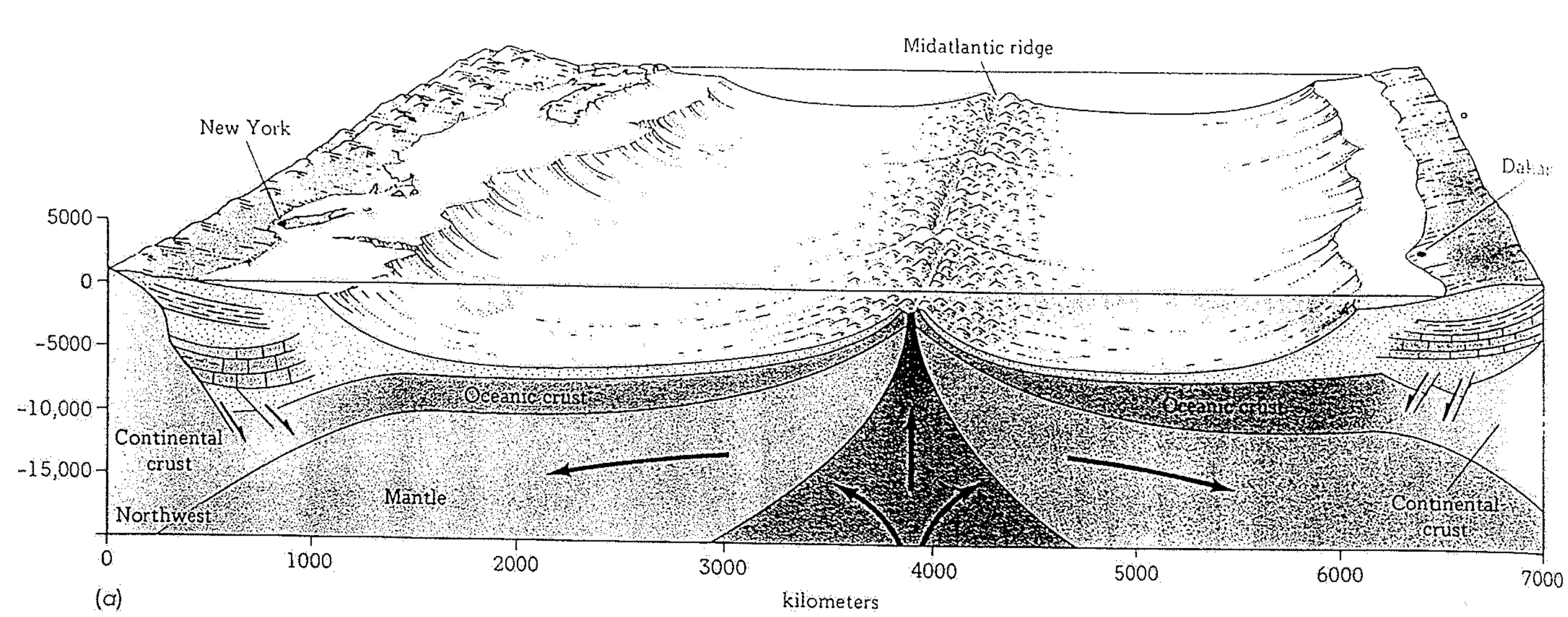

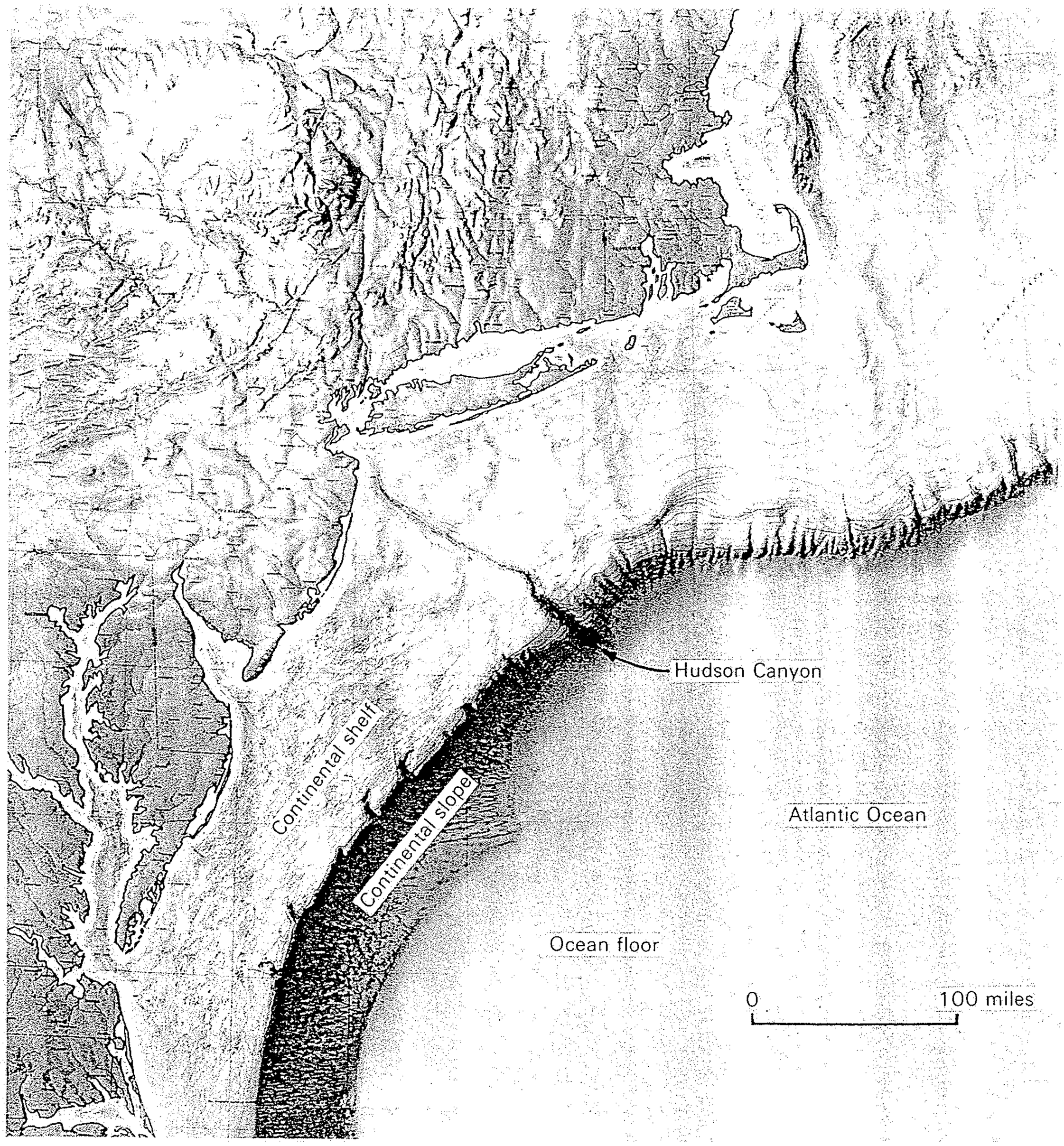

FIGURE 16–30 *Relief model showing the land and submarine topography of the northeastern United States. Submarine canyons abound on the steep continental slope (partly in shadow). The irregularly ridged submarine topography in the upper right corner is submerged glacial topography. (Courtesy of the Aero Service Corporation, Philadelphia, Pennsylvania.)*

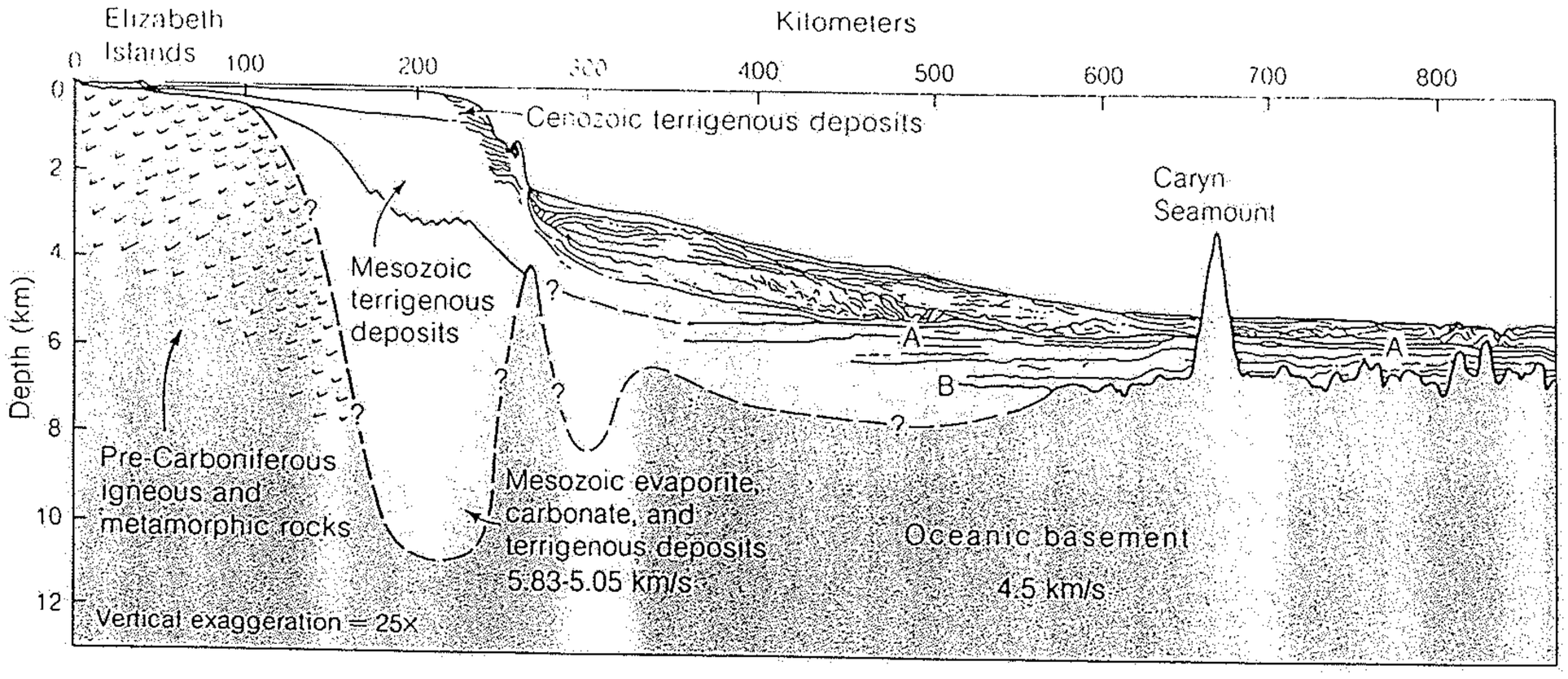

Figure 11-31

A profile of the Atlantic continental margin of North America off southern New England based on seismic data. Stratification, based on continuous seismic profiling, is shown diagrammatically for the younger sediments. [From *Atlantic Continental Margin of North America* by K. O. Emery and E. Uchupi. Copyright © 1972 by American Association of Petroleum Geologists.]

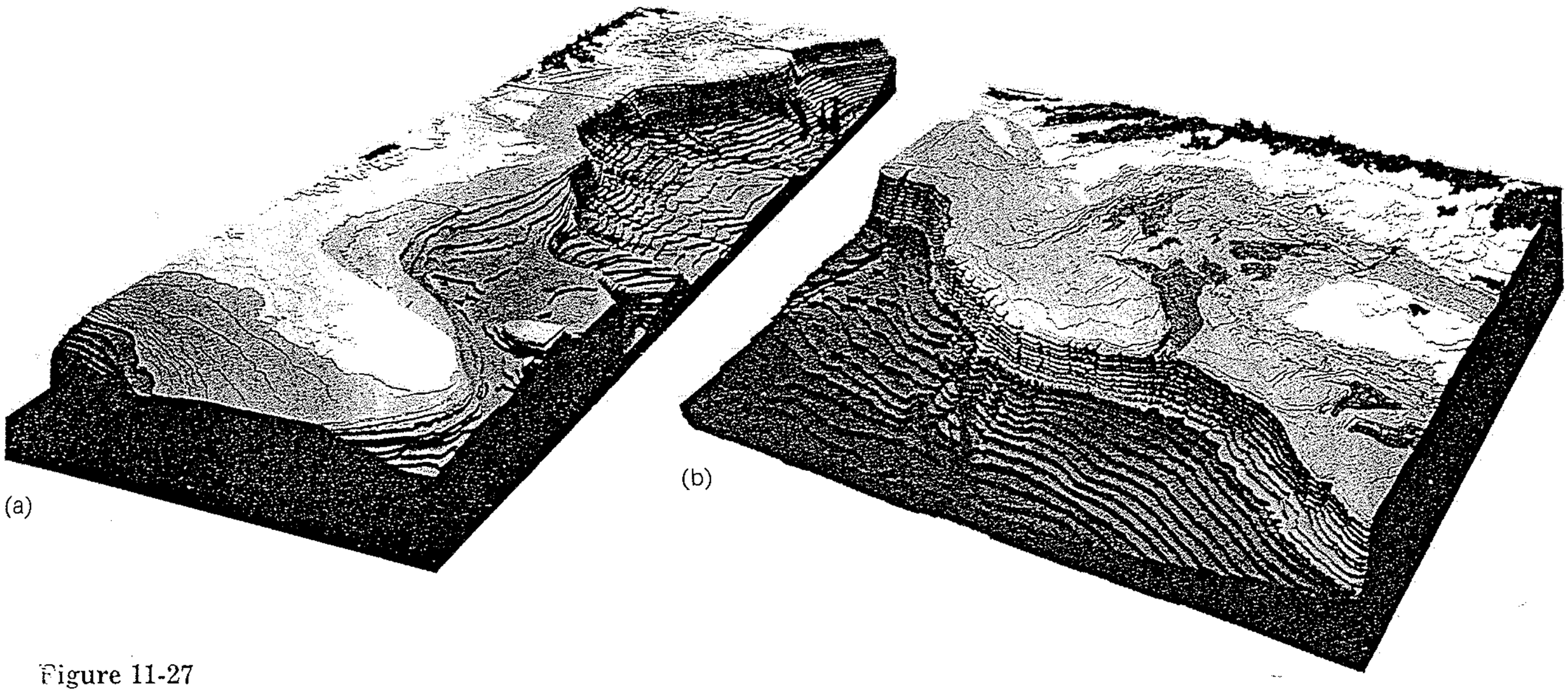

Figure 11-27

Two views of a three-dimensional model of the Atlantic continental shelf, slope, and rise of part of North America. (a) View looking northwest; Florida is in the foreground, Nova Scotia and part of the Grand Banks at the far edge. (b) Closeup of the section from Nova Scotia at right to New York and Long Island at left. Near the left margin is the Hudson submarine canyon, and in the middle foreground is the area of Georges Bank, off Cape Cod. [Courtesy of K. O. Emery and E. Uchupi, Woods Hole Oceanographic Institution.]

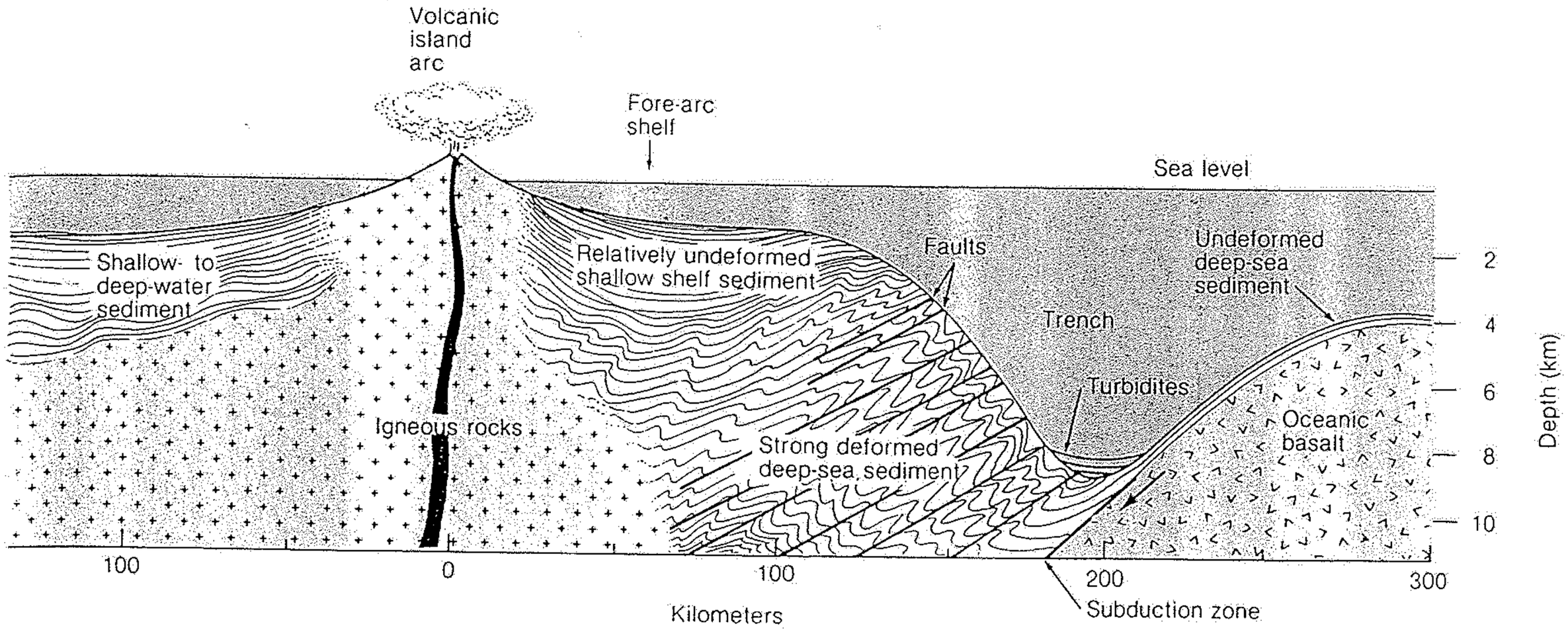

Figure 11-33

Generalized topography of a typical subduction zone in the western Pacific. The area between the volcanic island and the trench, the fore-arc shelf, is built up by shallow-water sedimentation; the inner trench wall is built up by the deformed deep-sea sediment scraped off the surface of the descending oceanic lithosphere slab. The horizontal and vertical dimensions of different arcs may vary considerably.

Fig. 629. Map showing the distribution of continental rises (black) and deep-sea trenches (chevrons). (After Emery 1970. Compiled from various sources)

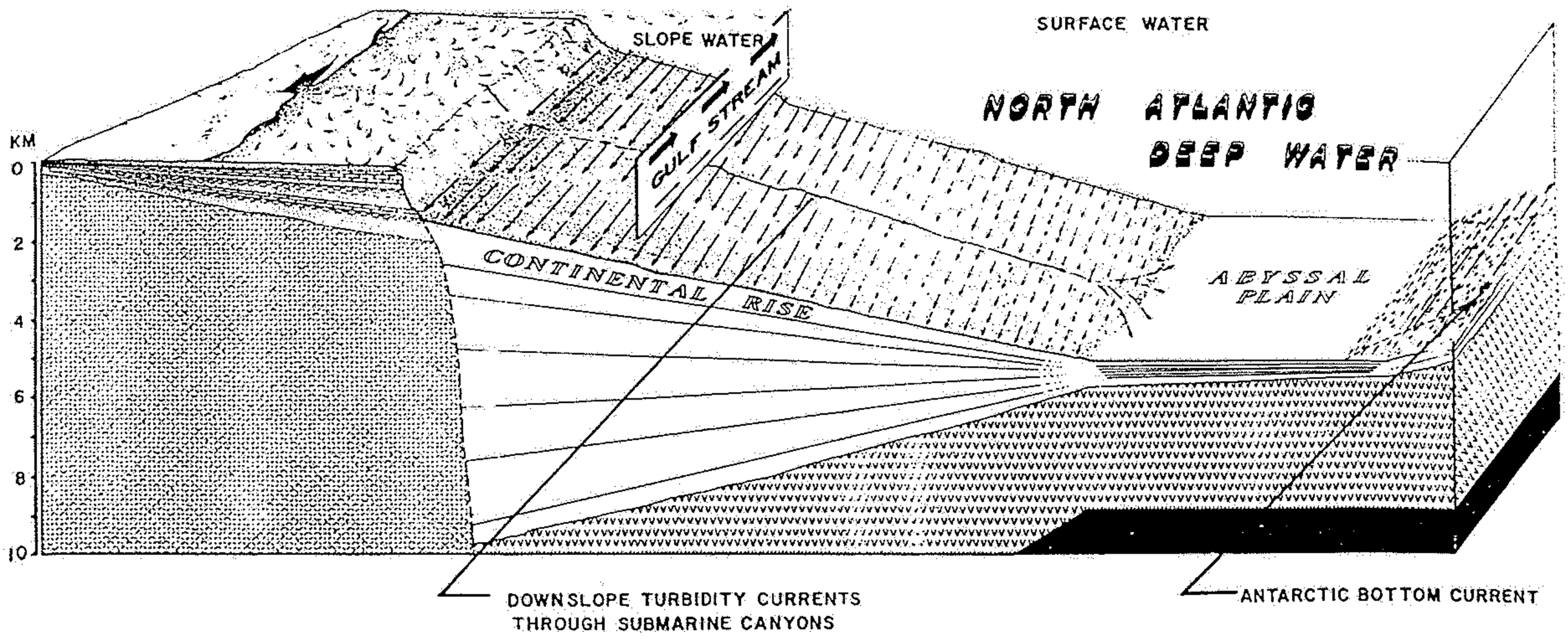

Fig. 656. Diagram illustrating the shaping of the continental rise by geostrophic contour currents. Arrows denote prevailing bottom currents. The continental and oceanic crust is shown by patterns. The mantle is solid black. Sedimentary rocks are shown by conventional symbols. Turbidite deposits are shown by horizontal ruling, and continental rise deposits are shown by open wedges. In addition, the transport directions are supported by underwater photographs on the continental rise of Nova Scotia and on the Western Bermuda Rise. This diagram depicts the principal processes active in shaping a "normal continental rise". (After Heezen et al. 1966)

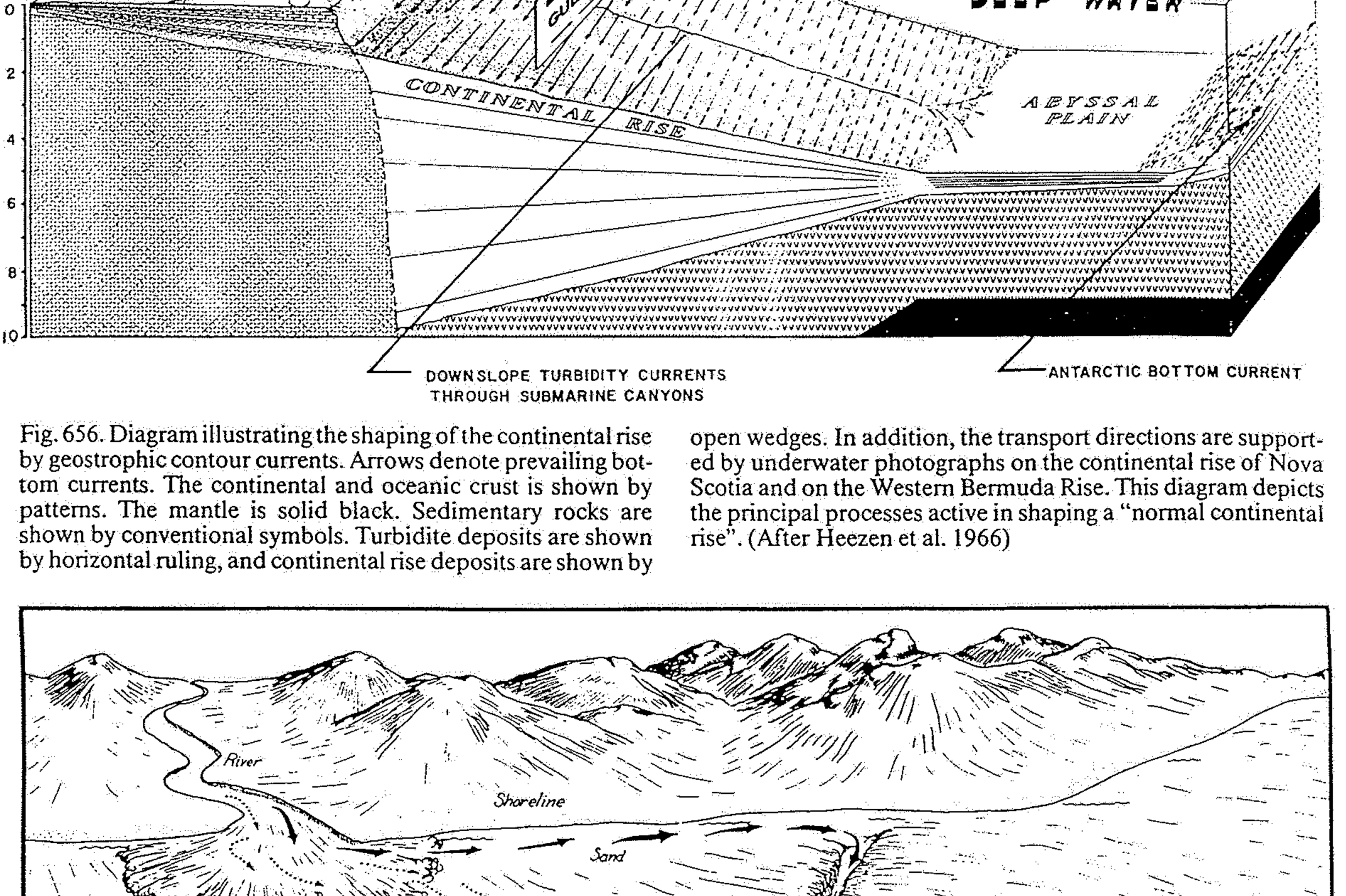

Fig. 636. Schematic representation of the routes of transportation of sand (solid arrow) and mud (dotted arrow) from river mouth to deep-sea basin floor. (After Moore 1969)

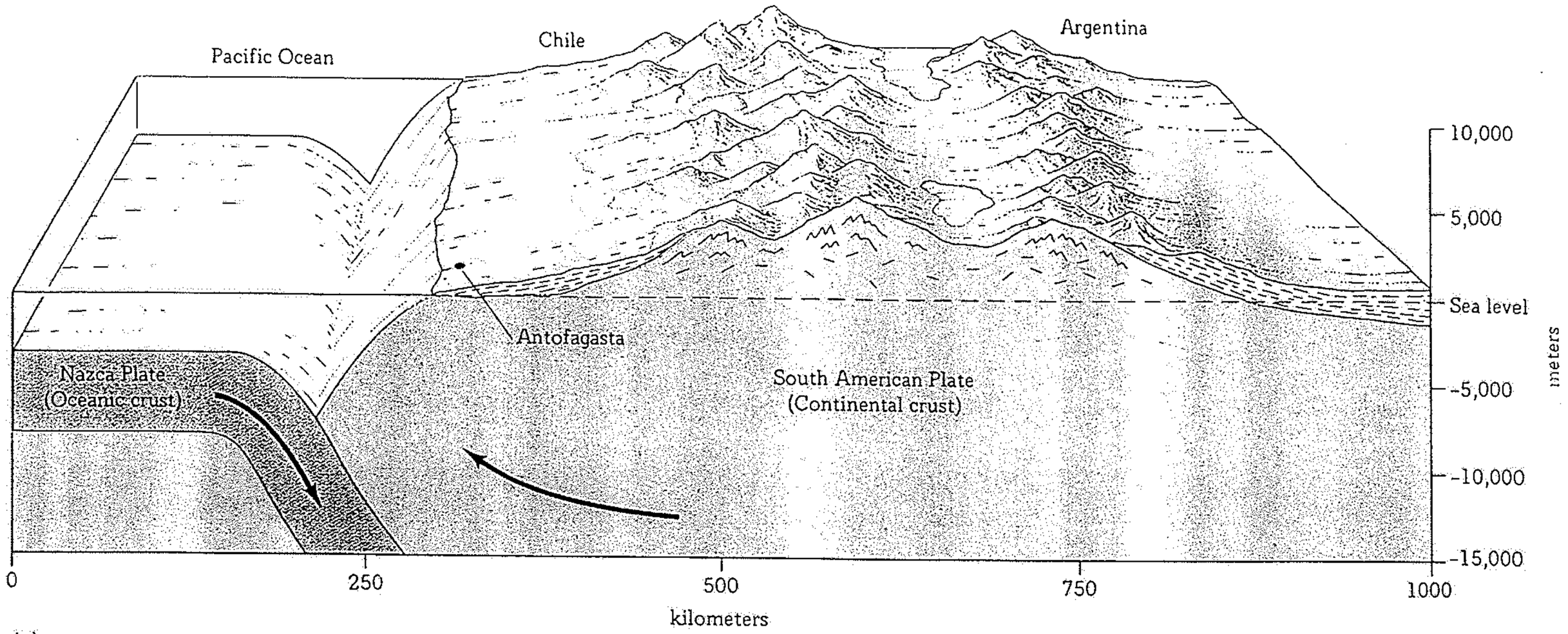

(a)

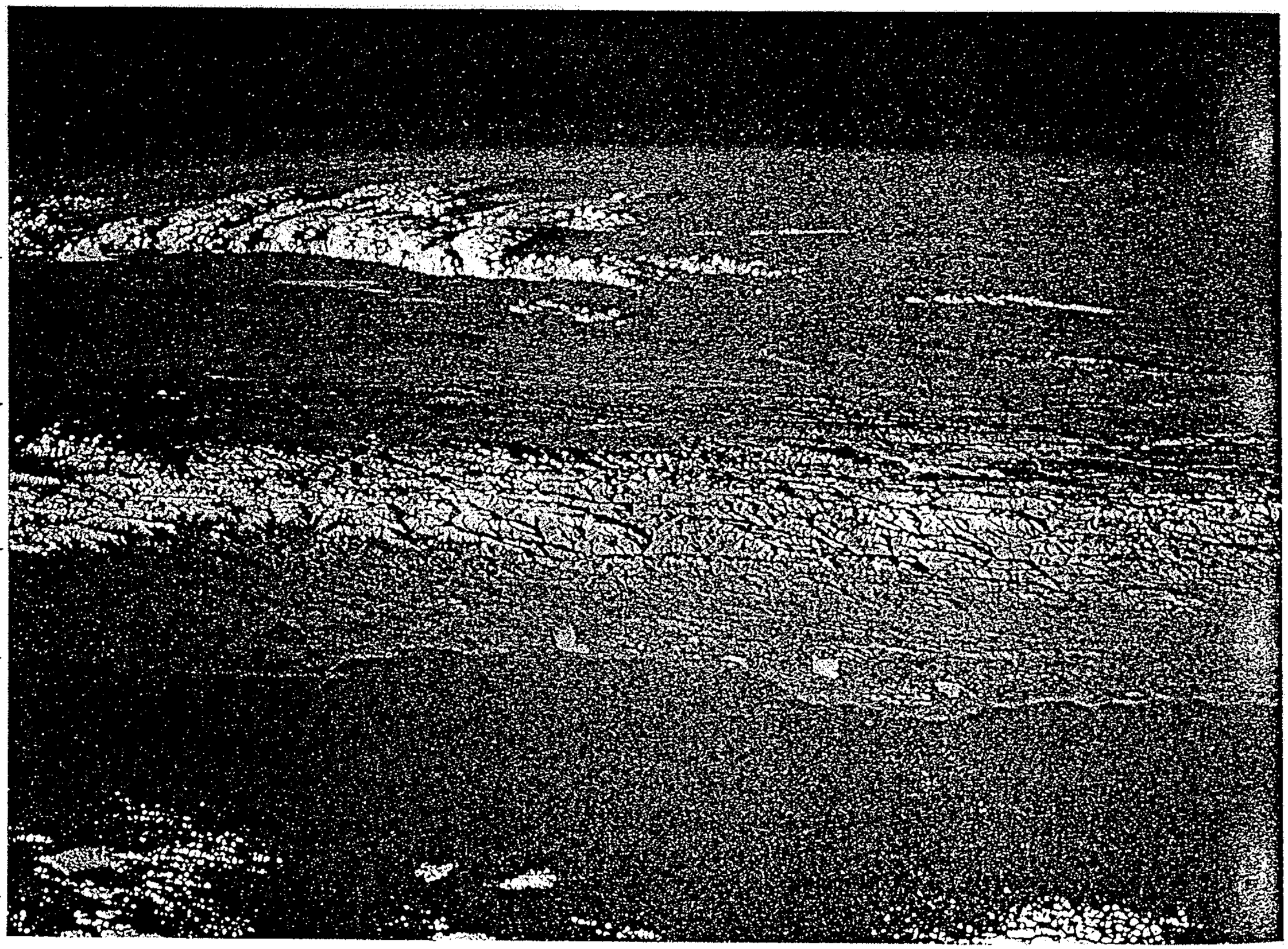

(b)

16.10 The western coast of South America is a converging border between a continental plate and an oceanic plate. (*a*) A geologic and topographic sketch at 23½°S. (*b*) The same area as seen looking toward the Chilean coast from Earth orbit. Clouds over the Andes form as the mountains force moist, warm air upward to cooler elevations. [Photo by NASA.]

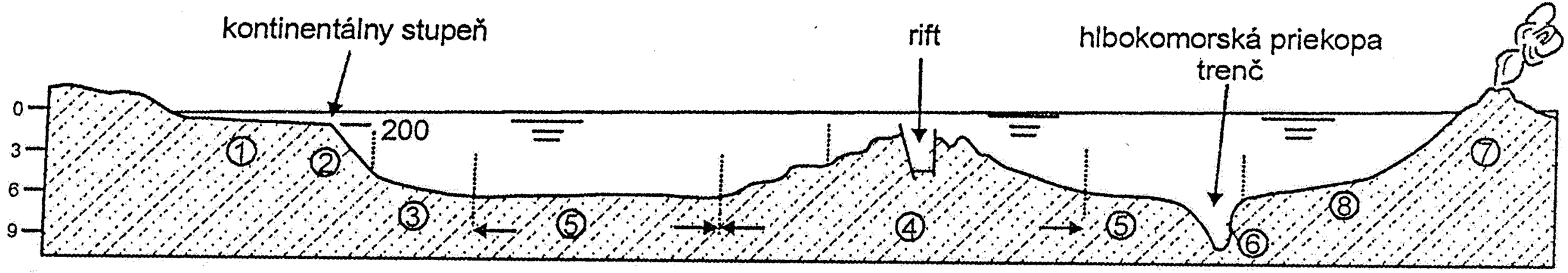

Obr. 18.2. *Morfoštruktúrne prvky dna oceánov: 1 – šelf, 2 – pevninský svah, 3 – úpätie; 4 až 6 – oceánske dno tvoria 4 – stredooceánske chrbty s riftovým údolím, 5 – oceánske panvy, 6 – hlbokomorské priekopy (trenče), 7 – ostrovné oblúky, 8 – vulkanické úpätie ostrovného oblúku (upravené podľa Plummera – McGearyho 1992)*

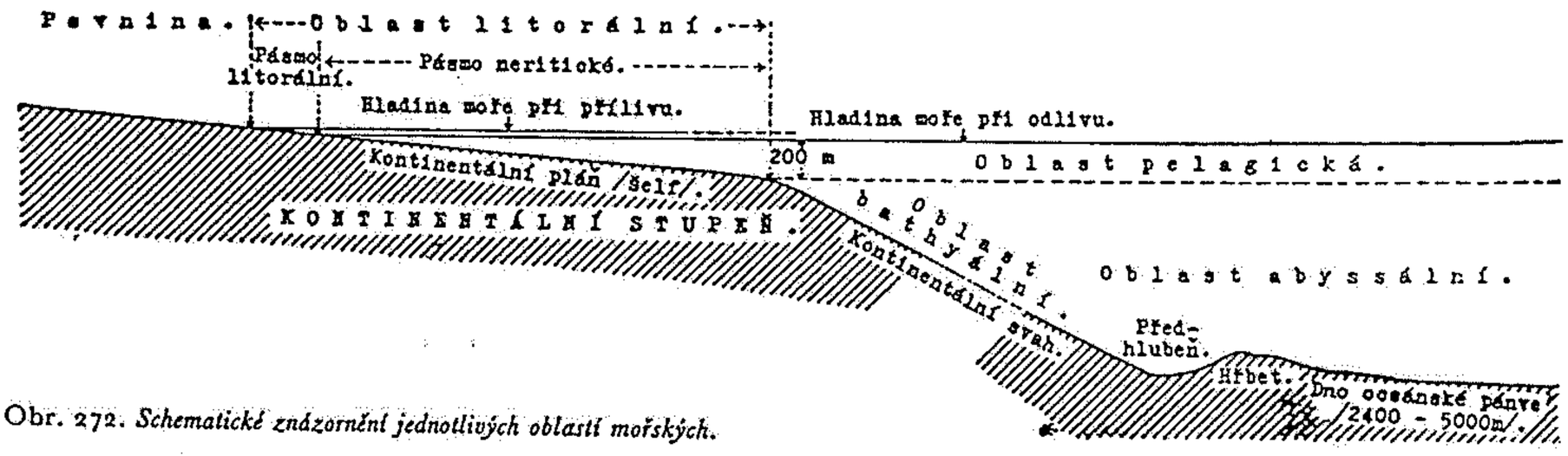

Obr. 272. *Schematické znázornění jednotlivých oblastí mořských.*

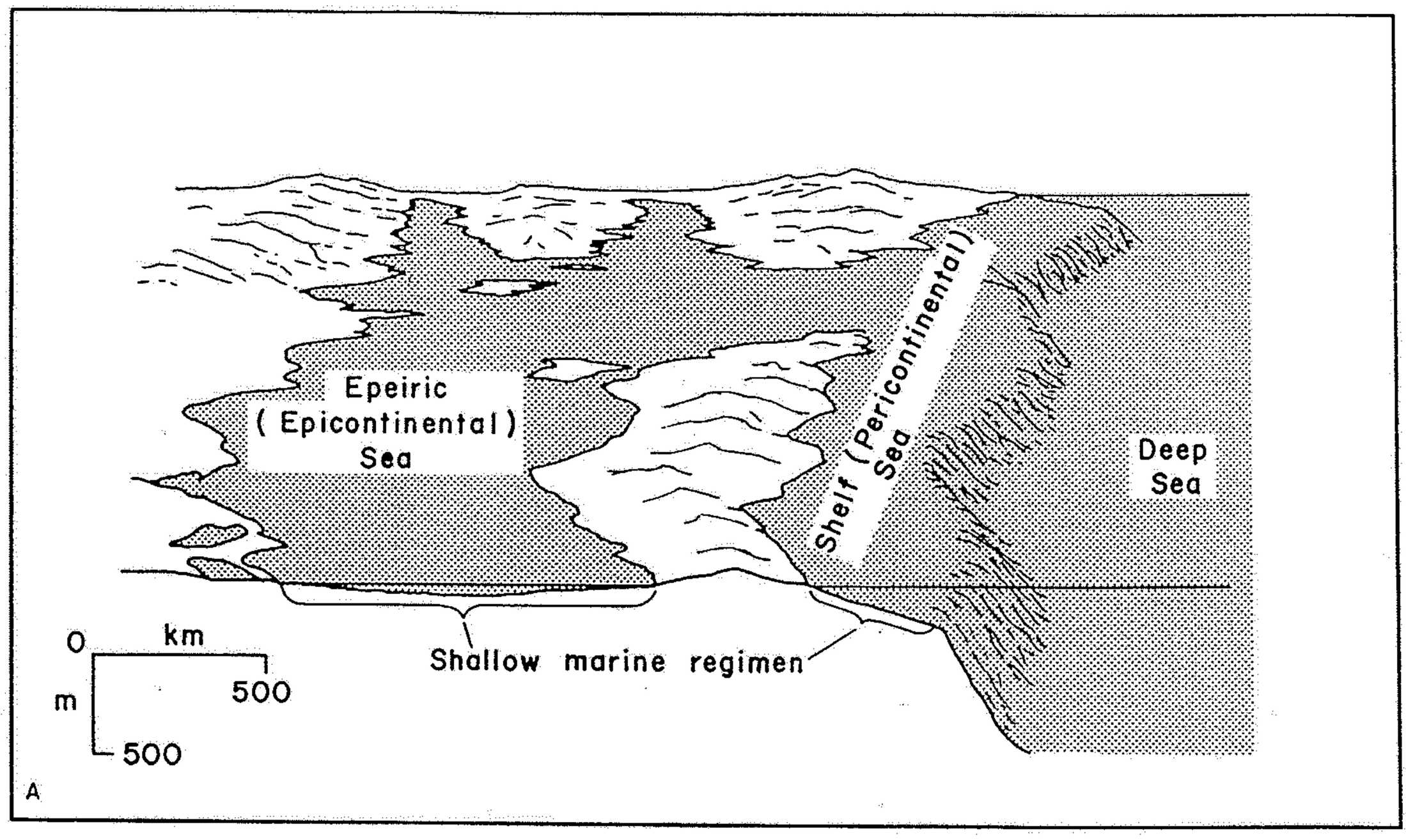

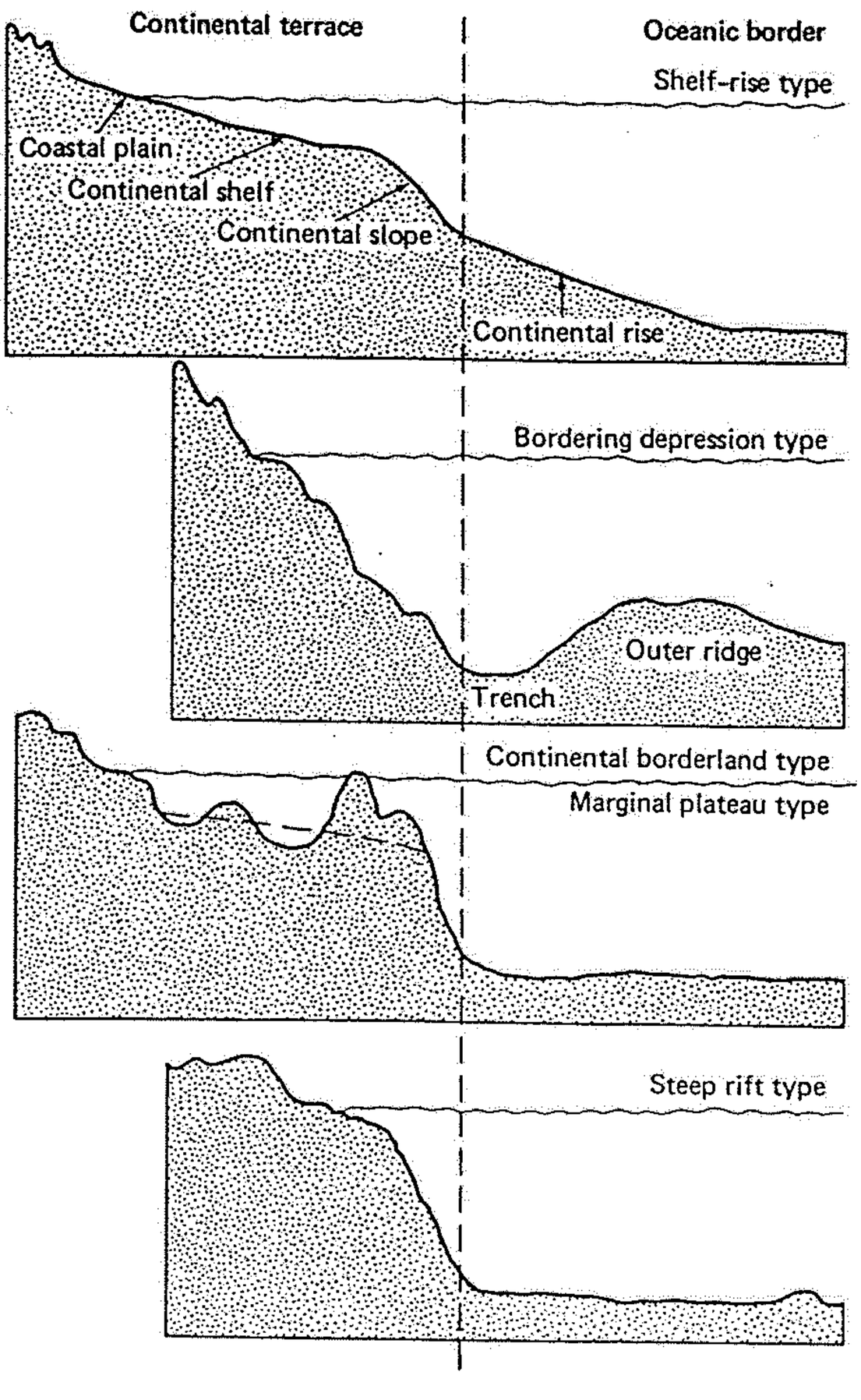

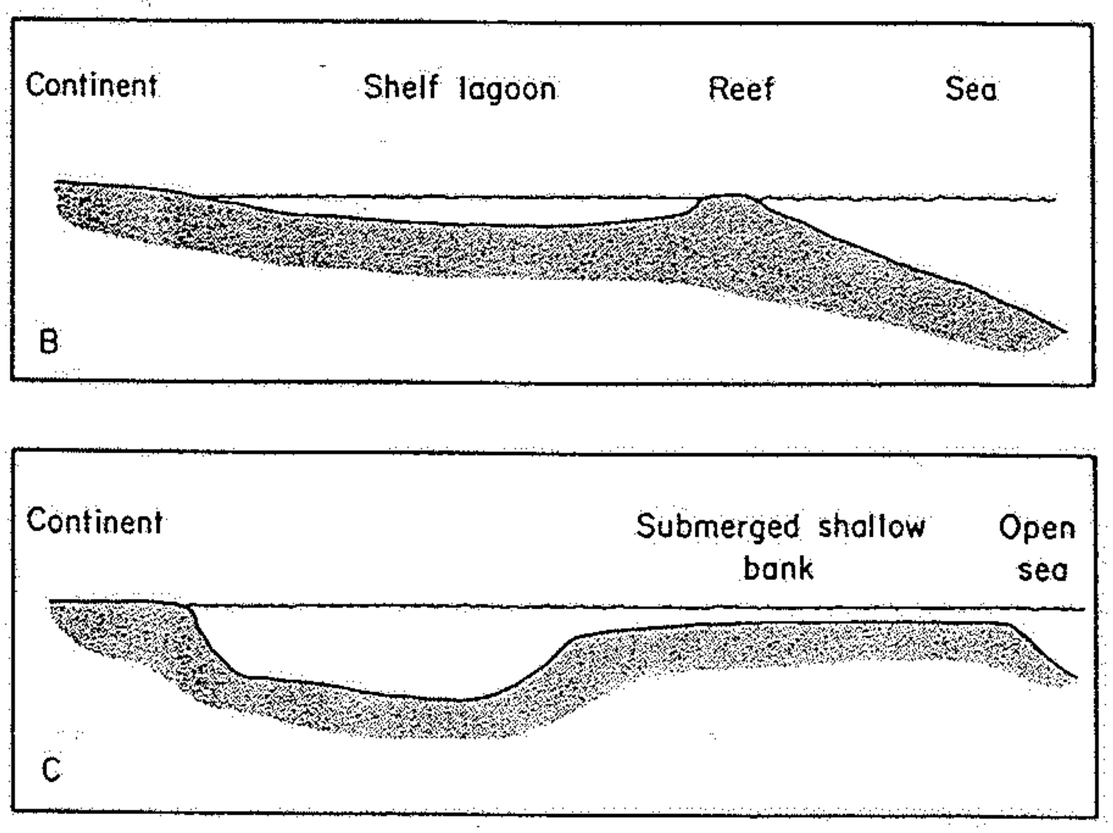

Figure 12-18 *Schematic views of shelf- and epeiric seas.*

A. Shelf (pericontinental) and epeiric (epicontinental) sea. Shelf seas cover margins of modern continental blocks. Epeiric seas, which in the geologic past spread across large parts of the interiors of continental masses, are not present in the modern world. Text explains distinction between shelf seas and epeiric seas. (After P. H. Heckel, 1972, Fig. 1, p. 227.)

B. Shelf lagoon between margin of a continental block and a reef tract that is situated at the edge of the continental mass.

C. Tidal sea covering a submerged shallow bank that is surrounded on all sides by the deep sea.

Figure 15–1 Generalized profile across the continental margin to the abyssal plain. Vertical exaggeration is about ×200. (After Curray, 1969.)

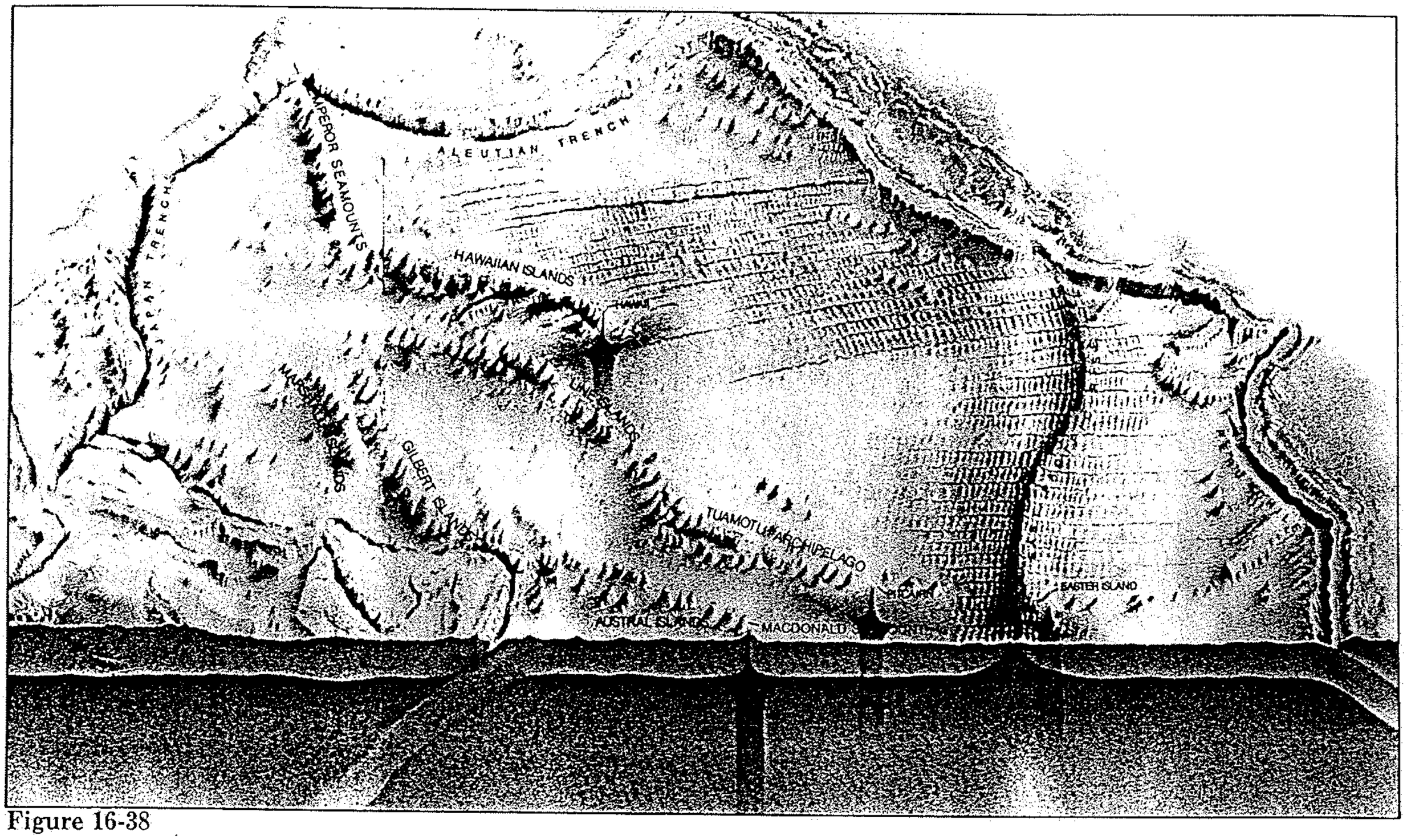

Figure 16-38

If hot spots are stationary, the "tracks" of the Hawaiian and Emperor Seamount chains and the parallel Tuamotu–Line and Austral–Gilbert chains would trace movement of the Pacific plate over the hot spots marked by the active volcanoes on Hawaii, Pitcairn Island, and Macdonald Seamount. All three chains would indicate the same motion of the Pacific plate; the bends in the chains formed 40 million years ago record a change in direction of plate motion at that time. [After "The Earth's Hot Spots" by G. E. Vink, W. J. Morgan, and P. R. Vogt. Copyright © 1985 by Scientific American, Inc. All rights reserved.]

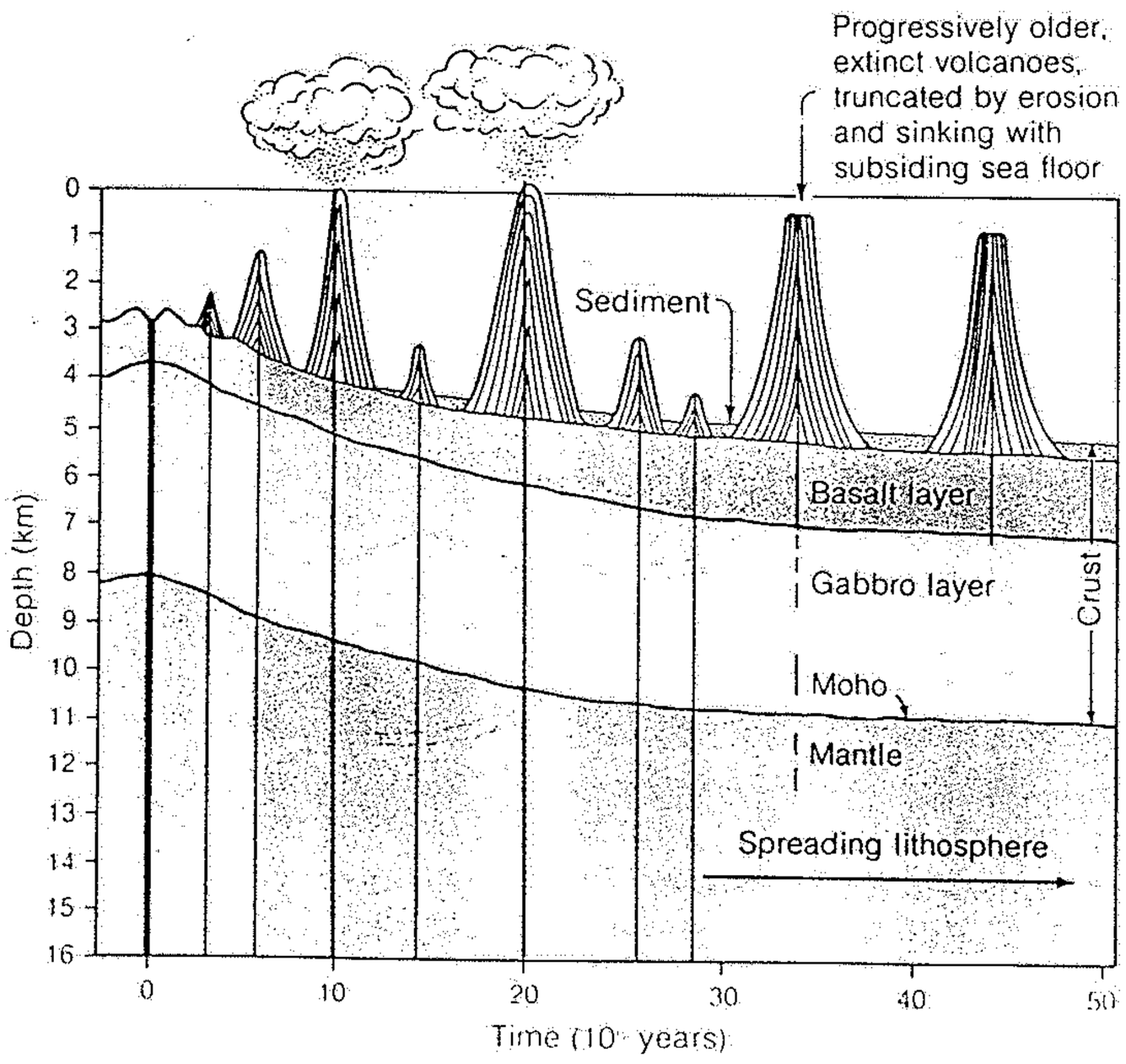

Figure 16-39

Guyots probably began as undersea volcanoes that grew near spreading centers. Many projected above sea level, became extinct, and were eroded down to flat-topped cones by wave action. The volcanoes rode along on the moving plate as they grew, were then truncated, and finally sank beneath the sea surface as the plate that carried them subsided. [After "The Deep Ocean Floor" by H. W. Menard. Copyright © 1969 by Scientific American, Inc. All rights reserved.]

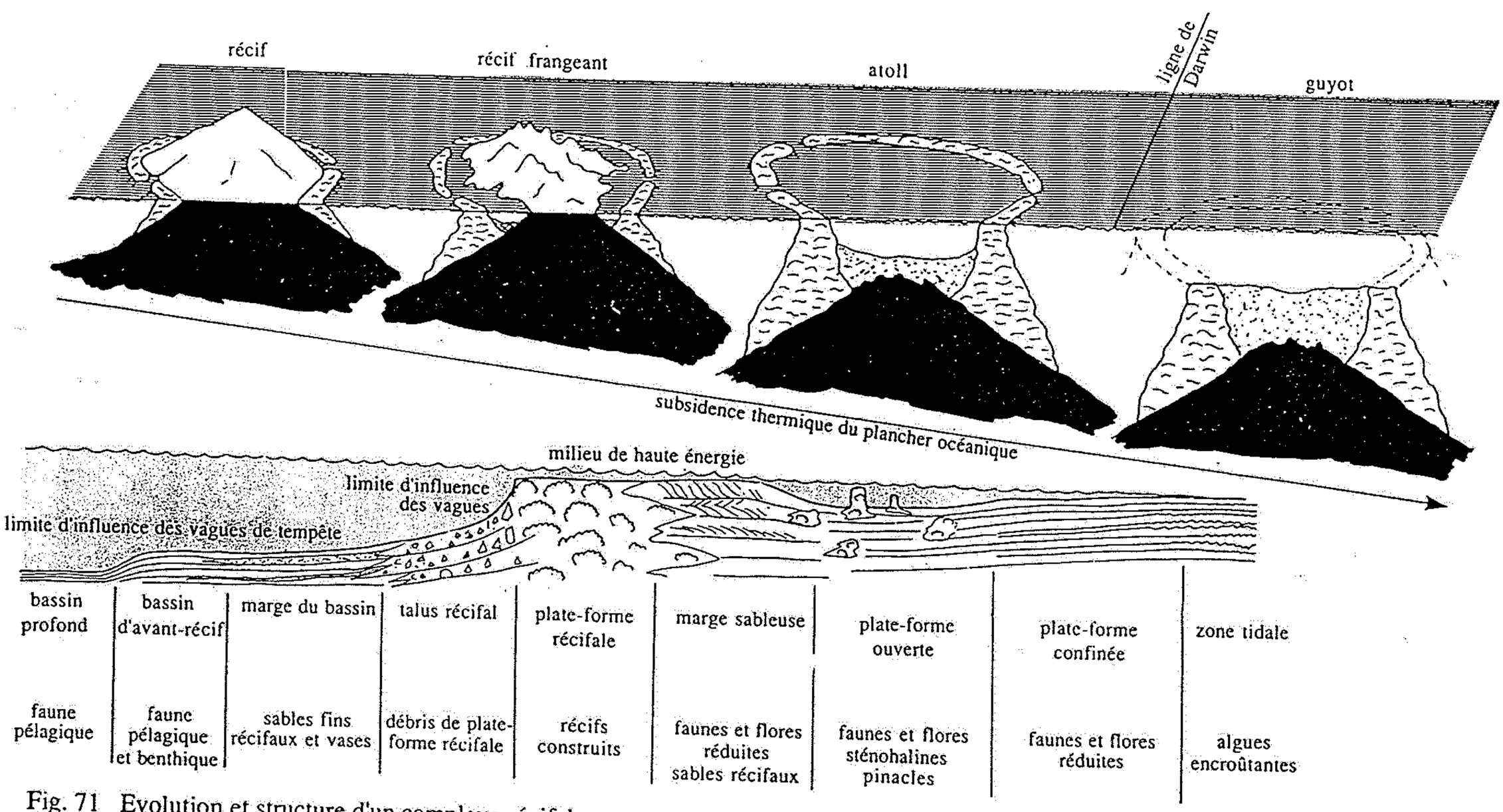

Fig. 71 Evolution et structure d'un complexe récifal.
a. La subsidence thermique du plancher océanique transforme le complexe récifal en récif frangeant puis en atoll. Si lors de sa migration l'atoll dépasse la "ligne de Darwin" (28° N ou S), les conditions de vie récifale se détériorent, la subsidence l'emporte sur la croissance, et l'atoll se transforme en guyot.
b. Coupe radiaire d'un récif frangeant.

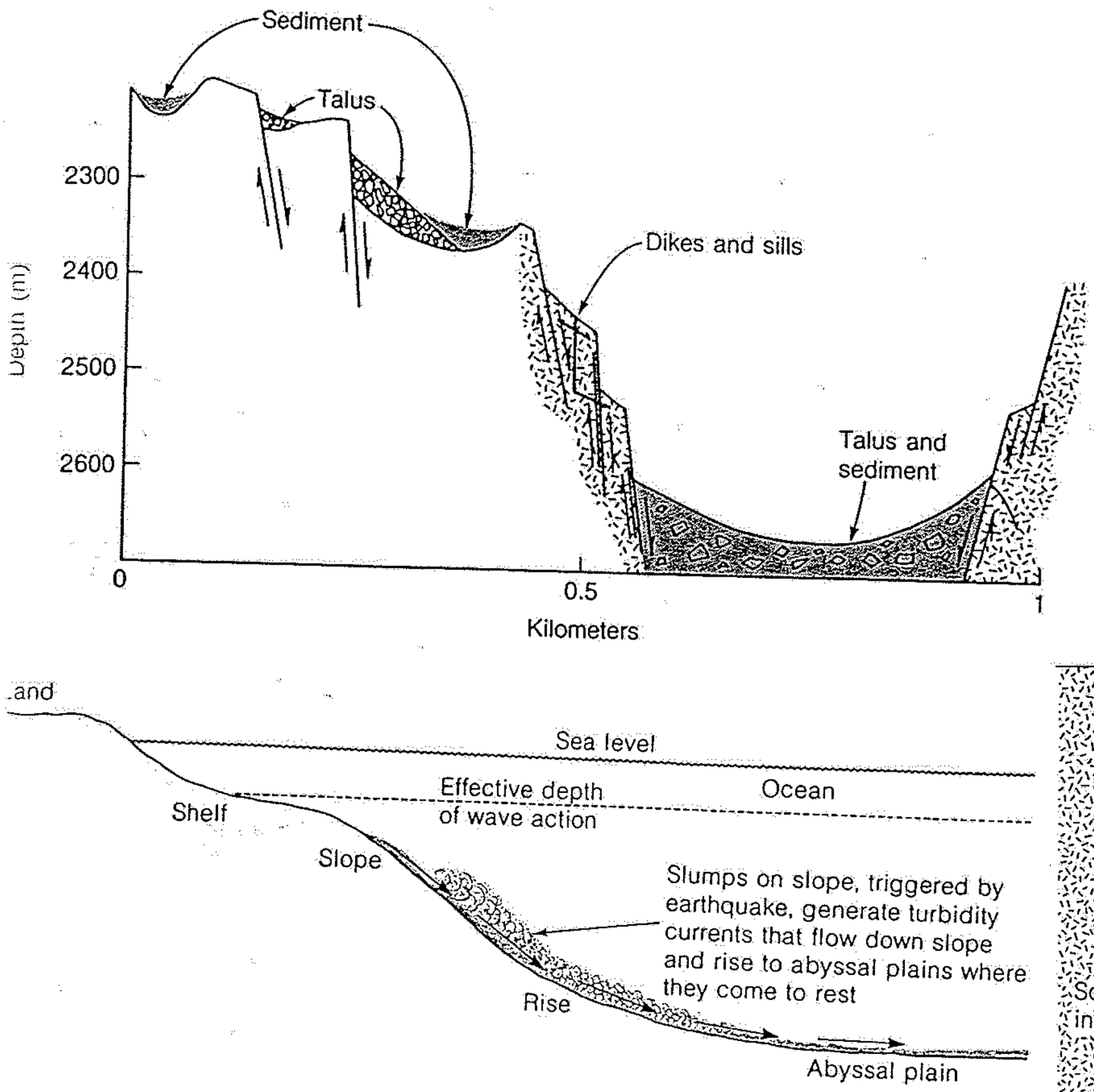

Figure 11-40

Detail of a portion of the central rift valley of the mid-Atlantic ridge in the FAMOUS (French–American Mid-Ocean Undersea Study) area southwest of the Azores. The deep valley, the narrow site where most of the basalt is extruded, is bounded by a series of faults that have created local depressions where basalt talus blocks and pelagic sediment have accumulated. [Modified from "Transform Fault and Rift Valley from Bathyscaph and Diving Saucer," by ARCYANA, *Science*, v. 190, pp. 108–116, 1975.]

Figure 11-36

Typical formation of turbidity currents in the ocean. Slumps on the continental shelves generate turbidity currents that flow downslope to abyssal plains, where they gradually slow to a stop and deposit turbidite sediments.

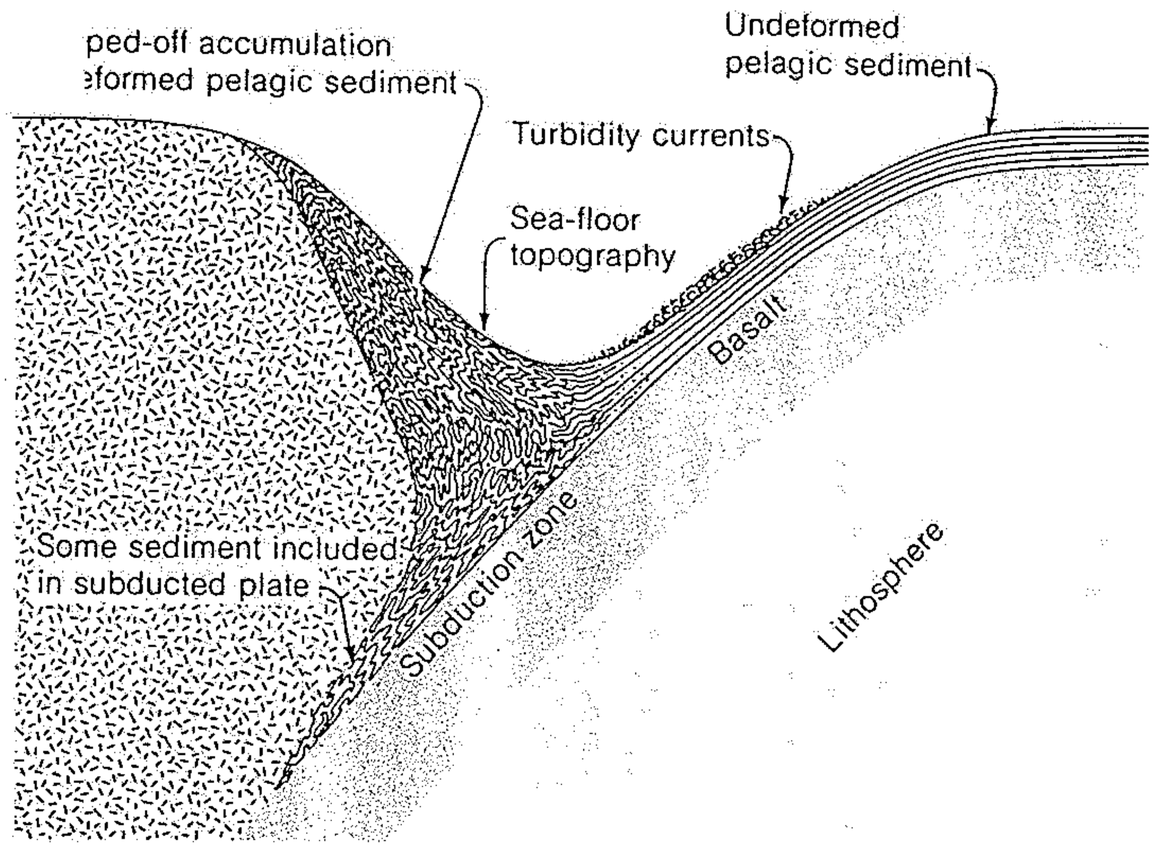

Figure 11-43

Sedimentation and deformation of sediment in an oceanic trench and subduction zone. Much of the pelagic sediment and turbidity-current deposits in the trench are "scraped off" as the oceanic plate moves down the subduction zone, the sediments being of much lower density than the underlying lithospheric rocks. Some sediment may be carried along with the subducting plate.

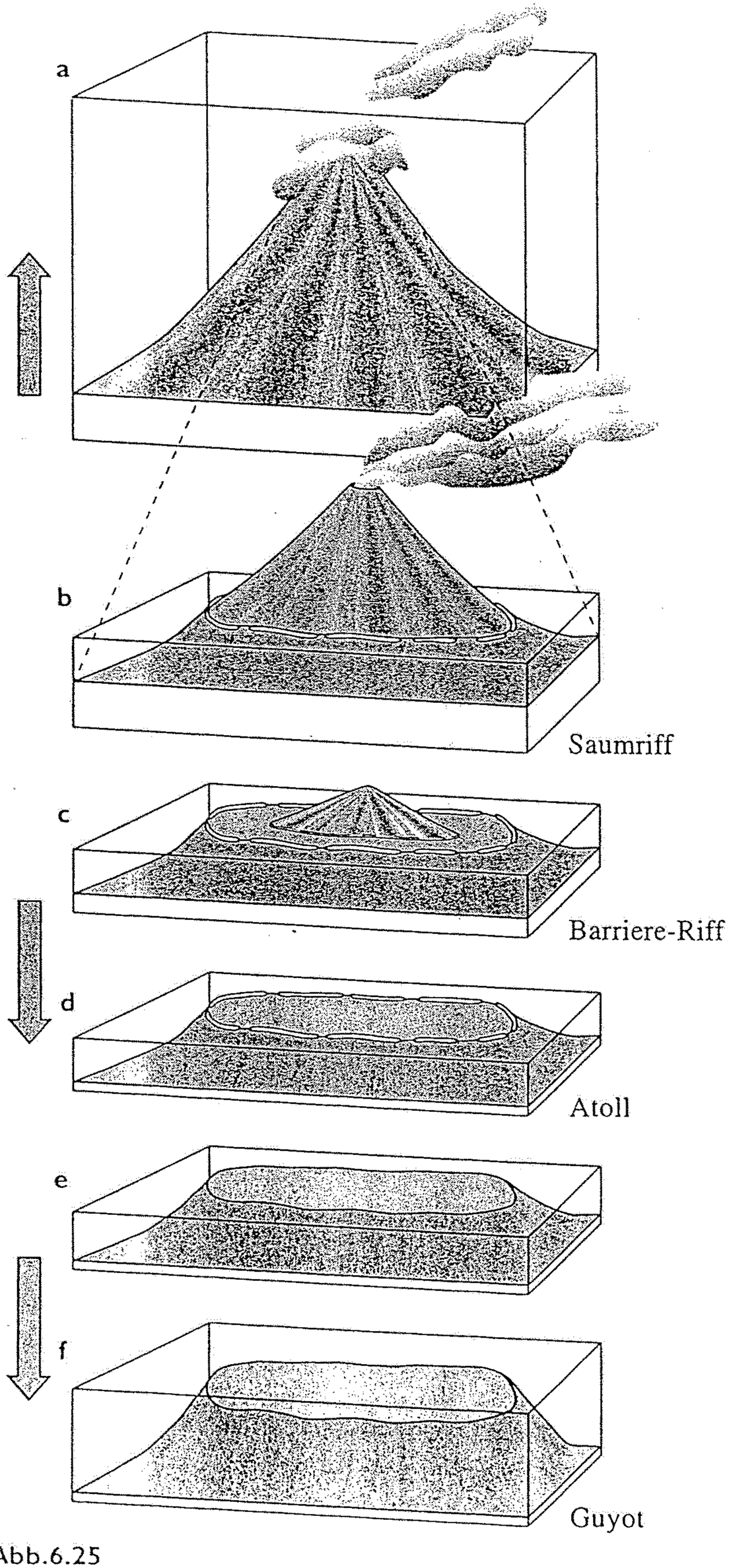

Abb.6.25
Die Entwicklung eines Atolls ist eng mit der Eruptions- und Absinkgeschichte von Vulkaninseln verbunden (nach GARRISON, 1993).

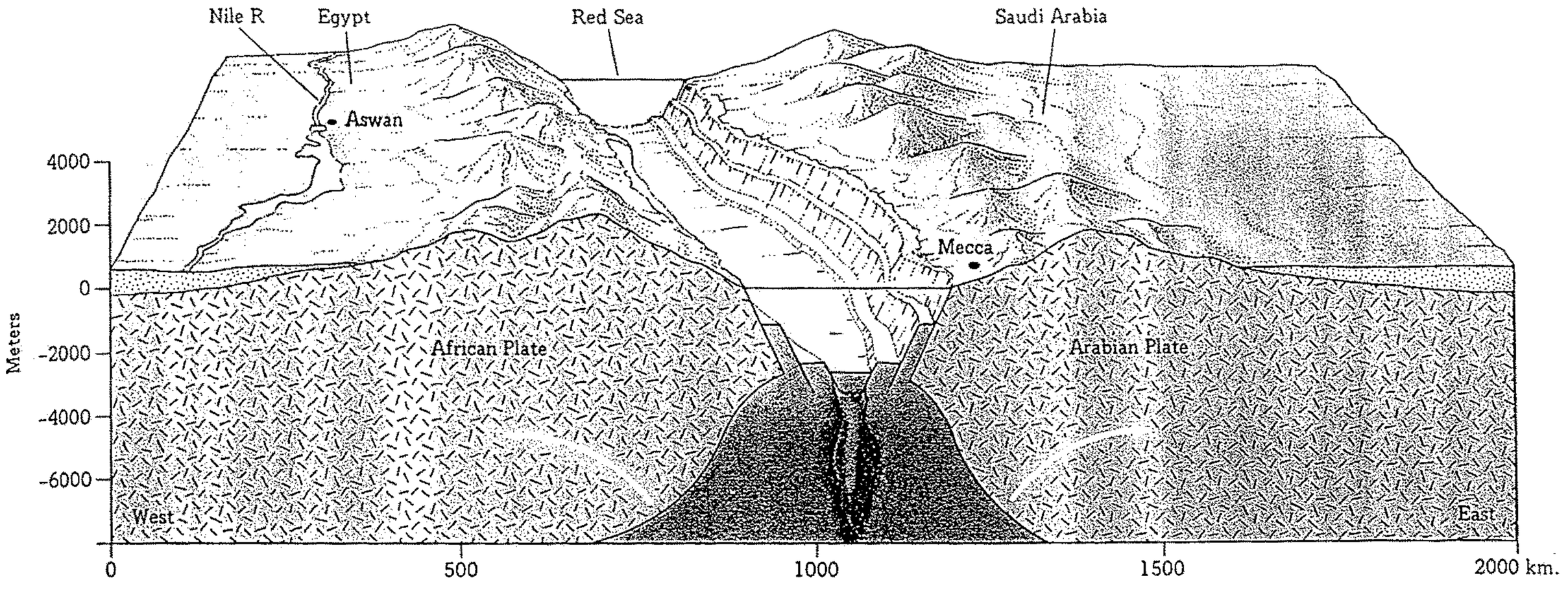

(a)

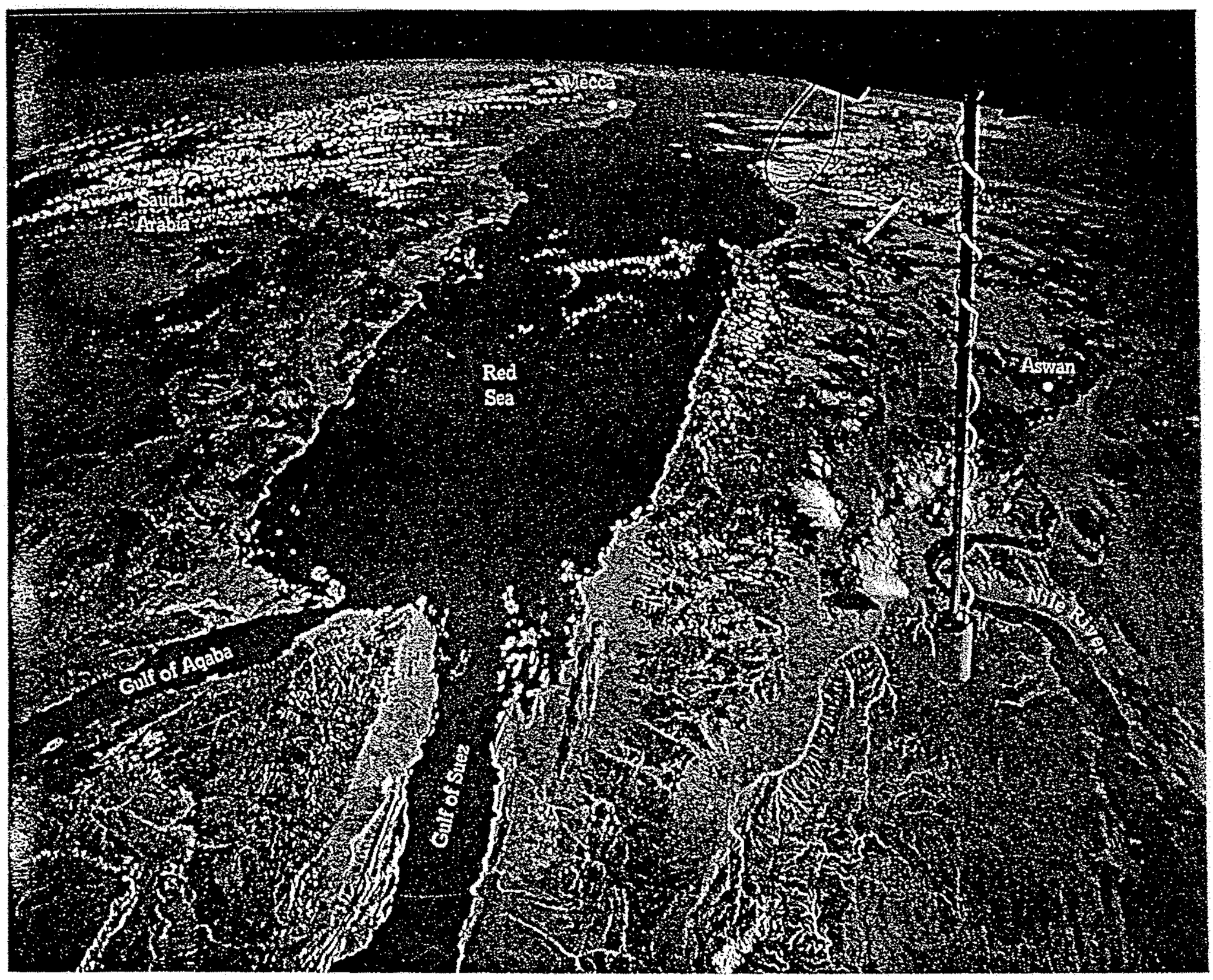

(b)

16.11 An early stage in the rifting of a continent is represented by the present-day Red Sea. The continued widening of the sea floor from a similar rift produced our modern Atlantic Ocean with its Midatlantic Ridge, as shown in Figure 16.12. (*a*) A geologic and topographic section looking north toward Aswan, Egypt, and Mecca, Saudi Arabia. (*b*) A photograph taken from Earth orbit looking south. The Gulf of Aqaba (left) and the Gulf of Suez (center) open into the Red Sea. The Nile River (right) flows toward viewer. [NASA.]

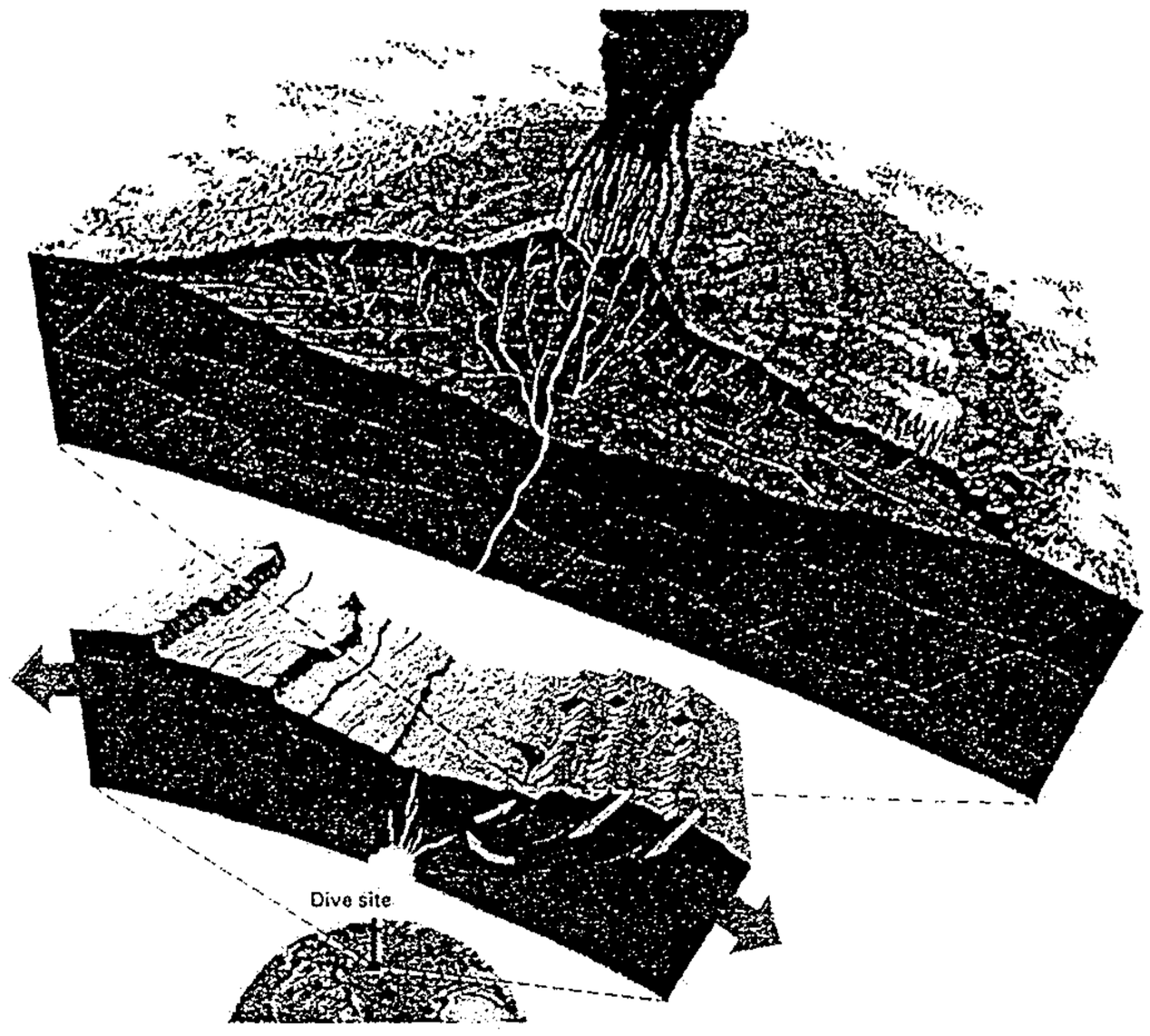

:gure 10.12 A schematic cross-section of the TAG hydrothermal mound, 26°N Mid-Atlantic Ridge (the co-ordinates give the dive site). Hot vent-fluid (shown in pale blue) flows up an open fissure in the deeply faulted oceanic crust, and then percolates out through the entire sulphide mound along a tortuous network of interconnected channels, giving rise to the highest-temperature (350–365°C) black smoker fluids at the apex (50 m across and 50 m above the sea floor) and to the lower temperature (270–300°C), partly diluted white smokers around the outer section of the mound (200 m across and 20–30 m above the sea floor). Extinct chimneys are also seen across much of the outer mound, where earlier fluid flow has ceased because subsurface mineral precipitation has choked the flow-channels solid. Toward the flanks of the mounds, rubble deposits occur where oxidised and altered material from the hydrothermal mound has been broken up by mass-wasting ('landslide') events and carried out across the sea floor, to be deposited upon more typical volcanic basement and a thin veneer of more typical pelagic sediments (courtesy of Pierre Minon, © National Geographic Society).

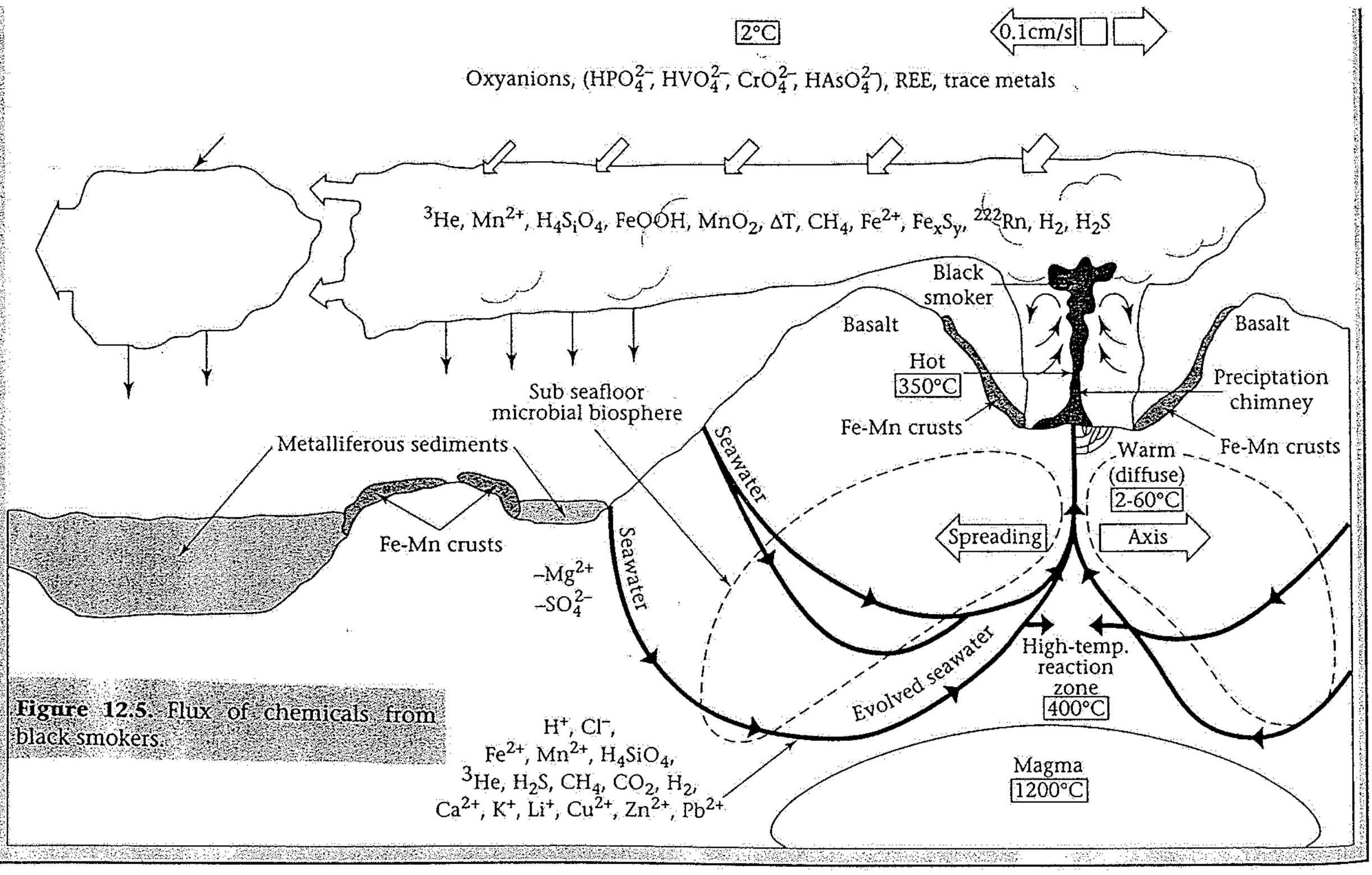

Figure 12.5. Flux of chemicals from black smokers.

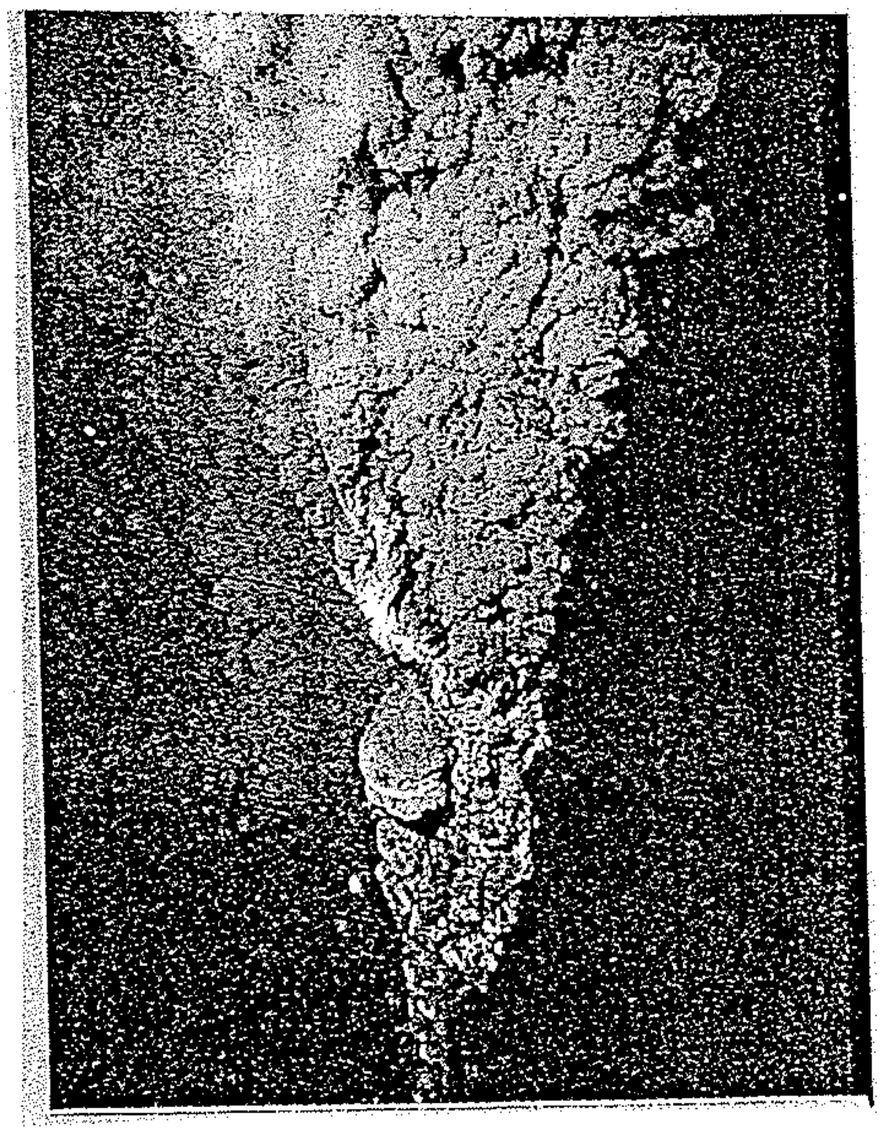

Figure 12.4. Black smoker. (*Source:* Courtesy of Woods Hole Oceanographic Institution; photograph by Robert D. Ballard 1979.)

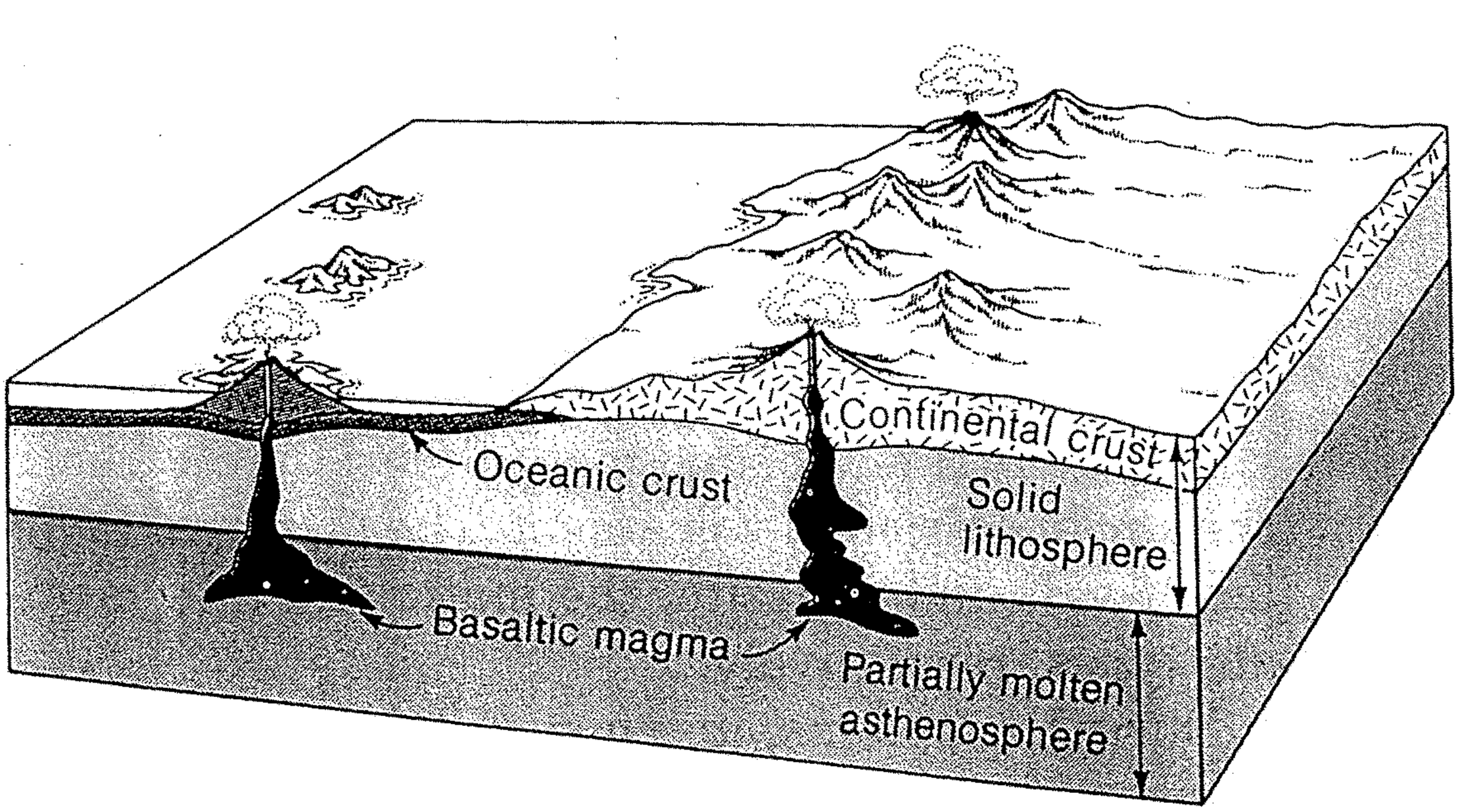

Figure 16-1

Basaltic magma, which originates in the partially molten asthenosphere, rises through the lithosphere to erupt as basaltic lava on the surface.

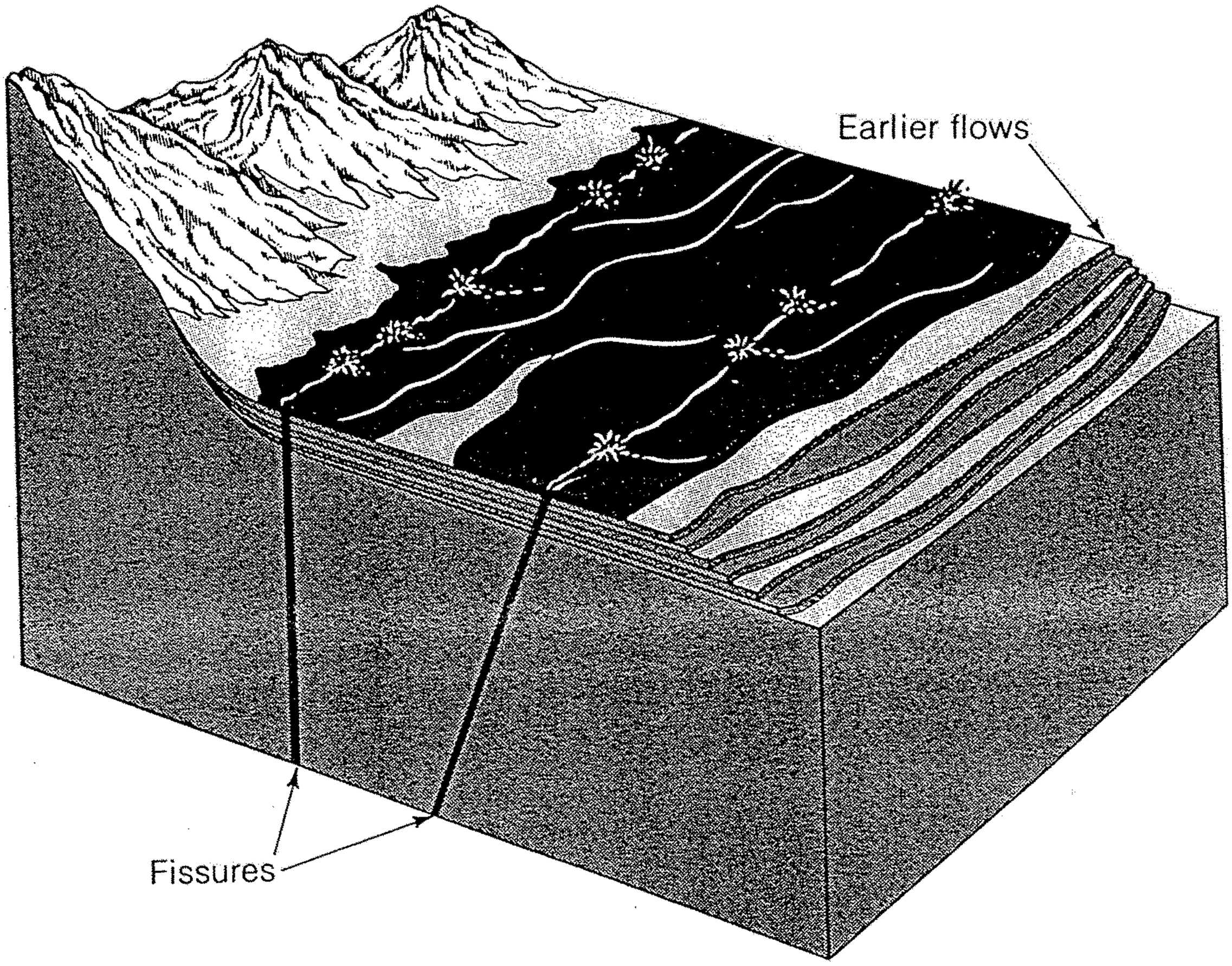

Figure 16-15

In a fissure eruption of highly fluid basalt, lava rapidly flows away from fissures and forms widespread layers, rather than building up volcanic mountains. [After R. S. Fiske, U.S. Geological Survey.]

(a)

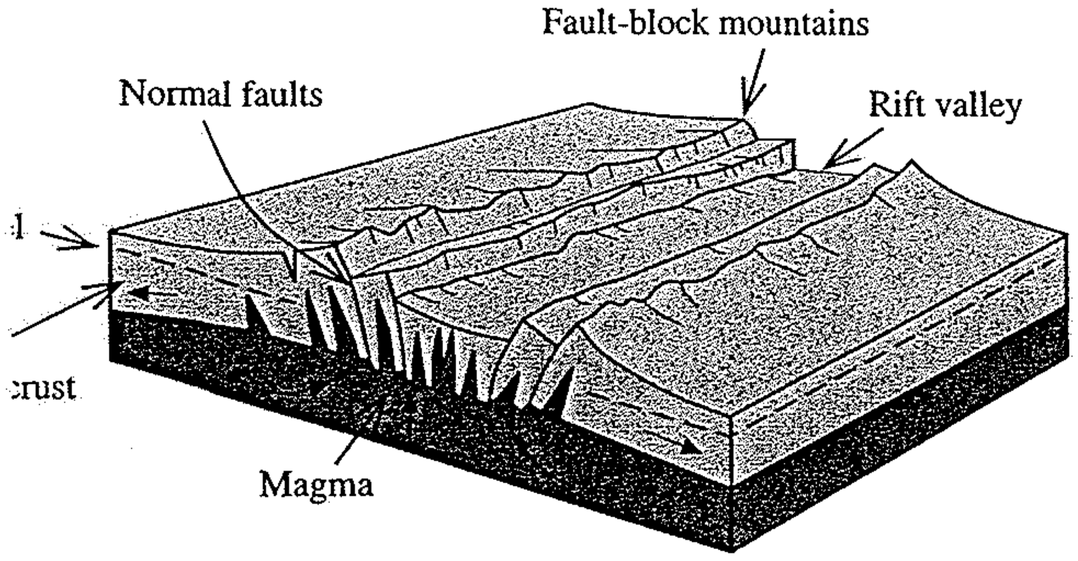

(b)

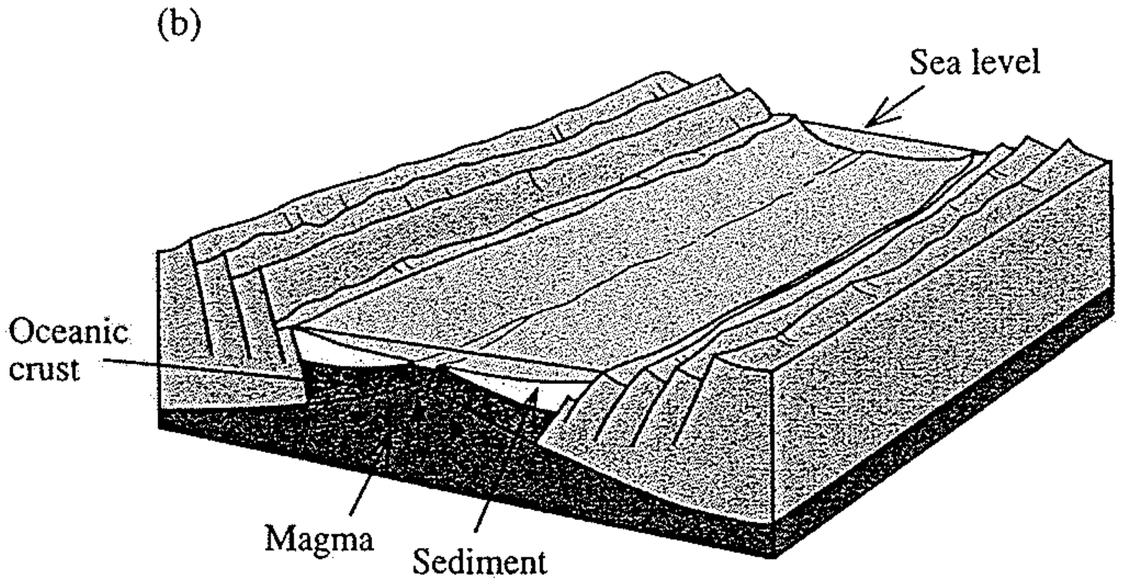

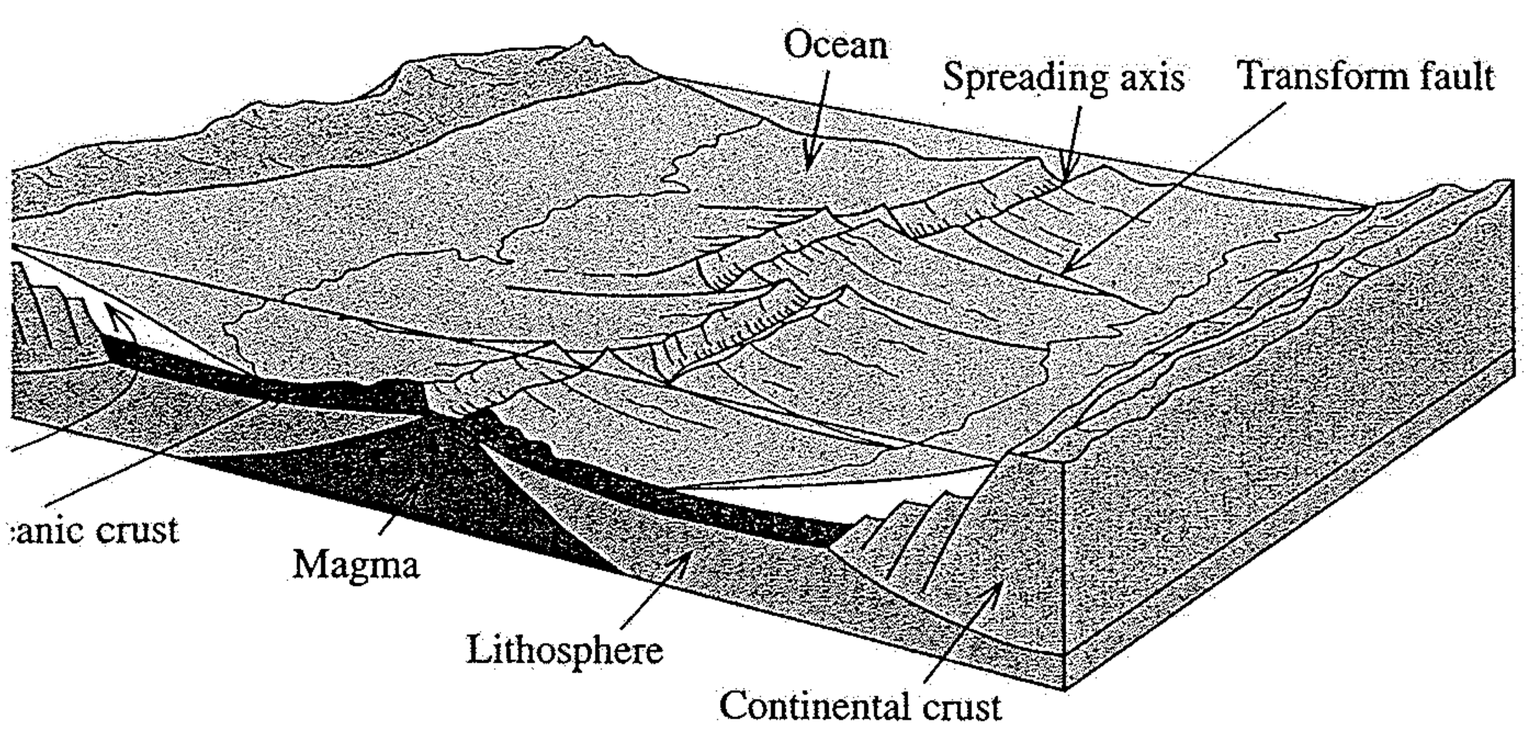

(d)

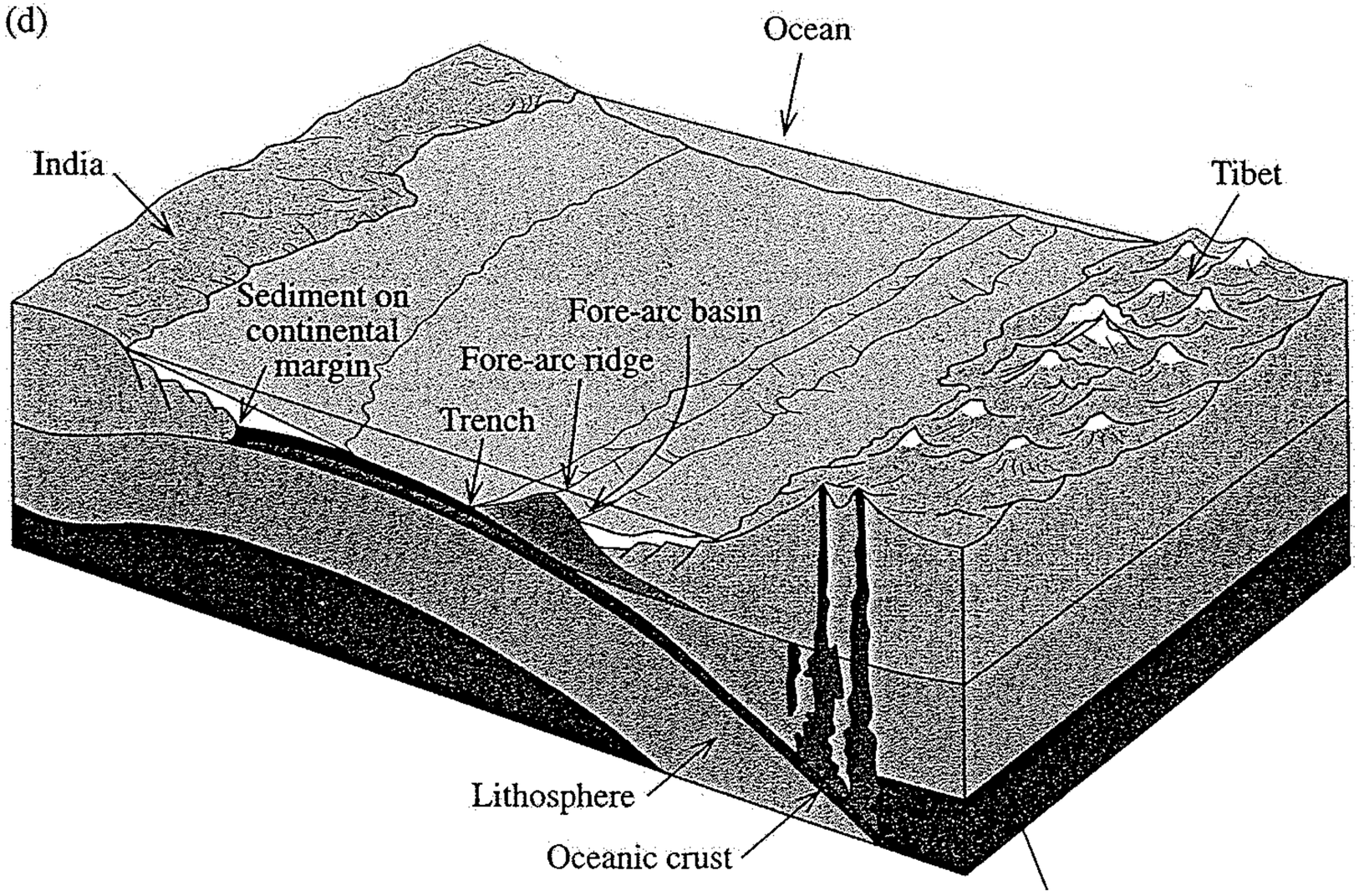

(e)

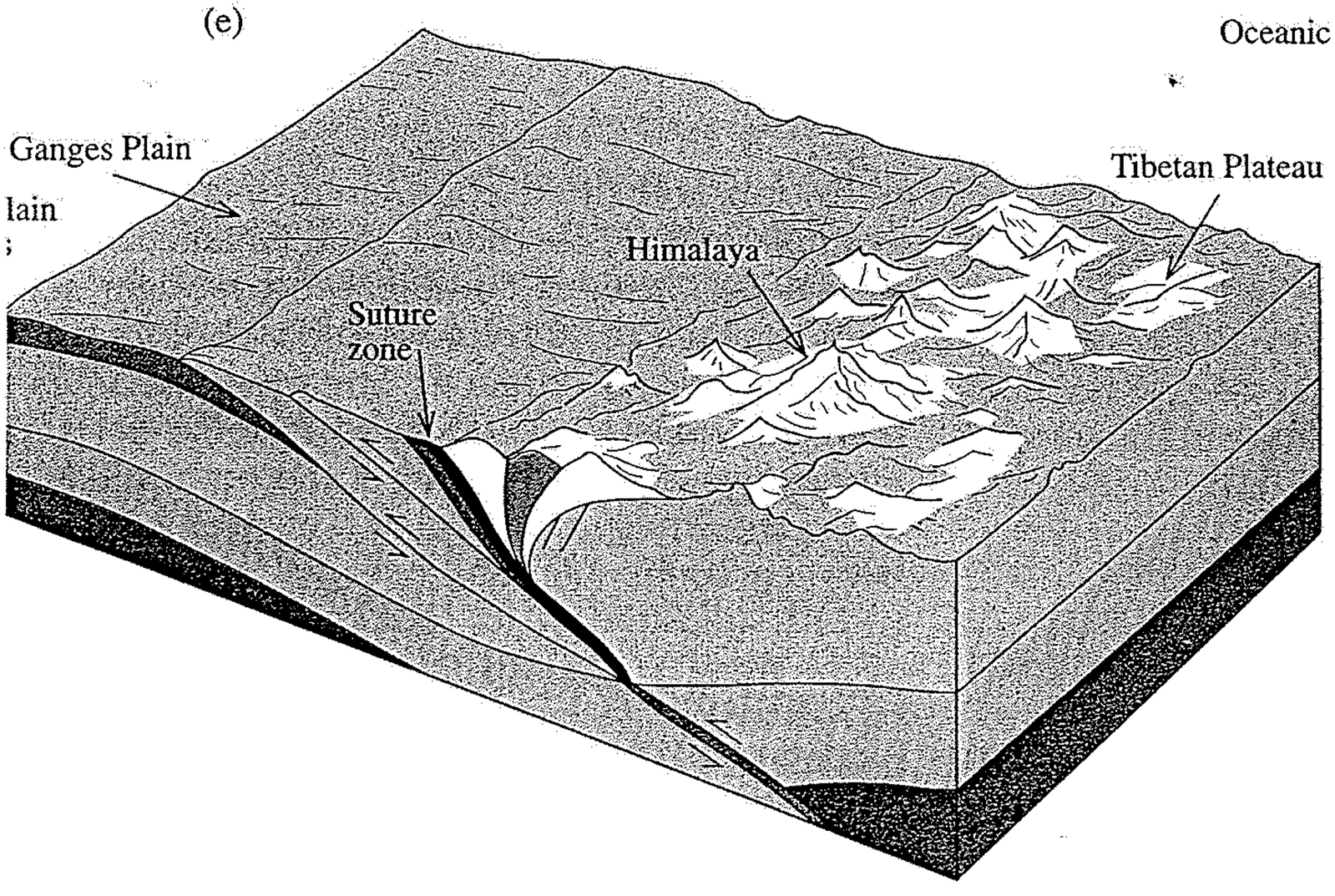

Figure 8.9 Schematic block diagrams showing the Wilson cycle of plate tectonic activity. (a), (b), and (c) illustrate the rifting of a continent to form a new ocean basin bounded by rifted continental margins. (d) and (e) illustrate the destruction of an ocean basin, initially by subduction of the oceanic lithosphere (d), followed by full-scale continental collision (e). See the text for more discussion.

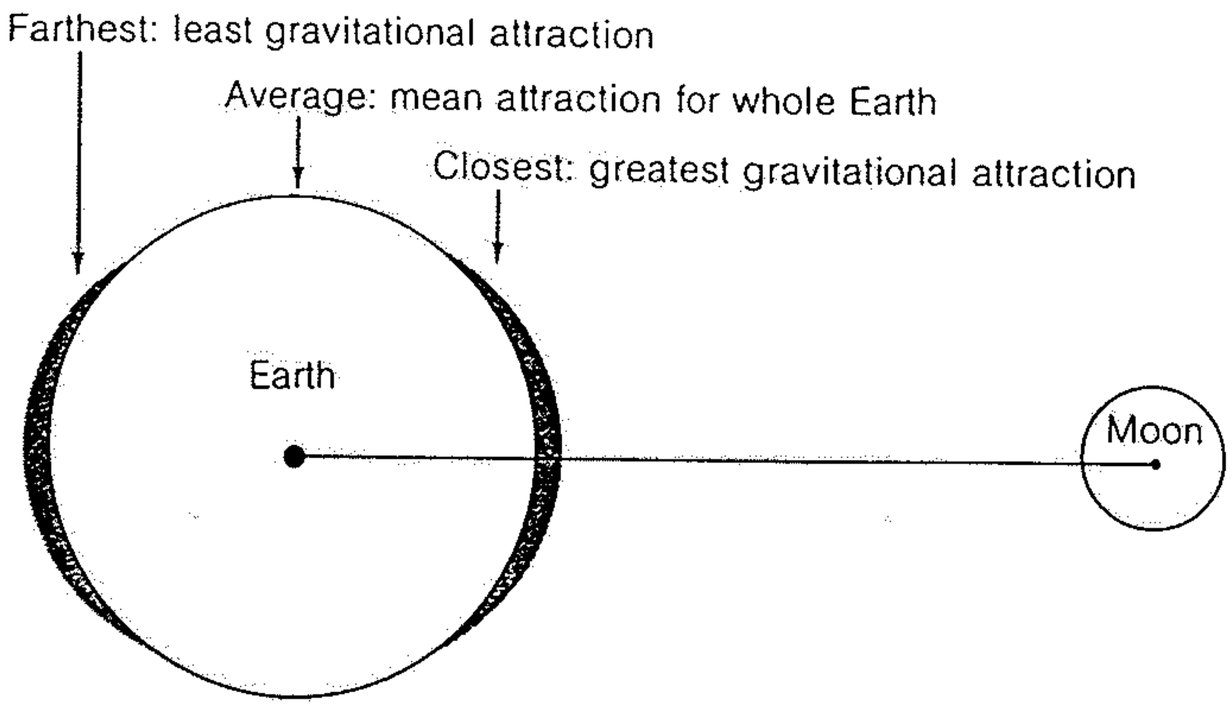

Figure 11-23

Moon's gravitational attraction causes two bulges of water on the Earth's oceans, one on the nearest side and one on the farthest side. As the Earth rotates, the bulges always face the Moon. Thus two high tides (bulge closest to Moon and bulge farthest from Moon) pass each point on Earth's surface each day.

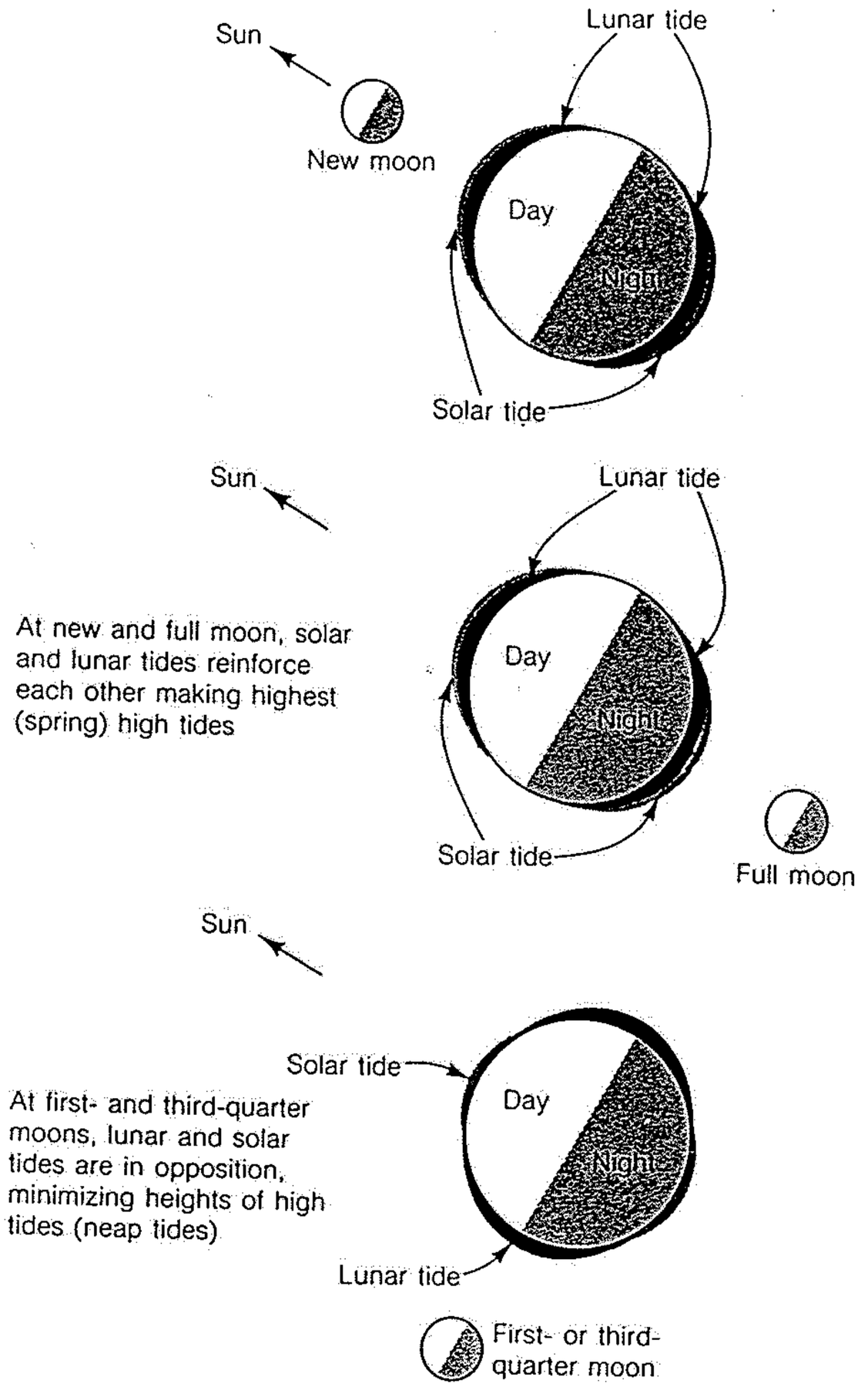

Figure 11-24

The relative positions of Earth, Moon, and Sun determine the heights of high tide during the lunar month. The highest high and lowest low tides (spring tides) come at new and full moons; the lowest high and highest low tides (neap tides) come at first- and third-quarter moon.

Figure 10.4. Range of temperature and salinity in the global ocean, as illustrated by contours enclosing values for 99 and 75 percent of all the water in the ocean. The range of salinity is relatively narrow compared with that of temperature. The very cold average temperature of the ocean reflects the high-latitude origin of most of the water in the deep ocean. (*Source:* Adapted from M. G. Gross and E. Gross, *Oceanography*, 7th edition. Englewood Cliffs, NJ: Prentice-Hall, 1996.)

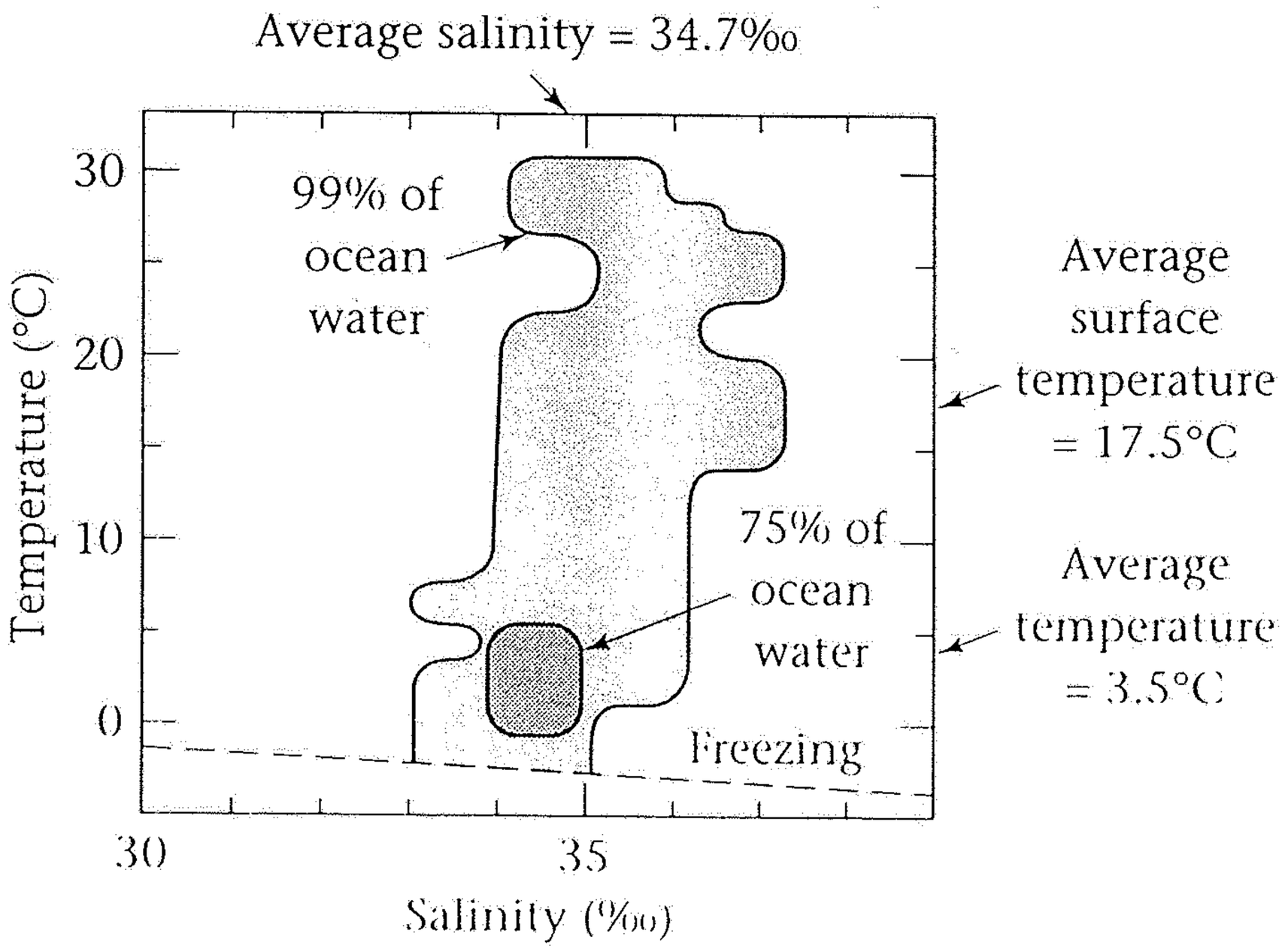

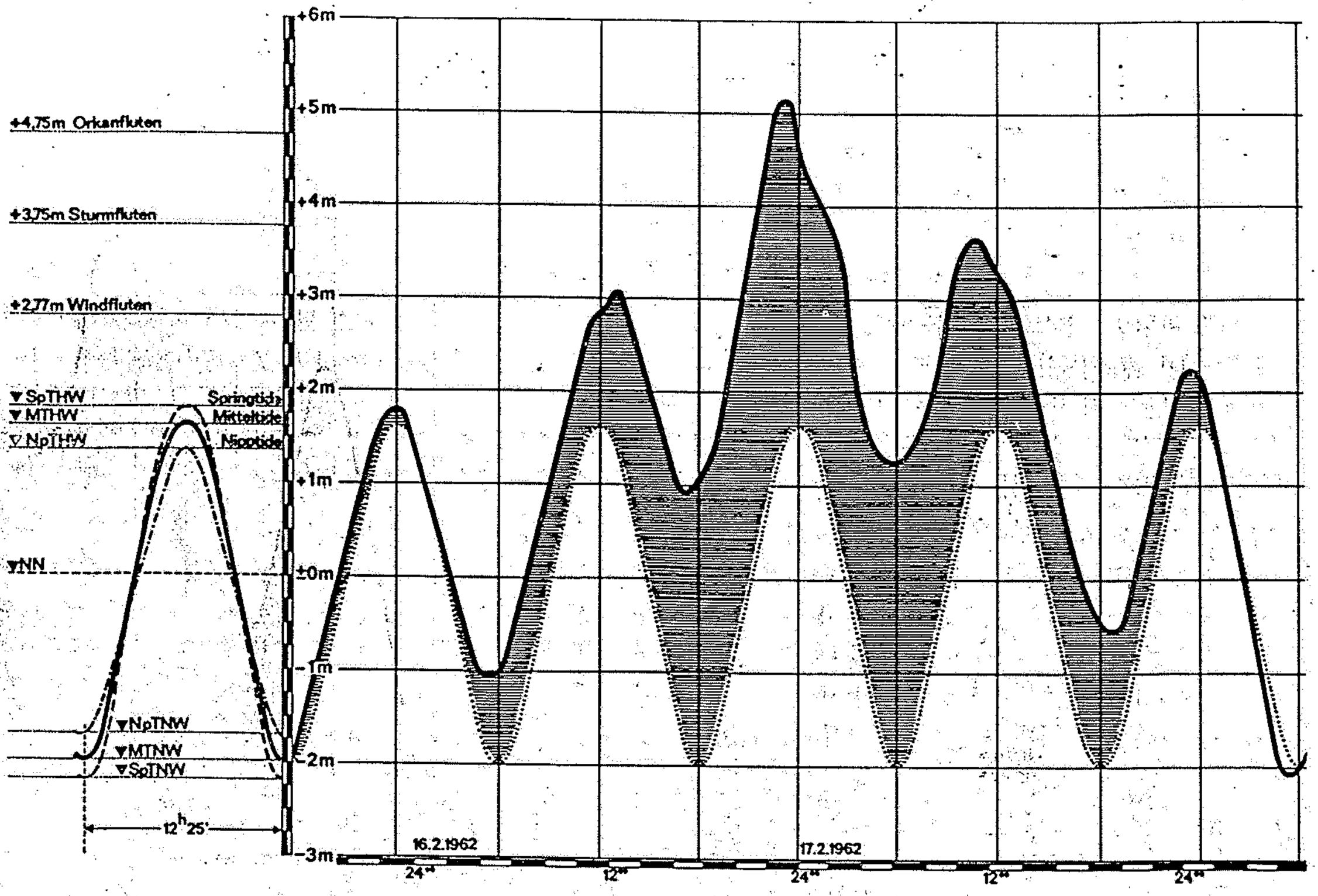

Abb. 12. Die Tidekurve bei Wilhelmshaven. Eingezeichnet wurde der mittlere Verlauf aller Tiden (ausgezogene Kurve), sowie der mittlere Verlauf von Springtiden (gestrichelt) und von Nipptiden (strichpunktierte Linie). Umgezeichnet nach Strombautaschenbuch. Das mittlere Springtiden-Niedrigwasser (SpTNW) entspricht dem Seekartennull. Bei Wilhelmshaven liegt es 2,25 m unter NN, bei Schillig 1,90 m. Im rechten Bildteil der Verlauf der Orkanflut 1962 (umgezeichnet nach REINECK 1962).

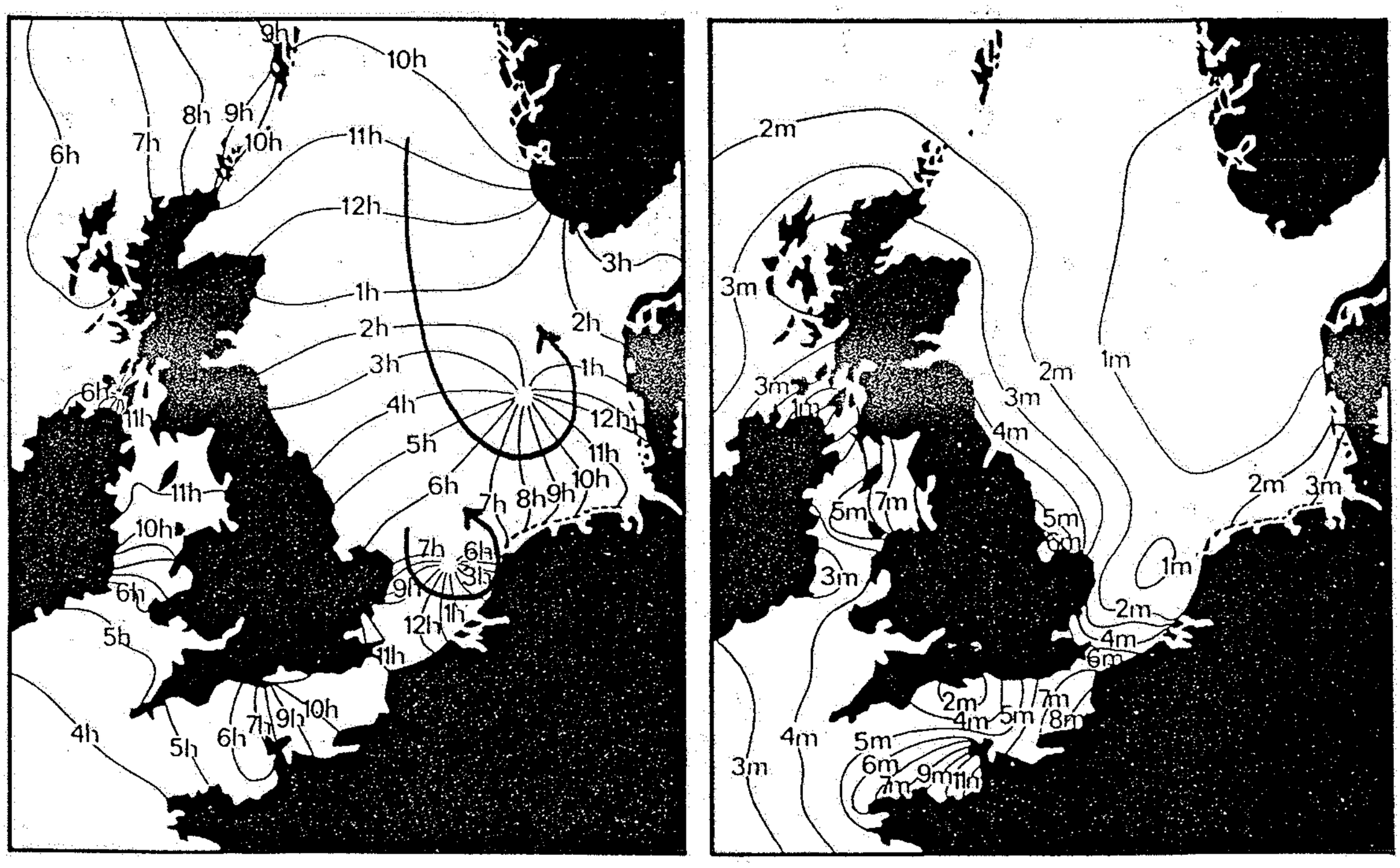

Abb. 9. Linien gleicher Tidehochwasser-Zeit. Die Gezeitenwelle läuft in der südlichen Nordsee gegen den Uhrzeigersinn (umgezeichnet nach Deutsches Hydrographisches Institut 1966).

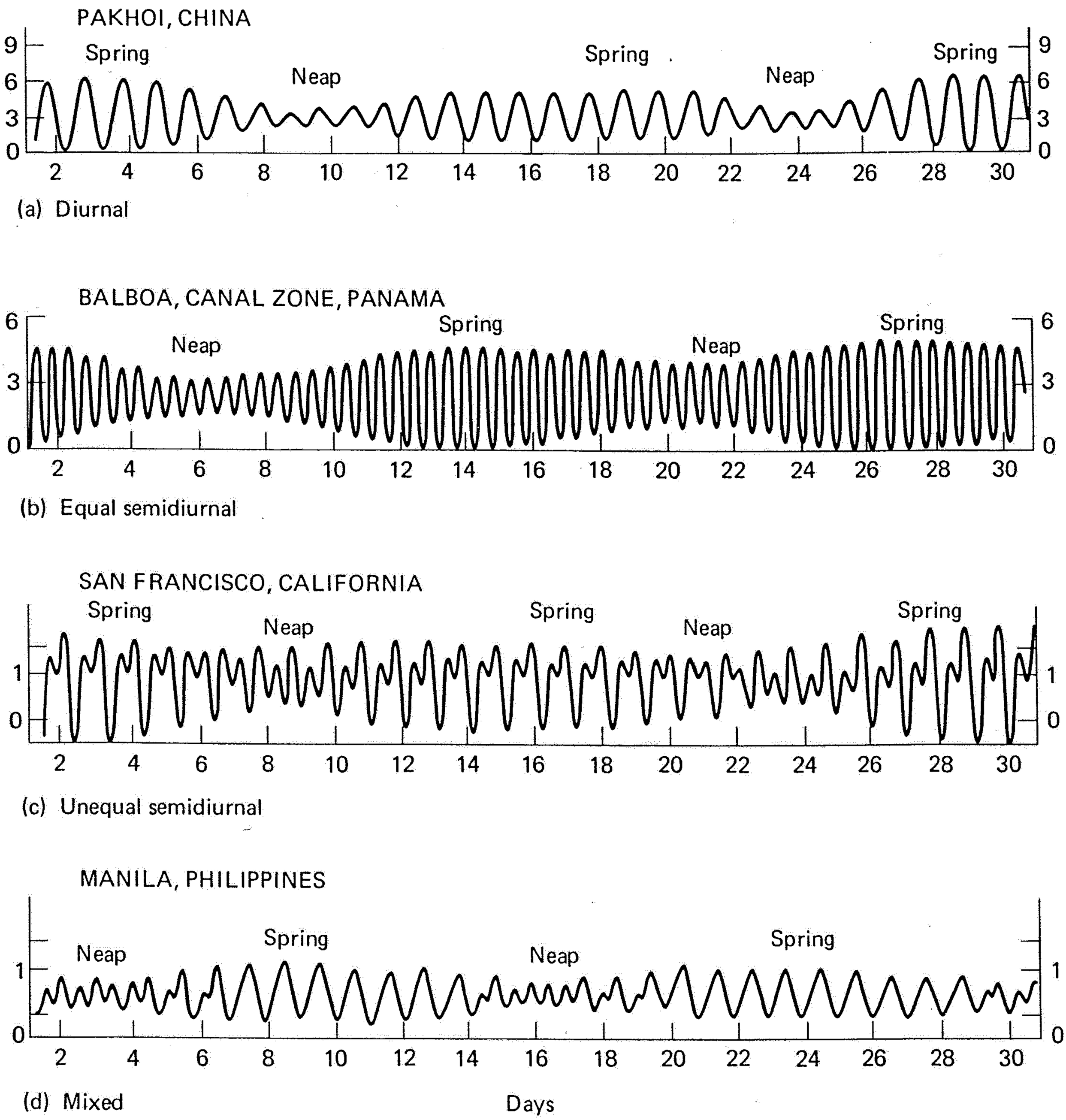

Figure 2–18 Tidal curves for a complete lunar cycle at locations which have diurnal, semidiurnal, and mixed tides.

Figure 10.9. Generalized surface circulation of the ocean and major surface currents and gyres. Compare surface currents shown on this map with general patterns of surface winds shown on Figure 10.8.

Figure 12.7. Ocean circulation of cold, salty, deep current and warm, less salty, shallow current. (*Source:* On the ocean circulation, Volume II, WHOI Technical Report WHOI-96-08, Woods Hole Oceanographic Institution; photograph by Bill Schmitz, 1996.)

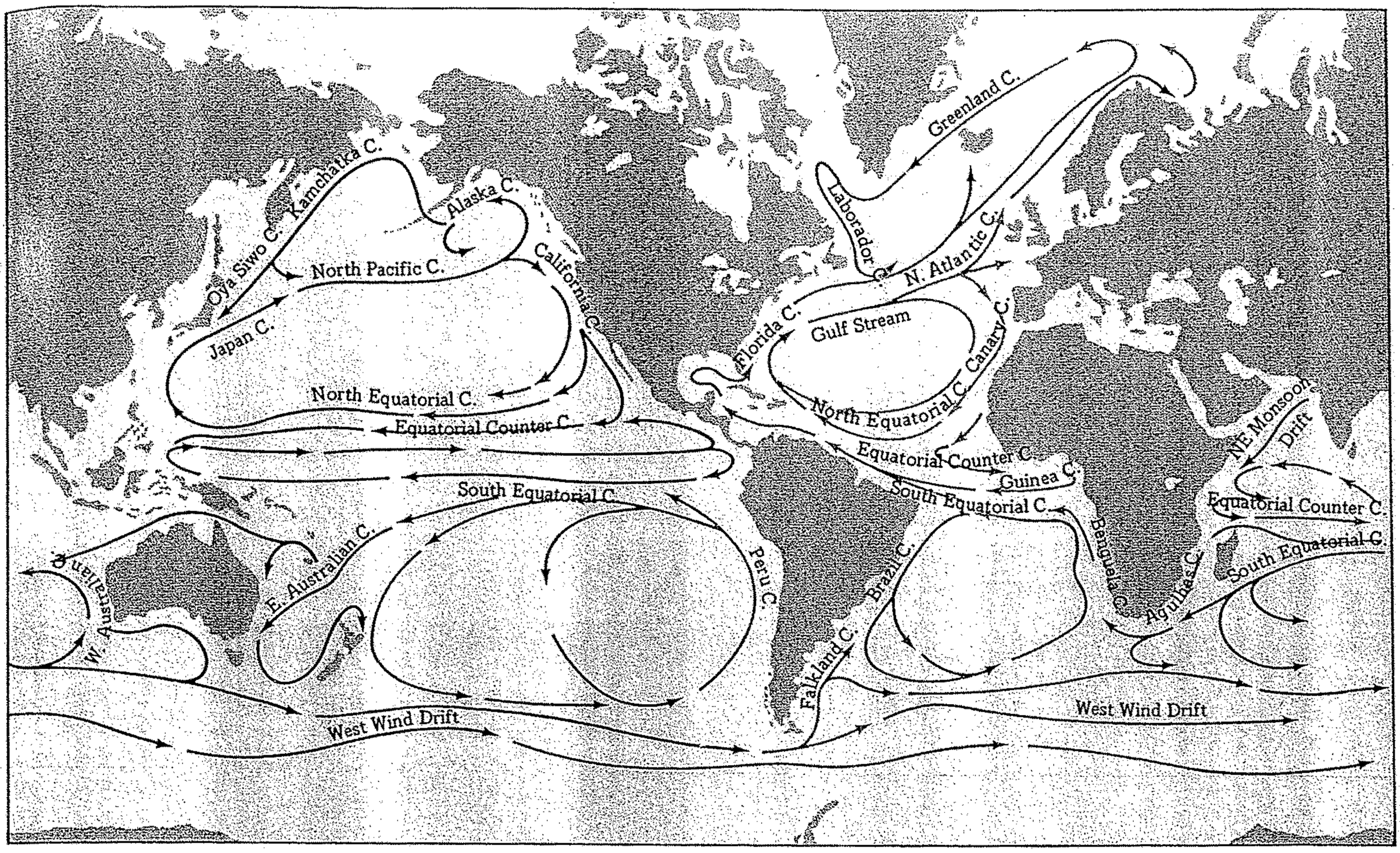

16.7 Major surface currents of the world.

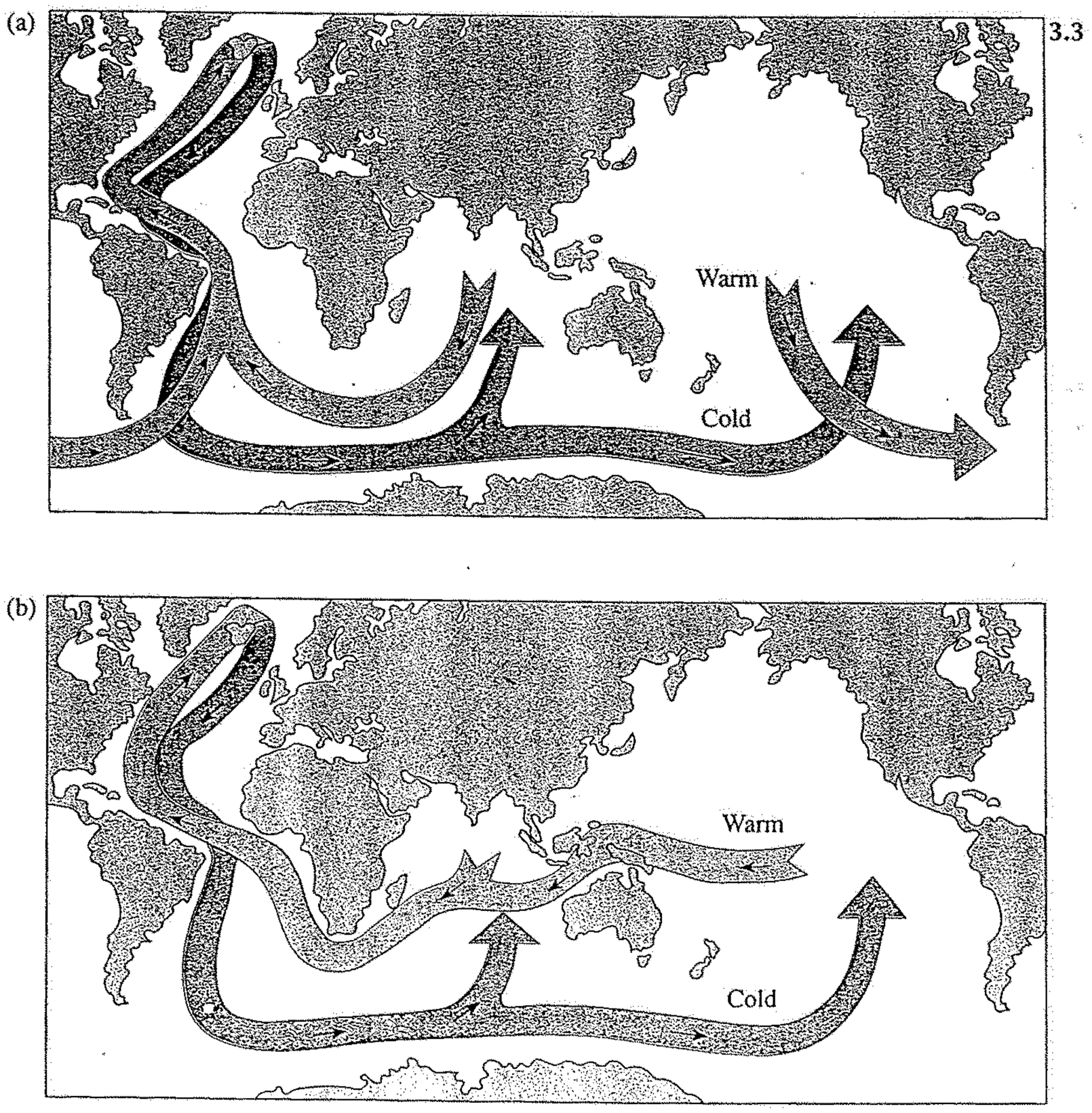

Figure 3.3 Schematic views of two versions of the 'conveyor' circulation of the oceans. Warm water associated with the surface and intermediate waters of the oceans (upper 1000 m) follows a pathway toward the northern North Atlantic Ocean, where it is subjected to intense winter cooling. This leads to the formation of cold North Atlantic deep water, which spreads southward into the Southern Ocean and returns to the Pacific Ocean. The conveyor is responsible for a northward transfer of heat throughout the whole of the Atlantic Ocean. (a) The upper water moving eastward from the Pacific into the Atlantic. (b) The upper warm water moving through the Indonesian Archipelago into the Indian Ocean and thence into the Atlantic Ocean.

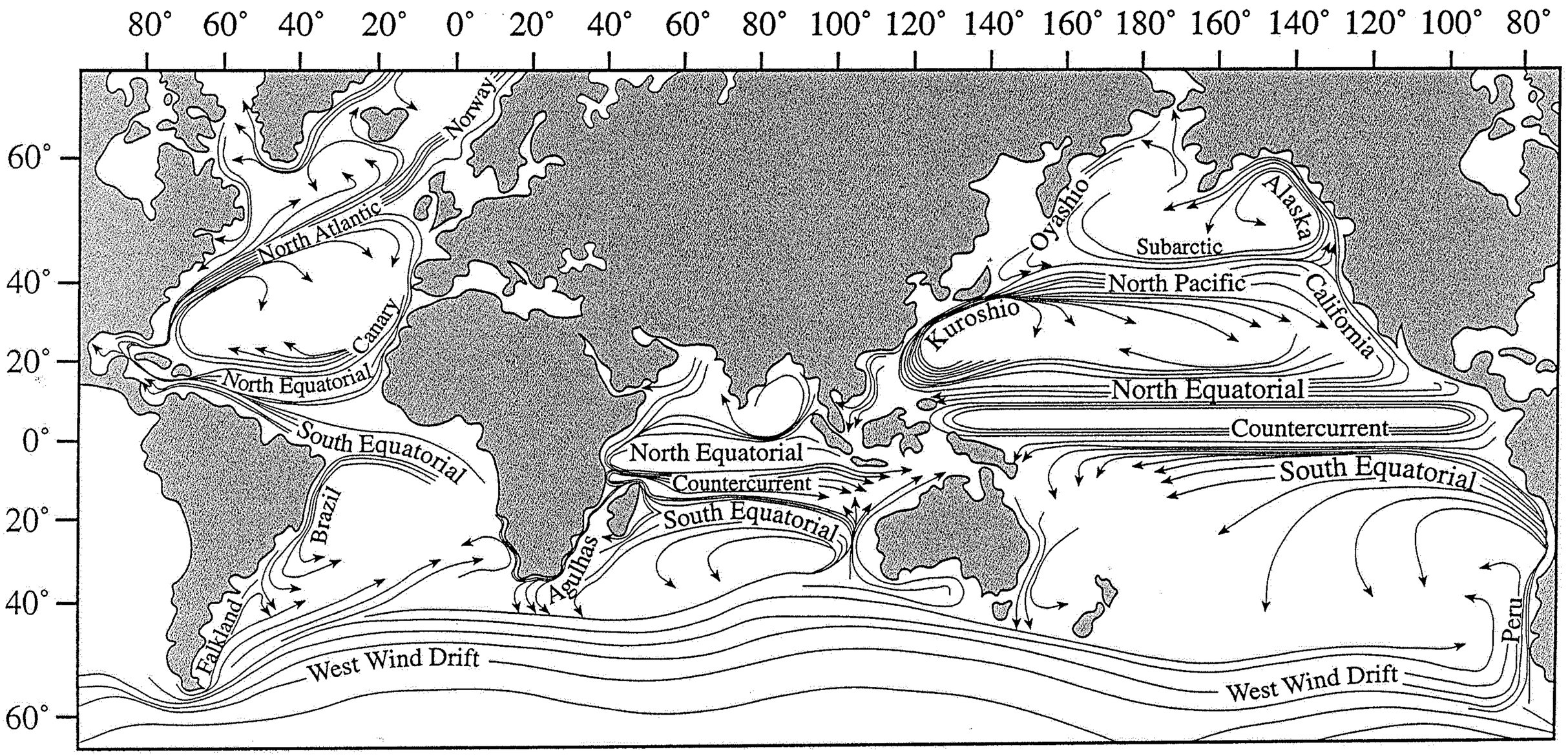

Figure 2.11 Schematic chart of the climatological average of the surface currents of the ocean (based on NRDC[12]).

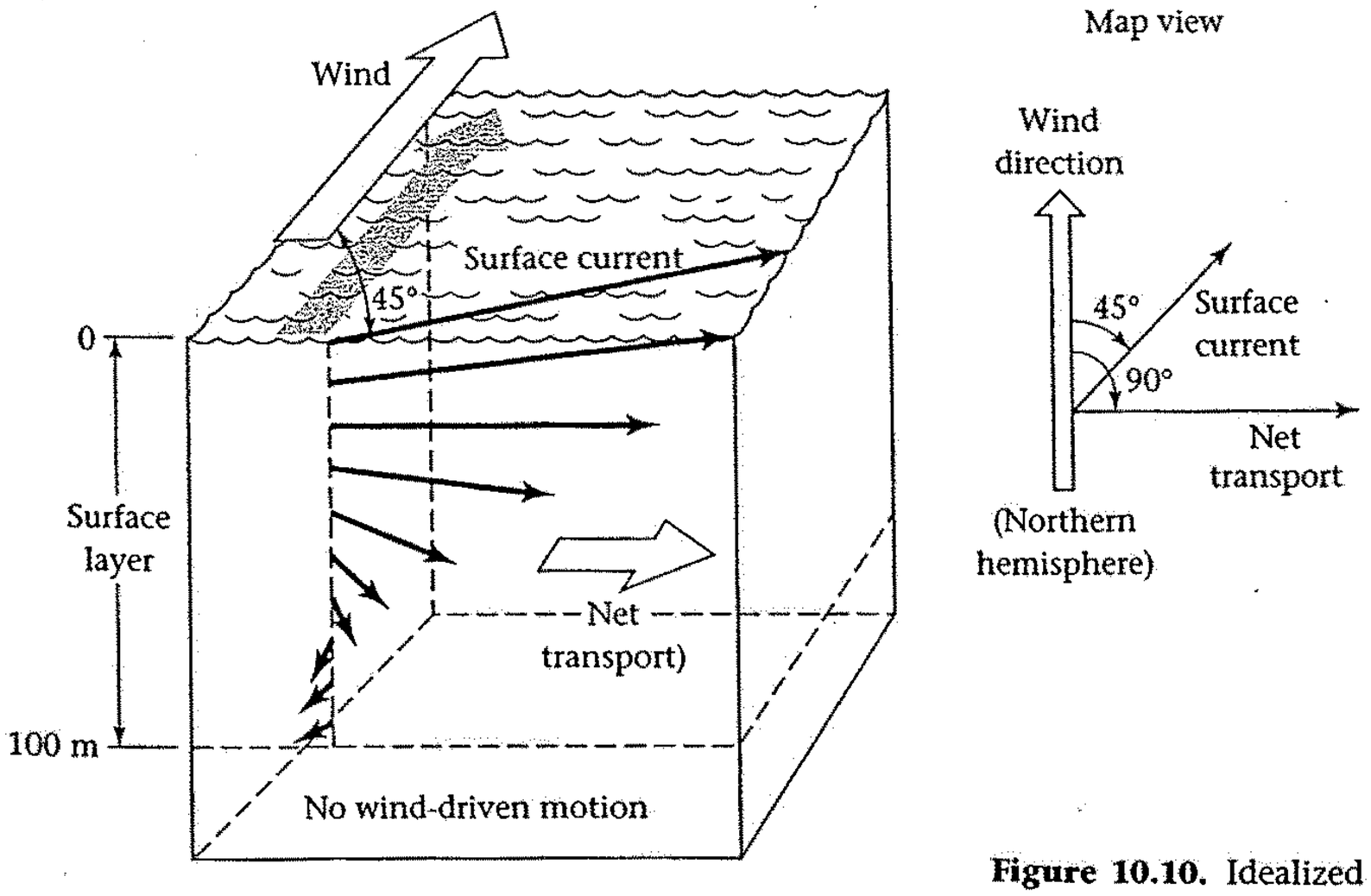

Figure 10.10. Idealized view of the wind-driven Ekman spiral and Ekman transport within the surface layer of the ocean (in the Northern Hemisphere). The lengths of the solid arrows depict the frictional decrease in velocity with depth; the directions of the arrows illustrate the results of the Coriolis effect on the motion of each succeeding layer down through the column. The Coriolis effect accounts for a 45° angle (to the right of motion in the Northern Hemisphere) between the direction of the wind and the direction of the wind-driven surface current, whereas the net drift of the entire surface layer is at 90° to the right of the wind. m = meters. (*Source:* Adapted from P. R. Pinet, *Oceanography*, West Publishing Company, 1992.)

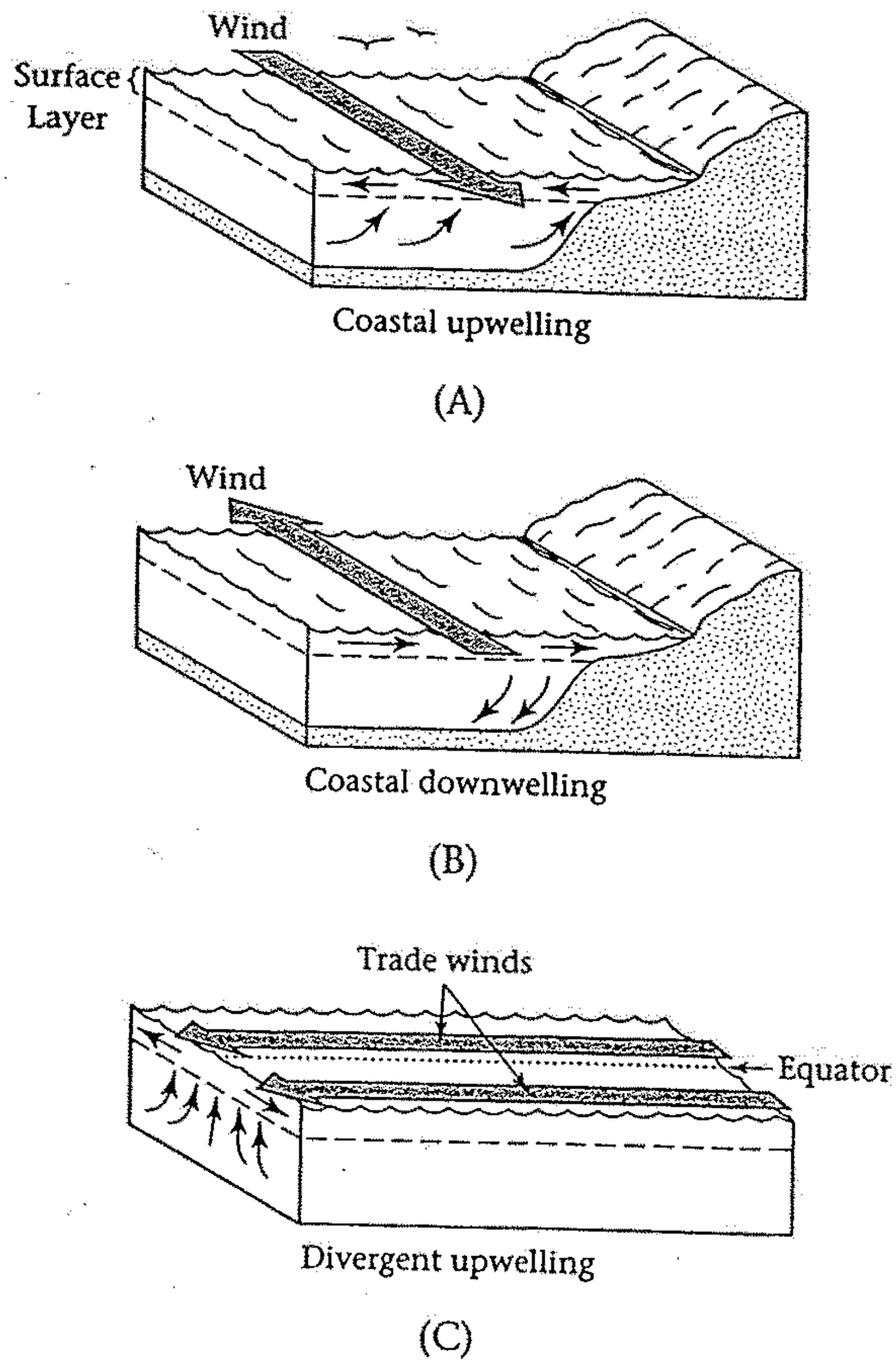

Figure 10.12. Schematic illustrations of (A) coastal upwelling, (B) coastal downwelling, and (C) open ocean divergent upwelling (in the Northern Hemisphere). All three types of vertical motion occur as a function of wind-driven Ekman transport (see Fig. 10.10). As winds blow equatorward (south) along the western side of a continent in the Northern Hemisphere, Ekman transport forces surface water seaward away from the coast (at 90° to the right of the wind direction). This latter water is in turn replaced by nutrient-rich intermediate water upwelled from below the surface layer, triggering high primary and secondary productivity. Conversely, the direction of Ekman transport is reversed if winds blow poleward in the same area, with the result that surface water undergoes downwelling (sinking) as it is forced against the coast. Equatorial divergent upwelling results where west-blowing northern trade winds induce northward Ekman transport at the same time that parallel southern trade winds (in the Southern Hemisphere) are inducing southerly Ekman transport. Thus, subsurface water is upwelled in the zone between the two opposing surface flows.

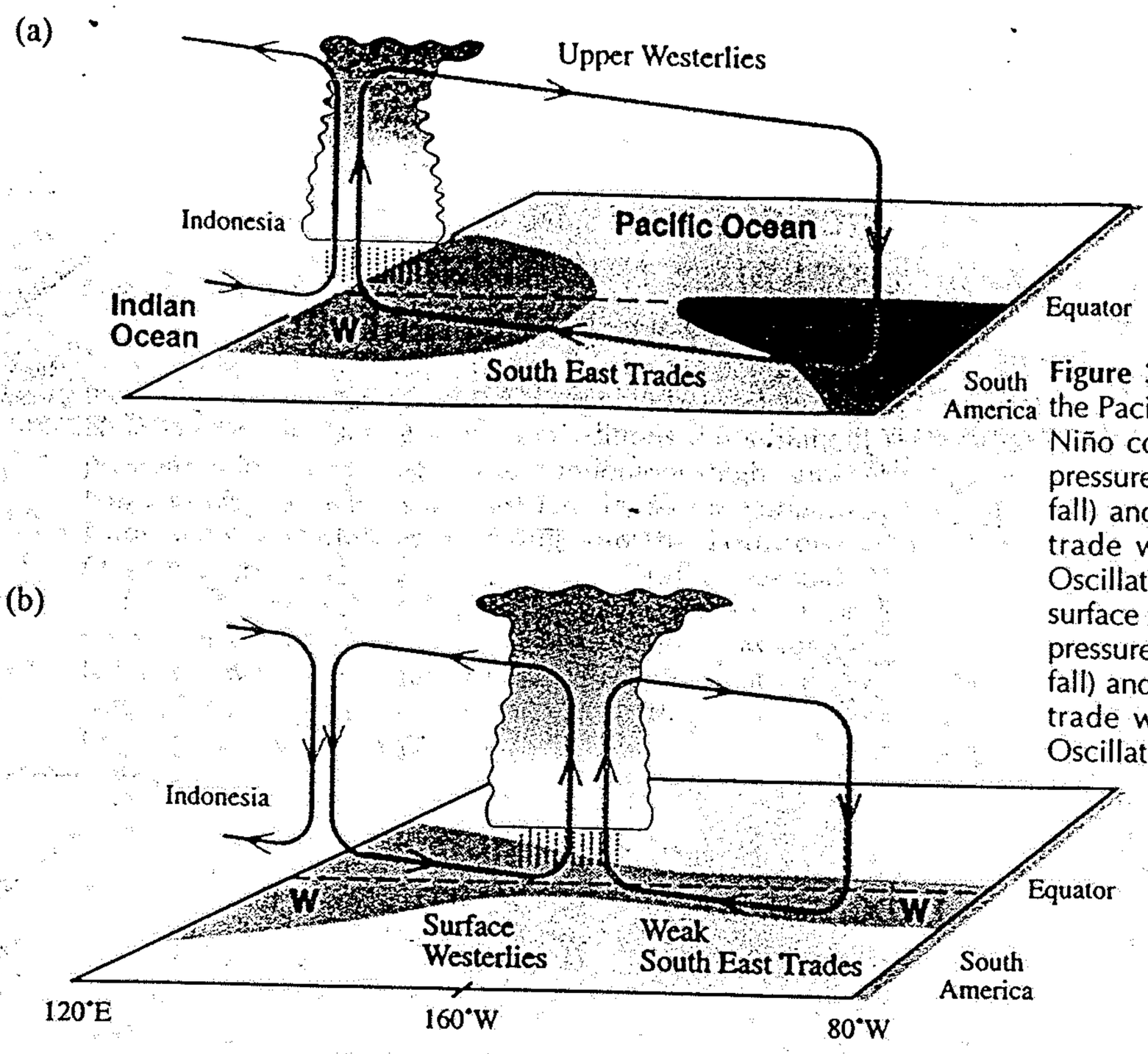

Figure 3.22 The tropical atmospheric circulation over the Pacific Ocean during (a) normal conditions and (b) El Niño conditions. During normal conditions the surface pressure is low over Australia and Indonesia (high rainfall) and high over the southeast Pacific, so the surface trade wind circulation is strong and the Southern Oscillation index ($P_{DARWIN} - P_{TAHITI}$, where P is the seasonal surface pressure) is high. During El Niño conditions, the pressure is higher over Australia and Indonesia (low rainfall) and lower in the southeast Pacific; consequently the trade wind circulation is weaker and the Southern Oscillation index is low (W, warm; C, cold).

Figure 3.23 The tropical Pacific Ocean during (a) normal and (b) El Niño years. During normal years the strong trade winds drive the warm water westward and intensify upwelling of cooler subsurface waters in the east Pacific. During El Niño years the weaker atmospheric circulation allows the warmer lighter water to flow eastward, replacing the cooler upwelling waters.

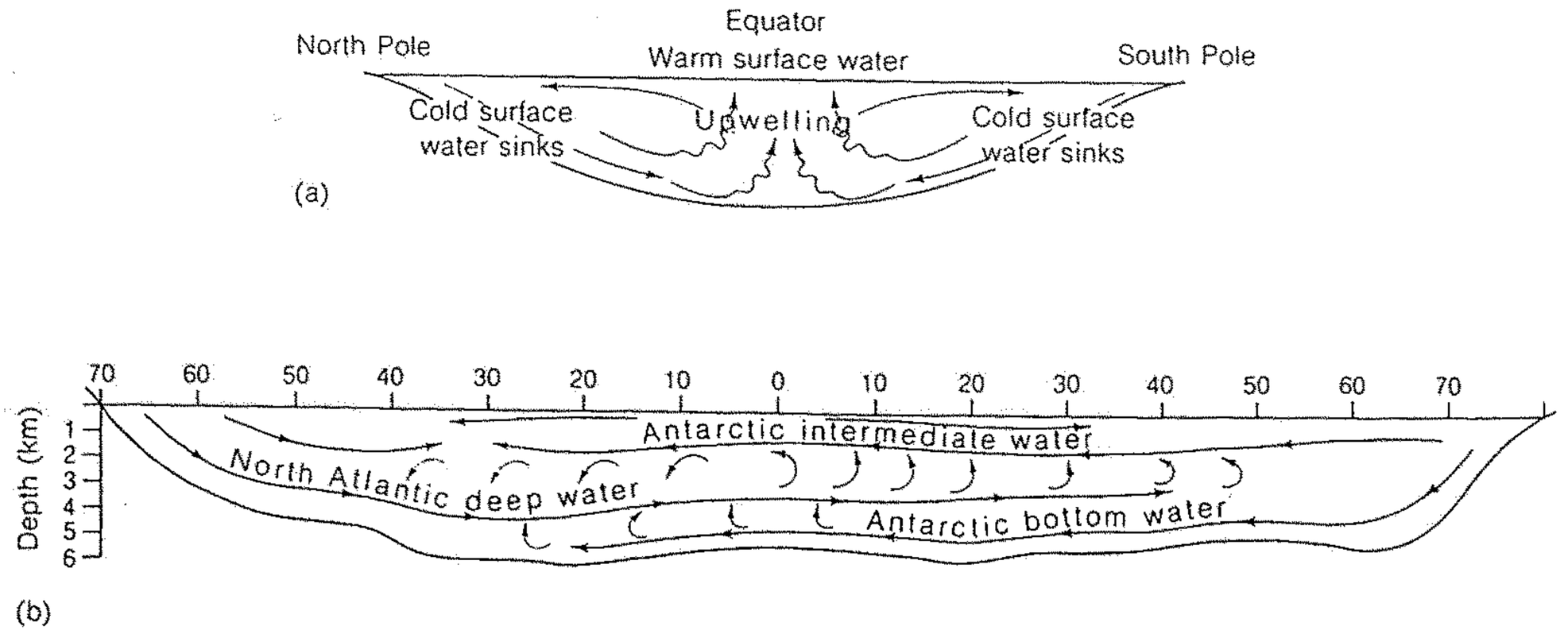

Figure 11-47

Generalized vertical circulation of the Atlantic Ocean. (a) An ideal model of a north–south ocean that is cooled at the poles and warmed at the equator. Colder waters sink because they are denser, replacing warmer water, which rises. (b) Simplified model of Atlantic Ocean circulation, showing how Antarctic bottom water flows along the bottom more than 20° north of the equator, displacing the Arctic bottom water to an intermediate level.

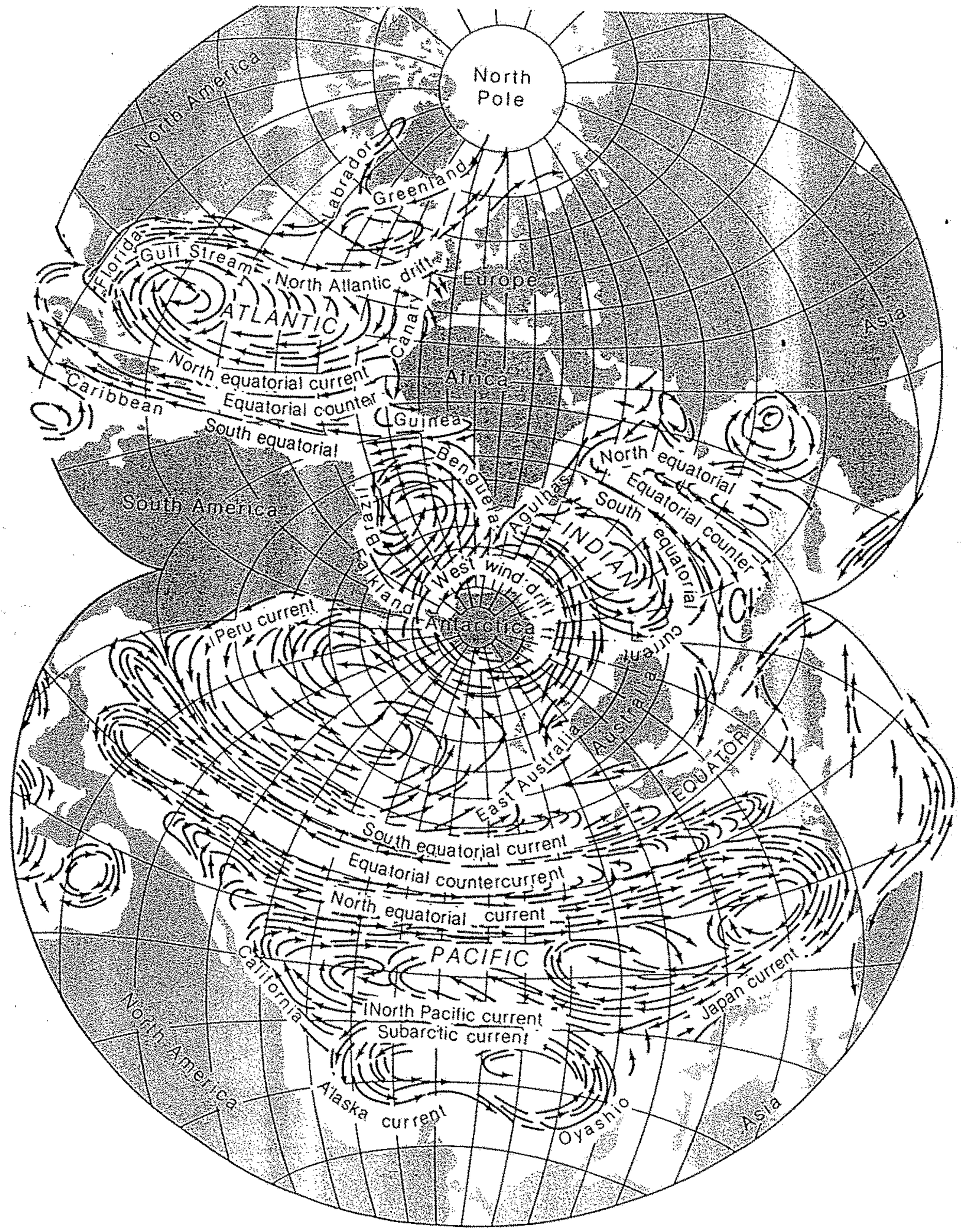

Figure 11-46

Major ocean currents shown on a map centered on the South Pole. [From "The Circulation of the Oceans" by W. Munk. Copyright © 1965 by Scientific American, Inc. All rights reserved.]

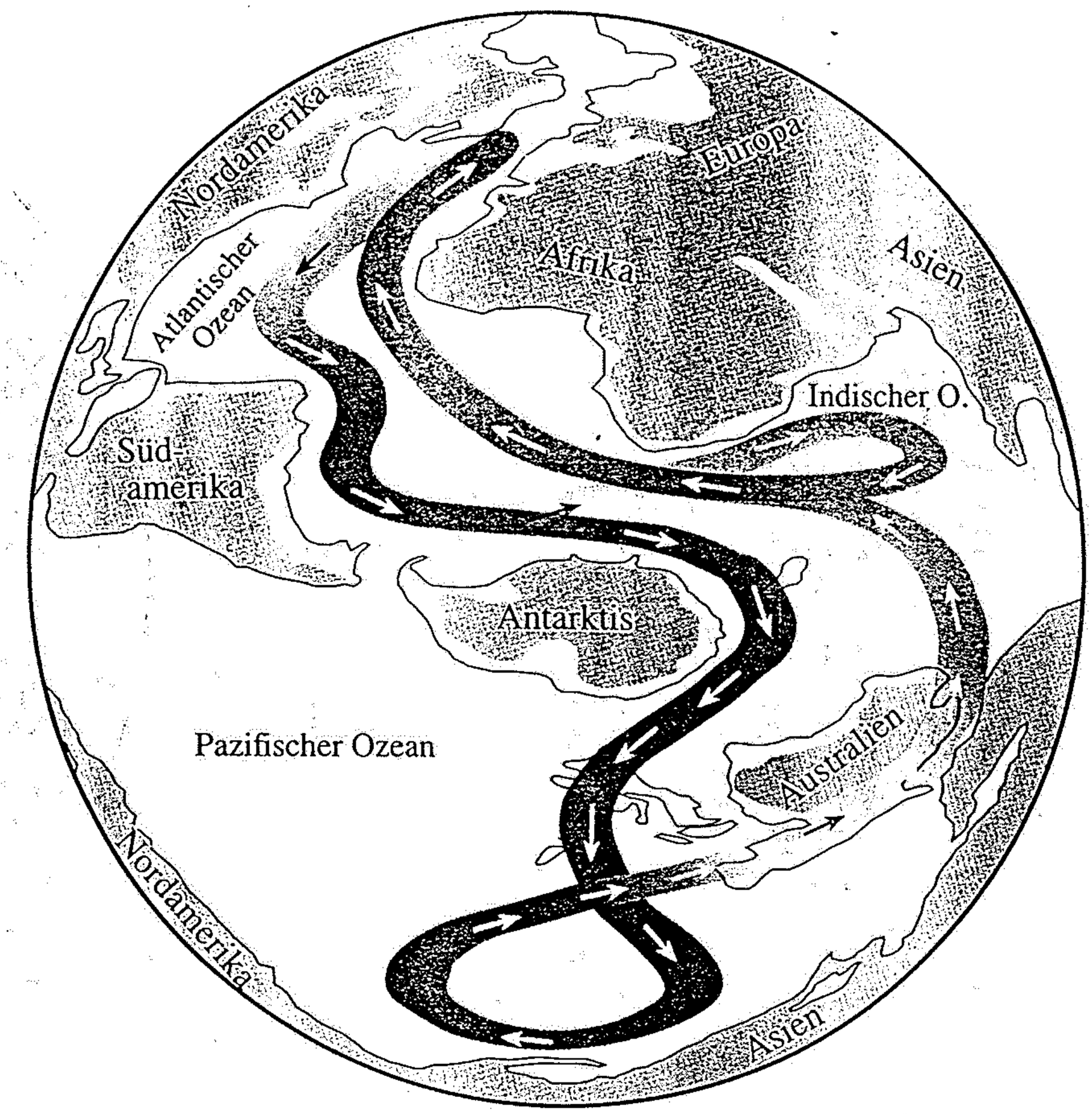

Abb. 6.4
Der erdumspannende Strömungspfad der 'Ozeanischen Klimapumpe'. Die im Nordatlantik abgesunkenen kalten und dichten Wassermassen fließen als Tiefenströmung (blau) in den Pazifik und steigen in seinem westlichen Teil nach etwa 1000 Jahren wieder zur Oberfläche auf (rot) und strömen in den Atlantik zurück (nach BROECKER, 1987 und DEGENS, 1989).

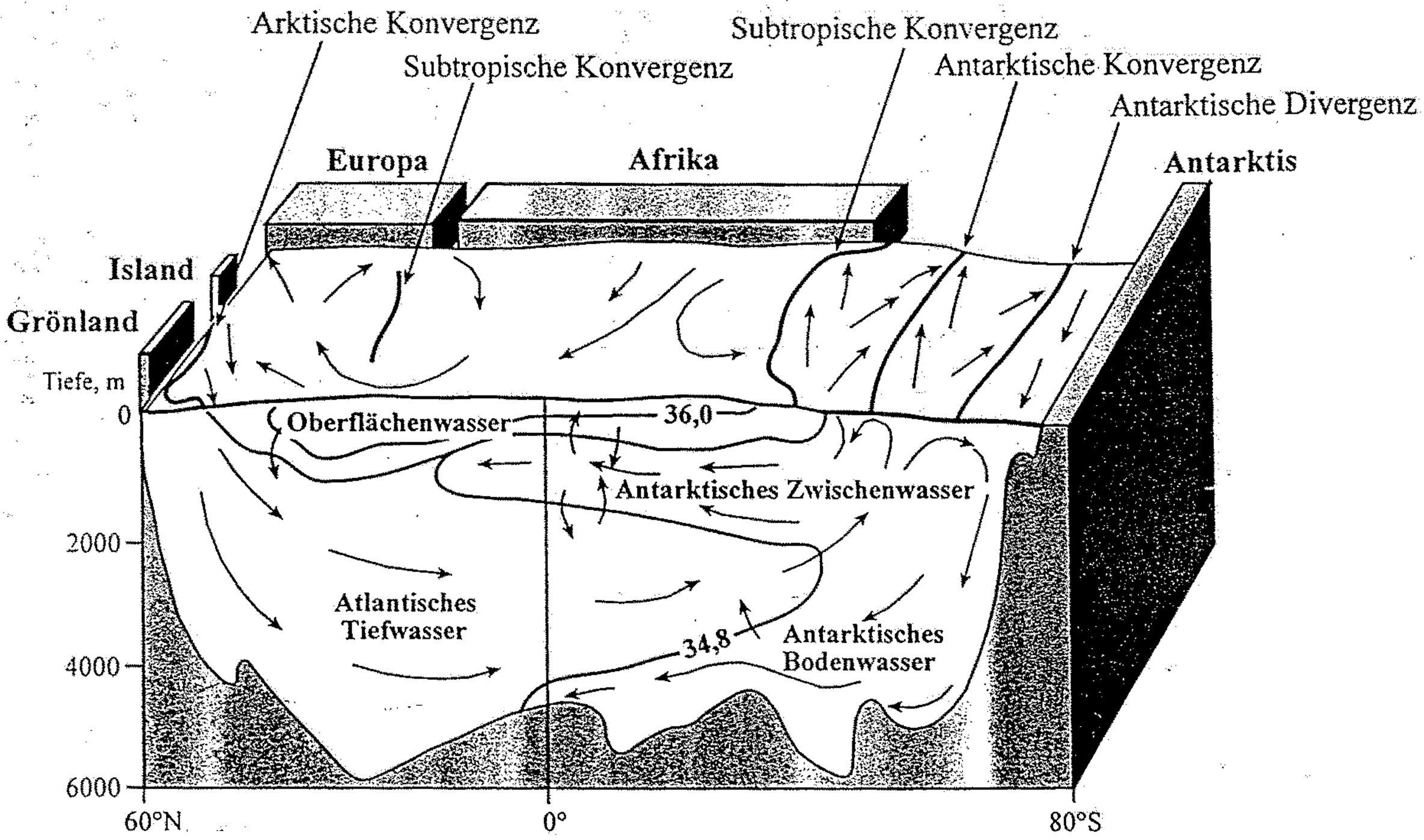

Abb. 6.3
Schematischer N-S Schnitt durch den Atlantik. Die unterschiedlichen Tiefenströmungen sind bzgl. ihrer vertikalen Position durch ihre Dichte bestimmt. So hat das an der Antarktis abgekühlte Antarktische Bodenwasser eine hohe Dichte und schiebt sich von S her unter das von N strömende Atlantische Tiefenwasser. An den Konvergenzen fließen Oberflächenströmungen zusammen und strömen in die Tiefe. An der antarktischen Divergenz erzeugen die von der Antarktis wehenden ablandigen Winde eine starke Strömung nach N. Durch sie wird Oberflächenwasser fortgetrieben und Tiefenwasser gleichsam zur Oberfläche gesogen, es teilt sich in zwei Strömungen: Eine kehrt durch Abkühlung in das Antarktische Bodenwasser zurück, die andere wird Teil der nach N fließenden Oberflächenströmung. Die Zahlen an einigen Isolinien geben Salinitäten in ‰ an. Der Meeresspiegel ist nicht wirklich eine ebene Fläche. In den Konvergenzzonen strömt Meerwasser zusammen und verursacht eine leichte Aufwölbung. In den Divergenzzonen strömt es auseinander und der Meeresspiegel ist niedriger. Die Niveauunterschiede betragen nur 1–2 m und sind hier überhöht dargestellt (nach DEGENS, 1989).

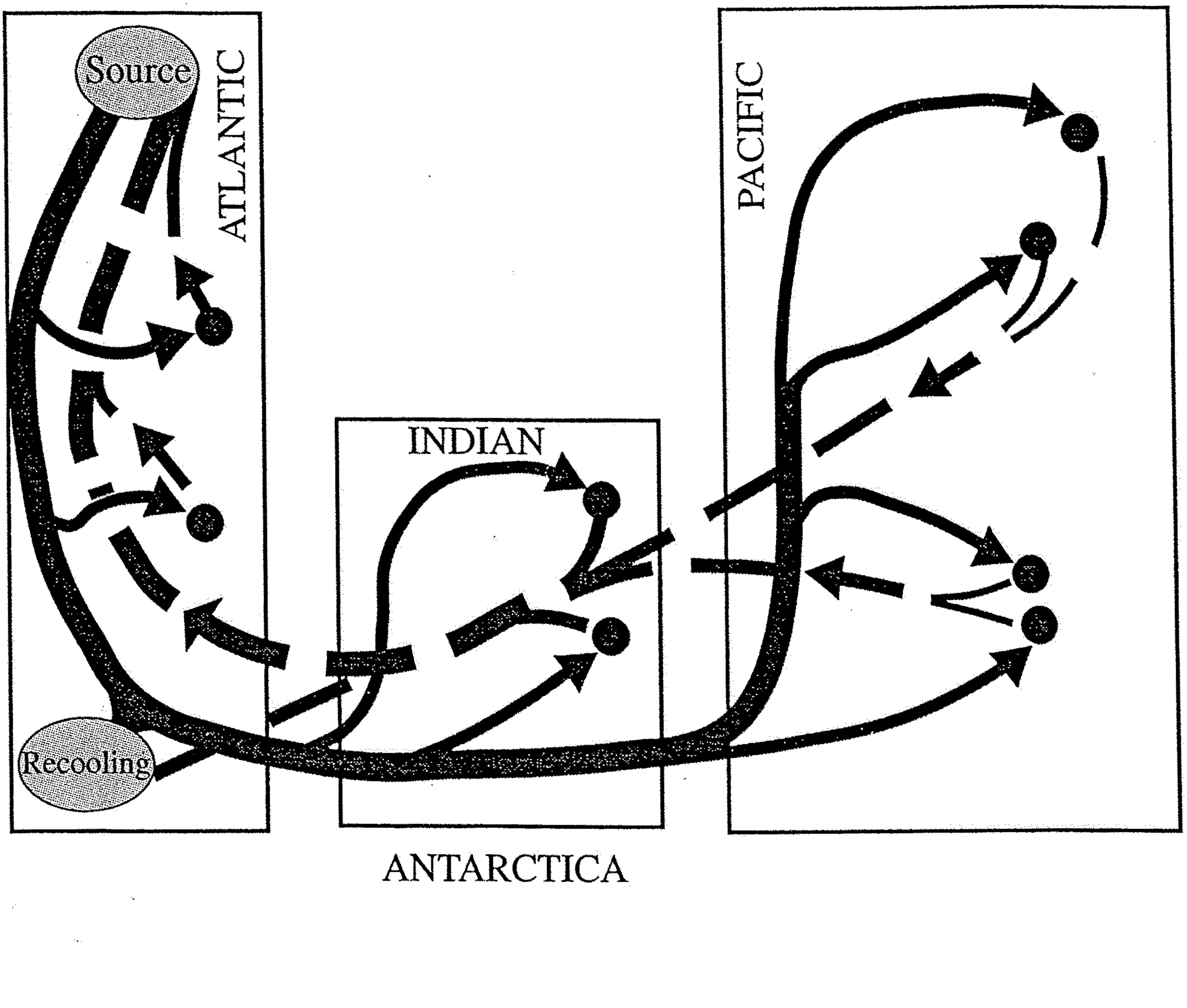

Figure 11.13 Schematic representation of the circulation of deep water in the major ocean basins (Broecker and Peng[3]; with permission from the authors). The solid lines show the flow of deep water, originating largely by sinking in the far North Atlantic Ocean. The dashed lines show the flow of surface water and the filled circles represent areas of localised upwelling.

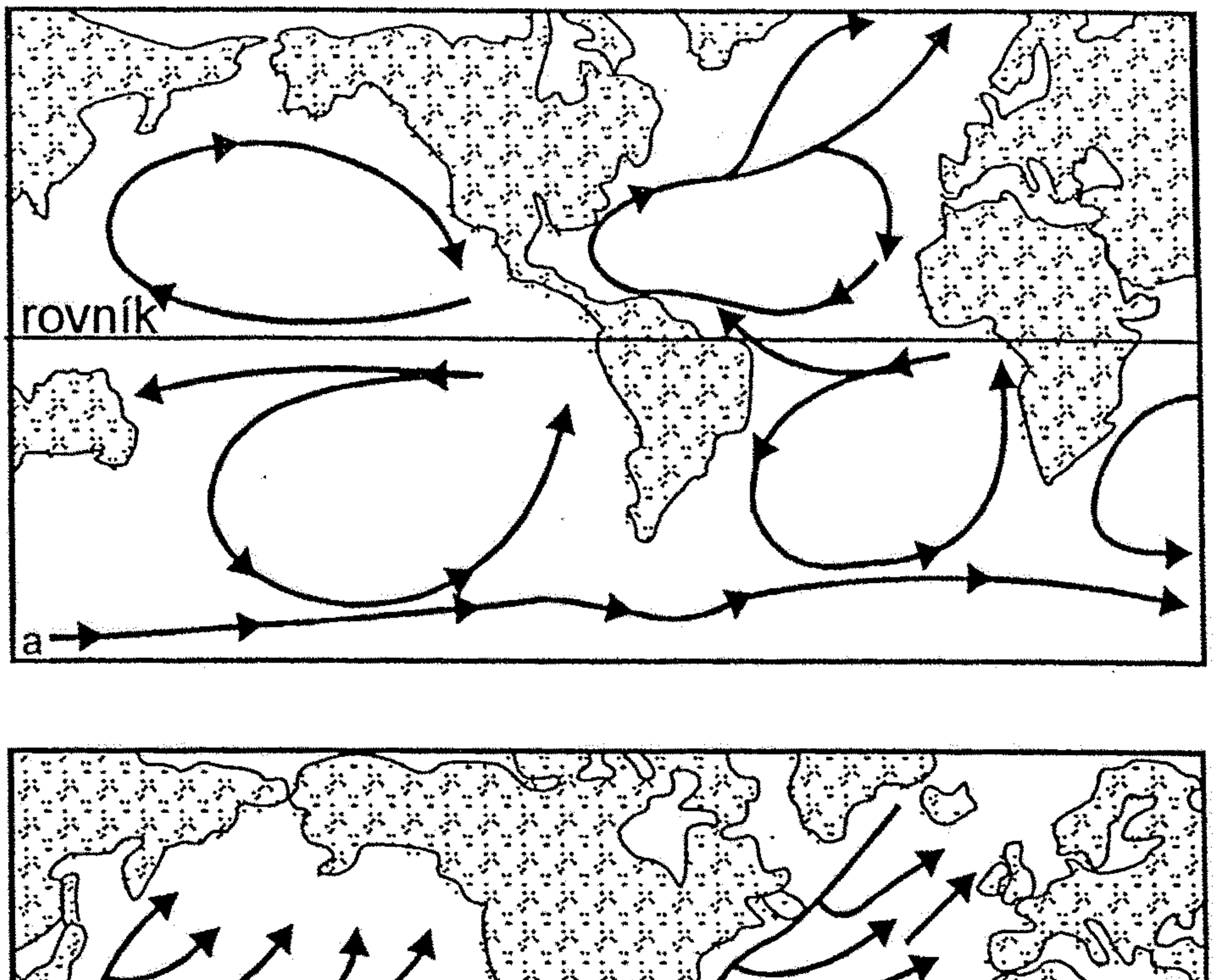

Obr. 18.13. *a – Schéma povrchovej oceánskej cirkulácie, ktorá je ovplyvnená hlavne smerom pravidelných vetrov. b – Schéma hlbinnej oceánskej cirkulácie. Na smer hlbinných prúdov má veľký vplyv morfológia dna. (prevzaté z Kukala 1984)*

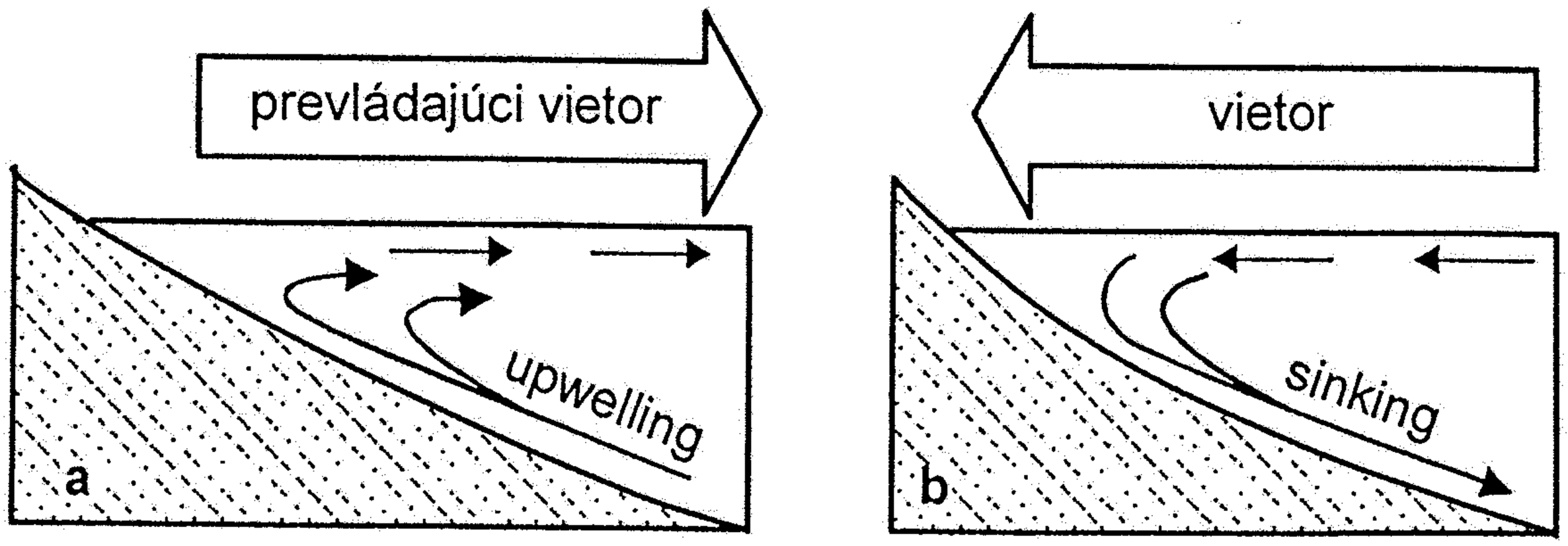

Obr. 18.14. *a – Výstup hlbinných vôd (upwelling) v miestach vetrom odtlačenej hladinovej vody; b – ponáranie (downwelling alebo sinking) vetrom k brehu nahrnutej povrchovej vody. (upravené podľa Skinnera – Portera 1987)*

2

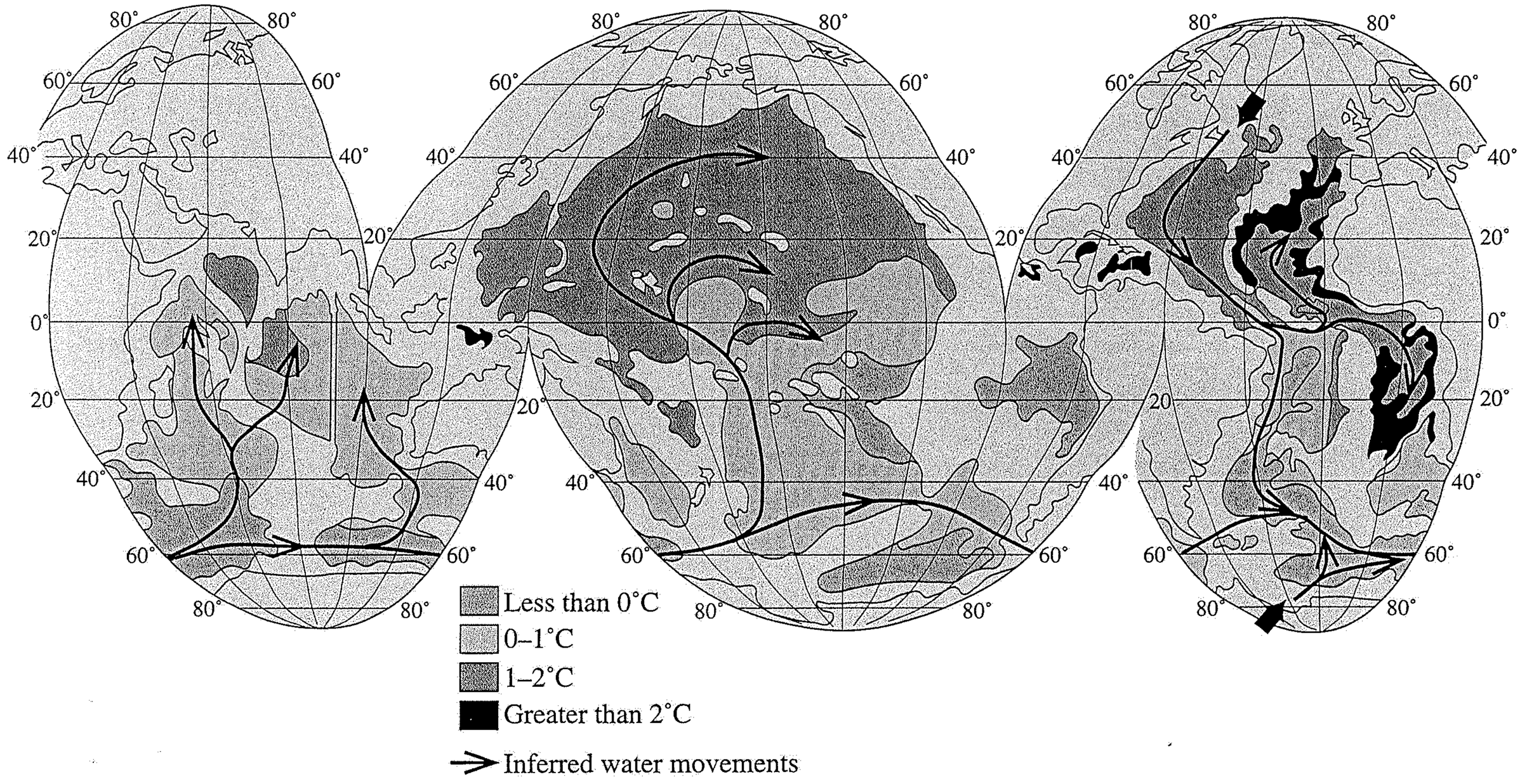

Figure 2.12 An impression of the flow pattern at 4000 m in the ocean. The major inputs are the North Atlantic Deep Water (NADW), which enters at the northern end of the Western Basin of the Atlantic, and the Weddell Sea Bottom Water, which enters from the margin of the Antarctic continent adjacent to the South Atlantic (based on Gross[6] and Broecker and Peng[3]).

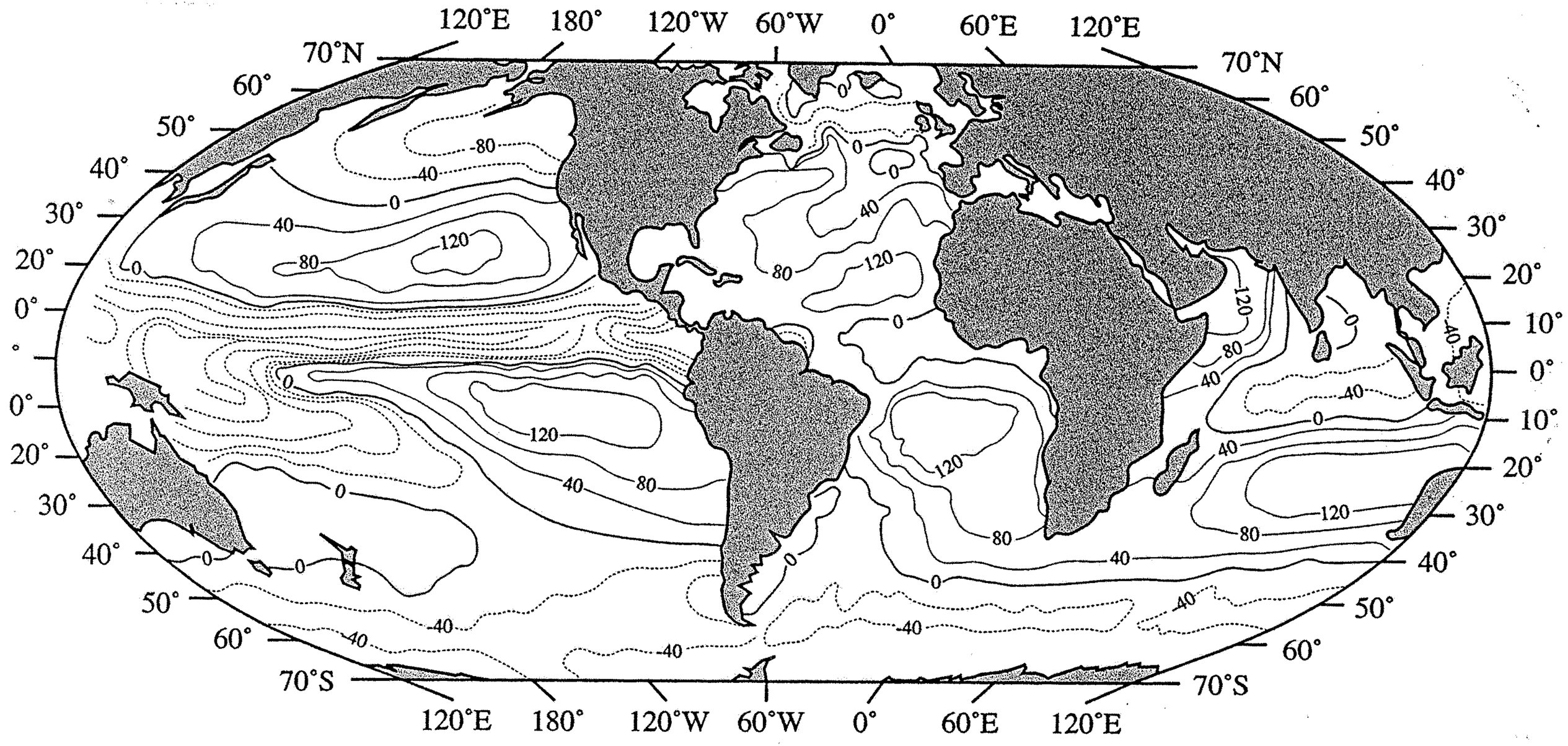

ıre 2.4 A chart of evaporation minus precipitation (*E-P*) over the ocean. Units are cm/yr; solid lines indicate *E>P*, hed lines *E<P* (from Schmitt and Wijffels[17]; the figures are derived from Schmitt *et al.*[16]).

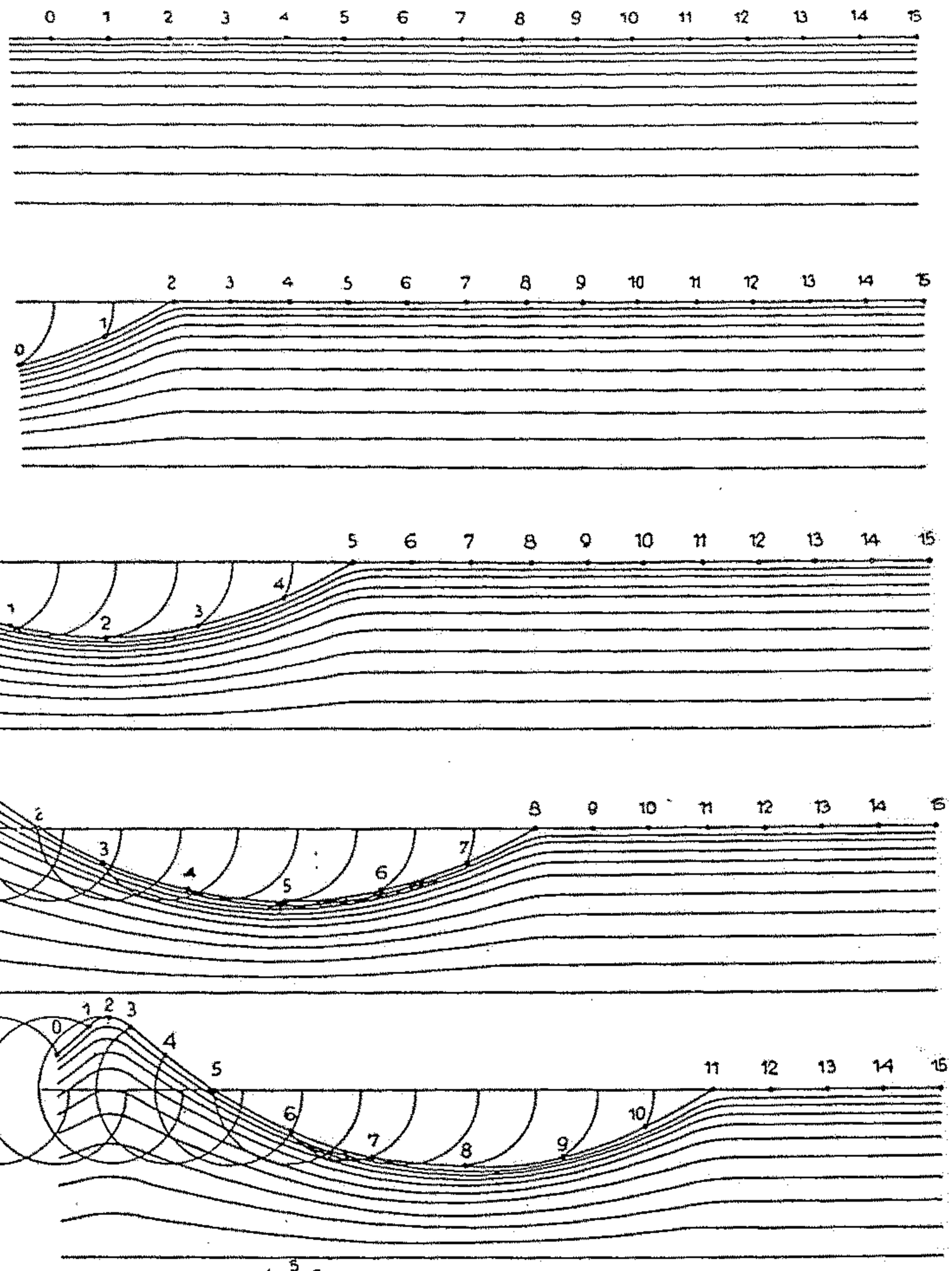

Obr. 275. *Tvoření se vodních vln kroužívým (orbitálním) pohybem vodních částic.* (Podle GRIMSEHLOVY učebnice fysiky.)

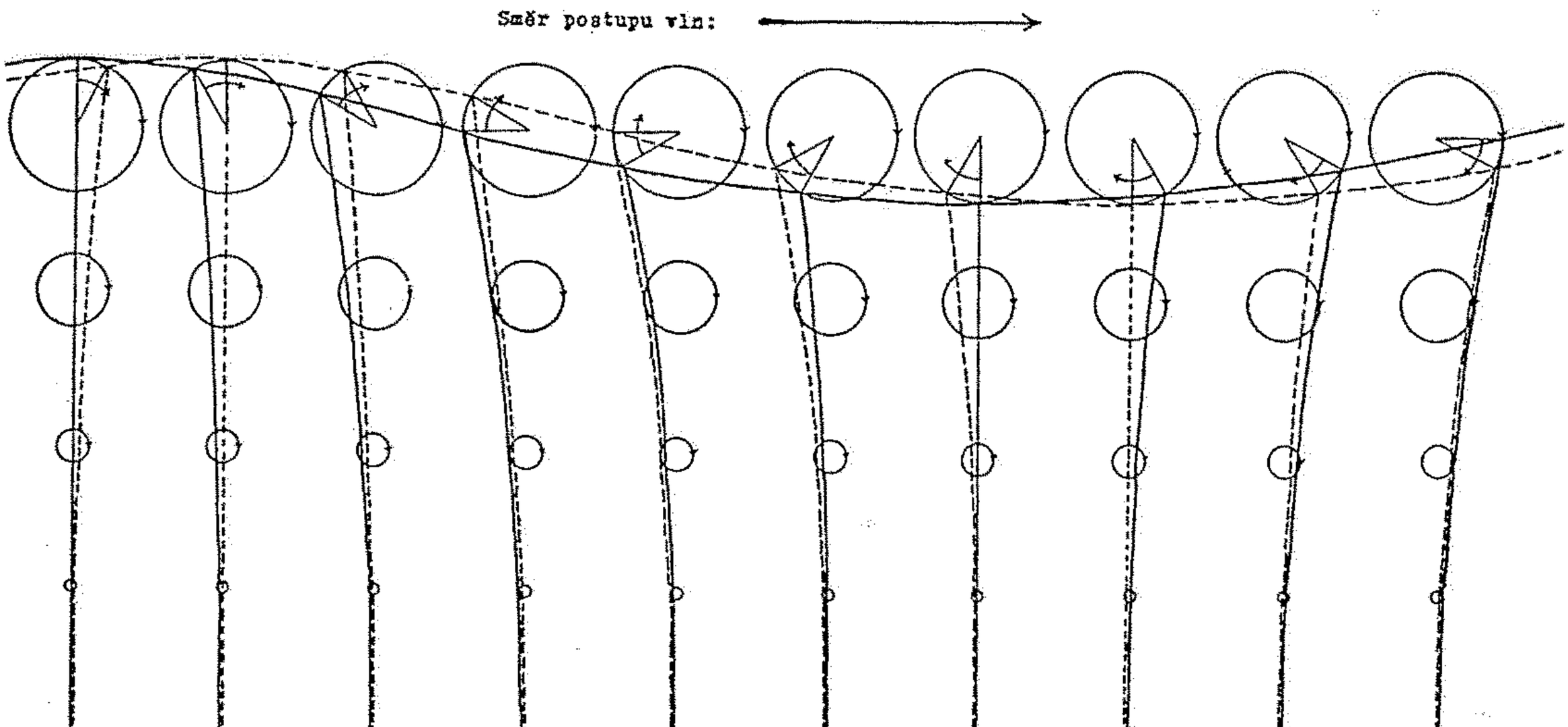

Obr. 276. *Vznik vodních vln podmíněný dutím větru a orbitální pohyb vodních částic.*

Abb. 6.11
Schema der Orbitalbewegung der Wasserteilchen in Flachwasser- und Tiefwasserwellen (nach GROSS, 1977).

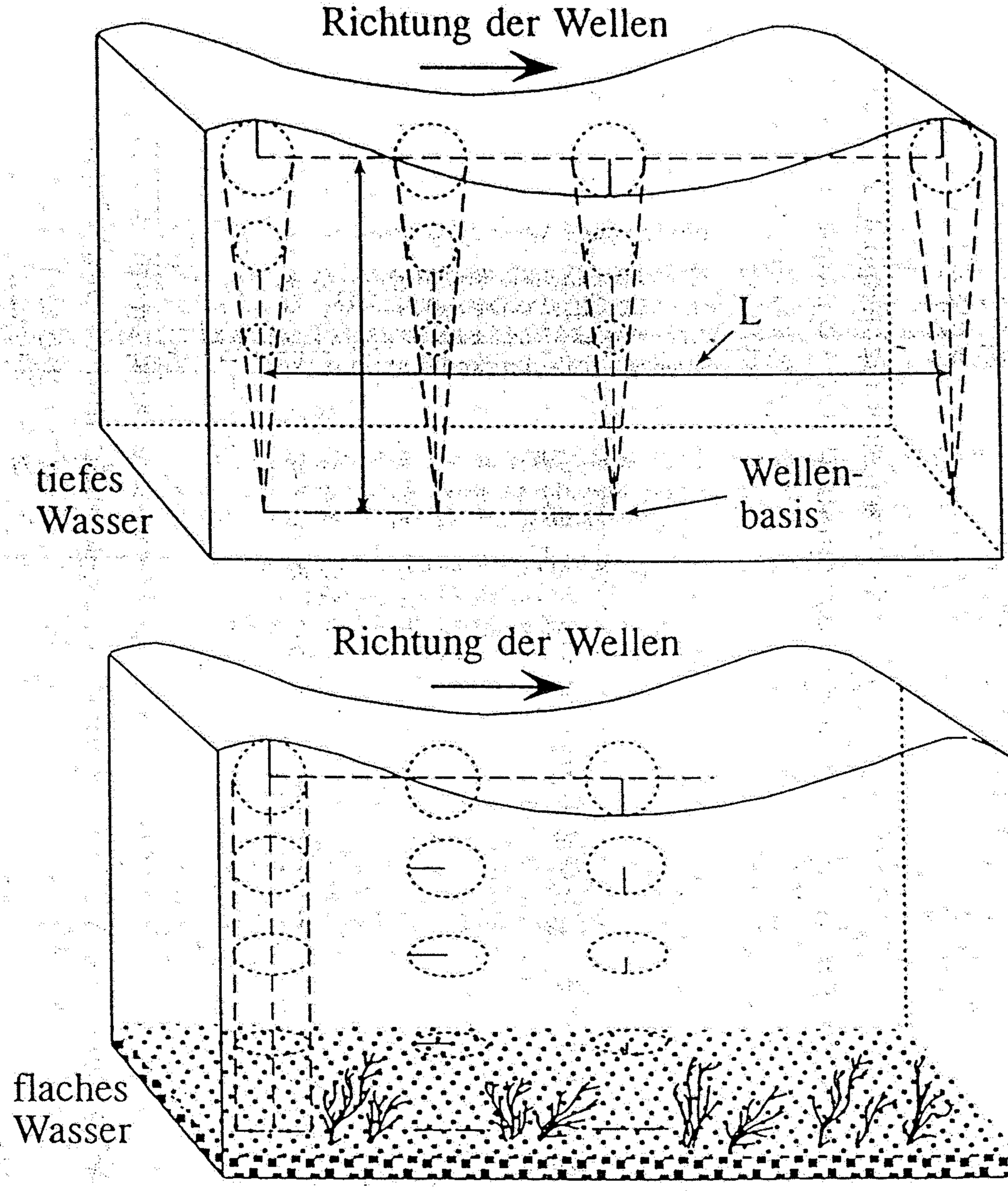

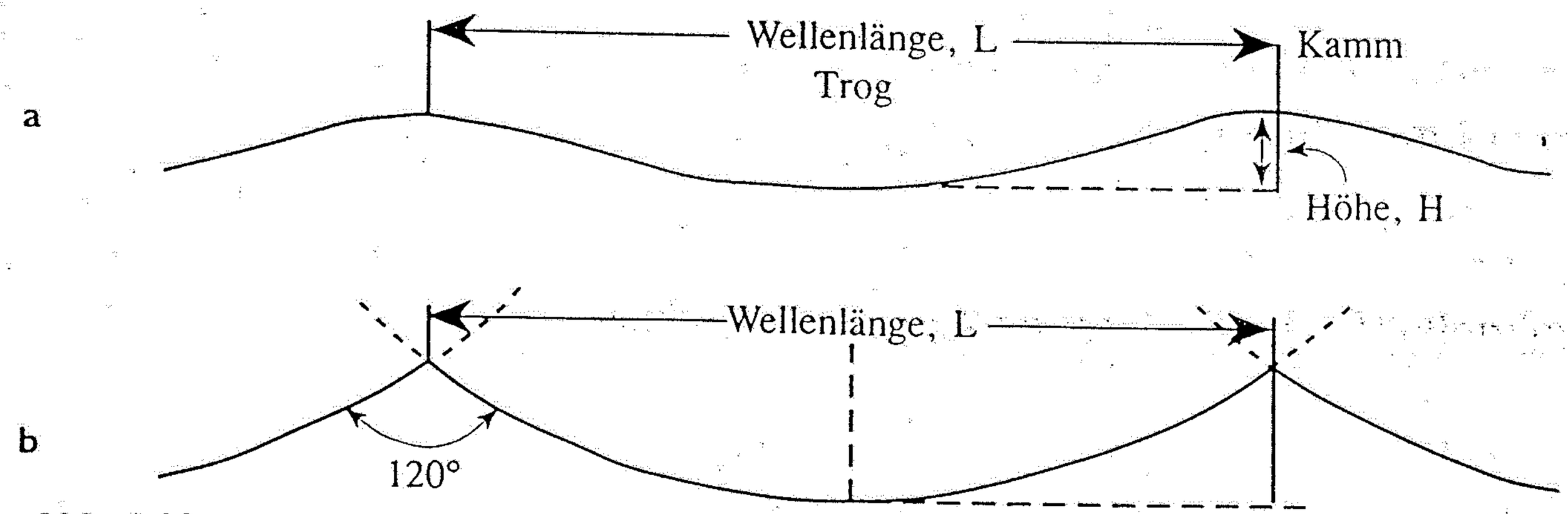

Bedingung für das Brechen einer Welle

$$\frac{H}{L} = \frac{1}{7}$$

Abb. 6.10
Das Brechen einer Welle sowie die Wellenstabilität ergibt sich aus dem Verhältnis der Amplitude *H* zur Wellenlänge *L* (nach GROSS, 1977).

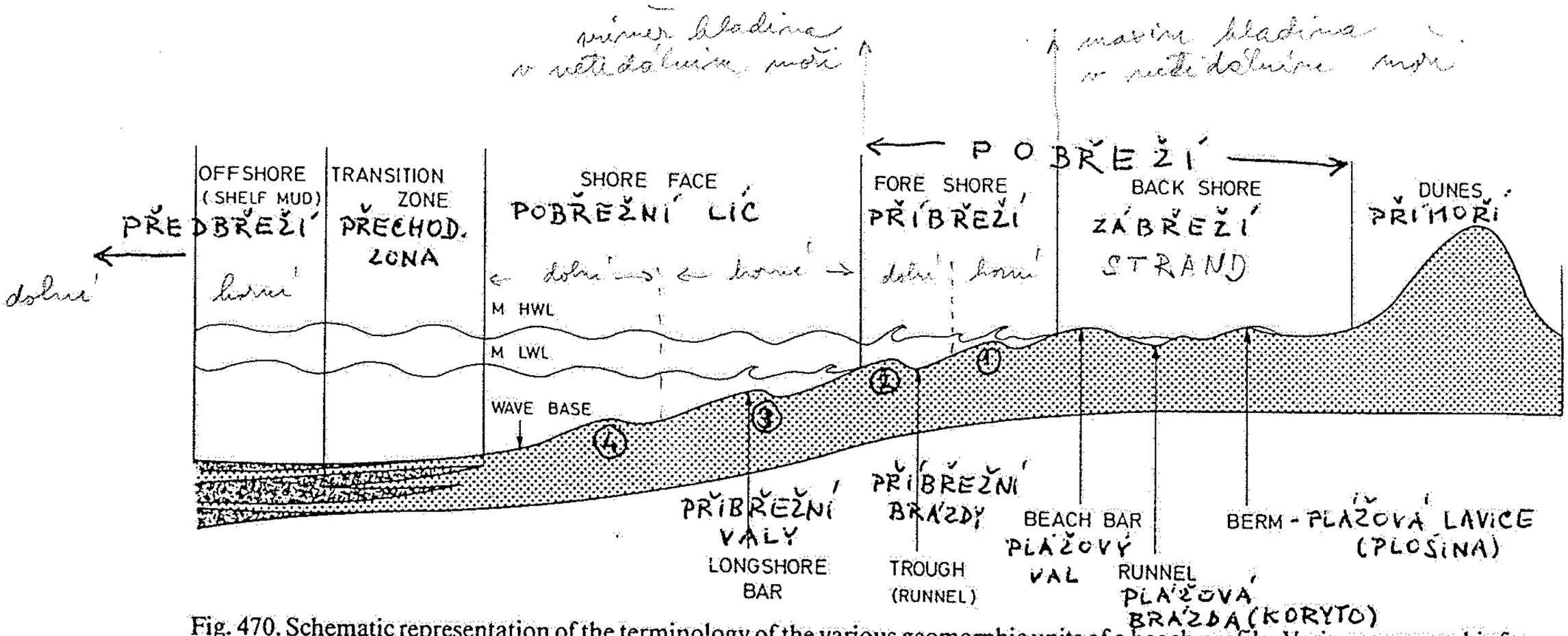

Fig. 470. Schematic representation of the terminology of the various geomorphic units of a beach profile. Various geomorphic features of a beach as well as transition to shelf mud are shown. The terminology is mainly based on Emery (1960a)

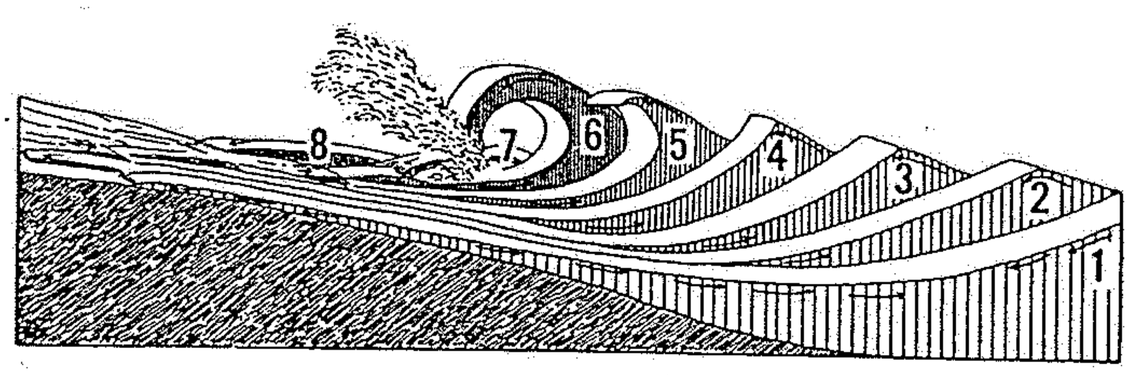

Obr. 277. *Diagram znázorňující rozdělenĕ postup a vznik lámajících se vln při mořském příboji na plochém pobřeží.* (Podle W. M. Davise.)

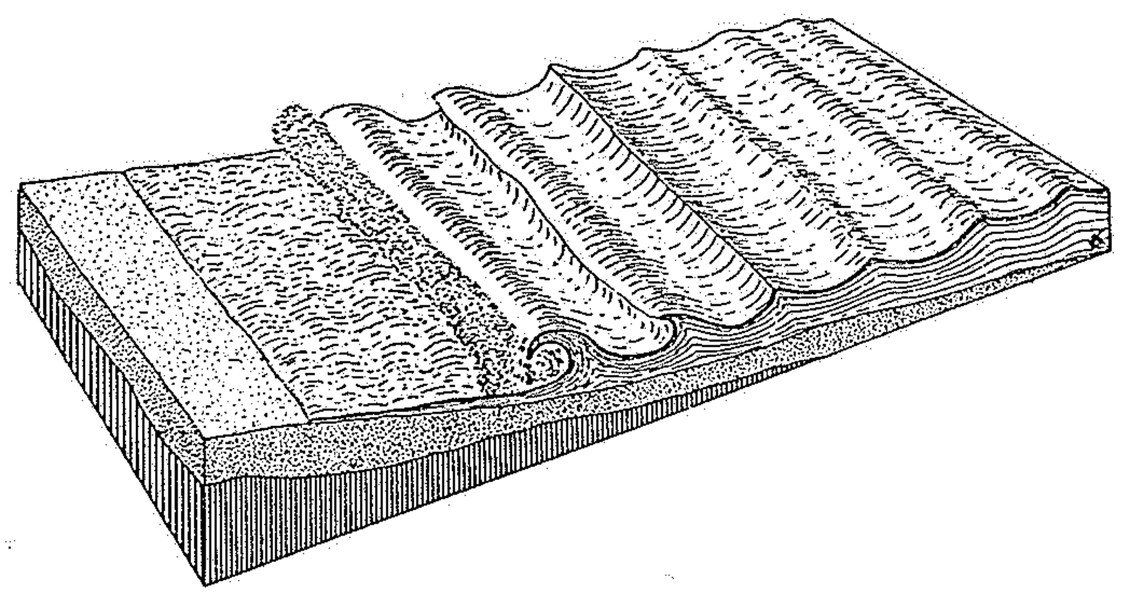

Obr. 278. *Diagram znázorňující postup mořských vln při příboji na plochém pobřeží a vznik lámajících se vln.* (Podle Cl. R. Stauffera.)

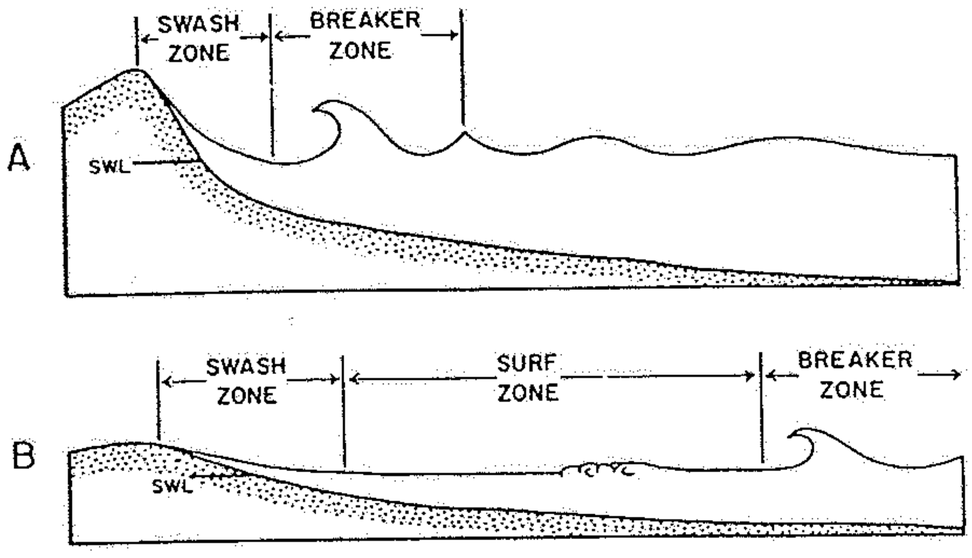

Fig. 473. Characteristic features of the surf zone. Existence and width of a surf zone is controlled by beach slope and tidal phase. Steep-sloped beaches rarely possess a surf zone, because relatively deep water causes waves to break close to shore, thus breaker zone meets swash zone directly (A). Gentle beaches always posses a surf zone as waves break at some distance from the seaward limit of the swash zone (B). On moderately sloping beaches surf zone is commonly lacking during high tide conditions (C), but it is present during all other phases of tidal cycle (D). SWL = still water line. (After Ingle 1966)

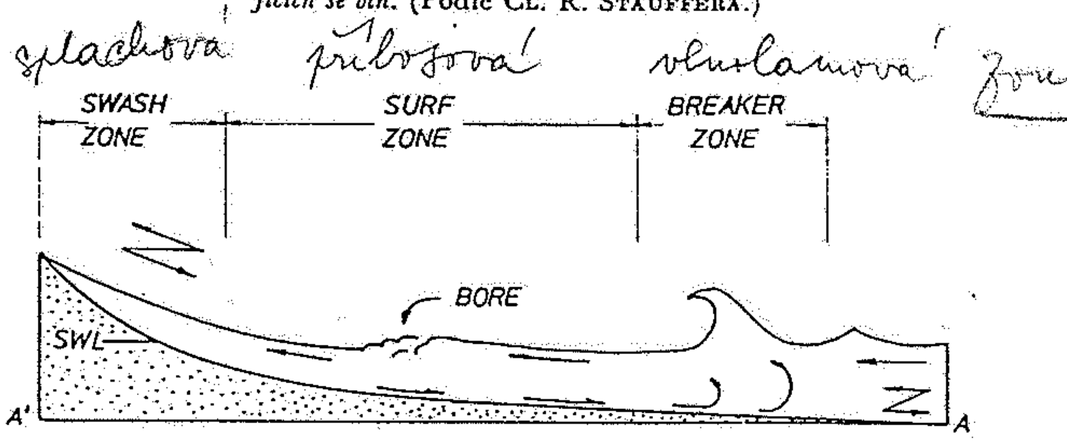

Fig. 472. Diagram showing terminology of the near-shore current system as seen in profile. (After Ingle 1966; originally modified after Shepard and Inman 1950)

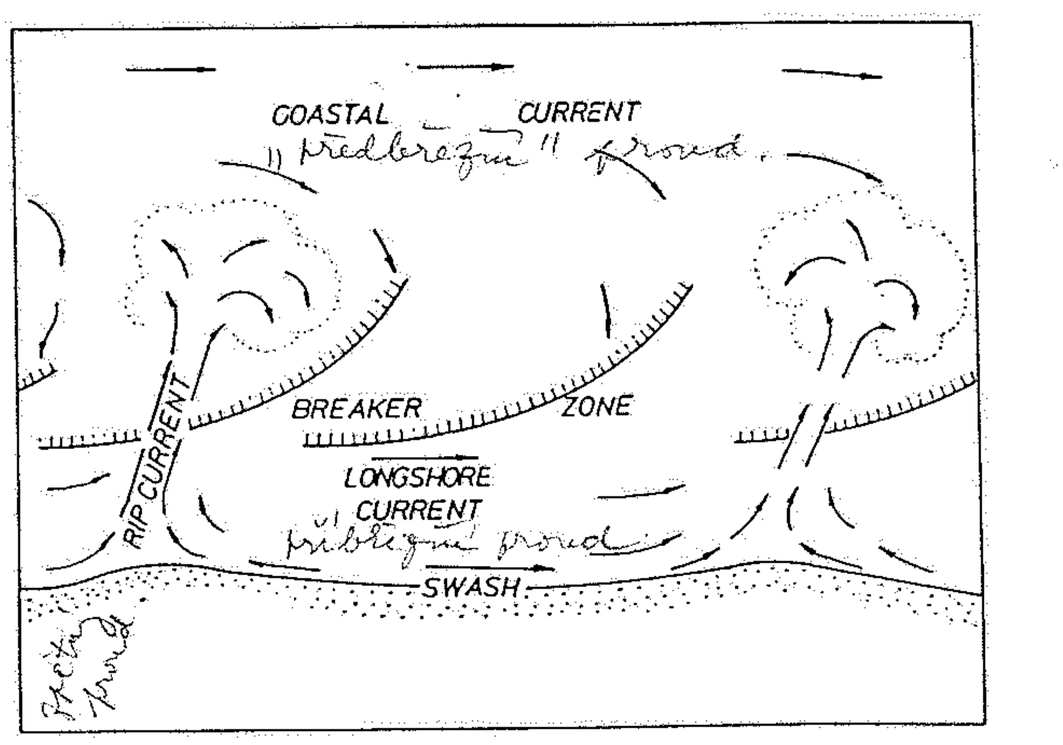

Fig. 474. Diagram depicting nearshore current system in plan view (see also Fig. 472). The incoming breaker generate longshore current, which produces pulsatory rip current moving towards sea. (After Ingle 1966)

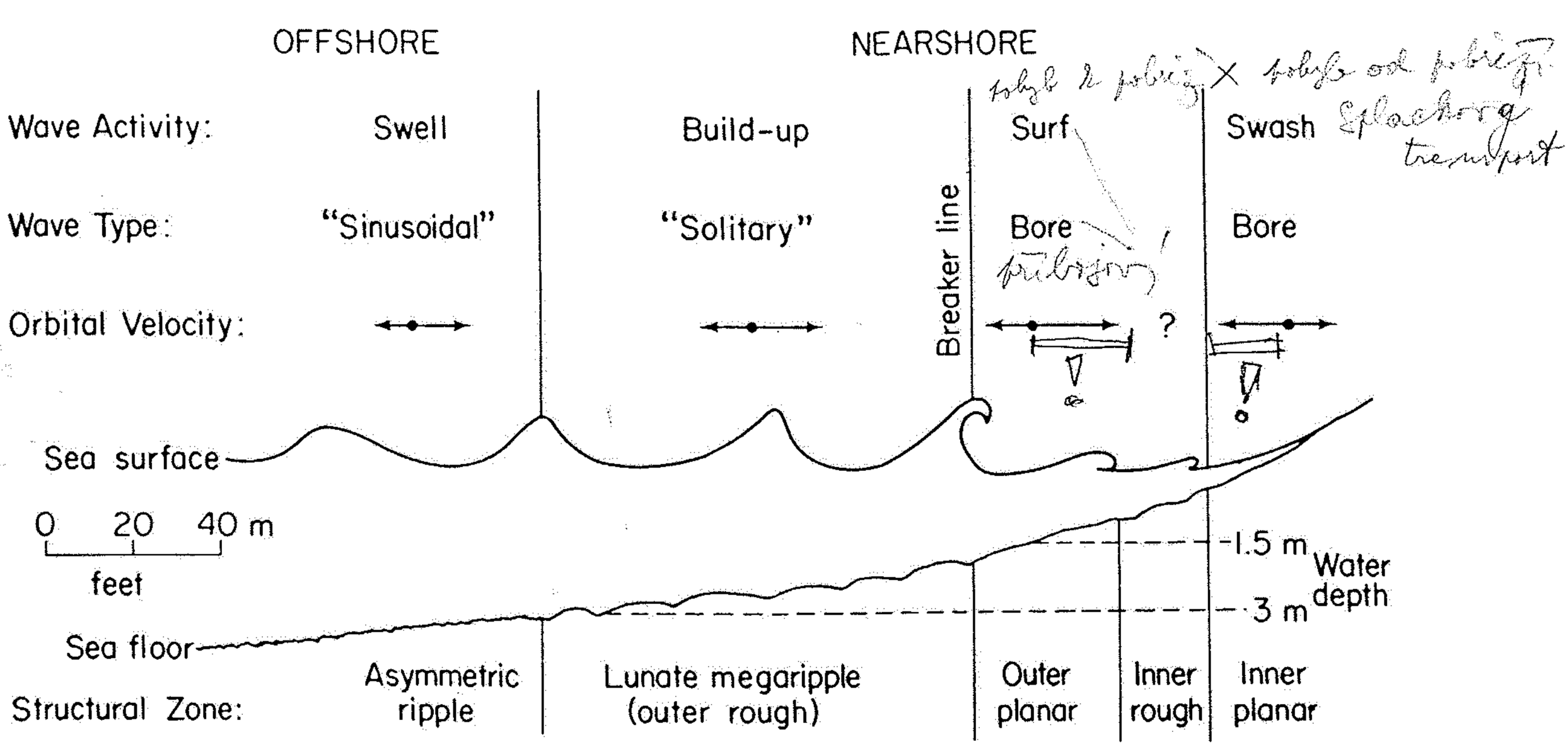

Figure 2–24 Diagram showing distribution of bedforms across the nearshore zone in a nonbarred coast. (After Clifton et al., 1971, p. 661.)

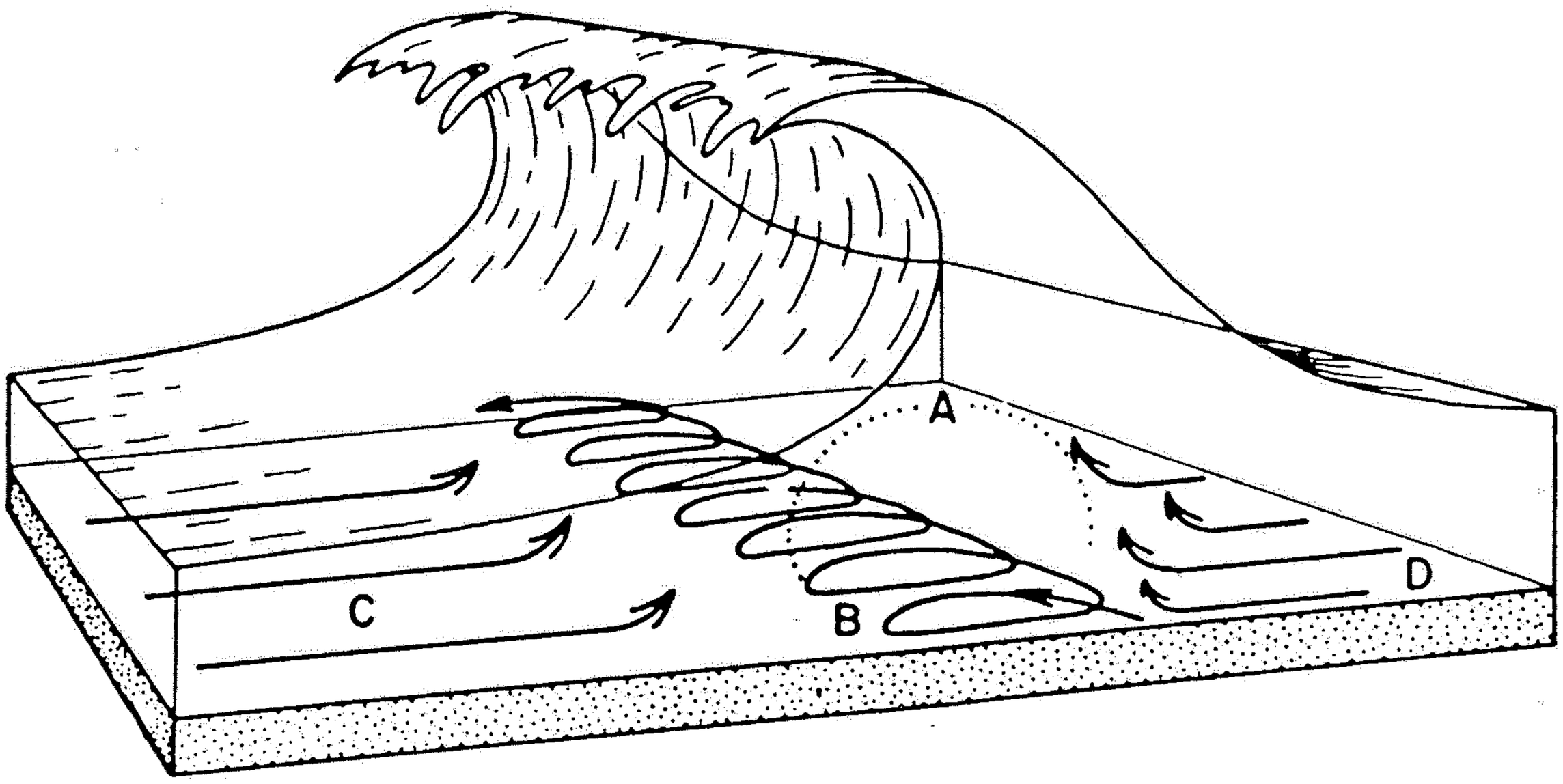

Figure 2–23 Diagram of grain motion associated with a breaking wave. Arrows show paths of largest grains (B), suspended particles (A), and those both landward (C) and seaward (D) of the wave. (From Ingle, 1966, p. 53.)

Abb. 6.13
Vorstrandprofil und Wasserbewegung. Der Querschnitt verdeutlicht die Bewegungsrichtungen des gegen das Ufer laufenden Wassers (nach KENNETT, 1984).

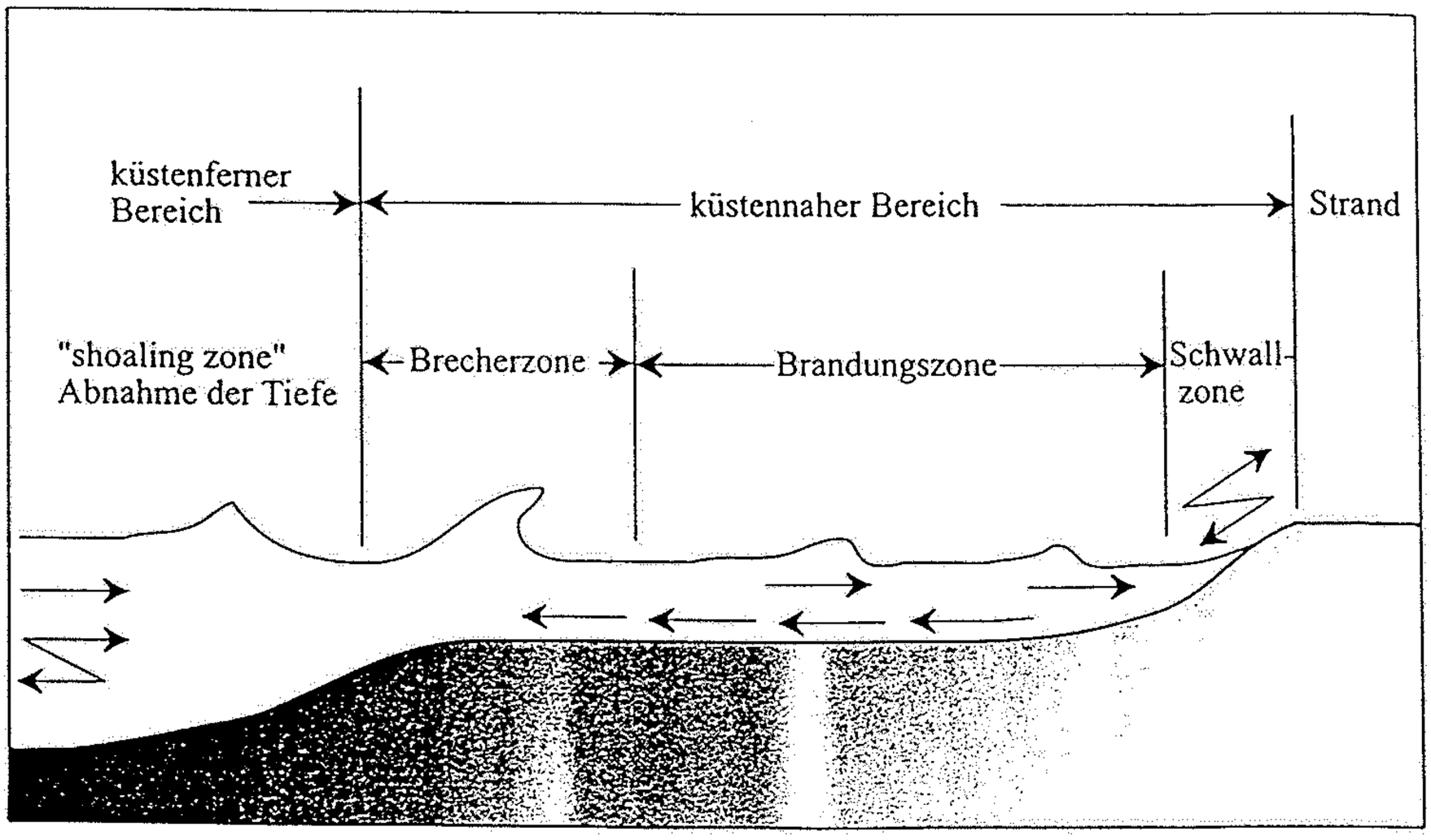

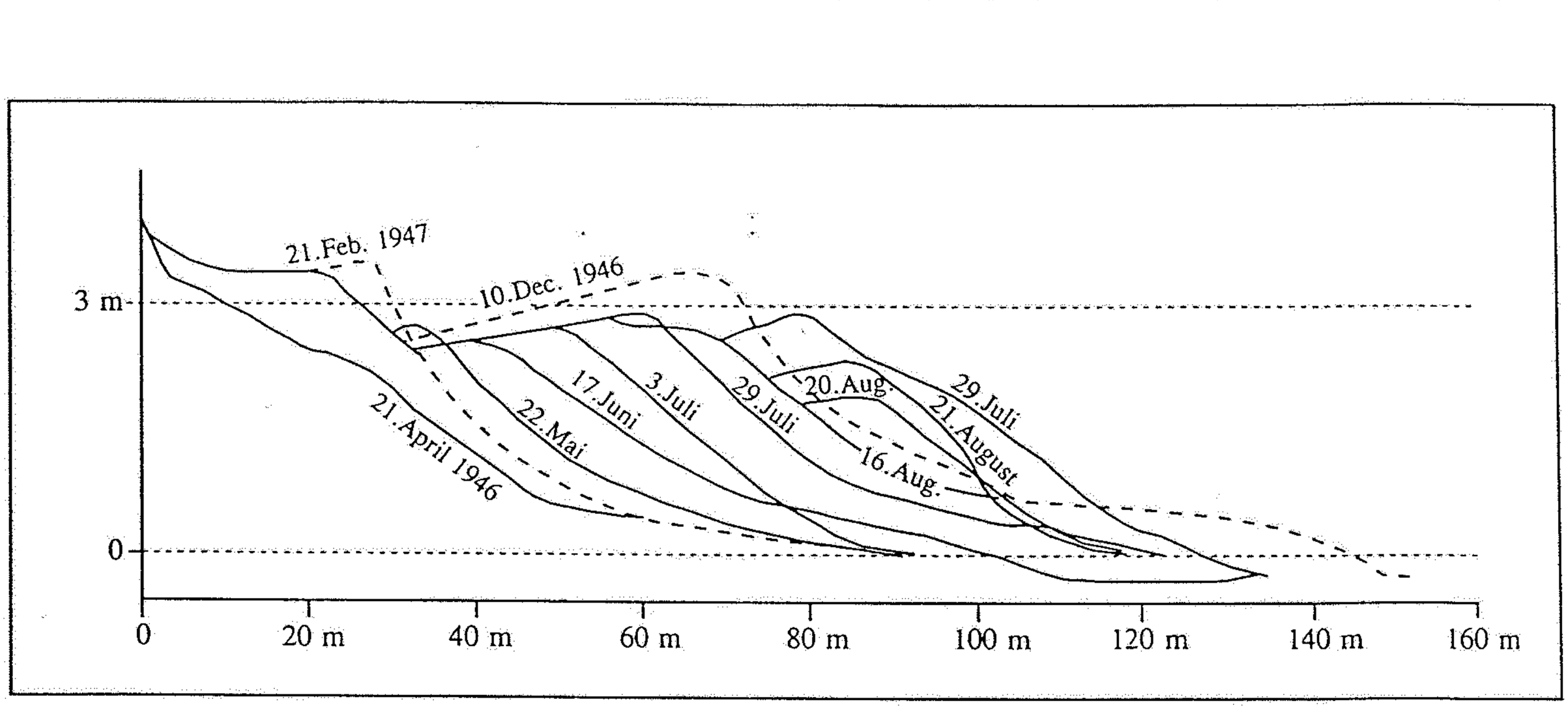

Abb. 6.14
Das Strandprofil verändert sich erheblich im Verlauf eines Jahres. Von April bis September 1946 baute sich der Strand von Carmel, Kalifornien, um 60 m vor. Niedriger Seegang und schwache Strömungen transportierten Sand zur Küste. Mit Einsetzen der Winterstürme im Dezember begann die Stranderosion durch große Wellen, die den Strand wieder zum Ausgangspunkt zurückverlagerte (nach GARRISON, 1993).

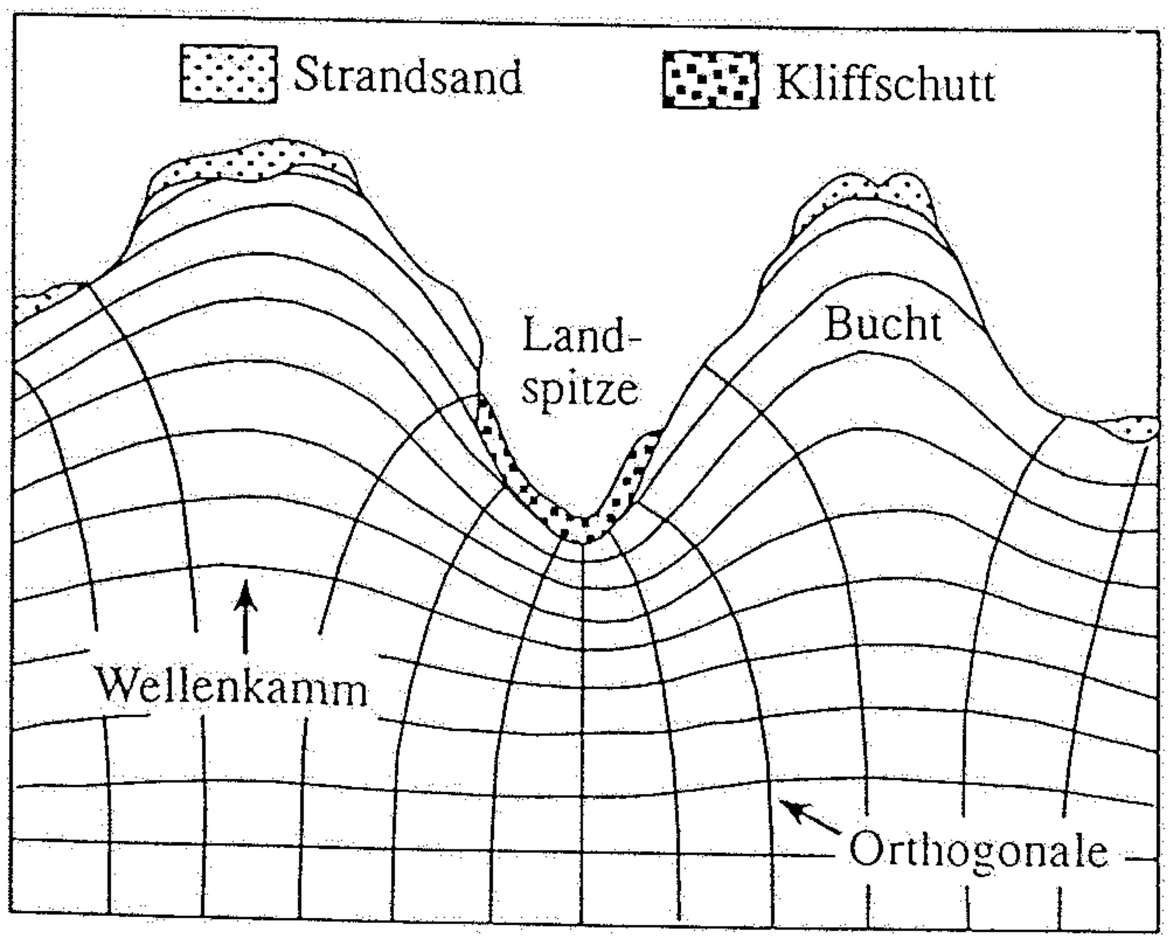

Abb. 6.15
Wellenrefraktion in Küstennähe. Die Linien senkrecht zu den Wellenkämmen, die Orthogonalen, zeigen die Energieverteilung entlang einer Küste. Je dichter ihr Netz, desto größer die Erosionskraft der anbrandenden Wellen (nach TUREKIAN, 1985).

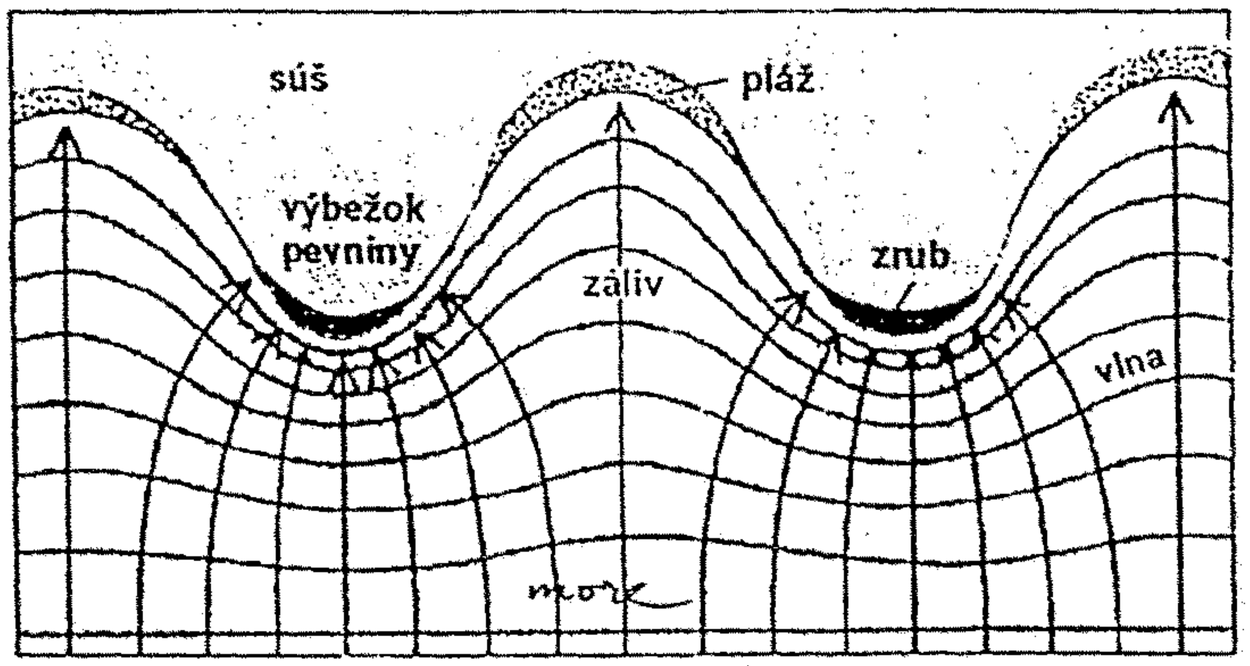

obr. 18.26. Schéma ohybu vĺn a sústredenia ich energie (vyjadrené šipkami) na čela výbežkov pevniny. Záliv so zníženou aktivitou vĺn sa zanáša sedimentami pláže.

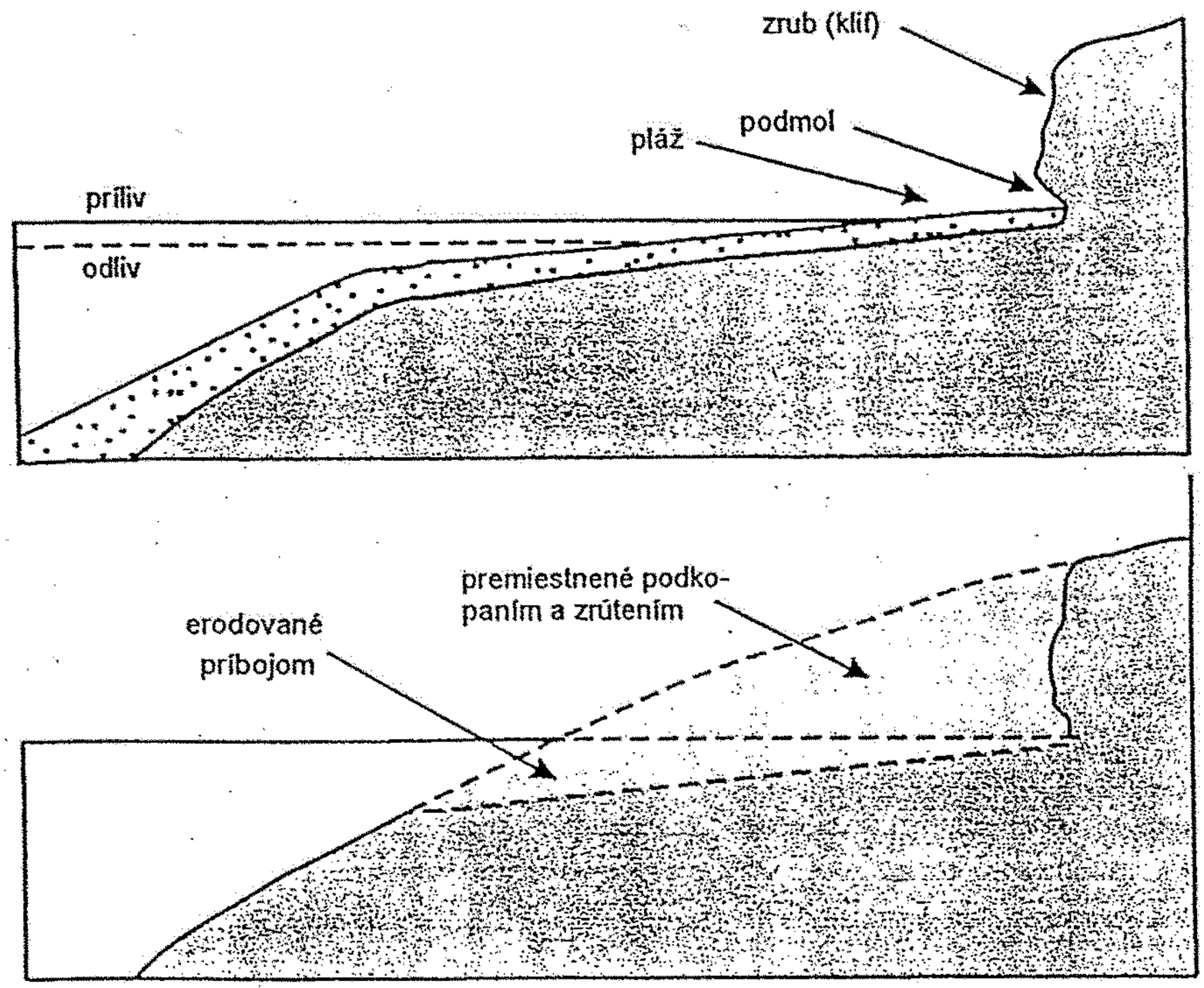

obr. 18.24. Vznik abráznej plošiny ústupom morského zrubu. Práca vĺn je potrebná len na podkopanie, skalná stena sa zrúti vlastnou váhou. Padnutý materiál sa stáva predmetom dalšej abrázie, drobí sa a na abráznej plošine vytvára pláž a povlak sedimentu, prípadne (odvalovú) haldu pred abráznou plošinou.

FIGURE 16–11
Vertical air photo and diagram showing bending of the waves (wave refraction) around a point of land. (After U.S. Hydrographic Office, Publ. No. 234.)

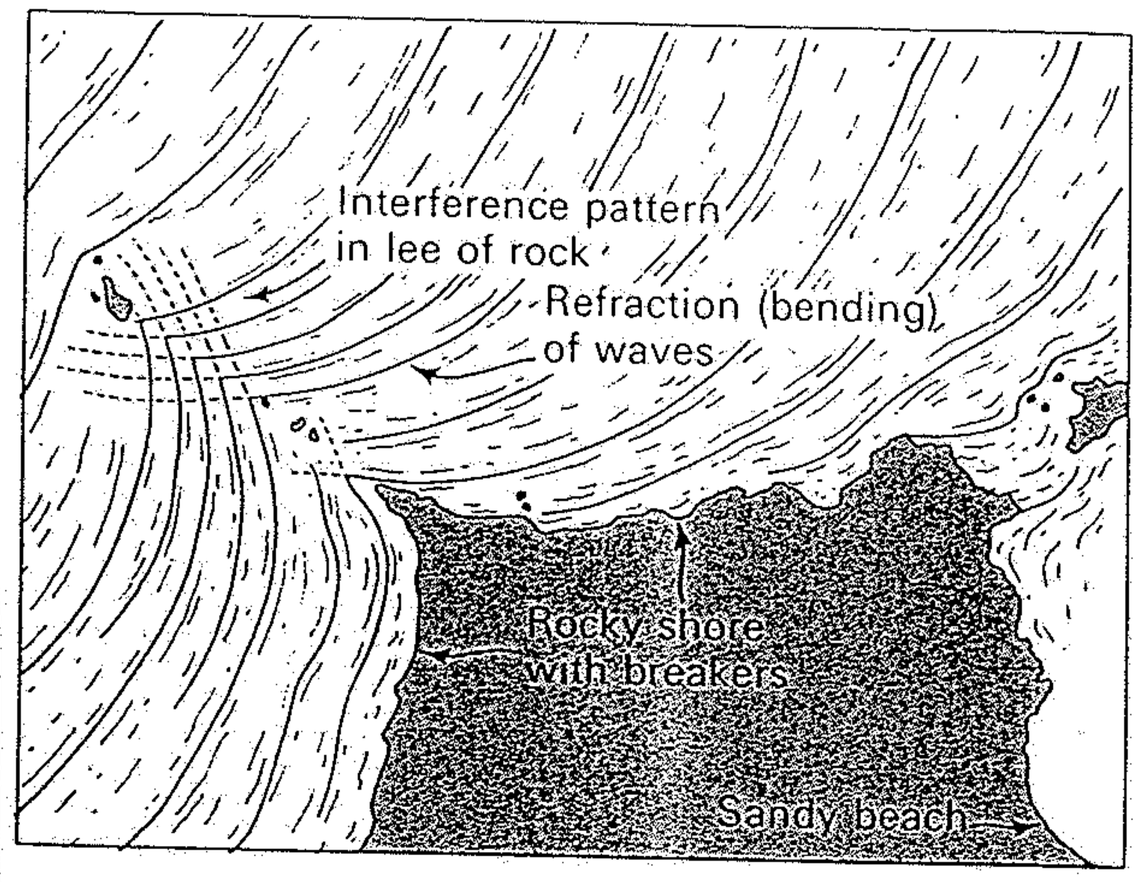

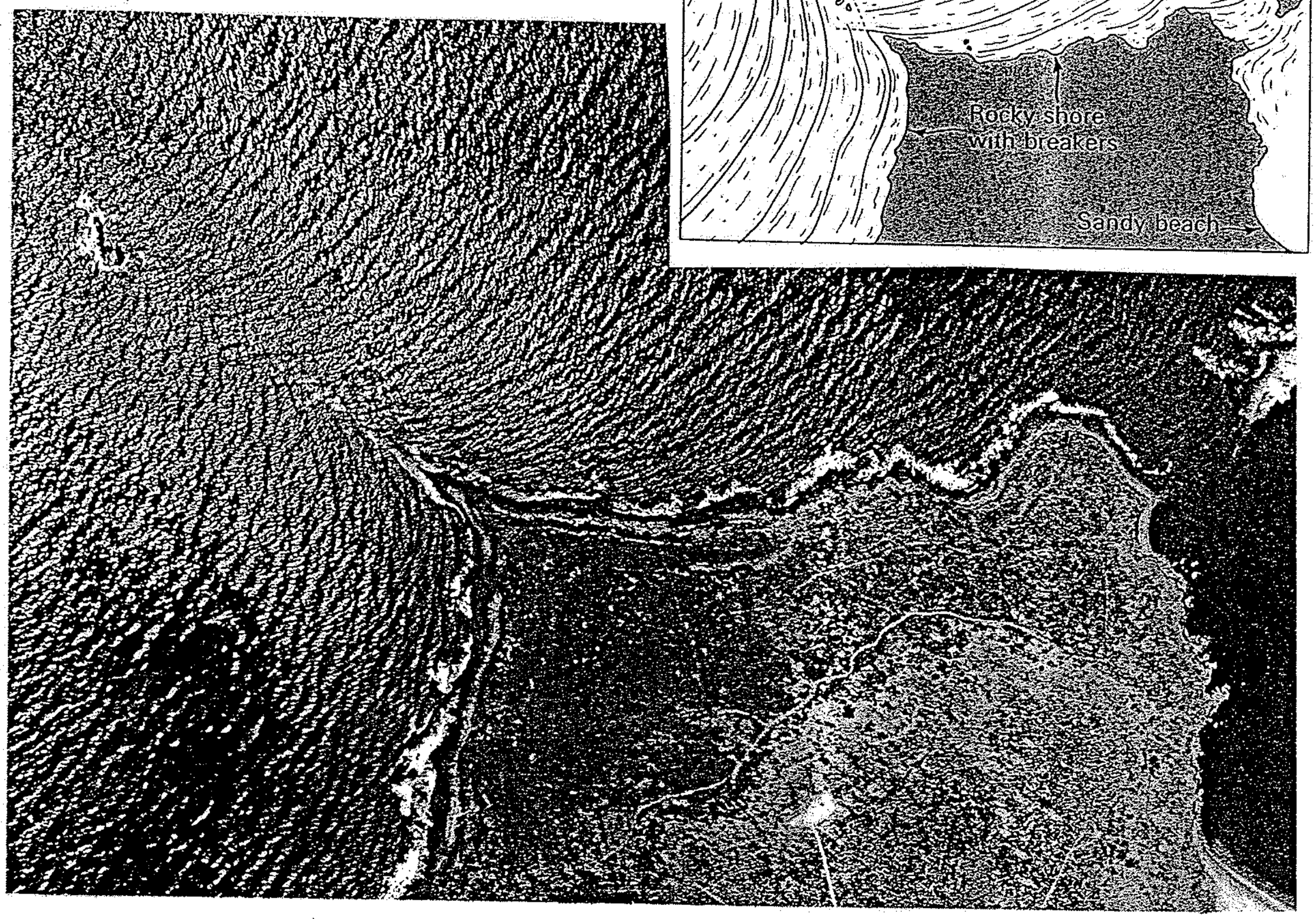

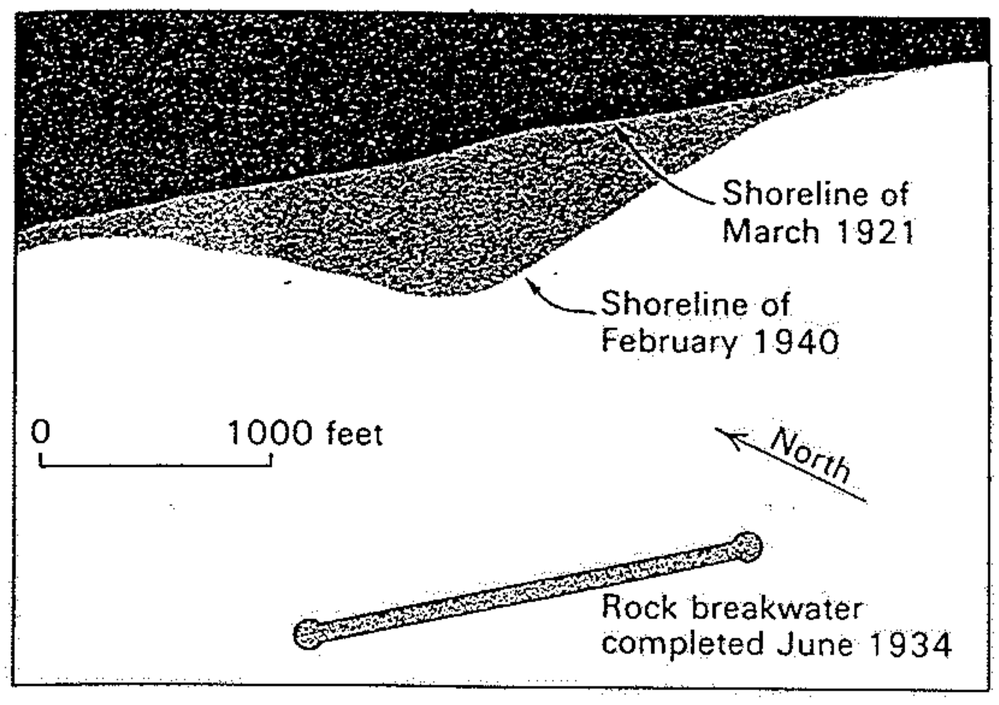

Map of the Santa Monica beach before and after building of the breakwater. The beach has continued to advance since 1940, but later surveys were not available. Direction of drift is southeastward.

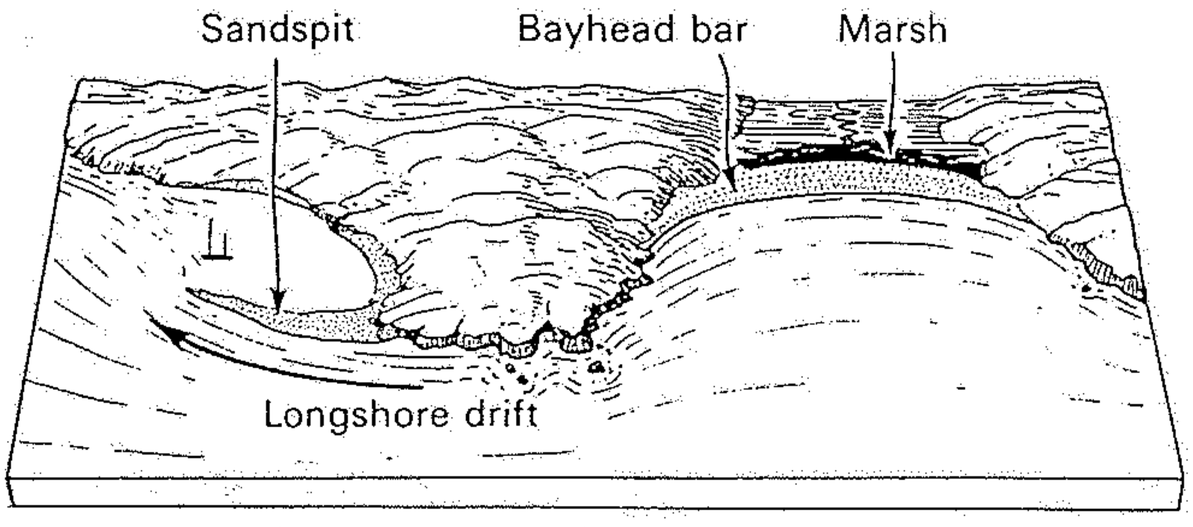

Sketch of an embayed coast, showing a sandpit springing from a headland, and a bayhead bar which encloses a marsh.

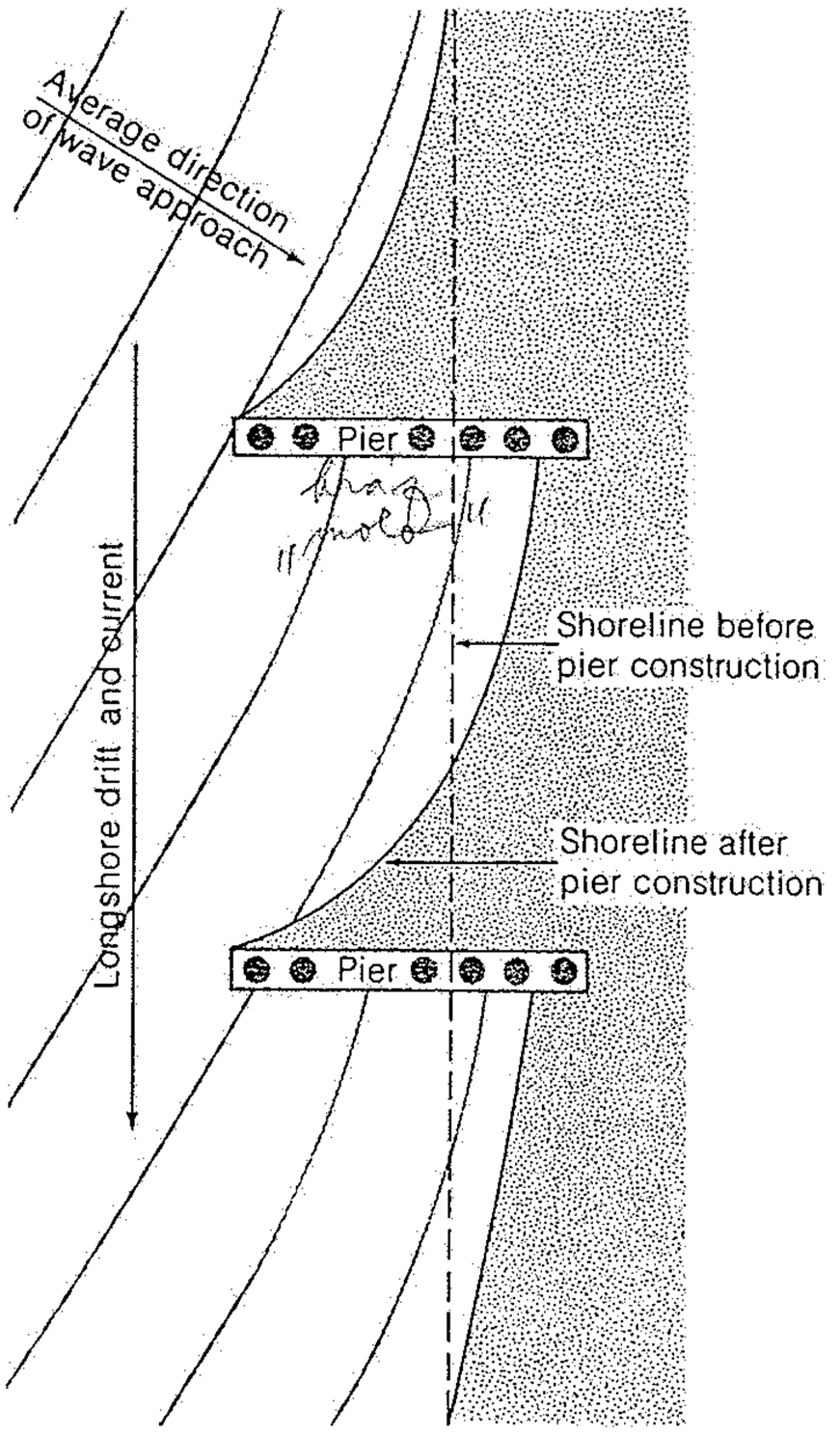

Figure 11-22

Construction of piers (frequently called "groins") along a shore to control erosion of a beach may produce unwanted changes if longshore current and drift are not considered. A typical change induced is erosion downcurrent of the pier.

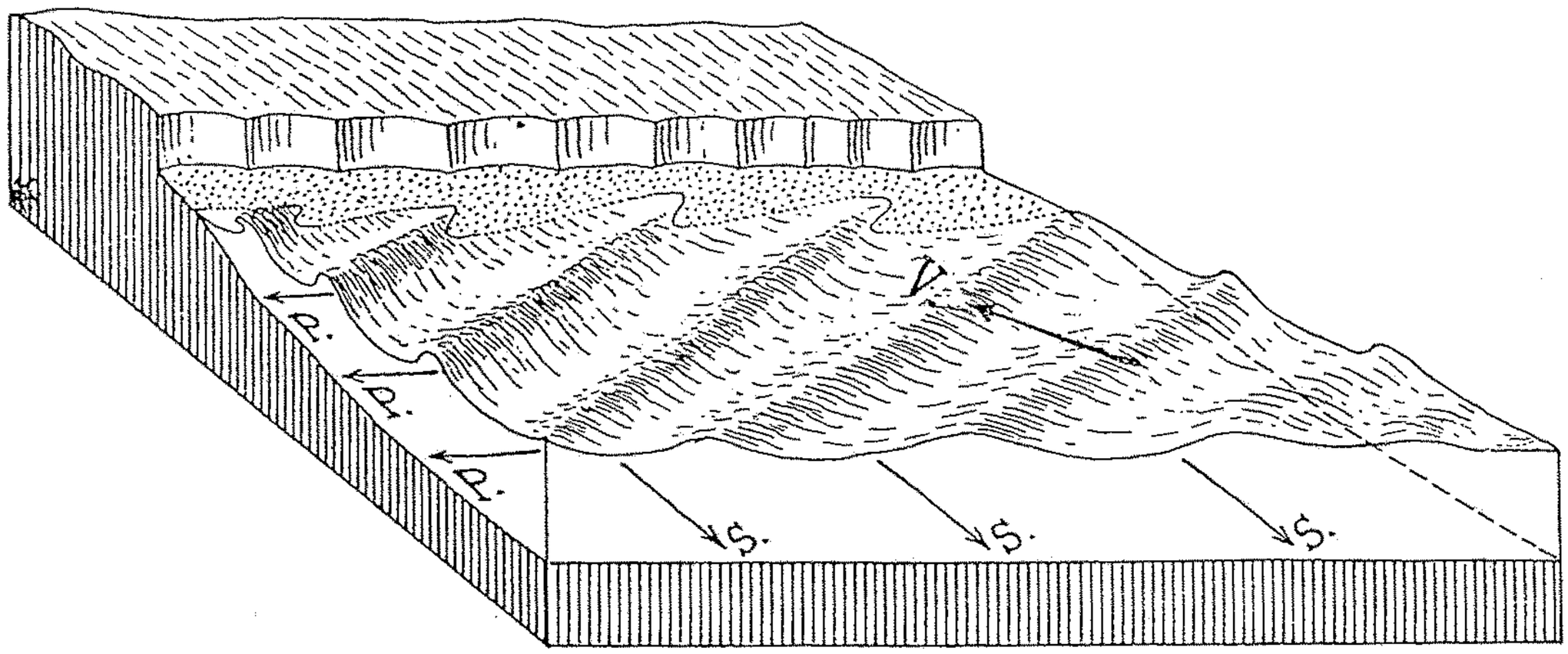

Obr. 285. *Vznik podélných (P.) a zpětných (S.) mořských proudů na mořském pobřeží při šikmém nárazu vln na břeh.* (Podle Ch. R. Longwella, A. Knopfa a R. F. Flinta.)

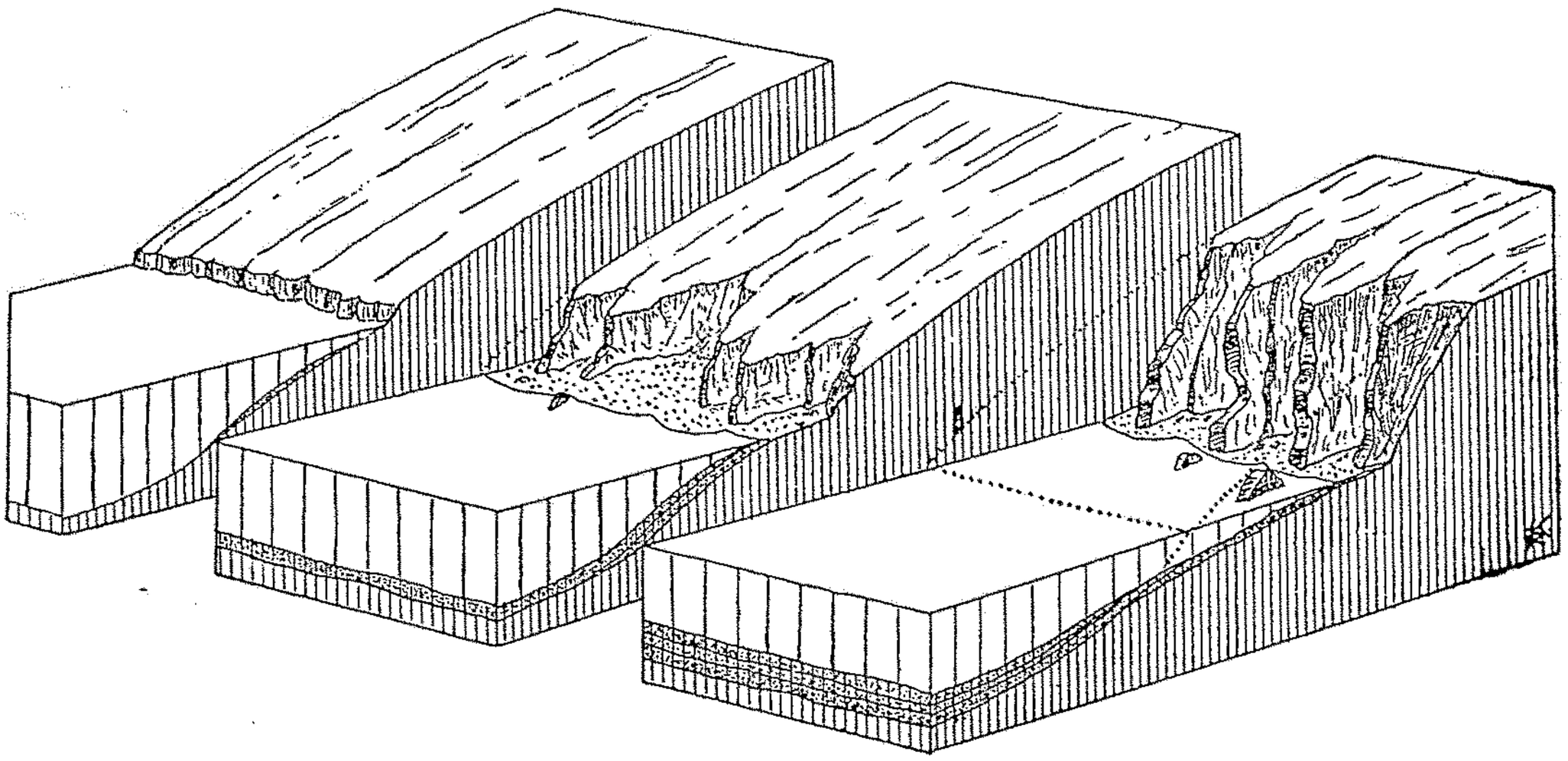

Obr. 289. *Postupující a selektivně působící mořská erose.* (Podle W. M. Davise.)

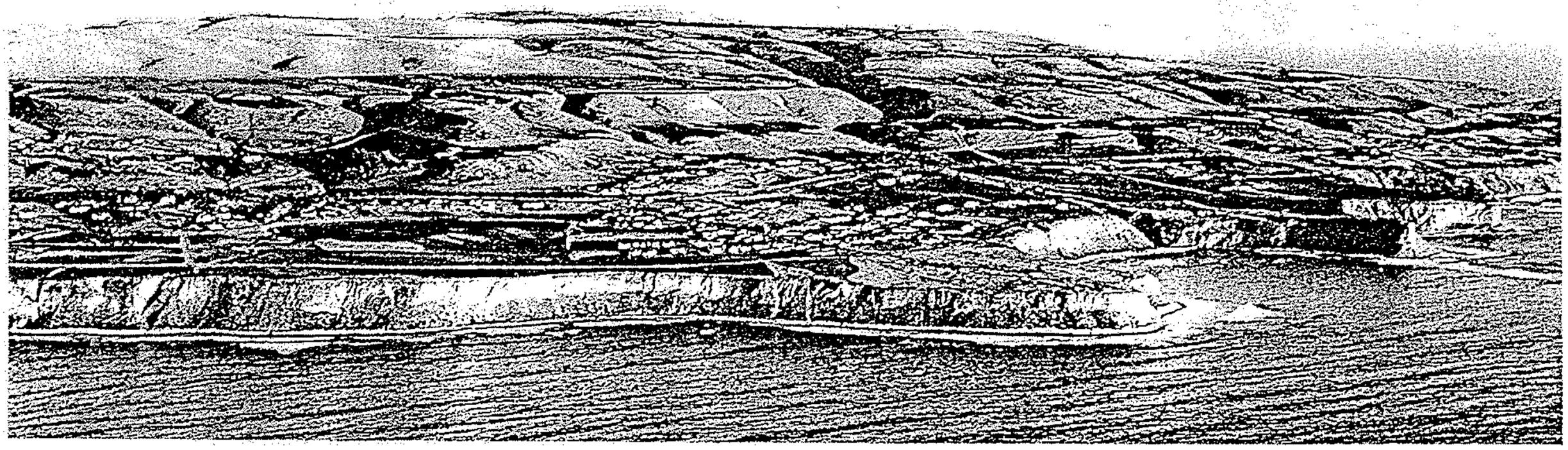

Figure 11-8

Uplifted marine terraces, Palos Verdes Hills, California. [Photo by J. S. Shelton and R. C. Frampton.

From *Geology Illustrated* by J. S. Shelton. W. H. Freeman and Company. Copyright © 1966.]

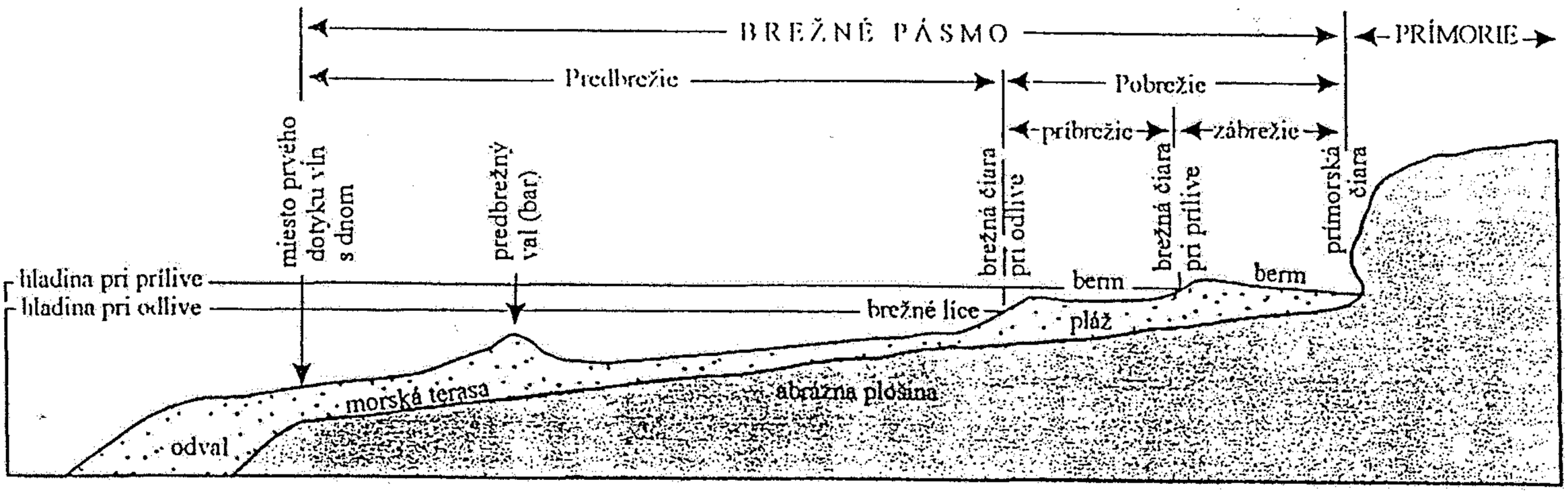

obr. 18.17. Názvoslovie brežného pásma.

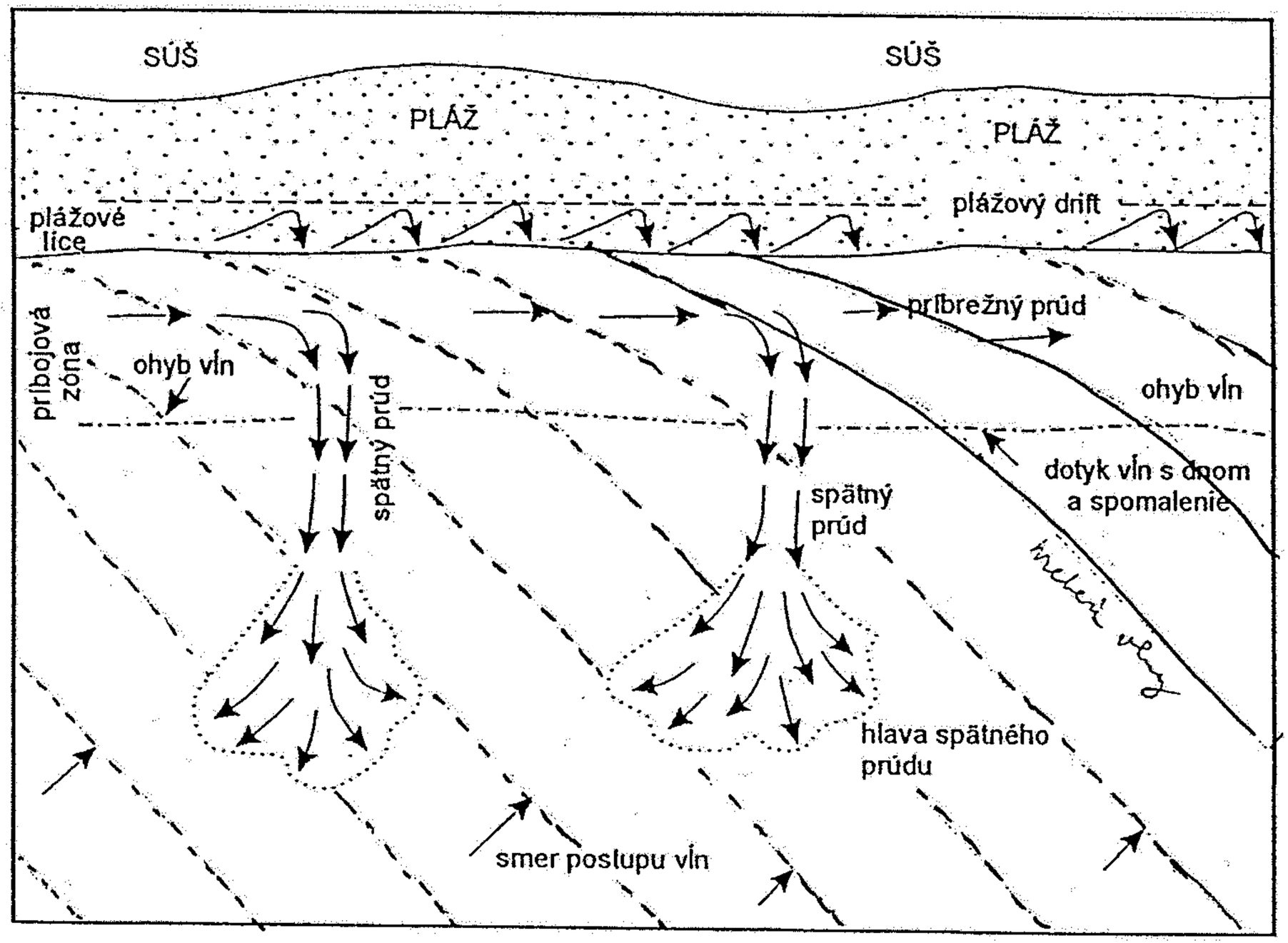

obr. 18.20. Príbrežná cirkulácia a posuv sedimentu pri šikmom nábehu vĺn na pobrežie. V príbojovej zóne nastáva brzdenie a ohyb hrebeňov, vĺn, hromadenie vody, ktorú odvádzajú s pobrežím súbežné (súbrežné) prúdy a do mora smerujúce spätné prúdy. Transport sedimentu zabezpečujú súbrežné prúdy a plážový drift.

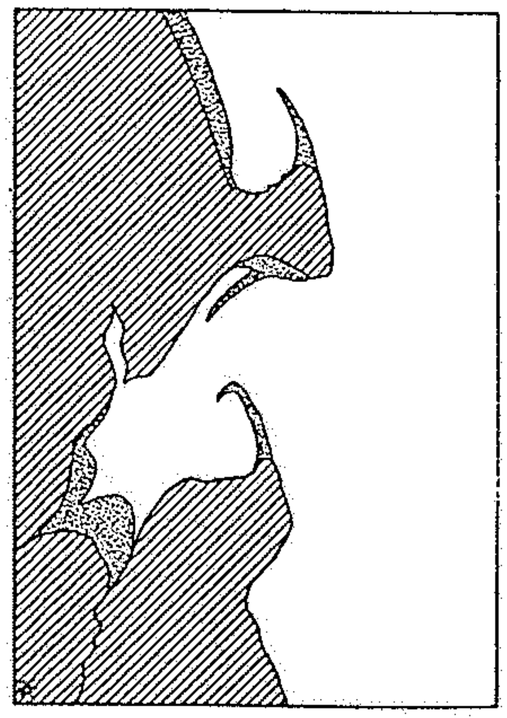

Obr. 299. *Jednoduché písečné kosinky na pobřeží u přístavu Port Orchard ve státě Washington, USA.* (Upraveno podle D. W. Johnsona.)

Obr. 300. *Jednoduchá (dole) a složená a srpovitě zahnutá kosinka (nahoře) u vstupu do přístavu Port Moller na Aljašce.* (Upraveno podle D. W. Johnsona.)

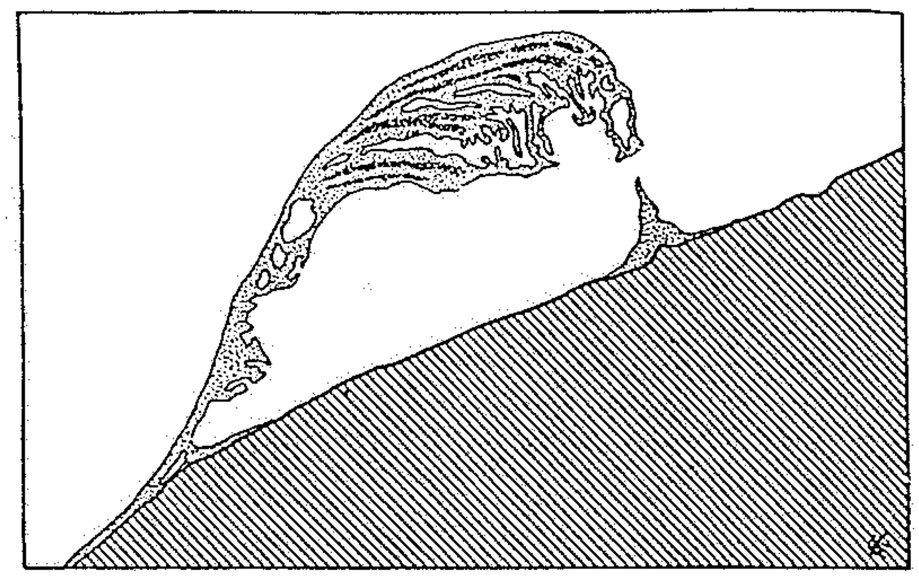

Obr. 302. *Složená kosinka Presque Isle na jižním pobřeží jezera Erie u města Erie, uzavírající lagunu.* (Podle D. W. Johnsona.)

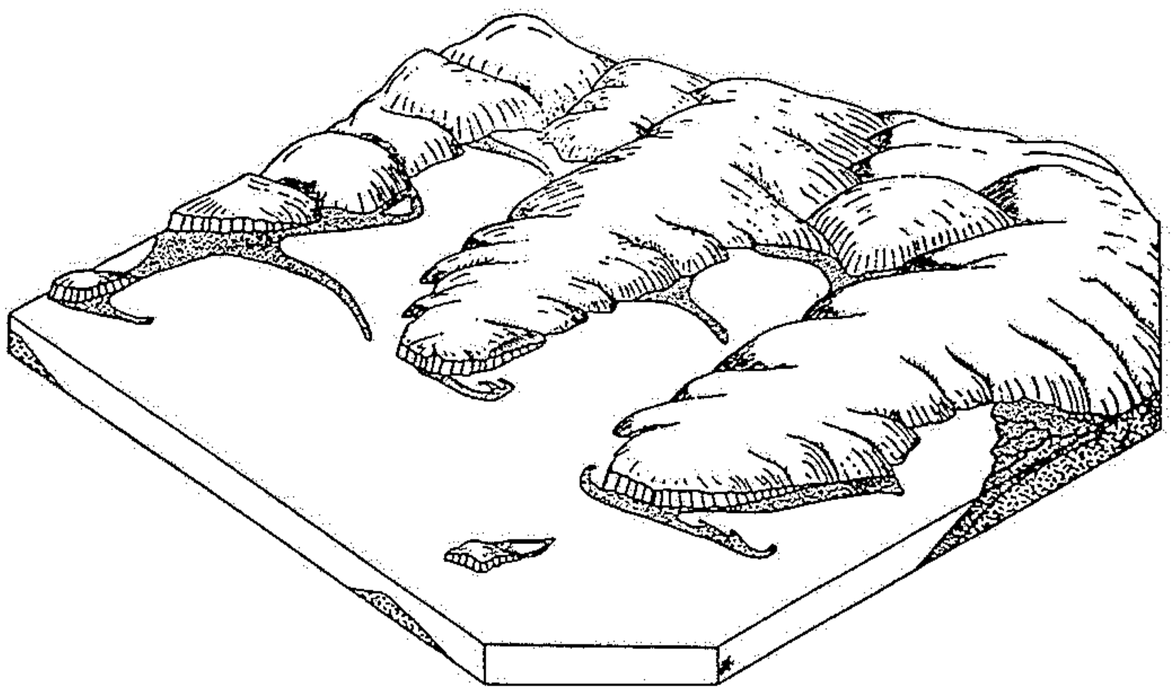

Obr. 306. *Klesající břežní oblast s hlubokými zálivy, poloostrovy a ostrovy a s různými typy písečných valů (kos, kosinek, prstencových uzavřených písečných hrází, tombola a pod.).* (Podle D. W. Johnsona.)

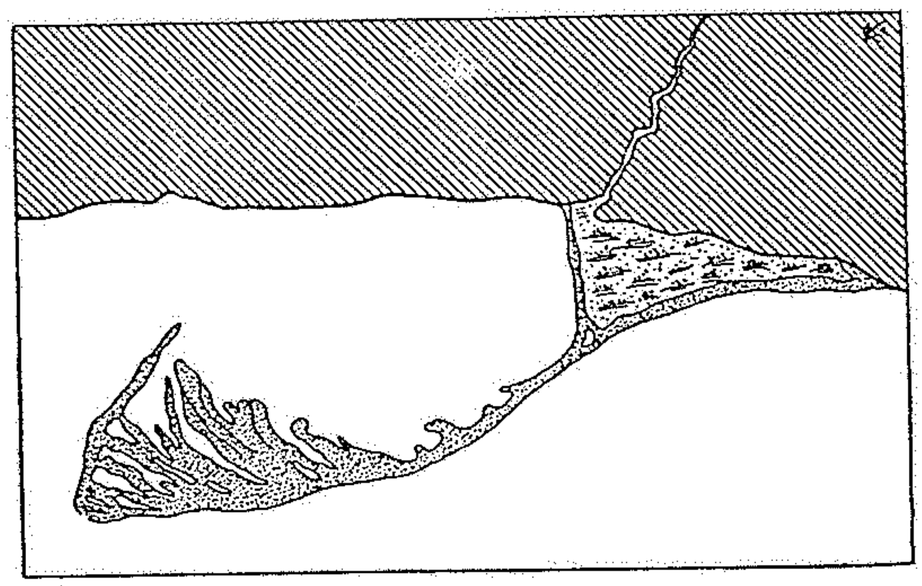

Obr. 301. *Složená kosinka, uzavírající přístav města Toronto na jezeře Ontario v Kanadě.* (Podle D. W. Johnsona.)

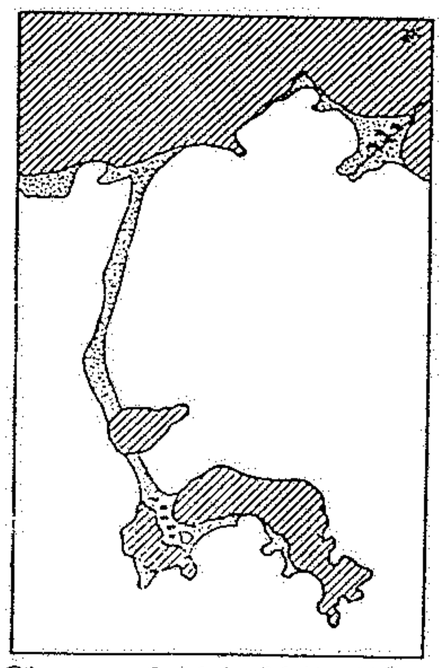

Obr. 304. *Ostrůvky Malý a Velký Nahant, spojené s pevninou tombolem, které uzavírá Nahantský přístav u Bostonu (Massachussetts, USA).* (Upraveno podle D. W. Johnsona.)

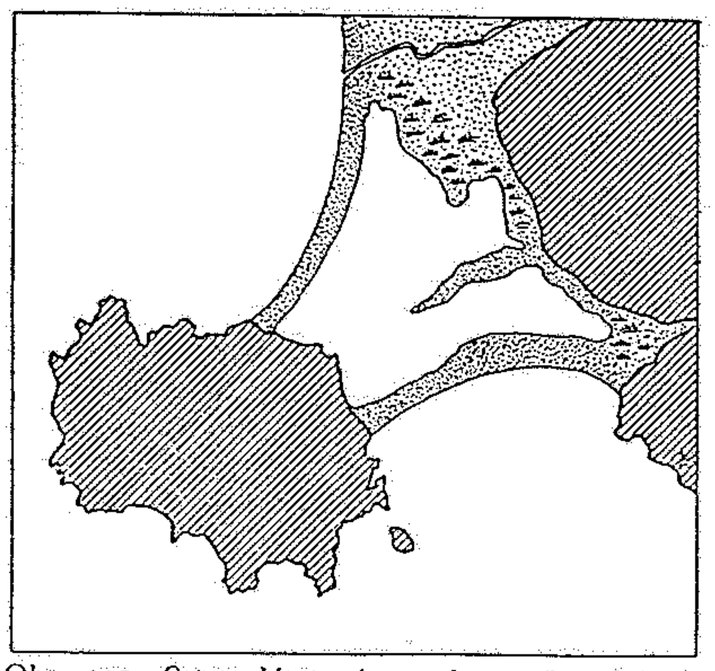

Obr. 305. *Ostrov Monte Argentario u města Orbetello v Italii, připoutaný k pevnině dvěma tomboly, mezi nimiž vznikla uzavřená laguna.* (Podle D. W. Johnsona.)

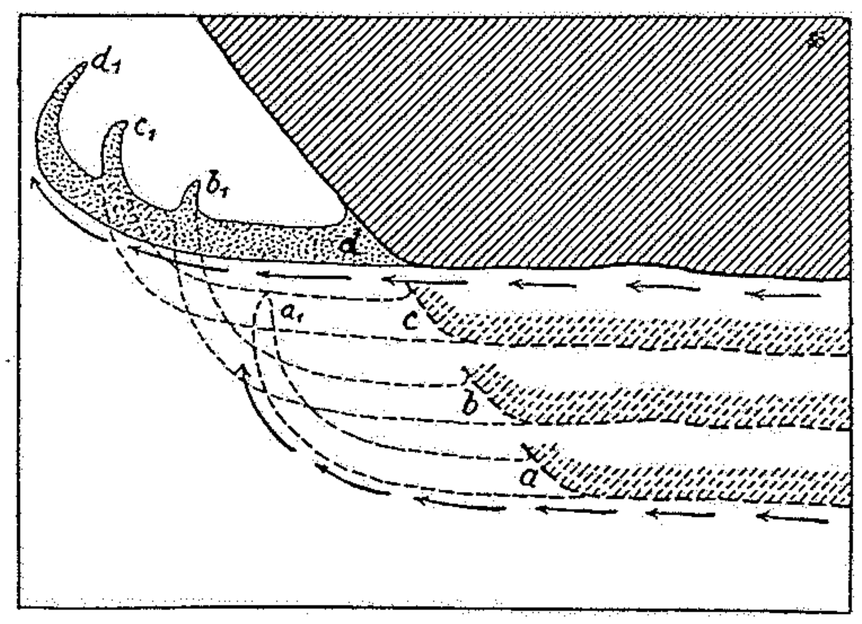

Obr. 303. *Postupná stadia při vzniku složených kosinek.* (Podle D. W. Johnsona.)

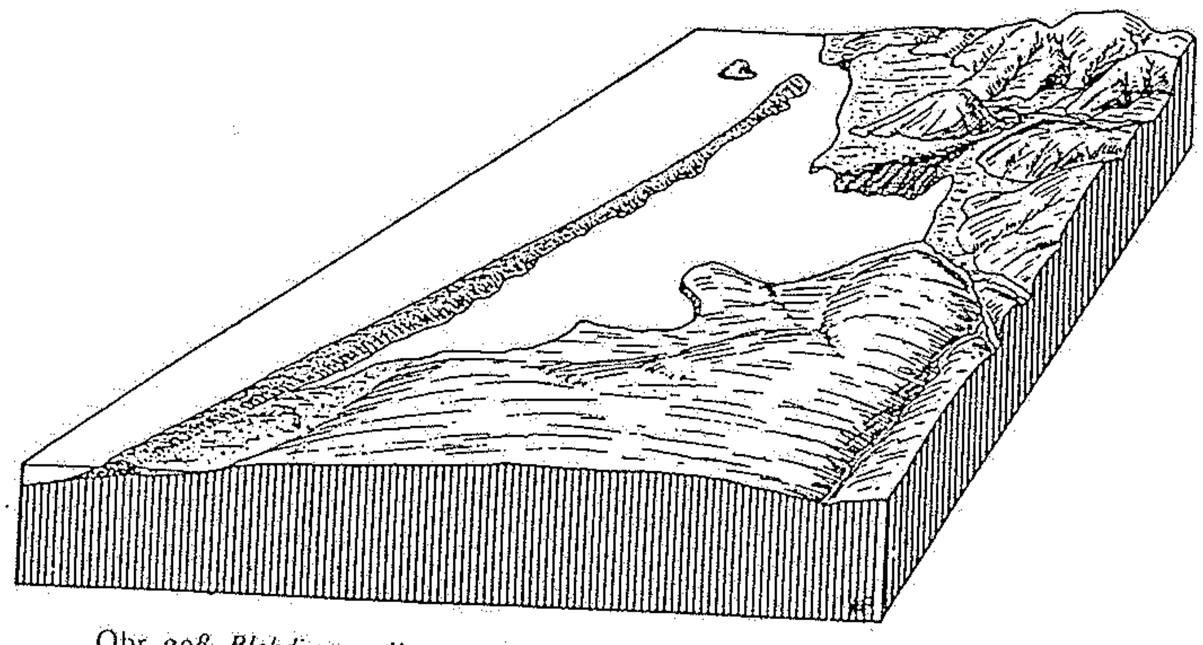

Obr. 298. *Blokdiagram limanu Morro Bay v Kalifornii, uzavřeného dlouhou kosou.* (Podle Ch. R. Longwella, A. Knopfa a R. F. Flinta.)

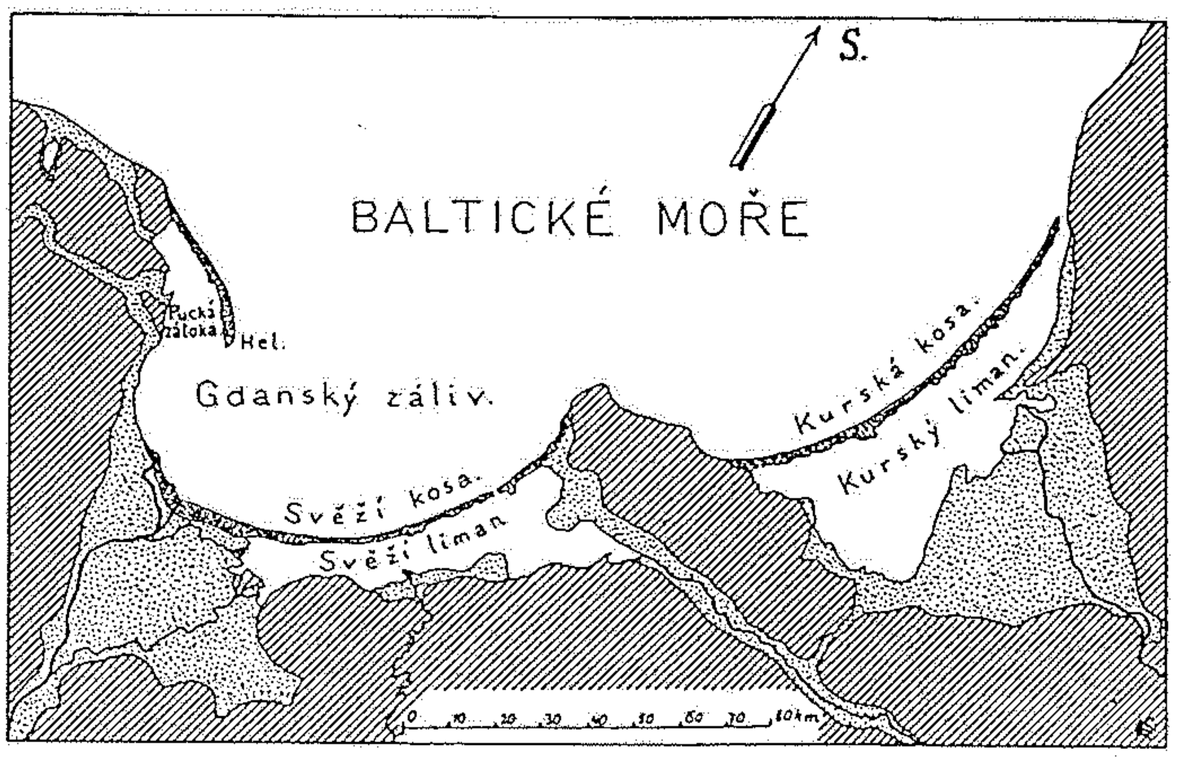

Obr. 297. *Kosy a limany v Baltickém moři.*

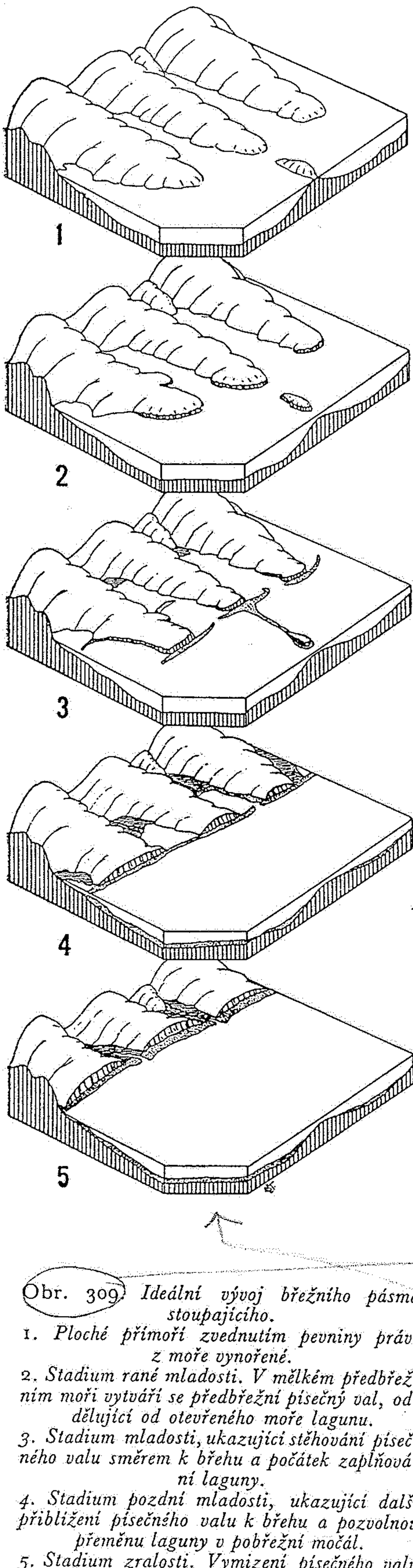

Obr. 309. *Ideální vývoj březního pásma stoupajícího.*

1. *Ploché přímoří zvednutím pevniny právě z moře vynořené.*
2. *Stadium rané mladosti. V mělkém předbřežním moři vytváří se předbřežní písečný val, oddělující od otevřeného moře lagunu.*
3. *Stadium mladosti, ukazující stěhování písečného valu směrem k břehu a počátek zaplňování laguny.*
4. *Stadium pozdní mladosti, ukazující další přiblížení písečného valu k břehu a pozvolnou přeměnu laguny v pobřežní močál.*
5. *Stadium zralosti. Vymizení písečného valu a laguny, takže vlny mořské útočí přímo na přímoří a vytvářejí zde zřetelný srub.*

(Podle Ch. R. Longwella, A. Knopfa a R. F. Flinta.)

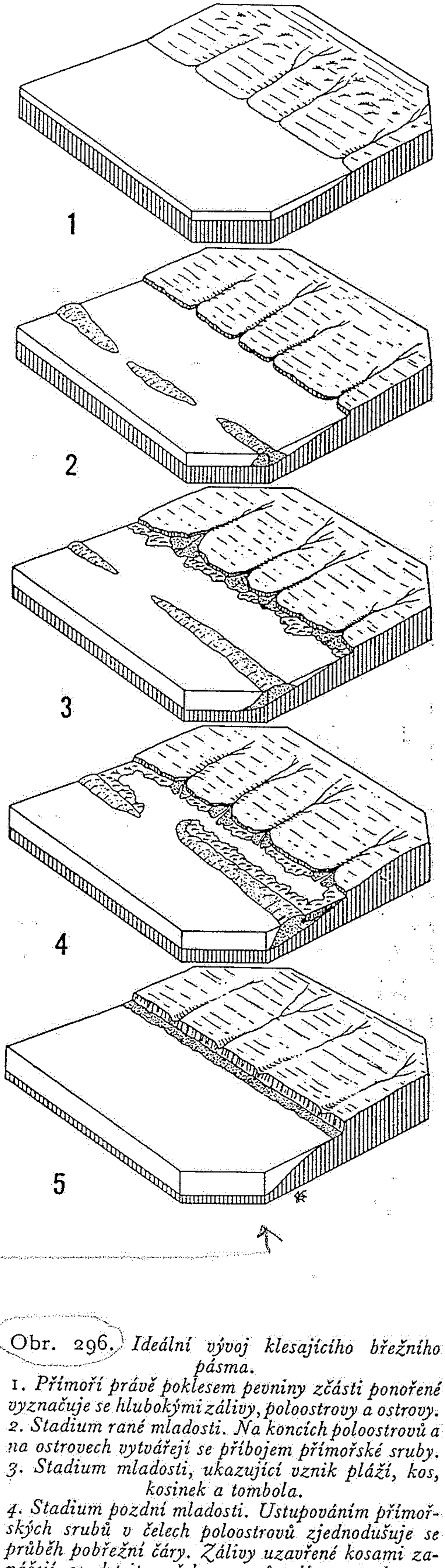

Obr. 296. *Ideální vývoj klesajícího březního pásma.*

1. *Přímoří právě poklesem pevniny zčásti ponořené vyznačuje se hlubokými zálivy, poloostrovy a ostrovy.*
2. *Stadium rané mladosti. Na koncích poloostrovů a na ostrovech vytvářejí se příbojem přímořské sruby.*
3. *Stadium mladosti, ukazující vznik pláží, kos, kosinek a tombola.*
4. *Stadium pozdní mladosti. Ustupováním přímořských srubů v čelech poloostrovů zjednodušuje se průběh pobřežní čáry. Zálivy uzavřené kosami zanášejí se detritem řek a zarůstají vegetací.*
5. *Stadium zralosti. Přímoří je omezeno vyrovnanou pobřežní čarou a výrazným srubem.*

(Podle Ch. R. Longwella, A. Knopfa a R. F. Flinta.)

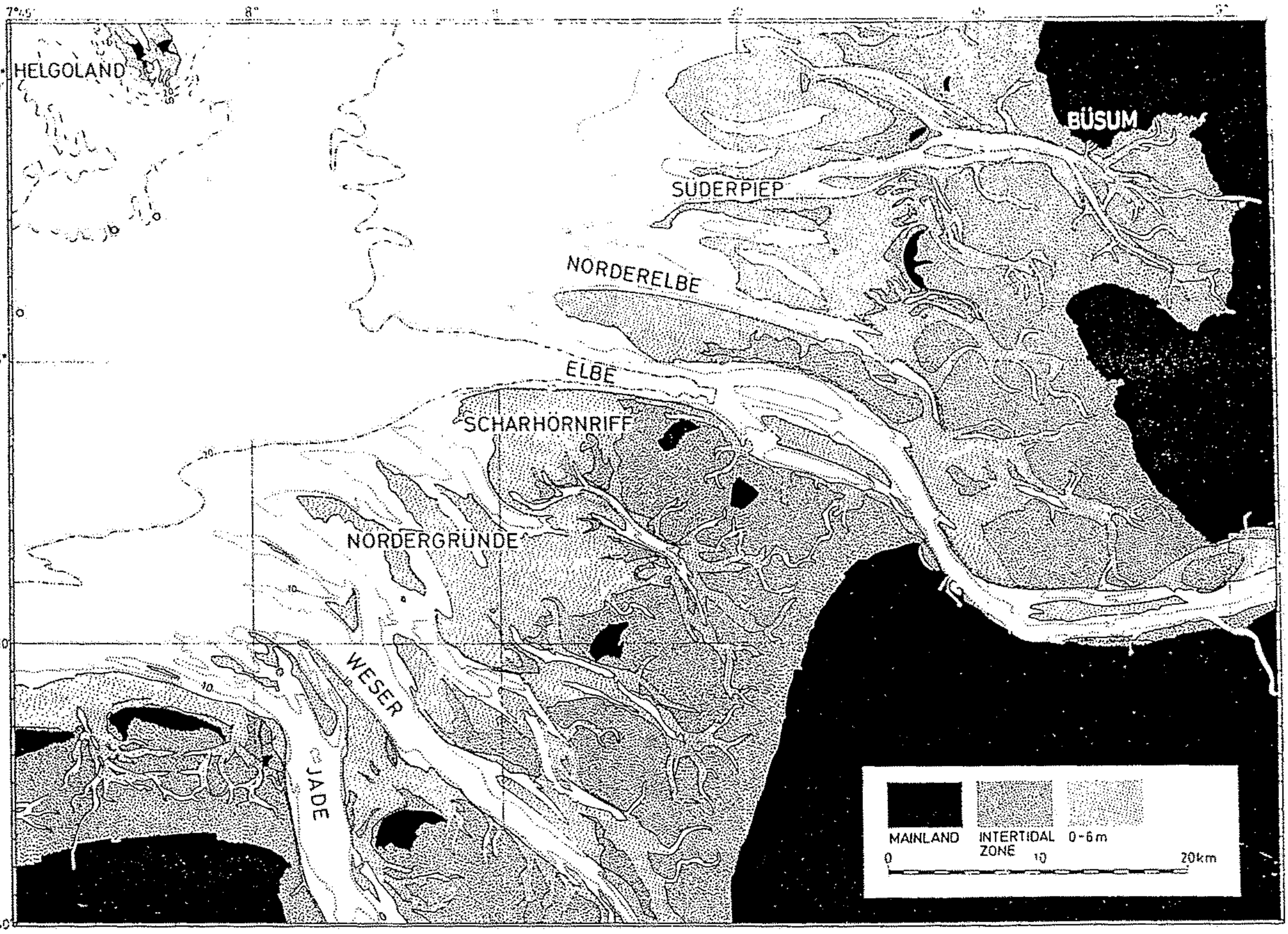

Fig. 535. Map of the southern part of the German Bay, North Sea. Channels and sand bars are in the Outer Jade: channel-sand tongue systems of the area are between the Weser and Elbe rivers (Nordergründe), and the area north of the Elbe (Büsum)

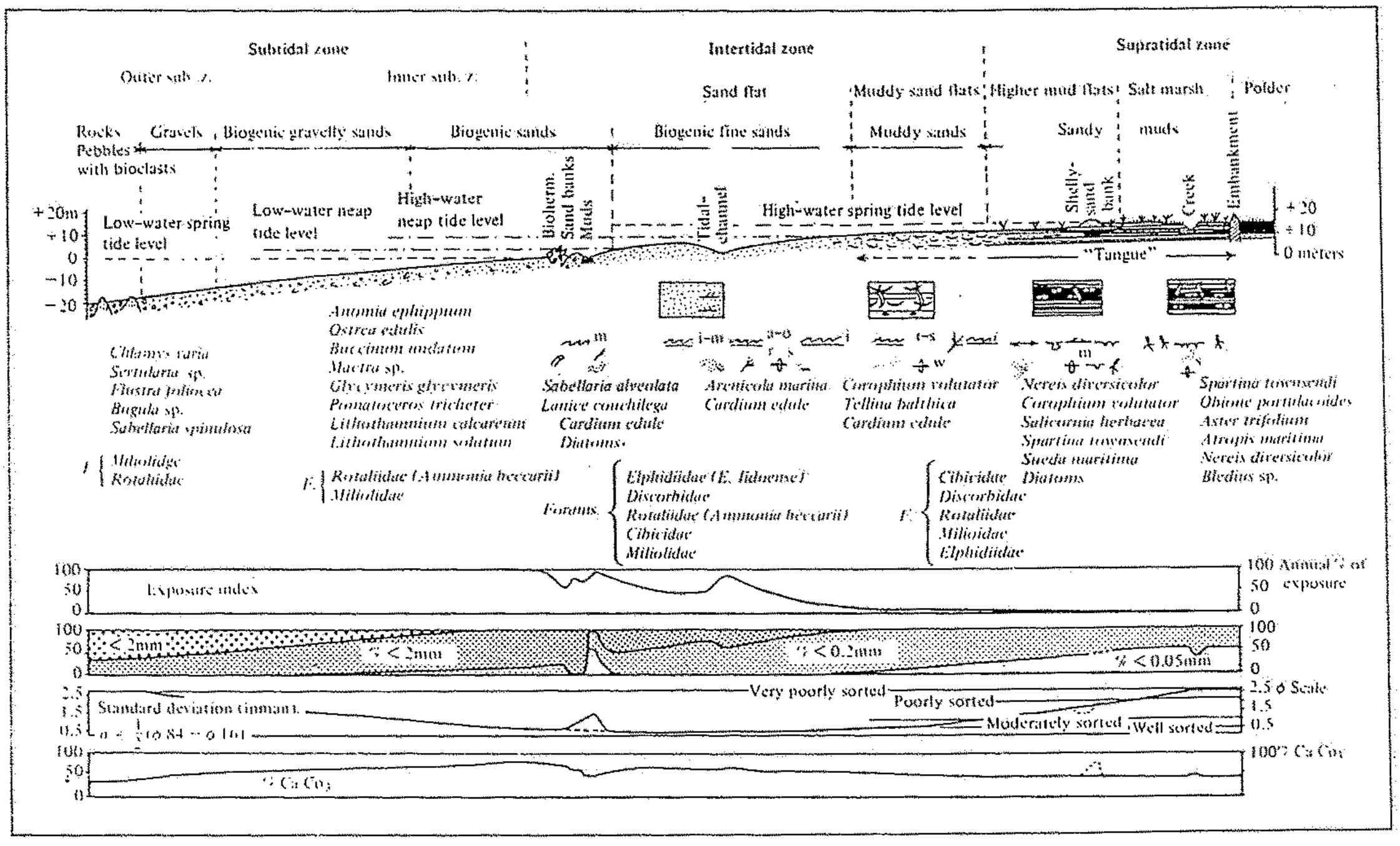

Fig. 616. Schematic section across the tidal flats of St. Michel, France to depict the sedimentation pattern, grain size variation, and faunal assemblages etc. (After Larsonneur 1975)

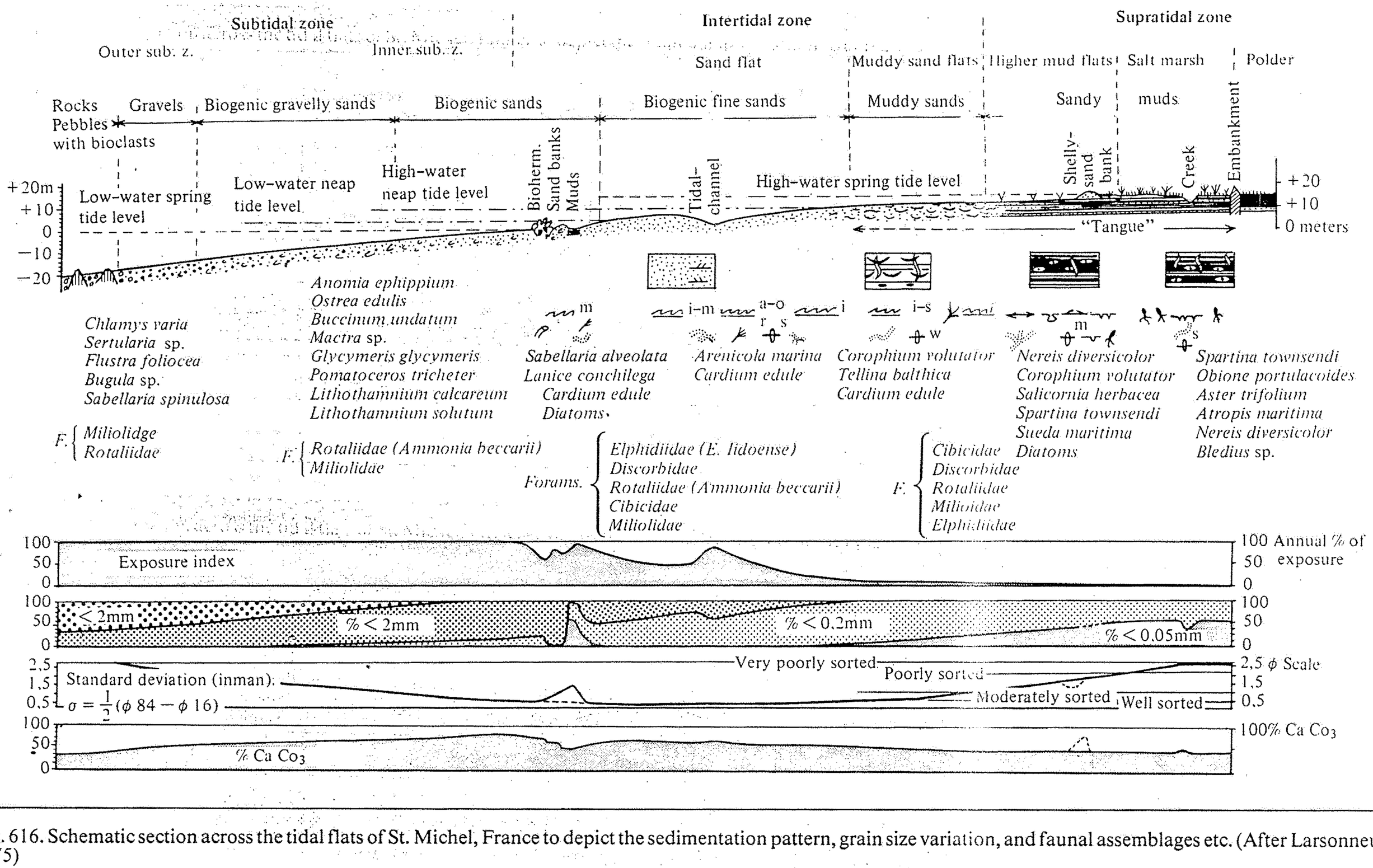

Fig. 616. Schematic section across the tidal flats of St. Michel, France to depict the sedimentation pattern, grain size variation, and faunal assemblages etc. (After Larsonneur 1975)

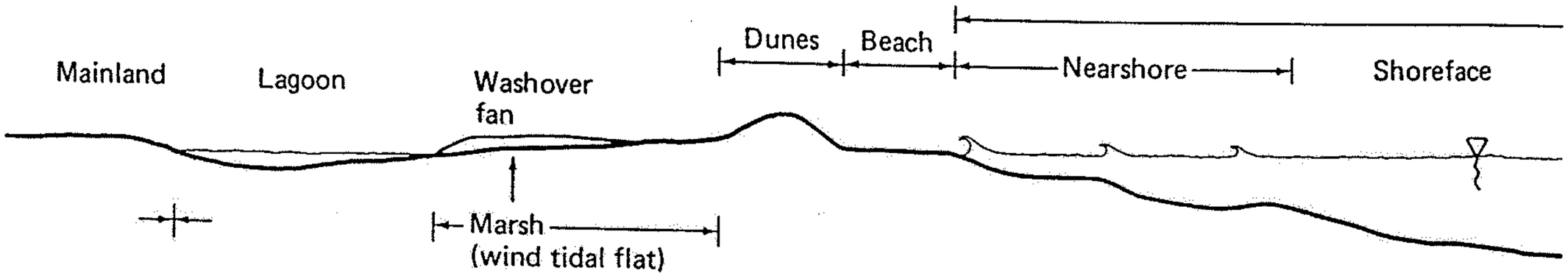

Figure 12–2 Profile diagram of barrier island complex, showing major environments.

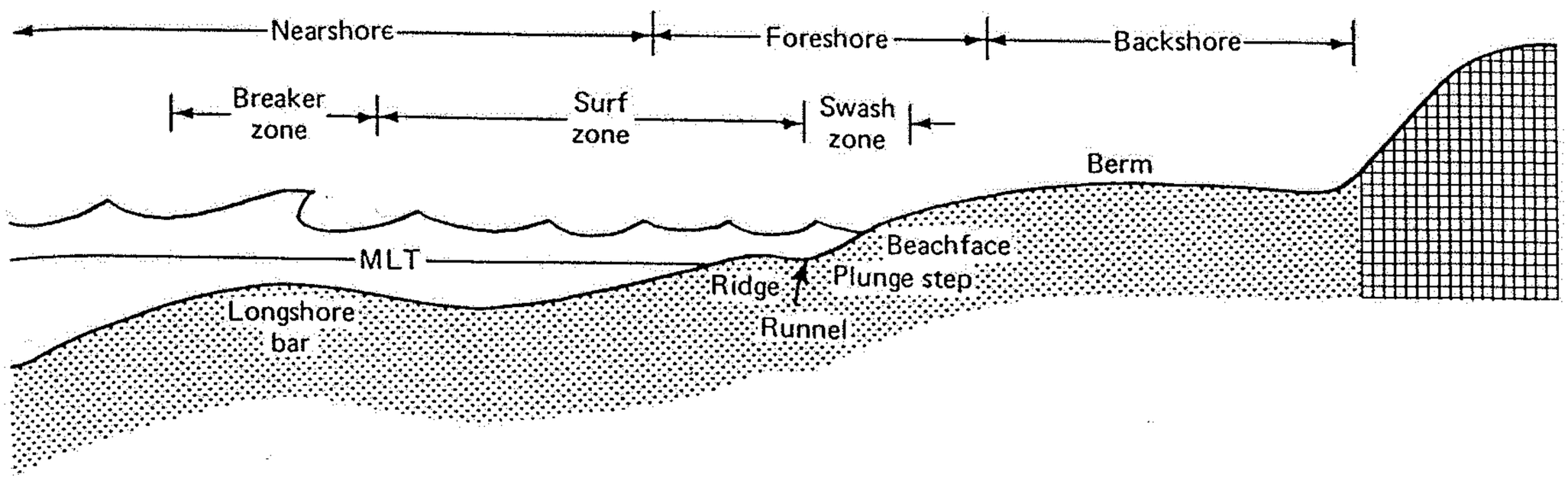

Figure 12–1 Diagrám showing major environments in the beach and nearshore zone.

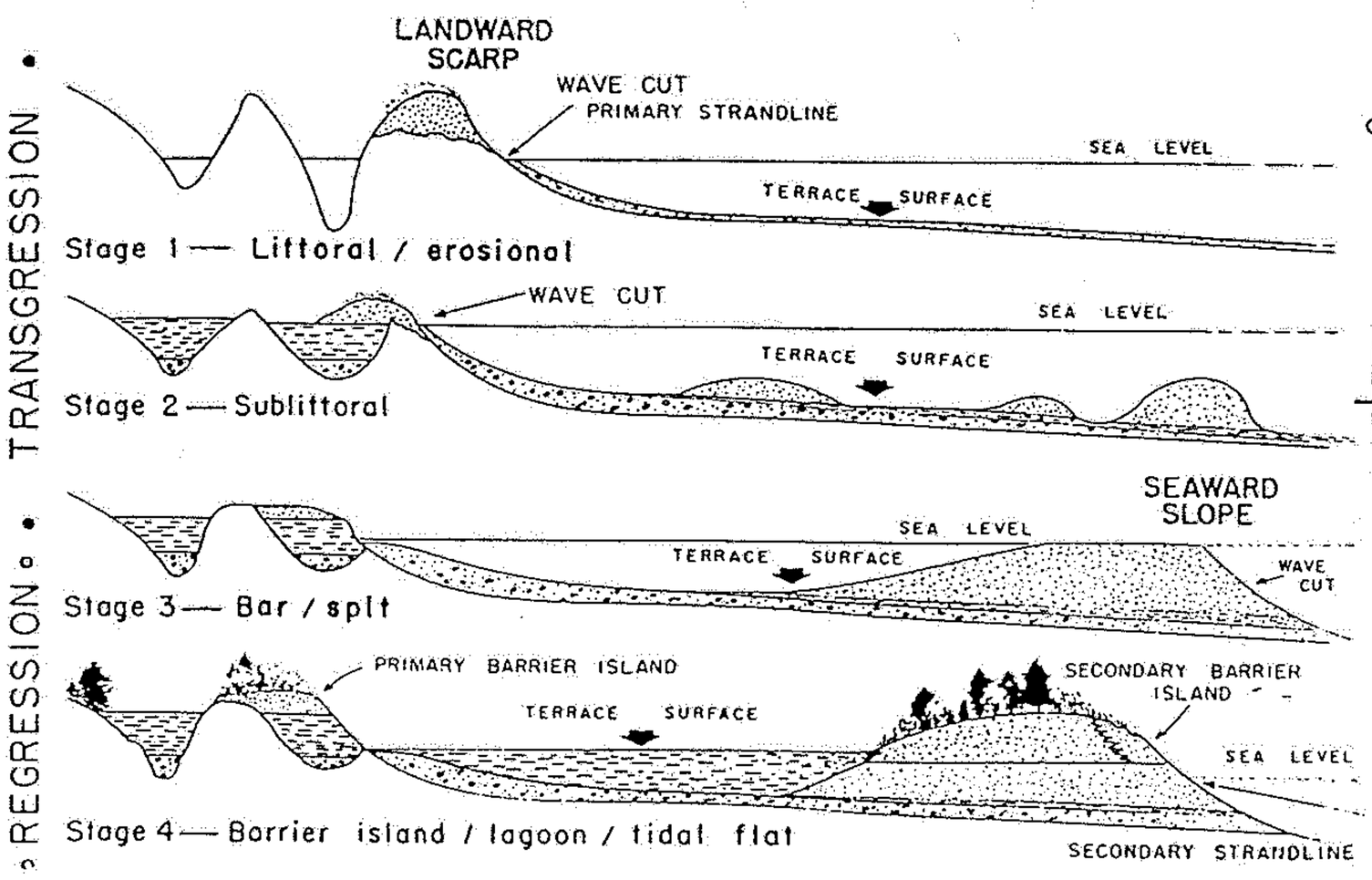

Fig. 464. Primary and secondary barrier islands formed during a transgression-regression cycle. (After Colquhoun 1969b)

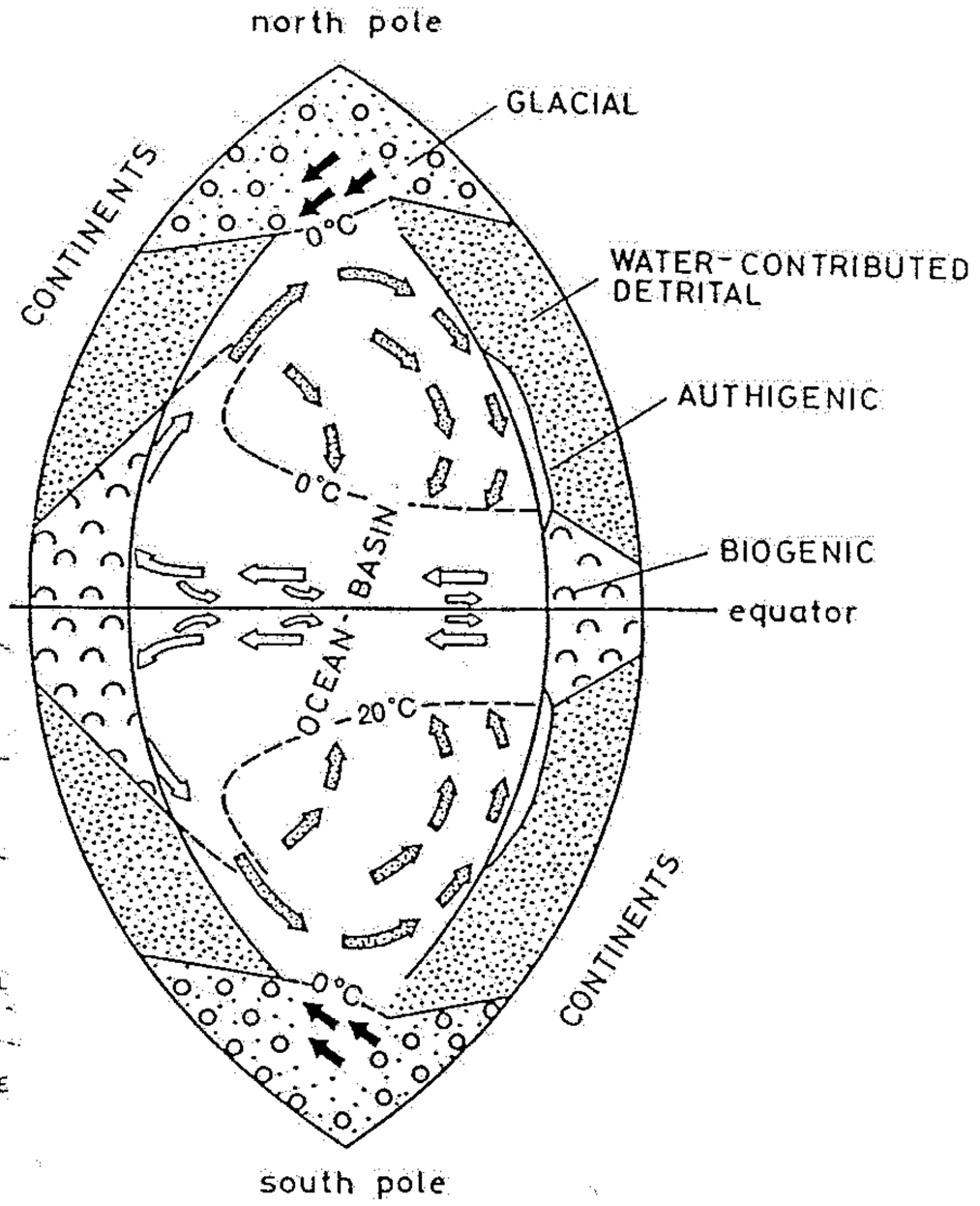

Fig. 521. Idealized distribution of various classes of sediment on continental shelves, where sediments are in equilibrium with their environment. White arrows–warm water; dotted arrows–upwelling water; black arrows–cold water. (After Reineck 1968b; originally modified after Emery 1968b)

Fig. 10.7B. Schematic block diagram of an Andros tidal flat (after Ginsburg and Hardie, 1975).

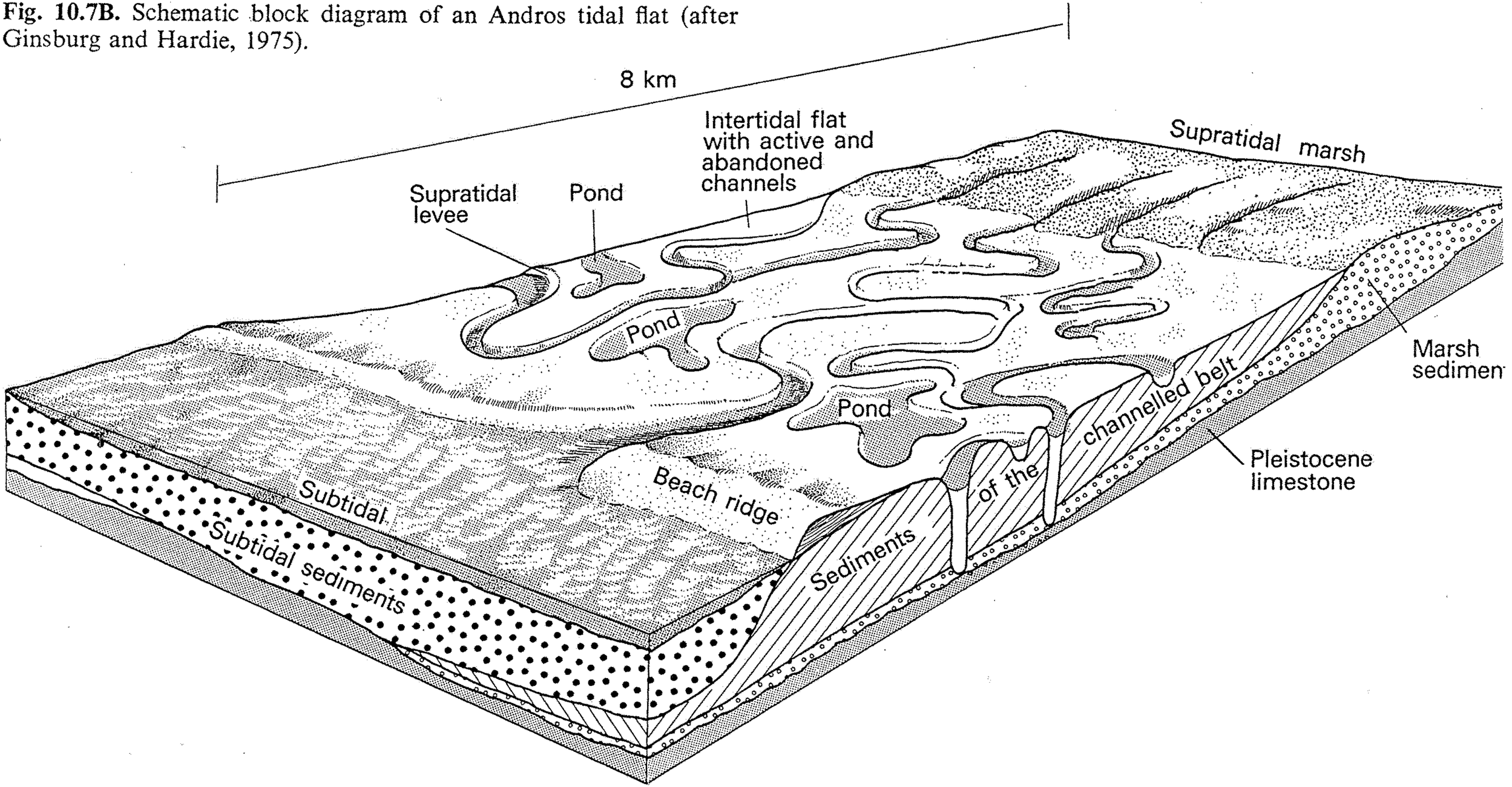

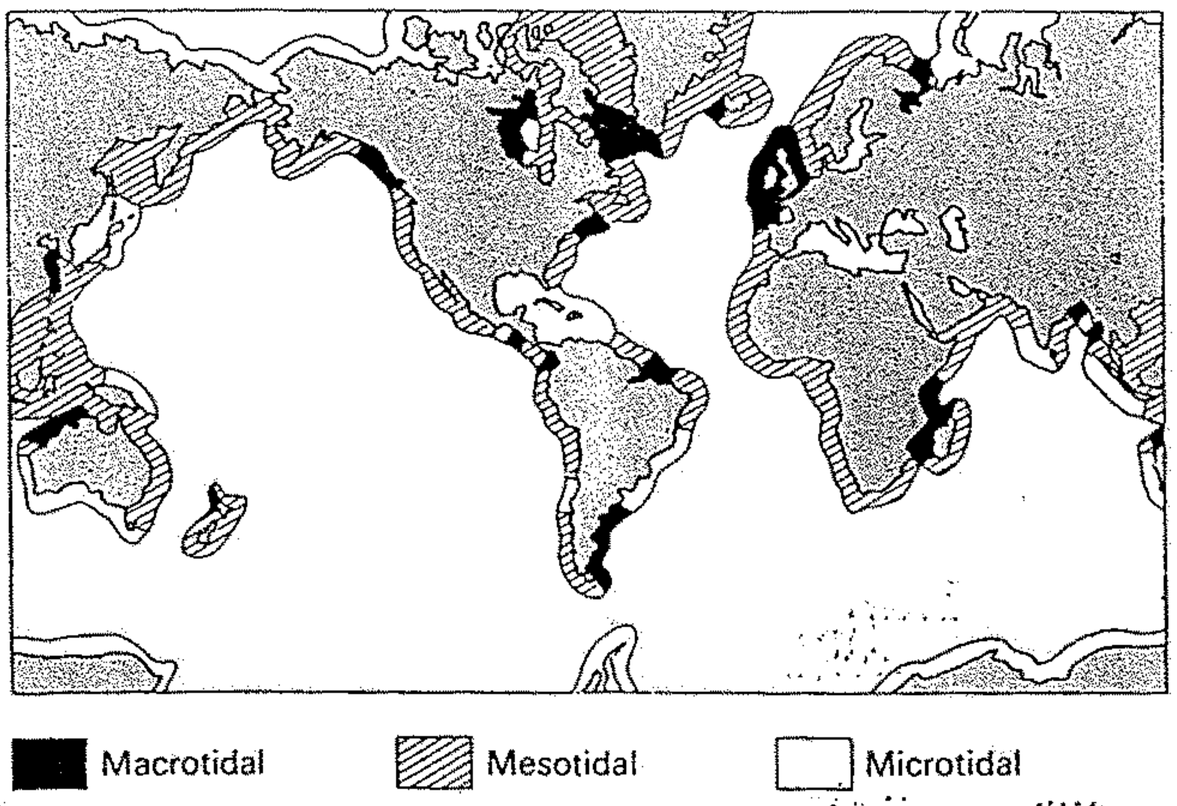

Fig. 7.1. Distribution of microtidal (<2 m), mesotidal (2–4 m) and macrotidal (>4 m) ranges (after Davies, 1964).

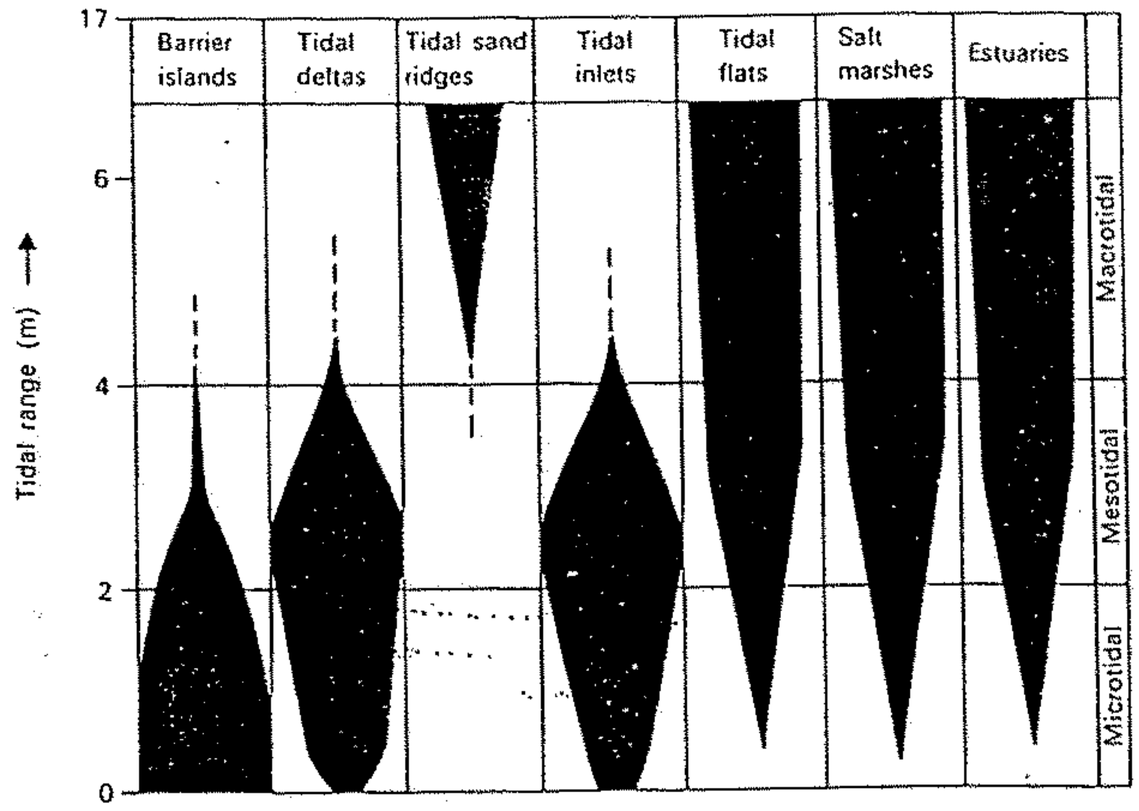

Fig. 7.2. Relationship between tidal range and coastal morphology (modified after Hayes, 1975).

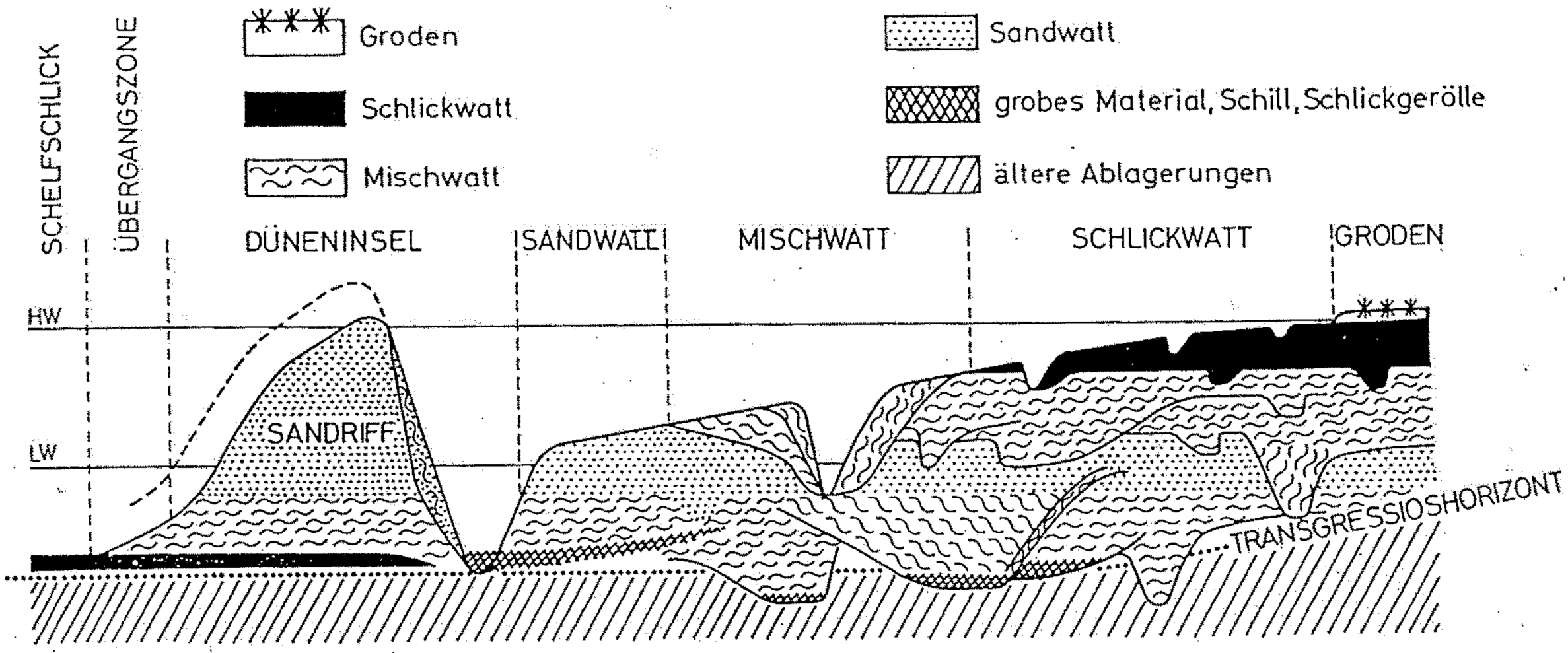

Abb. 74. Senkrechte Sedimentabfolge eines vorwachsenden Watts. Der Unterwasserbereich wird von Rinnenablagerungen aufgebaut. Links offene See.

Vertical sequence of slowly sedimentated progradational deposits reworked by meandering channels. The lower part (subtidal zone) is built up of channel deposits. Left side open sea.

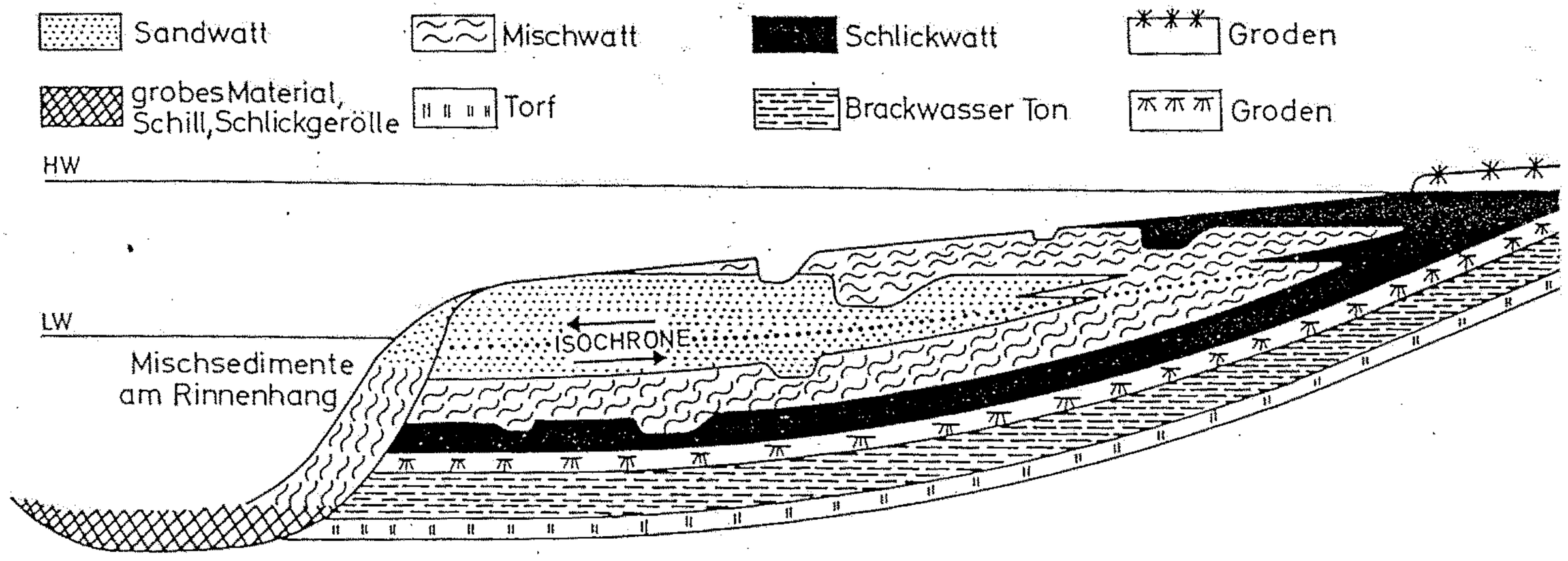

Abb. 75. Senkrechte Abfolge von Wattablagerungen während einer Transgression (untere Hälfte). Die senkrechte Abfolge liegt hierbei in umgekehrter Reihenfolge gegenüber der Abfolge des vorwachsenden Watts (obere Hälfte).

Full developed vertical sequences of transgression (transgressive deposits) and regression (progradational deposits). Instead of peat and brakish clay sometimes there may be found a transgression horizon.

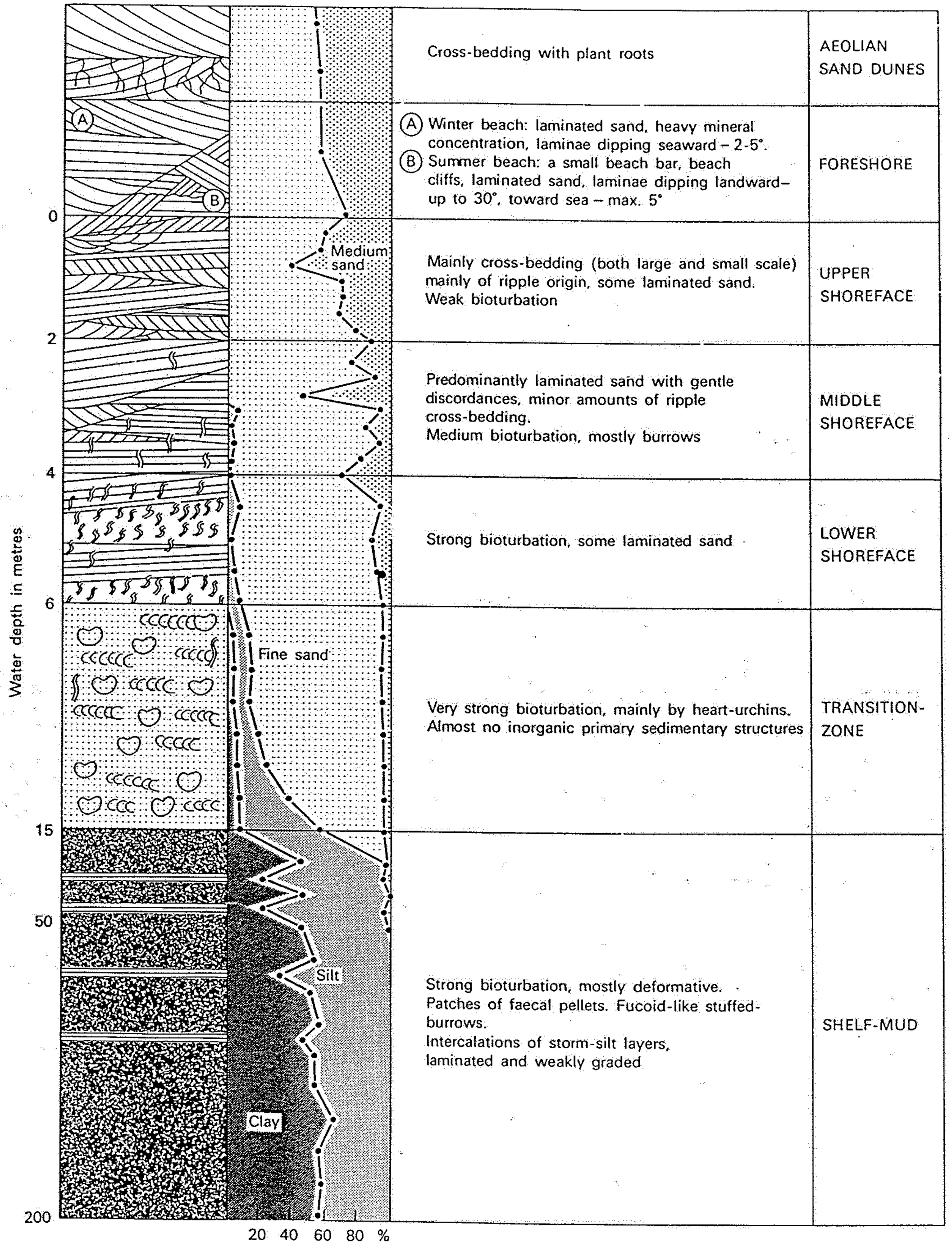

Fig. 7.18. An idealized summary of the coarsening-upward sequence which would develop by progradation of the low wave energy beach face in the Gulf of Gaeta, Italy; illustrating an upwards decrease in bioturbation structures and corresponding increase in wave-induced structures (after Reineck and Singh, 1971, 1973).

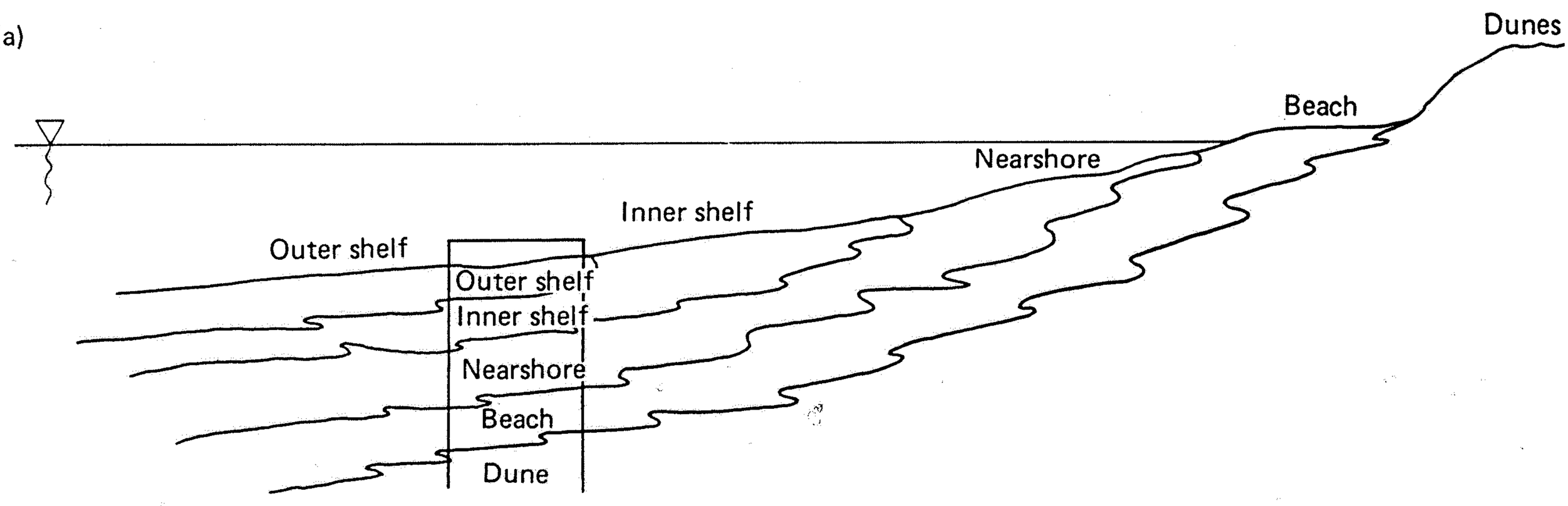

Figure 4–2 Generalized diagram depicting (a) a transgressive sequence and (b) a progradational sequence. A typical stratigraphic section is designated for each.

Fig. 3.24. The classical point bar model for a meandering stream (after Allen, 1964, 1970b).

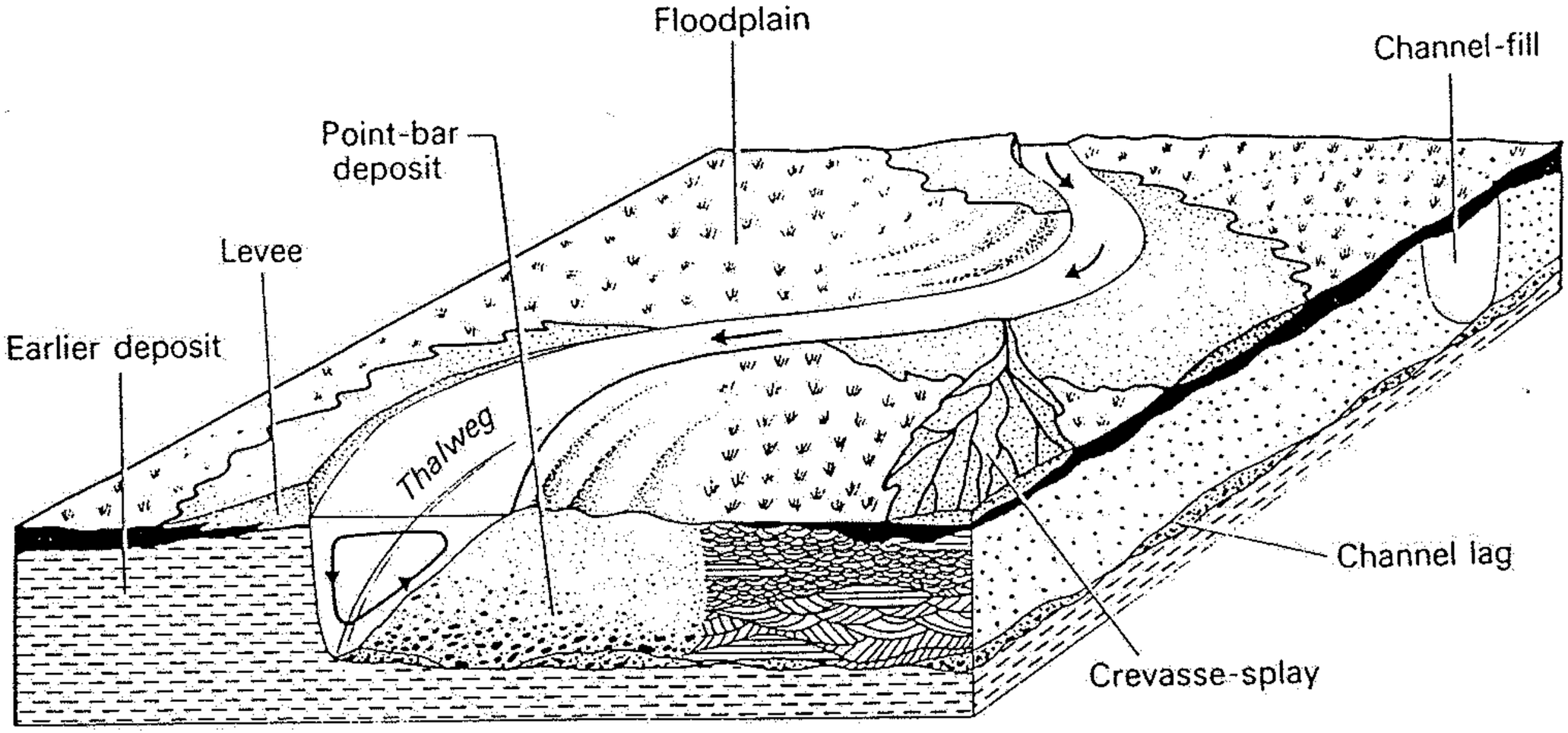

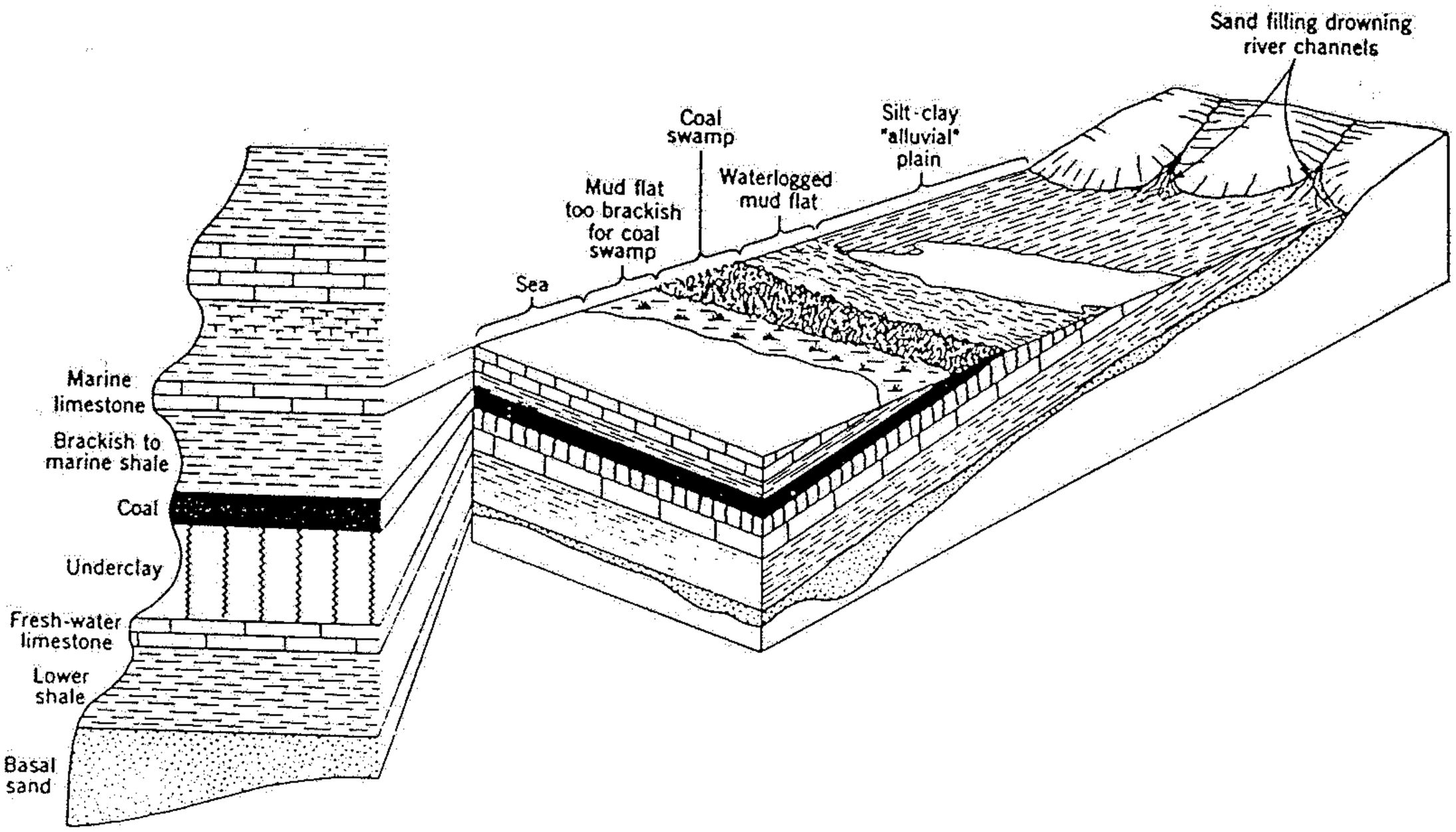

Fig. 19-1 Highly-simplified application of Walther's Law to interpretation of an ideal cyclothem. (After Weller, 1960, from Shaw, 1964.)

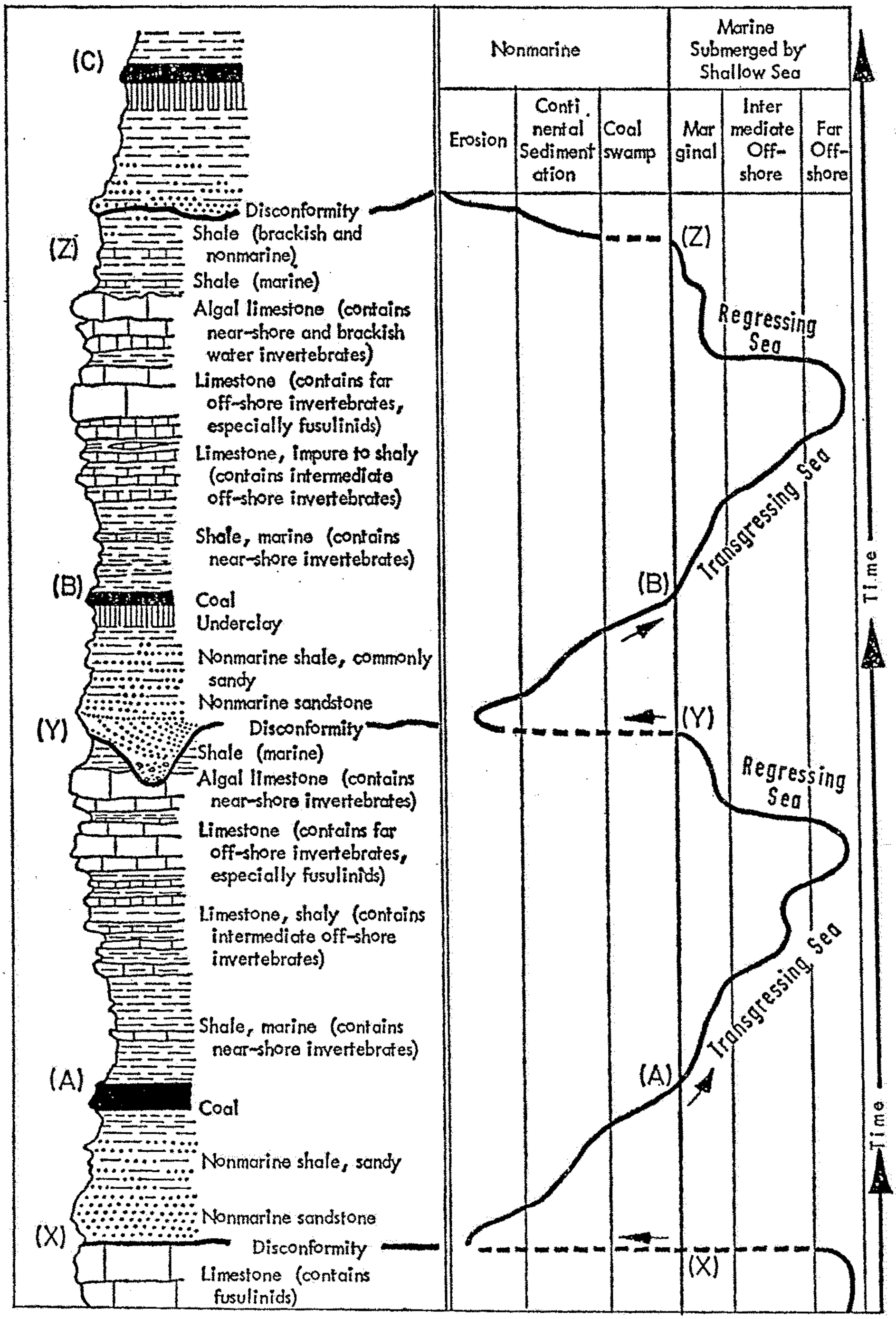

Fig.42. Diagrammatic section of Pennsylvanian rocks in Kansas showing cyclic sedimentation. (After R. C. MOORE, 1959.)

REGRESSIVE MARINE MODEL

Grain size	Sorting	Lithology	Sedimentary structures	Geometry
Tidal flat	Fine-medium	Poor-fair	Silt-clay Sand	Laminated, ripple X-beds scour & fill, mudcracks raindrop-scuffed ripples
Lagoon– Bay	Fine	Poor	Silt-clay (Sand)	Bored & churned plant remains
Dune	Fine-medium	Very good	Sand	Festoon & planar X-bedding
Littoral	Coarse			Swash & rill marks parallel to wavy bedding
Wave zone				Parallel bedding ripples
Shoreface				Graded bedding current structures thin bedded
Below wave zone	Very fine	Poor	Clay–silt	Bored & churned laminated (P)

Figure 4–3 Various characteristics of a coastal and open marine depositional

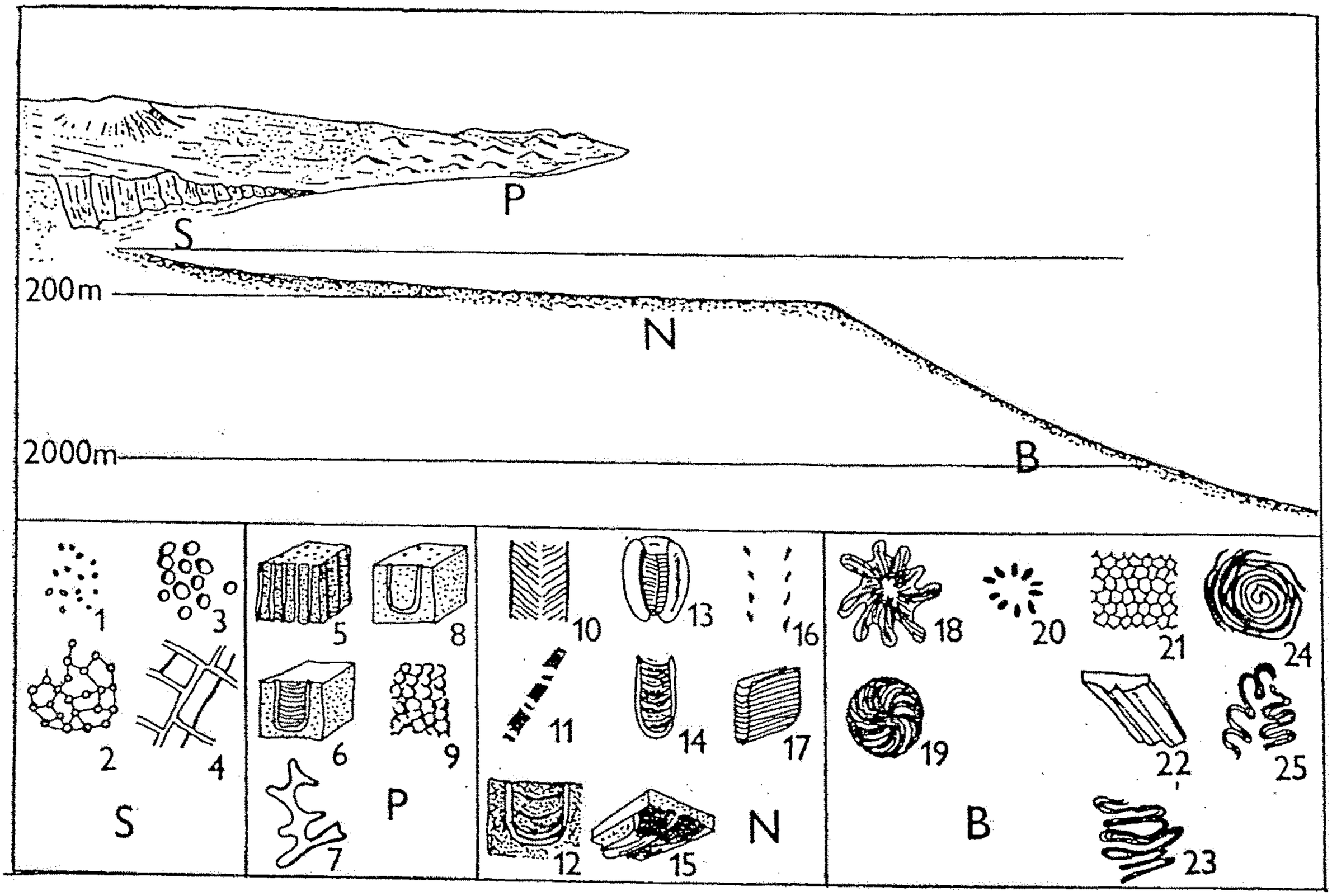

83. Batymetrické členění bioglyfů. S – skalnaté dno, D – pískové dno, N – neritikum, B – batyál a abysál. 1 – chodbičky červa Polydora, 2 – Entobia, stopy vrtavé houby, 3 – stopy vrtání echinoidů, 4 – vrtavé řasy, 5 – Skolithos, 6 – Diplocraterion, 7 – Thalassinoides, 8 – Arenicolites, 9 – Ophiomorpha, 10 – Cruziana, 11 – Dimorcoites, 12 – Corophioides, 13 – Rusophycus, 14 – Rhizocorallium, 15 – Phycodes, 16 – Diplichnites, 17 – Teichichnus, 18 – Zoophycos, 19 – Spirophyton, 20 – Lorenziania, 21 – Paleodictyon, 22 – Taphrohelminthopsis, 23 – Helminthoida, 24 – Spirorhaphe, 25 – Cosmorhaphe. Basan (1978).

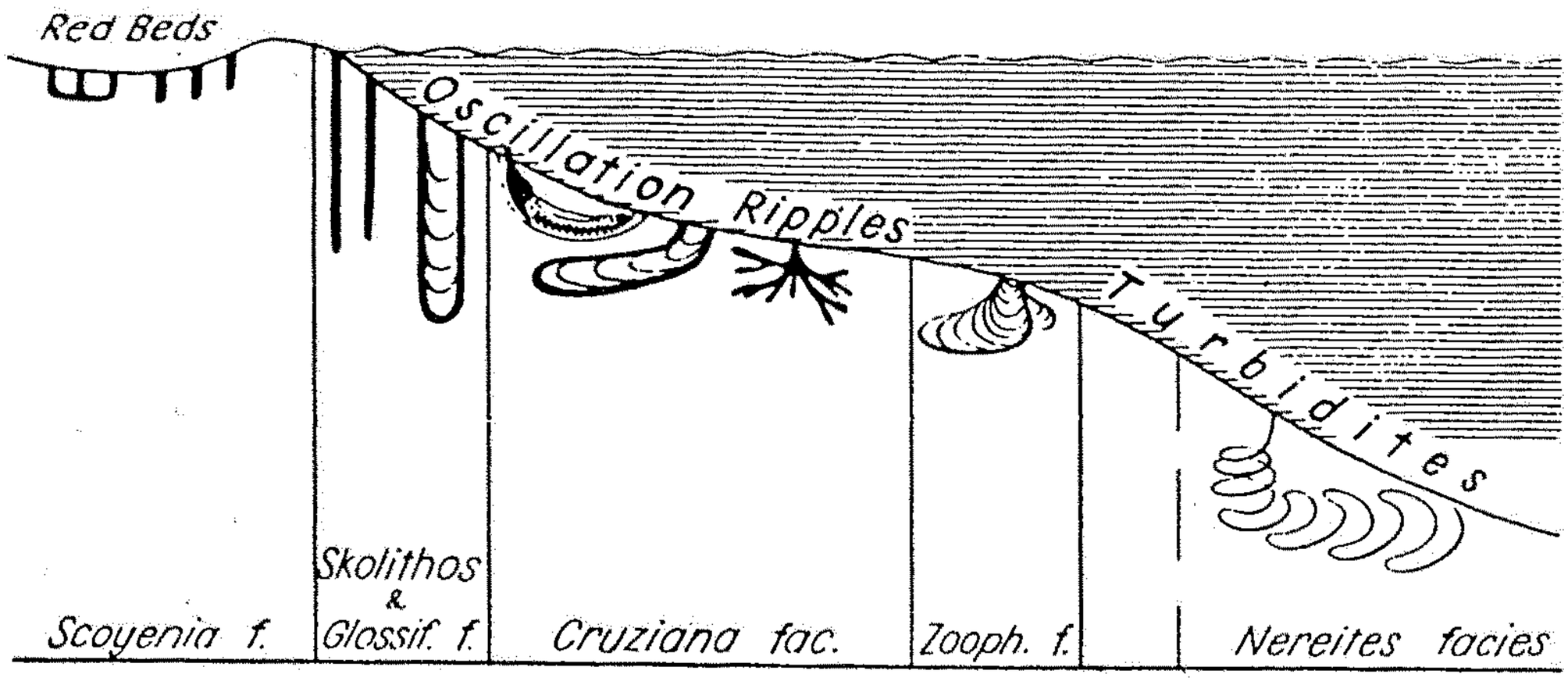

FIG. 18. Bathymetric zonation of trace fossil assemblages [*f* = facies] (Seilacher, 1967b).

Abb. 68. Sackungstrichter und Kotschlingen-Haufen des Pierwurms (*Arenicola marina*) in einem schlickig-sandigen Rippelfeld.

Burrow-funnels and faecal-matter accumulates of the polychaete *Arenicola marina* on a rippled surface.

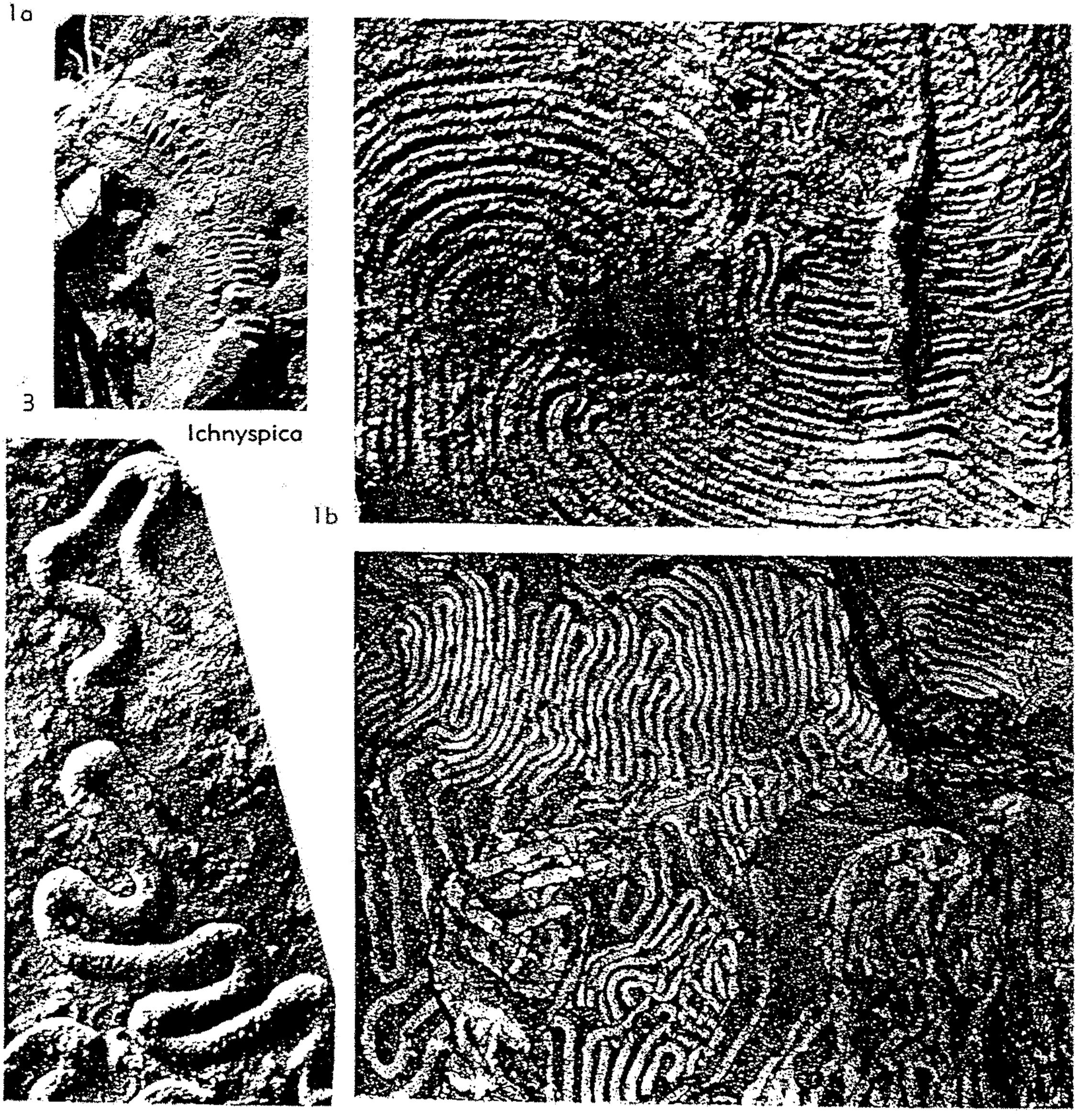

FIG. 44. Trace fossils (p. *W*70, 74).

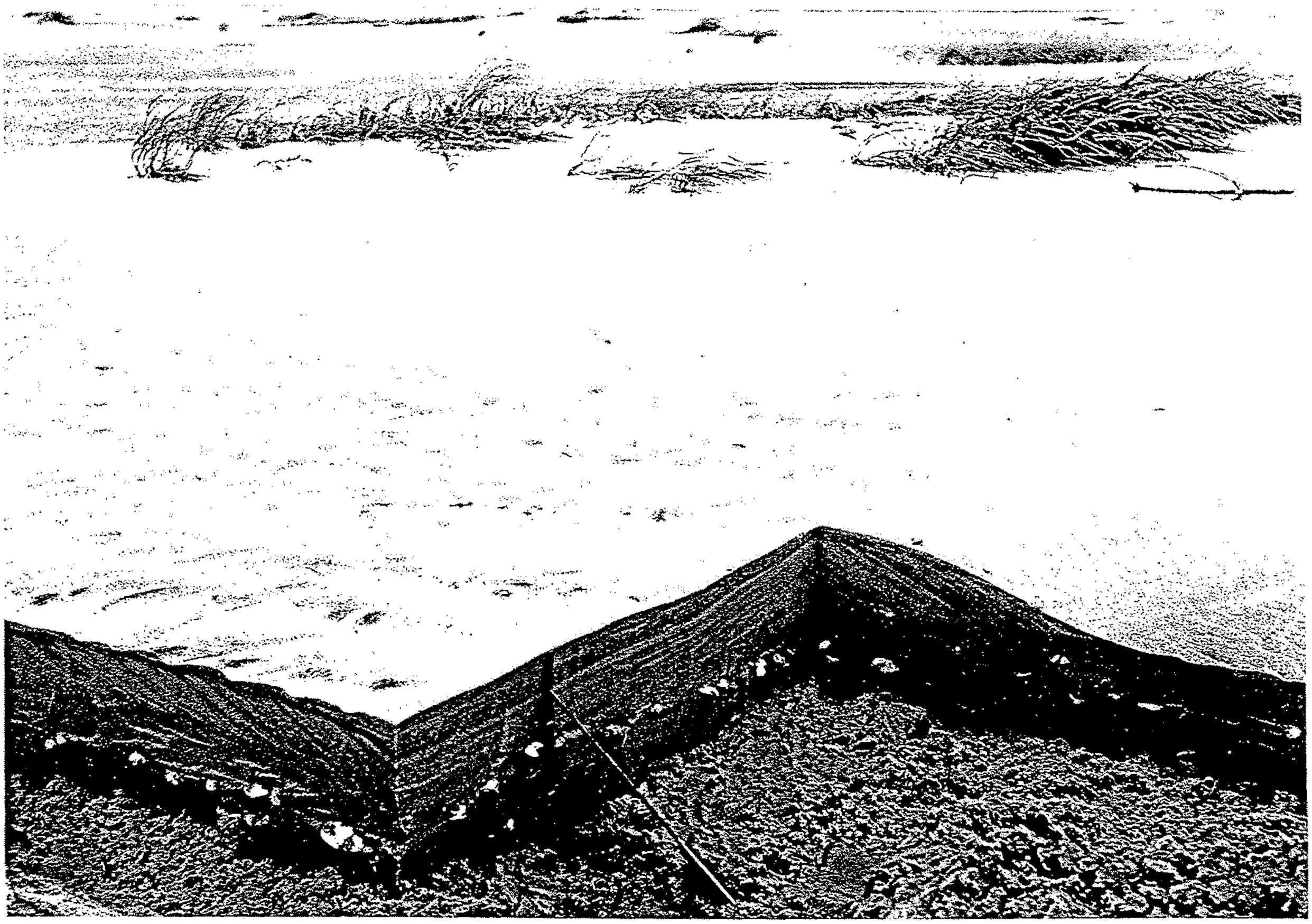

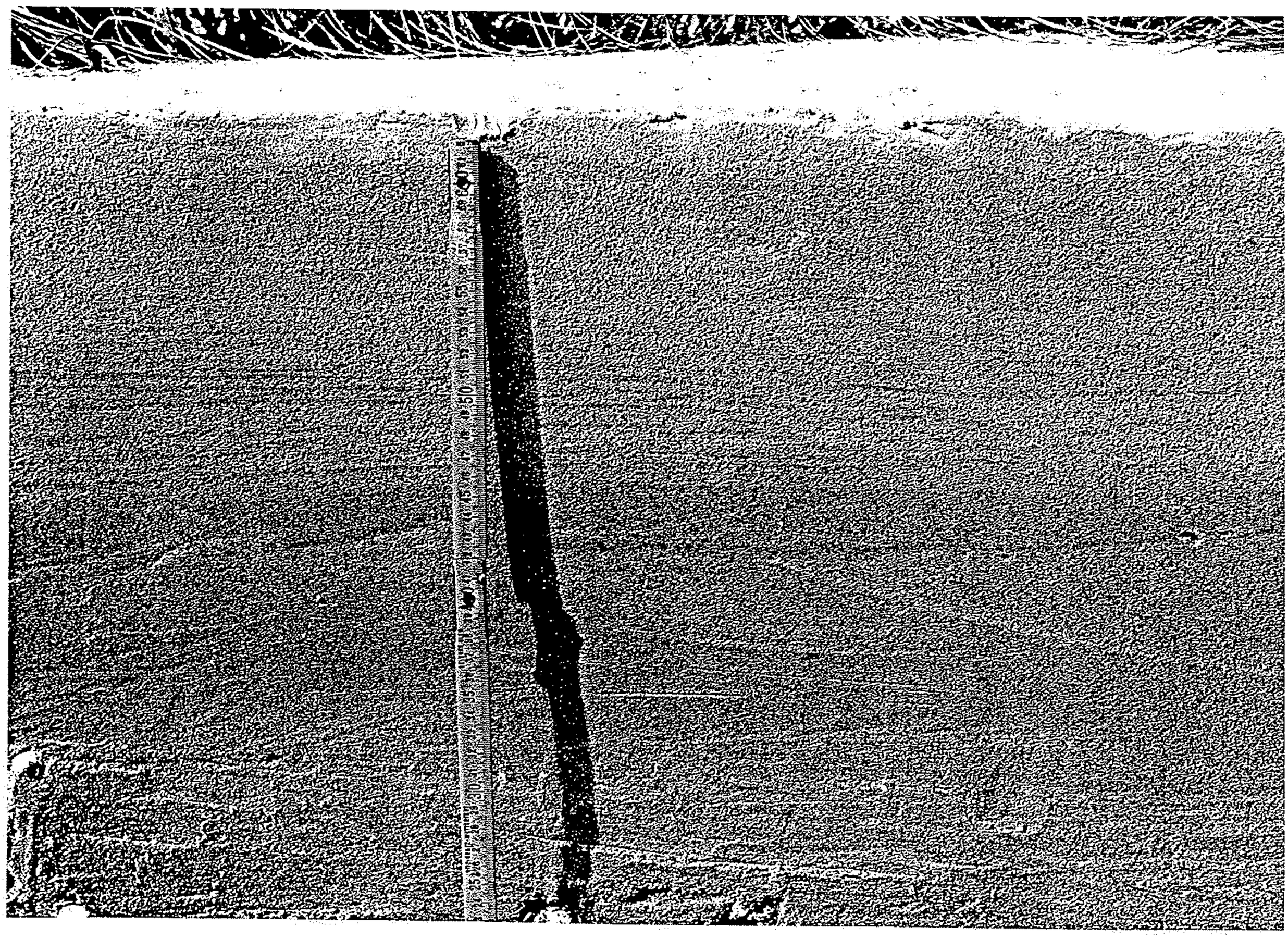

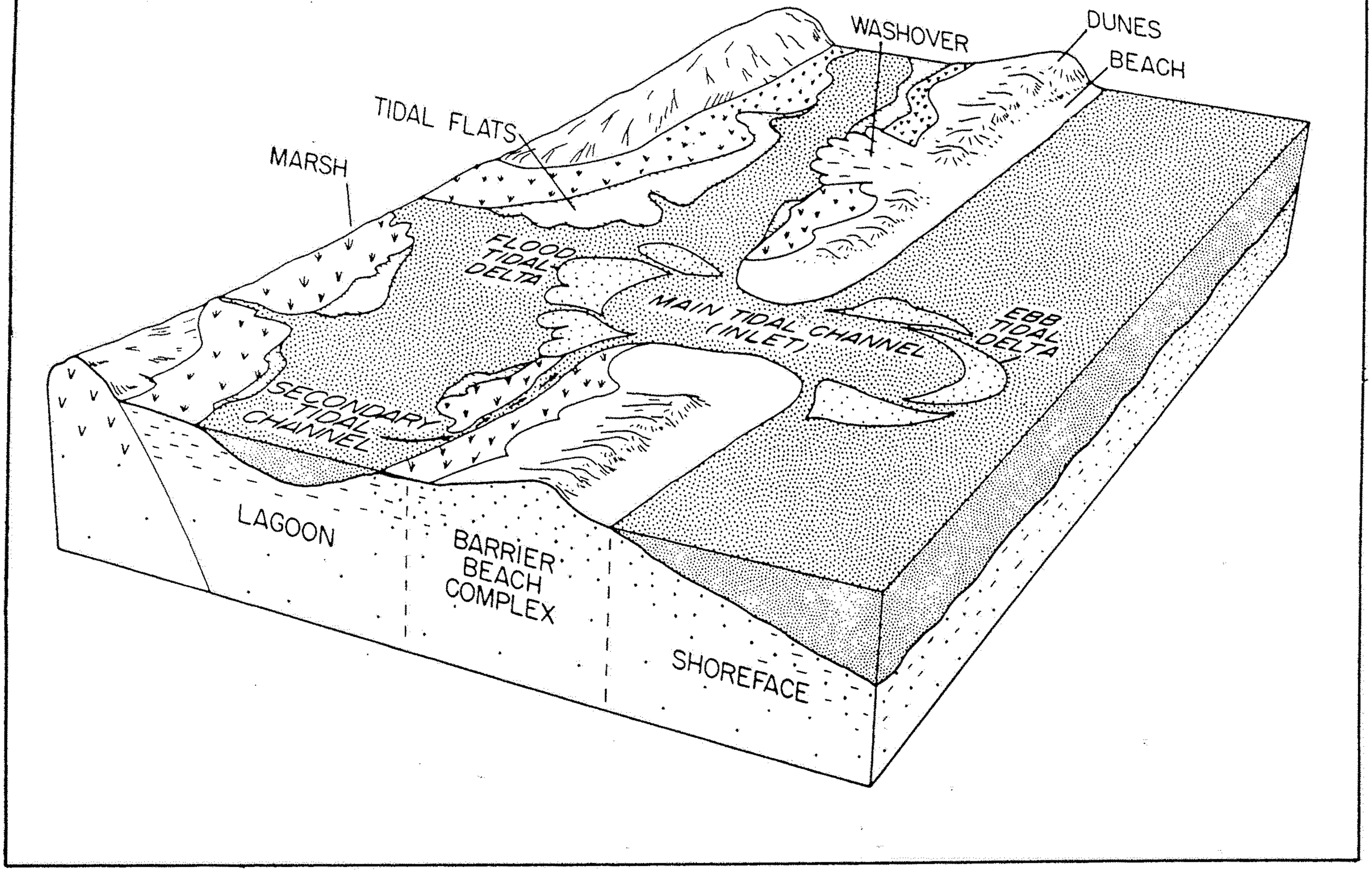

Figure 2

Block diagram illustrating the various subenvironments in a barrier-island system.

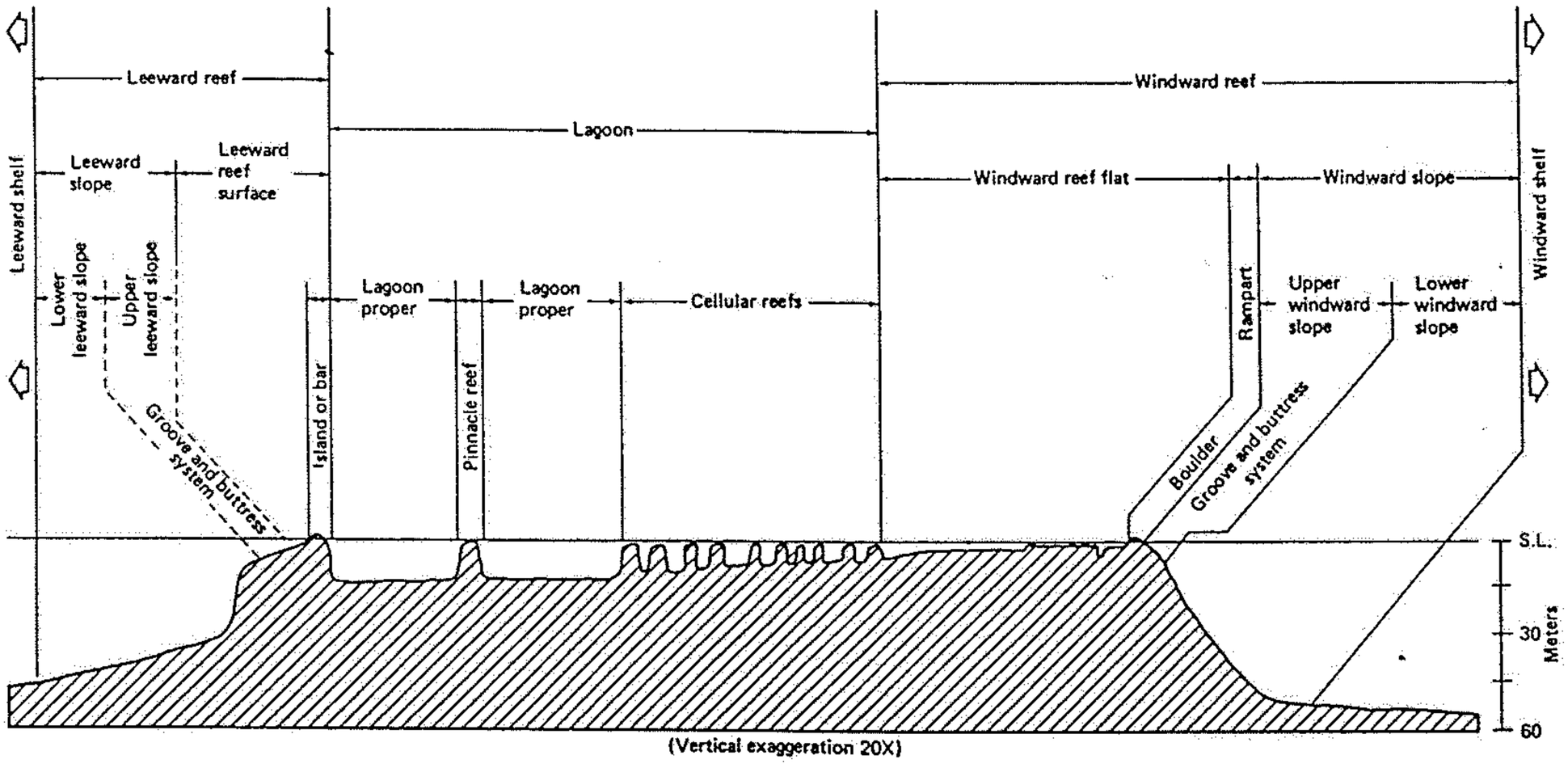

Figure 14-6 Diagram showing various environments across Alacran Reef, Campeche Bank, Mexico. These environments are representative of most closed reefs. (From Hoskin, 1963, Figure 4, p. 19.)

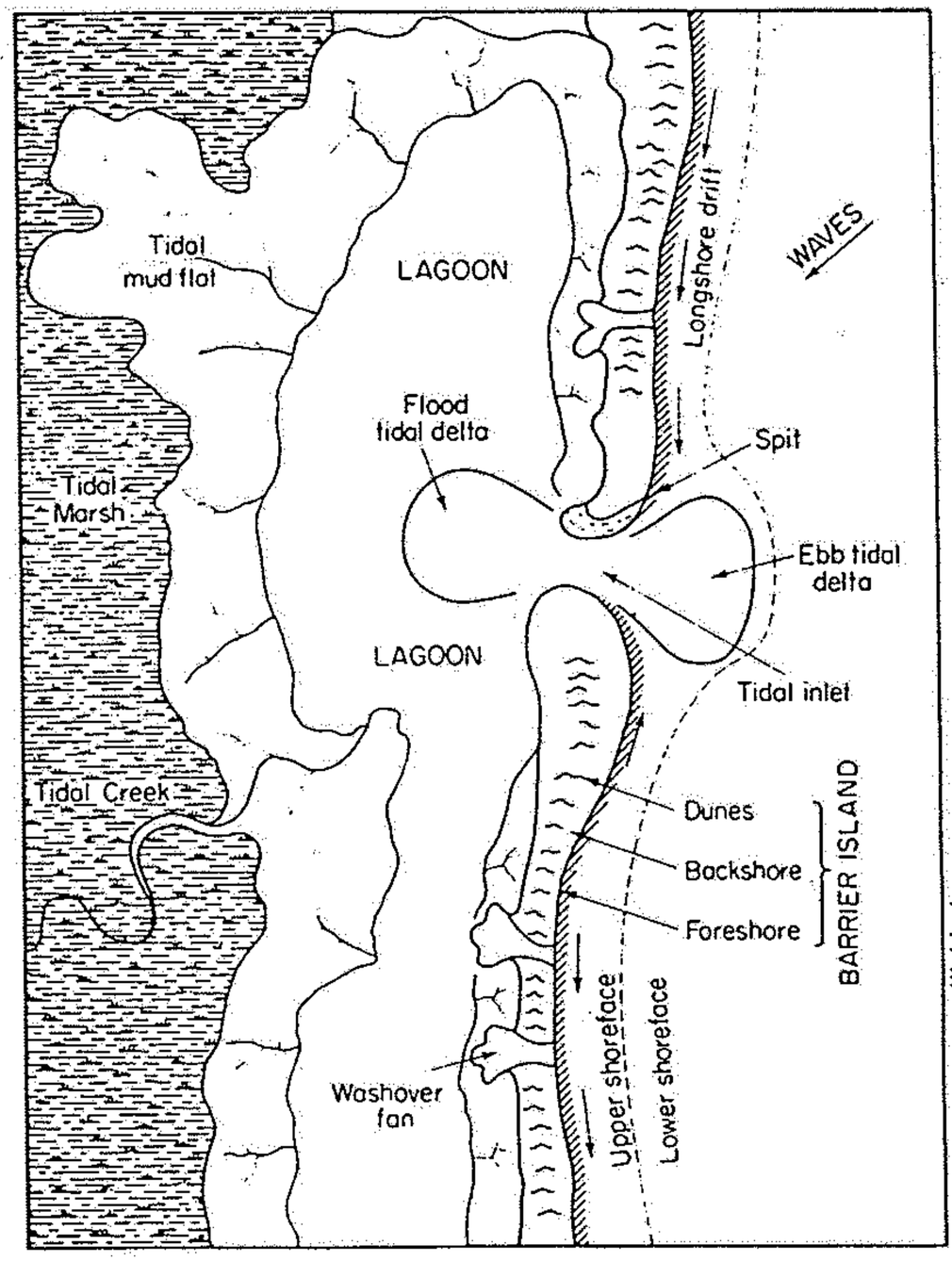

Figure 12-3 Sketch map of a barrier island complex, showing various sedimentary environments present. (From Blatt et al., 1980, Figure 19-14.)

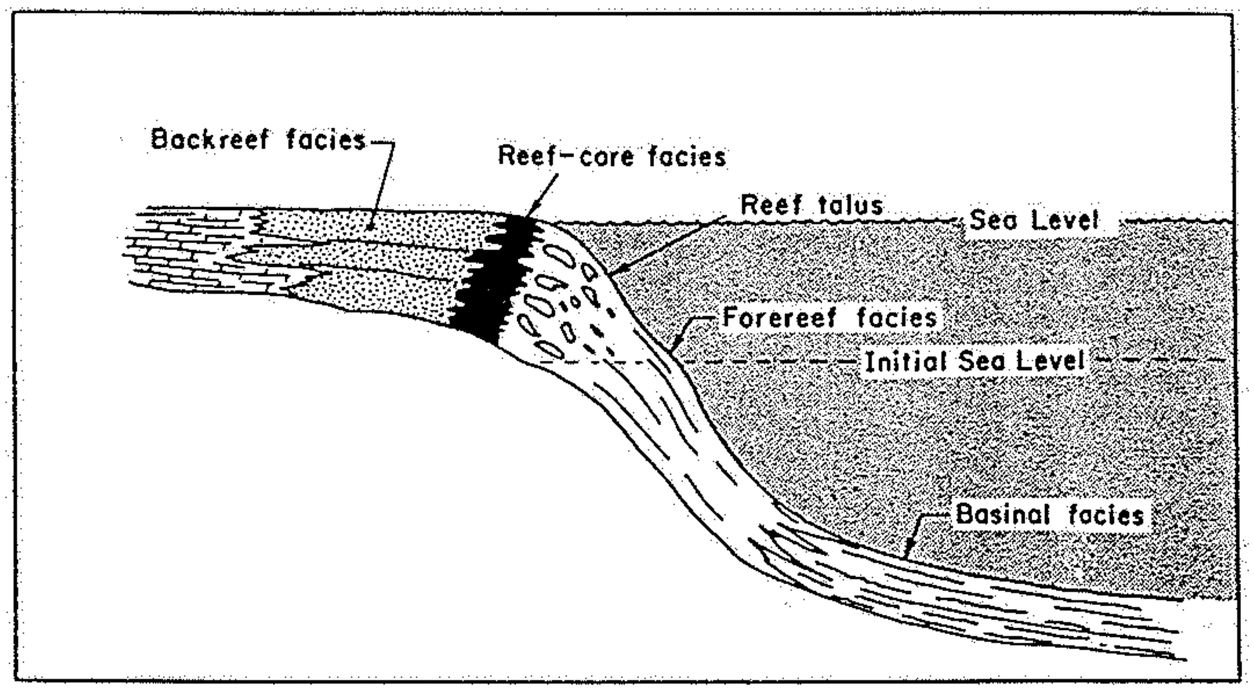

Figure 12-30 *Idealized profile and section (not to scale) across shelf-edge reef, as seen in many parts of the rock record, showing massive reef core (black), backreef (stippled), and forereef facies (showing steep initial dip, slightly exaggerated, toward basinal facies).*

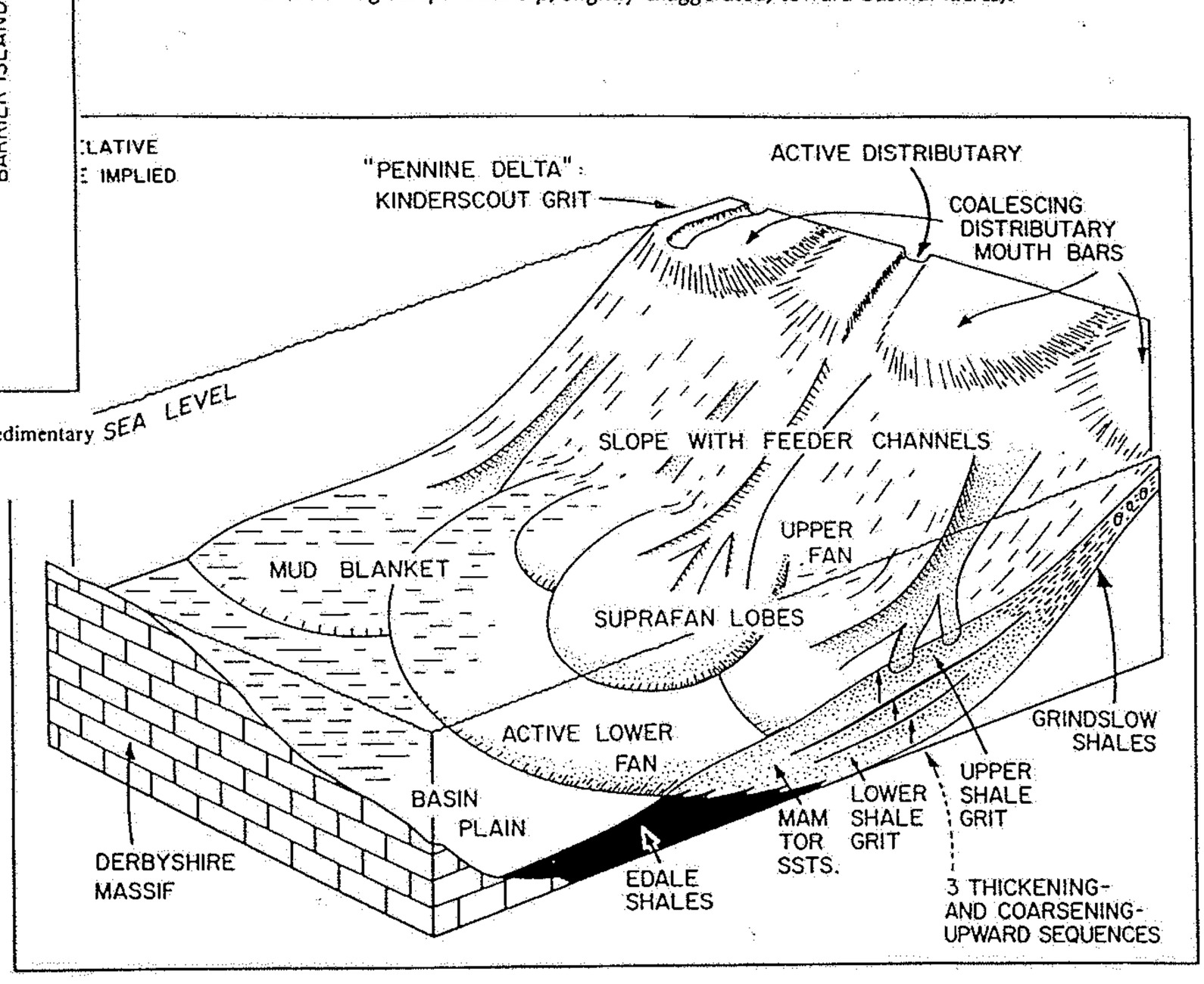

Fig. 647. Schematic block diagram showing depositional relationship of shale grit and associated formations to demonstrate various geomorphic units of deep sea fan valleys. (After Walker 1978)

Fig. 10.12B. Diagram showing coral zonation on the lagoon reef, Gan. A chute formation on the reef slope is shown (after Spencer Davies *et al.*, 1971).

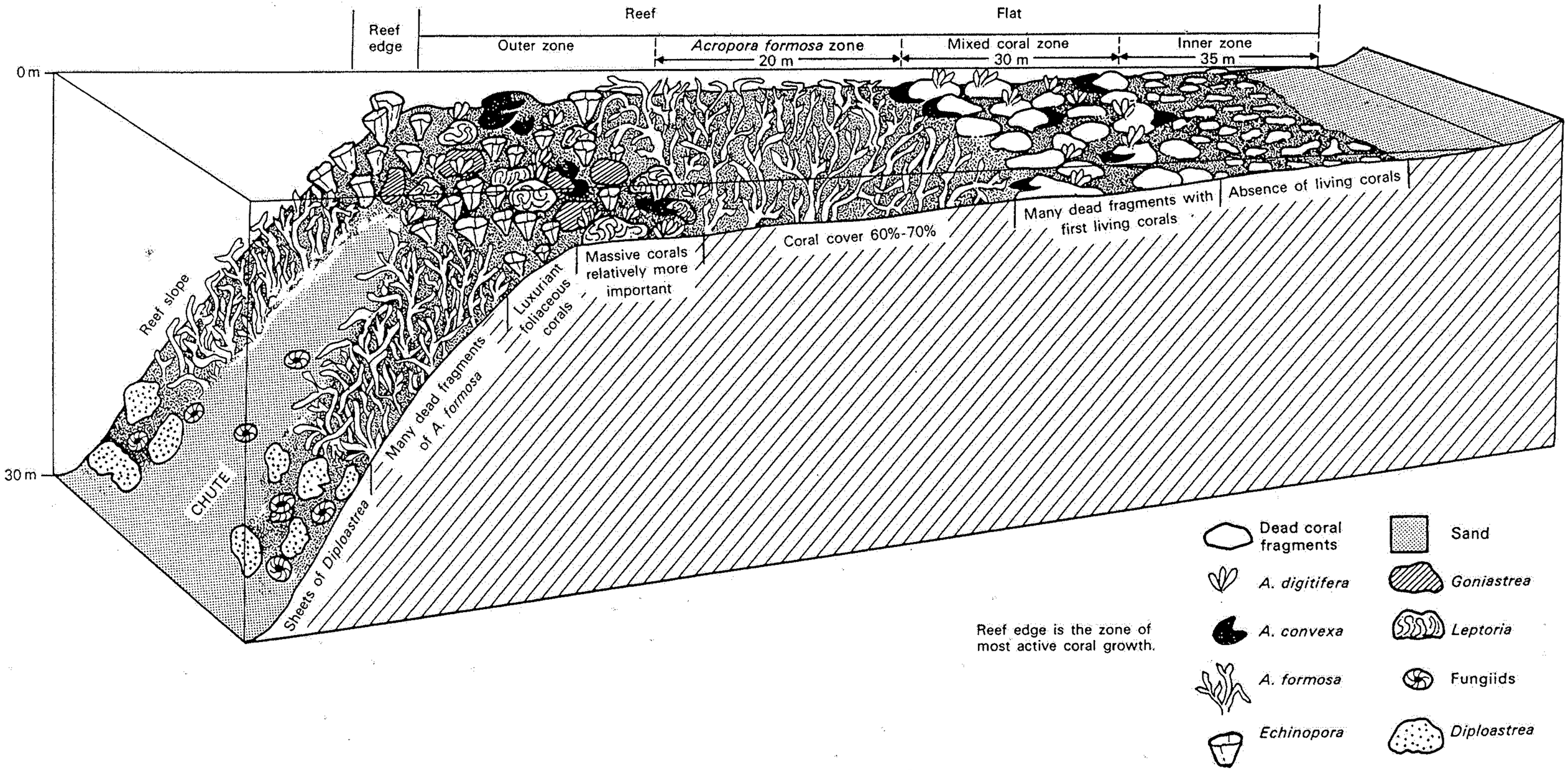

Reef edge is the zone of most active coral growth.

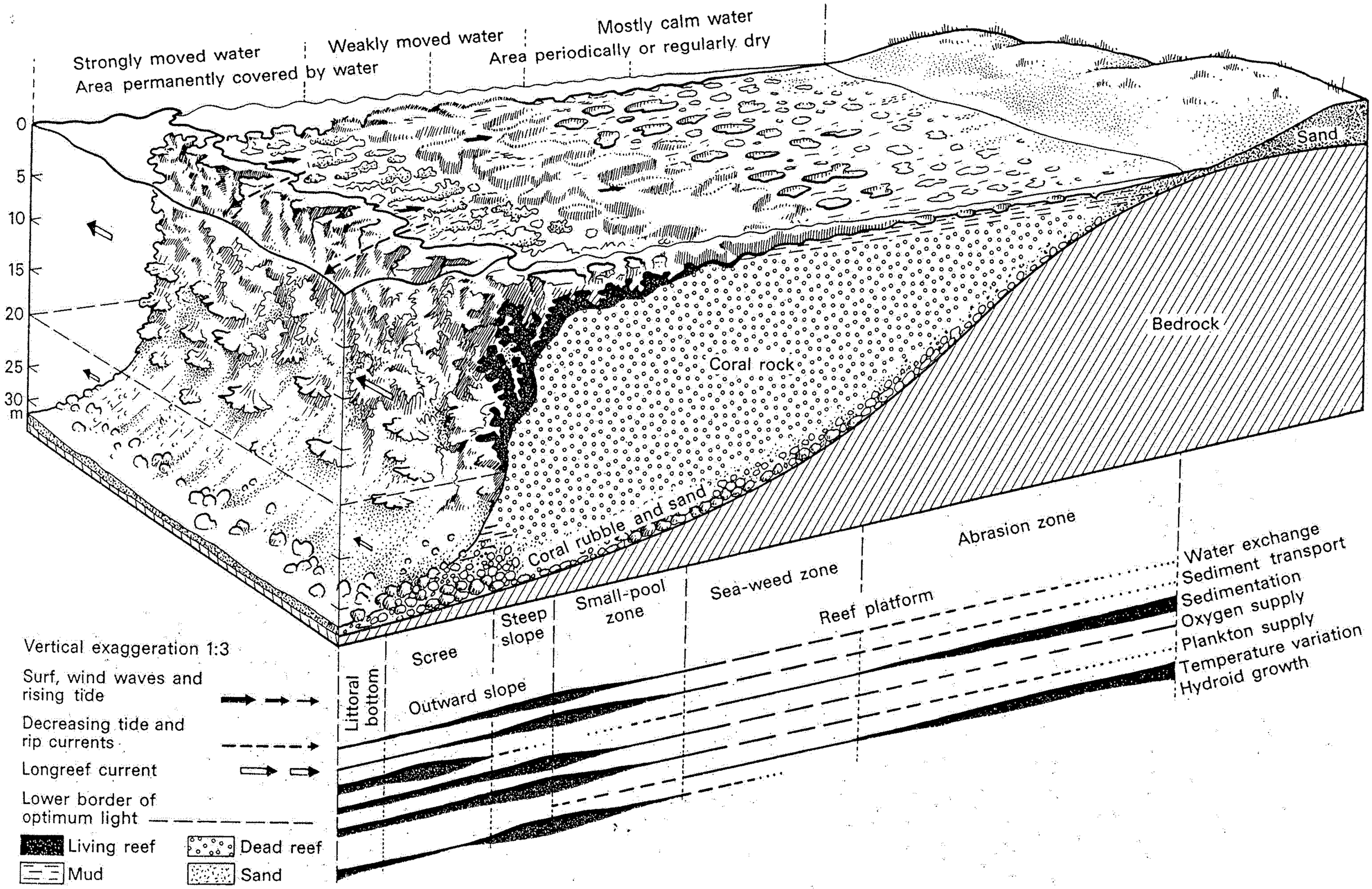

Fig. 10.40B. Block diagram of the northern fringing reef of Eilat illustrating the reef structure, zonation and major ecological conditions within the reef (after Mergner, 1971).

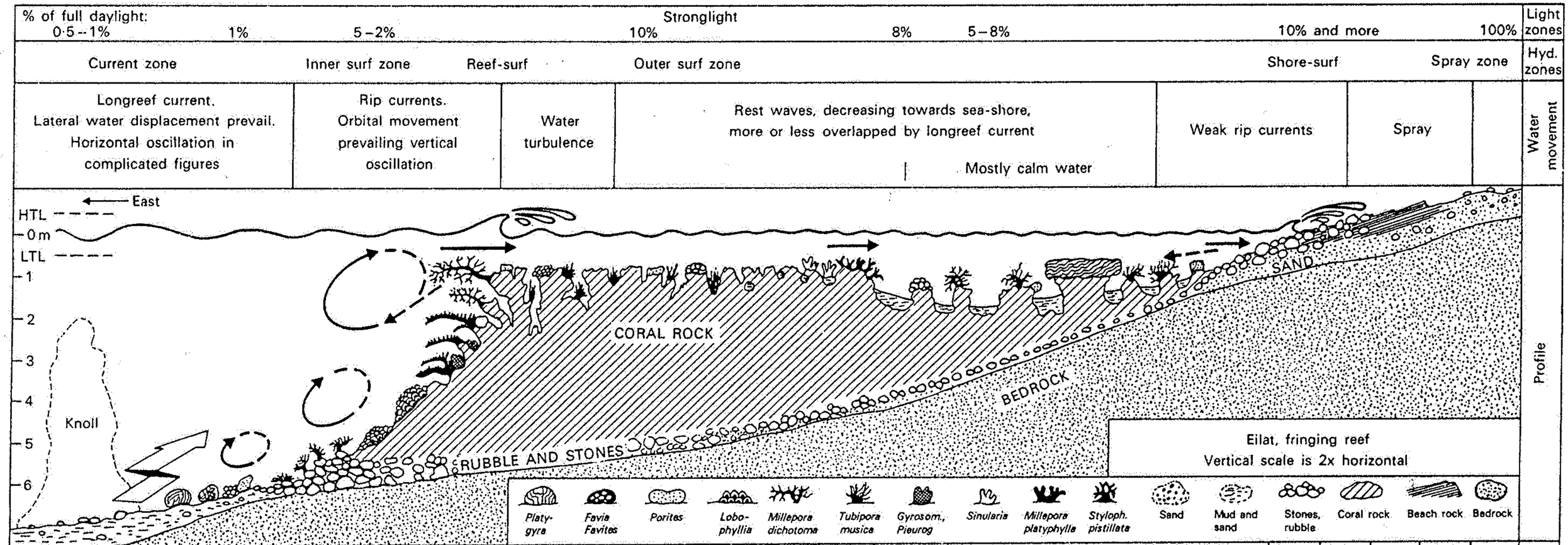

% of full daylight: 0·5–1%	1%	5–2%	Stronglight 10%	8%	5–8%	10% and more	100%	Light zones
Current zone		Inner surf zone	Reef-surf	Outer surf zone		Shore-surf	Spray zone	Hyd. zones
Longreef current. Lateral water displacement prevail. Horizontal oscillation in complicated figures		Rip currents. Orbital movement prevailing vertical oscillation	Water turbulence	Rest waves, decreasing towards sea-shore, more or less overlapped by longreef current. Mostly calm water		Weak rip currents	Spray	Water movement

Knolls: Favia-Porites z. / Galaxea zone / Acropora zone	Brain corals zone	Secondary Acropora zone	*Lobophyllia* zone	Primary Acropora zone	Millepora dichotoma zone	Tubipora musica zone	Millepora platyphylla z.	Stylophora pistillata zone	Nerita zone	Tetraclita zone	Littorinidae zone	Tectarius zone		Physiographic zonation
Coral detritus, sand and mud. Knolls: coral rock		Coral rubble	Mostly living corals on dead coral rock			Abrasioned dead coral rock. Coral detritus within the holes		Granite sand and organogenic sediments, dead coral heads, Platygyra-pseudoatoll	Granite pebble	Conglo-merate	Beach rock	Granite sand and stones		Sub-strate
Littoral flat with knolls	Fore reef	Scree	Outward reef slope	Reef edge	Buttress zone	Reef platform	Rear reef	Lagoon or channel	Shore zone					Str. zones
Upper sublittoral					Uppermost sublittoral				Eulittoral lower	Eulittoral middle	Eulittoral upper	Supra-litt.	Beach	Litt. zones
40-50 / 5-20	6(5-10) / 4-10	10(5-15) / 3-8		1-2 / 0,5	20(15-30) / 0,3-0,8		1 / 0,5-1	20(10-40) / 0,5-2	1-1,5	1	1-1,5	1	Broad deep	m

Fig. 10.40A. A profile through the northern fringing reef of Eilat showing the main ecological zones and their controlling influences (after Mergner, 1971).

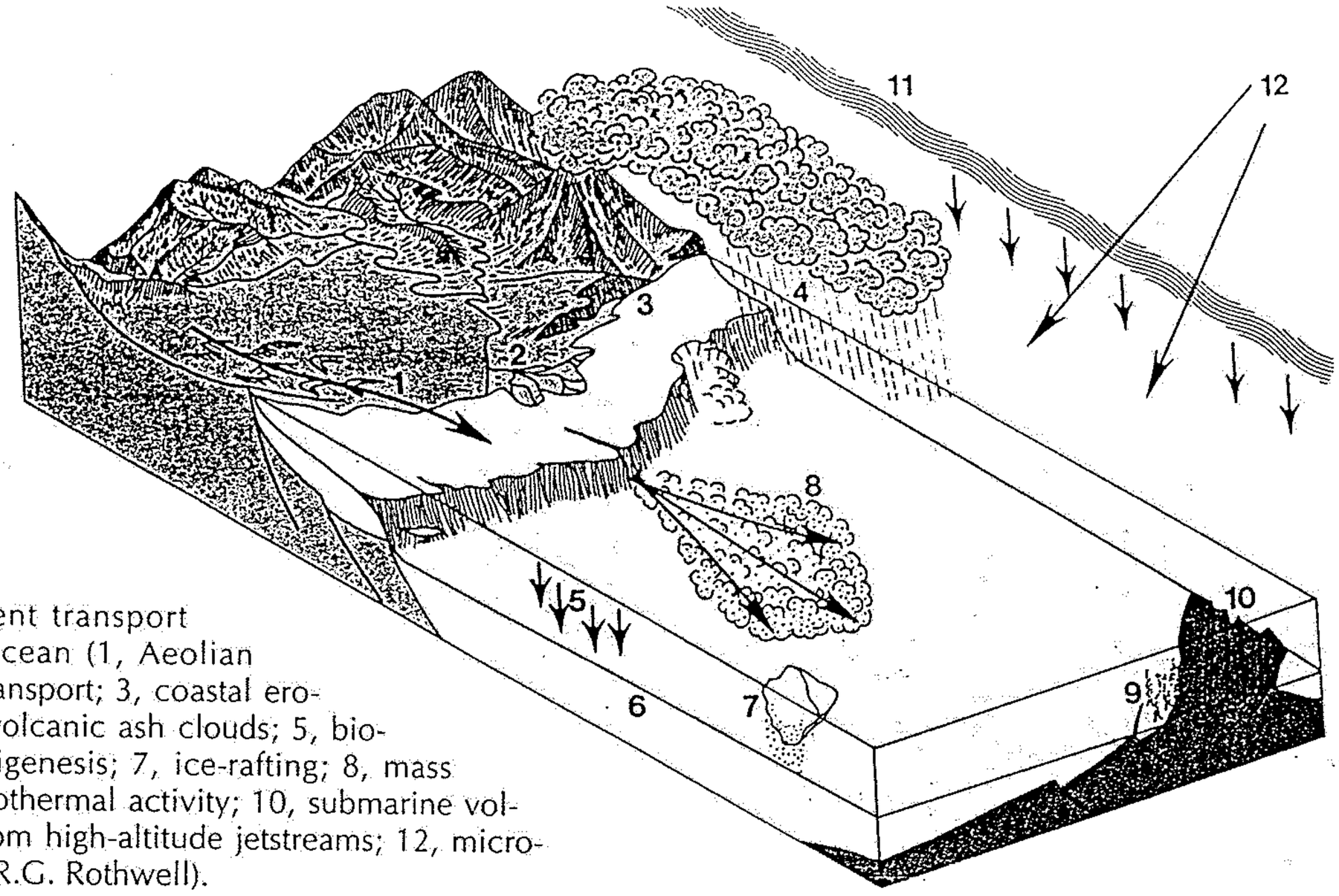

Figure 8.22 Sediment transport routes to the deep ocean (1, Aeolian transport; 2, fluvial transport; 3, coastal erosion; 4, fallout from volcanic ash clouds; 5, biogenic debris; 6, authigenesis; 7, ice-rafting; 8, mass gravity flows; 9, hydrothermal activity; 10, submarine volcanism; 11, fallout from high-altitude jetstreams; 12, micrometeorites; drawn by R.G. Rothwell).

Input	Output
Cliffs back of shore eroded by waves	Sedimentation in deep water by rip currents and waves
Beach eroded by longshore drift and current	Growth of beaches (including spits and bars) downcurrent due to deposition of sand by longshore drift and current
Rivers upcurrent eroded by longshore drift and current	Growth of backshore dunes due to deposition of sand by offshore winds

Figure 11-21

The beach budget is a complex balance between erosion and sedimentation in which such forms as spits and bars grow as beach cliffs and other sources supply sand. If input is out of balance with output, the beach tends to grow or to erode.

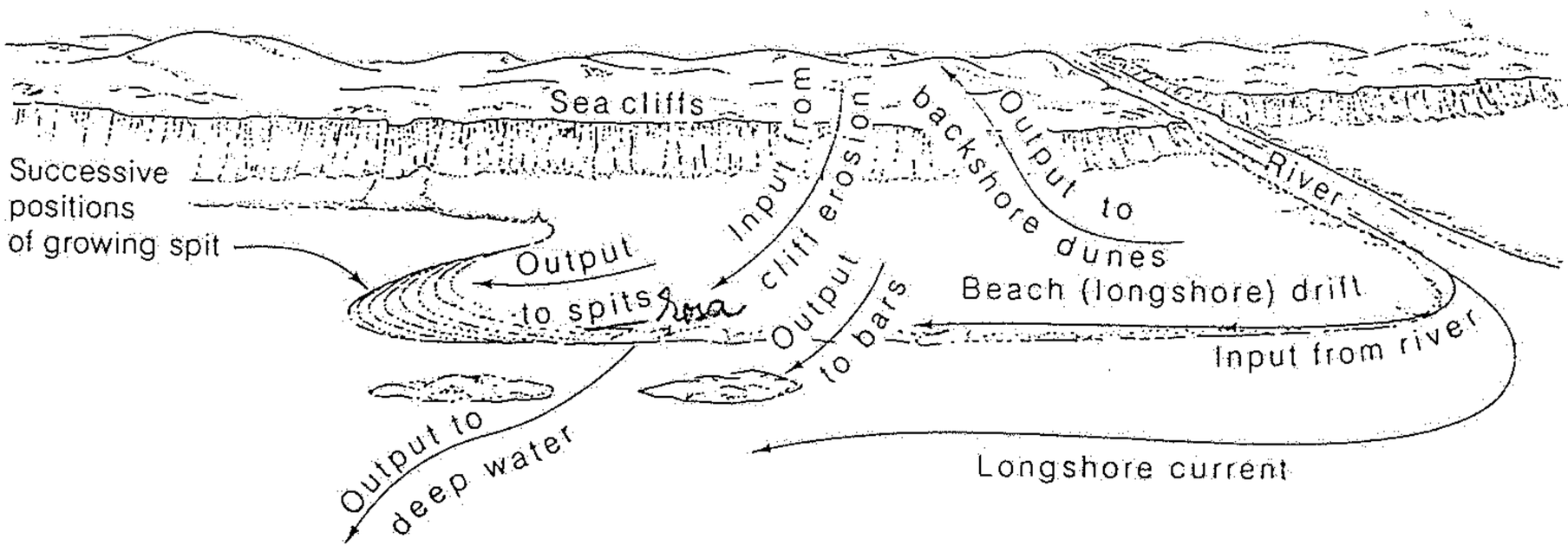

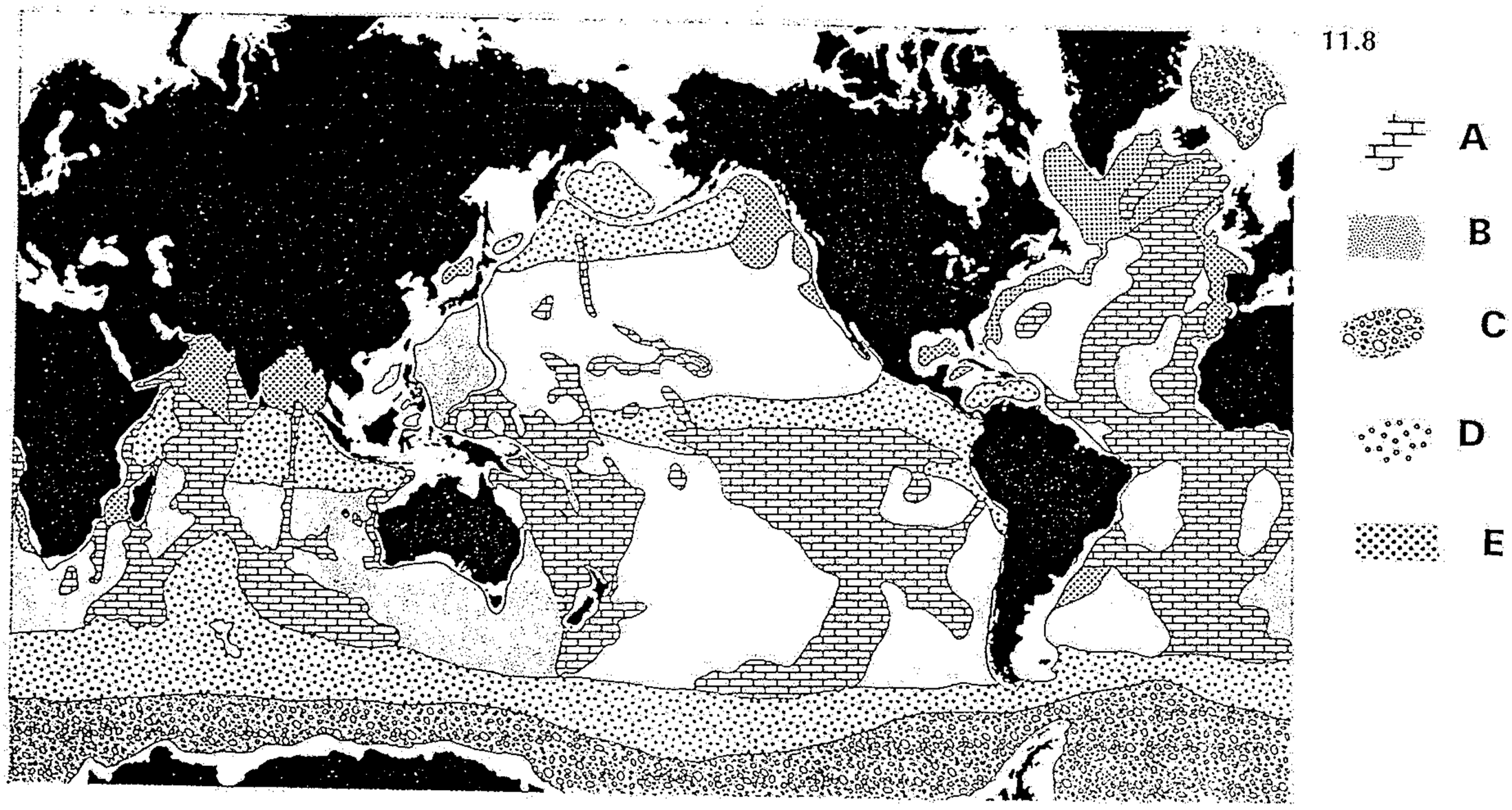

Figure 11.8 Dominant sediment types, classified by origin, in different areas of the deep-sea bed. Low concentrations of calcareous sediments in the North Pacific Ocean reflect a shallower calcite compensation depth (see text) in this region; a general tendency can be seen for high concentrations of calcium carbonate to occur on the mid-ocean ridges, where the depth of water is usually less than the calcite compensation depth (A, calcareous sediment; B, deep-sea clay; C, glacial sediment; D, siliceous sediment; E, terrigenous sediment; ocean margin sediments occur in the areas left blank; from Davies and Gorsline[6], with permission from the authors and Academic Press).

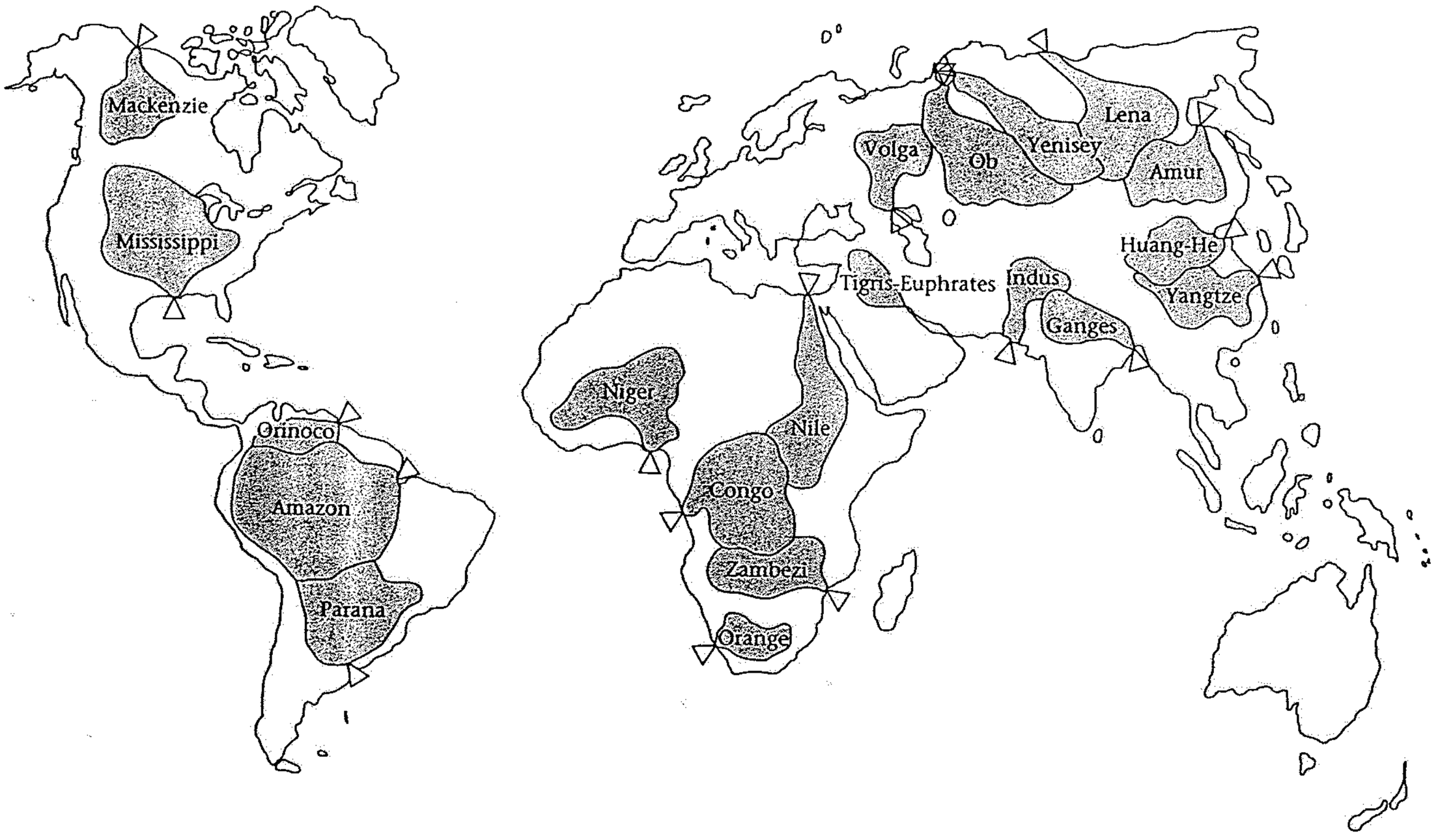

Figure 9.12. World's largest drainage, basins, showing the location of deltas at their mouths. (*Source:* Adapted from B. J. Skinner and S. C. Porter, *The Dynamic Earth*, John Wiley, 1987, figure 10.22, p. 234.)

Figure 9.13. Hydrologic flow paths leading to a river.

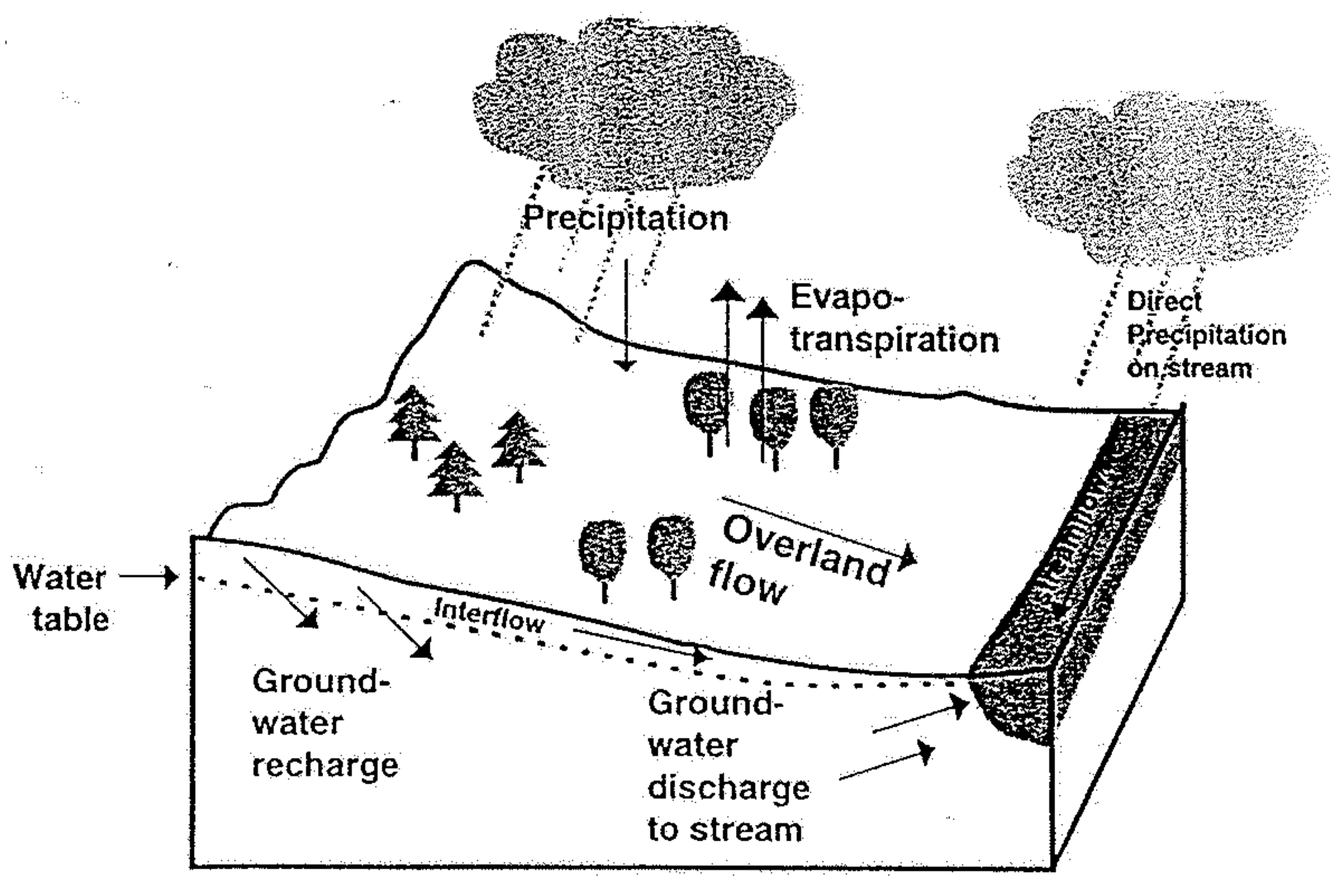

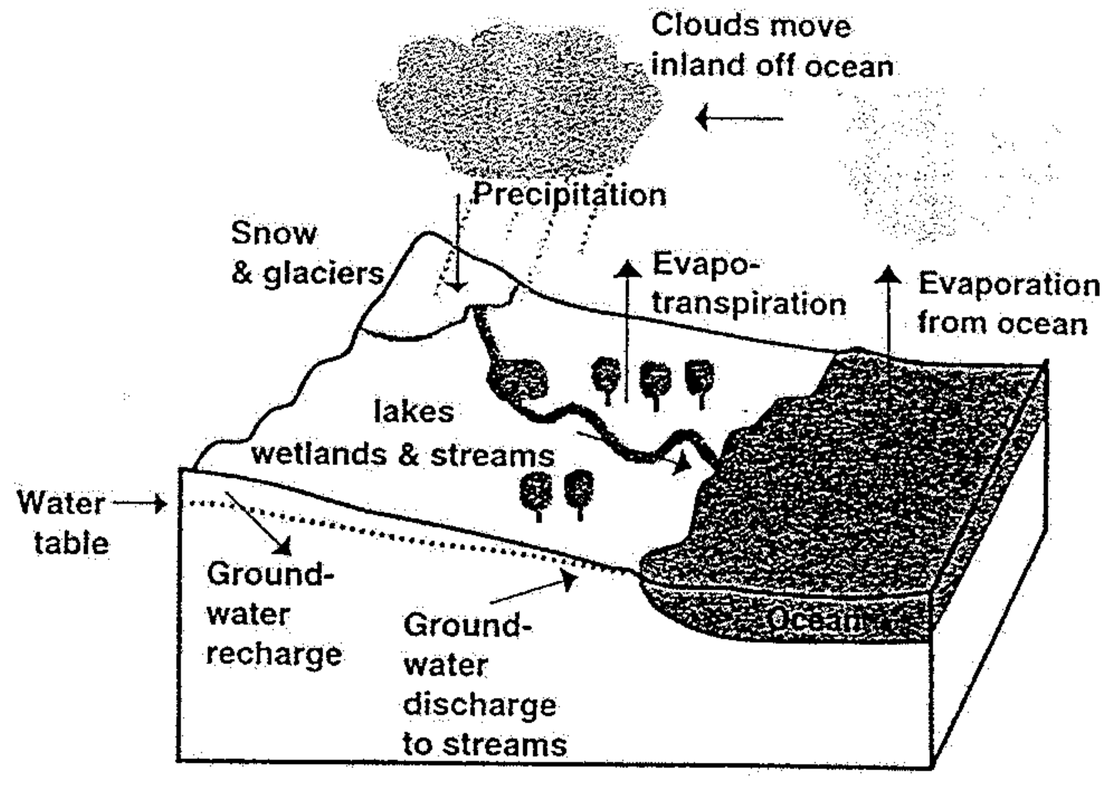

Figure 9.1. Schematic illustration of the hydrologic cycle.

Figure 9.2. The global hydrologic cycle, reservoirs of water (10^{15} kilograms and fluxes 10^{15} kilograms per year). (*Source:* Data from National Research Council, 1986.)

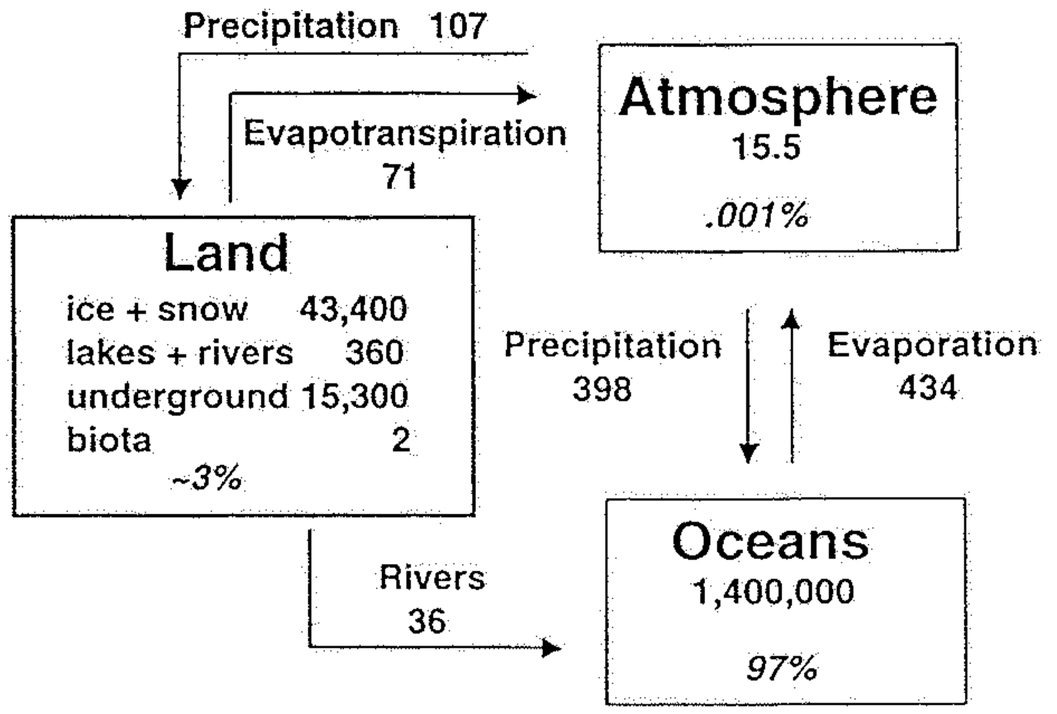

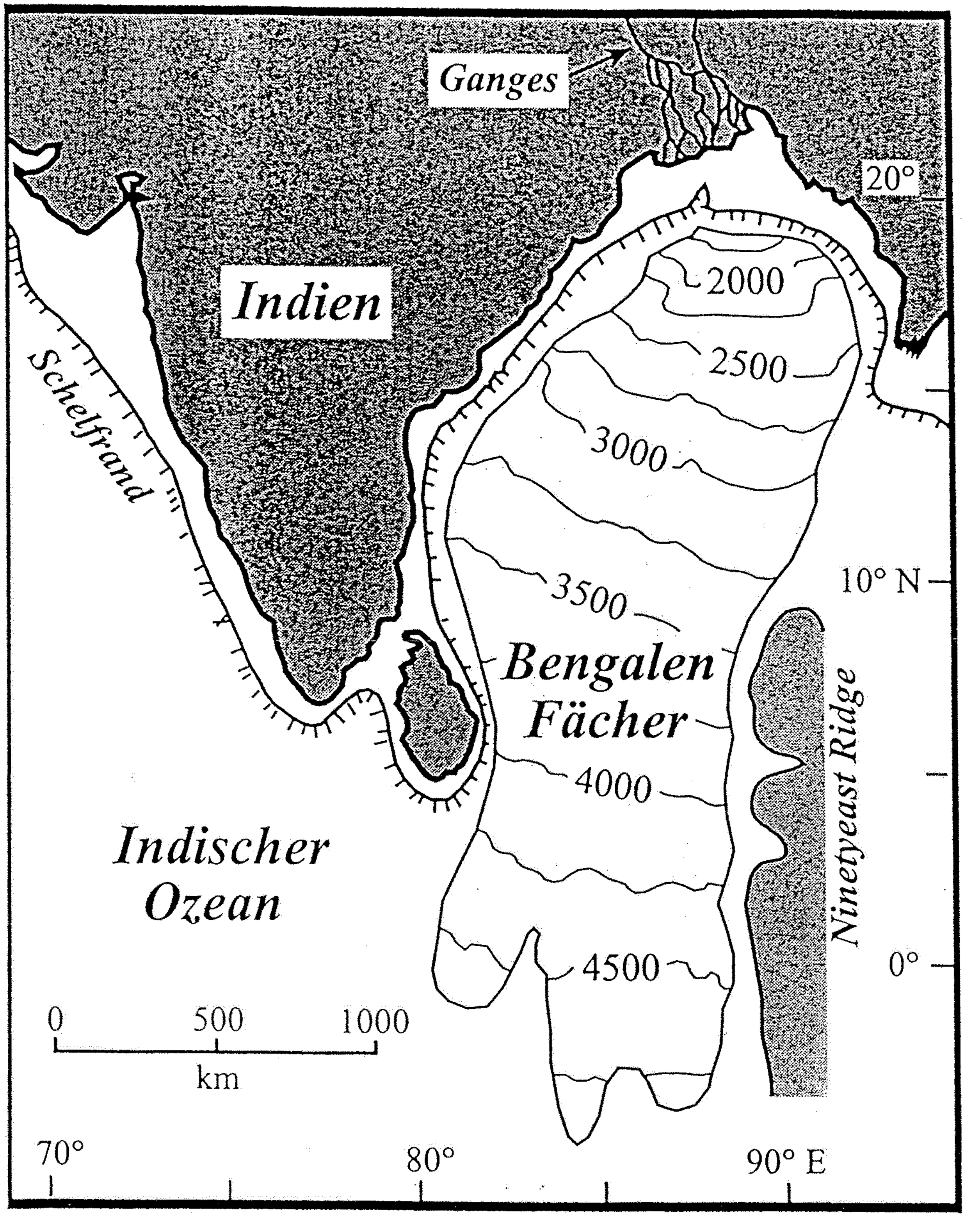

Abb. 6.28

a) Der Bengalen-Fächer wird von den großen Flußsystemen des Ganges und des Bramaputhra gespeist und besteht aus mächtigen Turbiditfolgen. In seiner flächigen Ausbreitung wird er durch die Kontinentalabhänge des östlichen Indien und vor Birma, sowie durch die Seamount-Kette des Ninetyeast-Rückens (Abb. 12.34) begrenzt. Die Kontourlinien im Bengalen-Fächer geben die Tiefe seiner Oberfläche in Metern unterhalb des Meeresspiegels an (nach EMMEL & CURRAY, 1985).

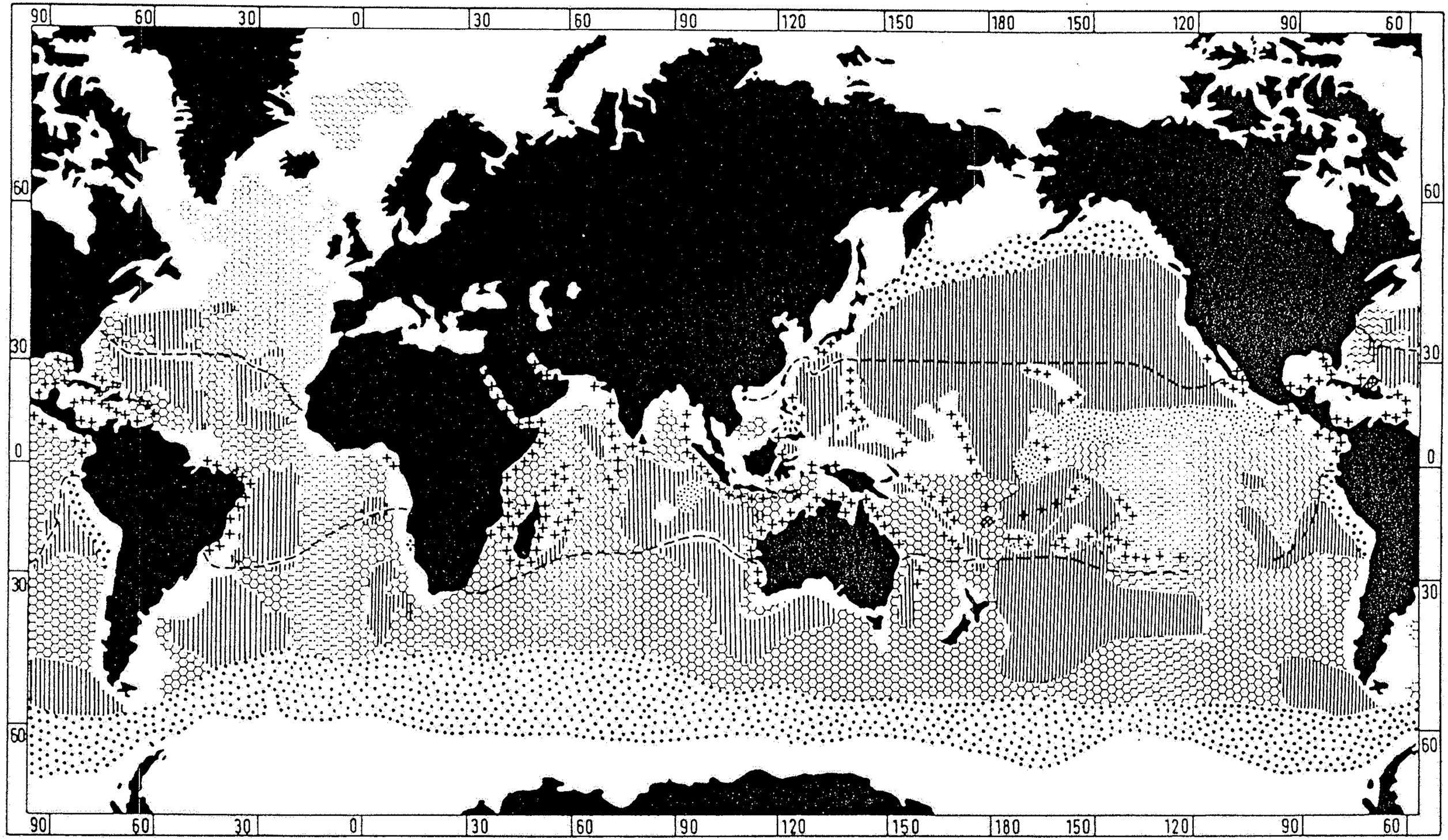

Abb. 6.29
Verbreitung pelagischer Sedimente auf den heutigen Ozeanböden (aus ZEIL, 1990).

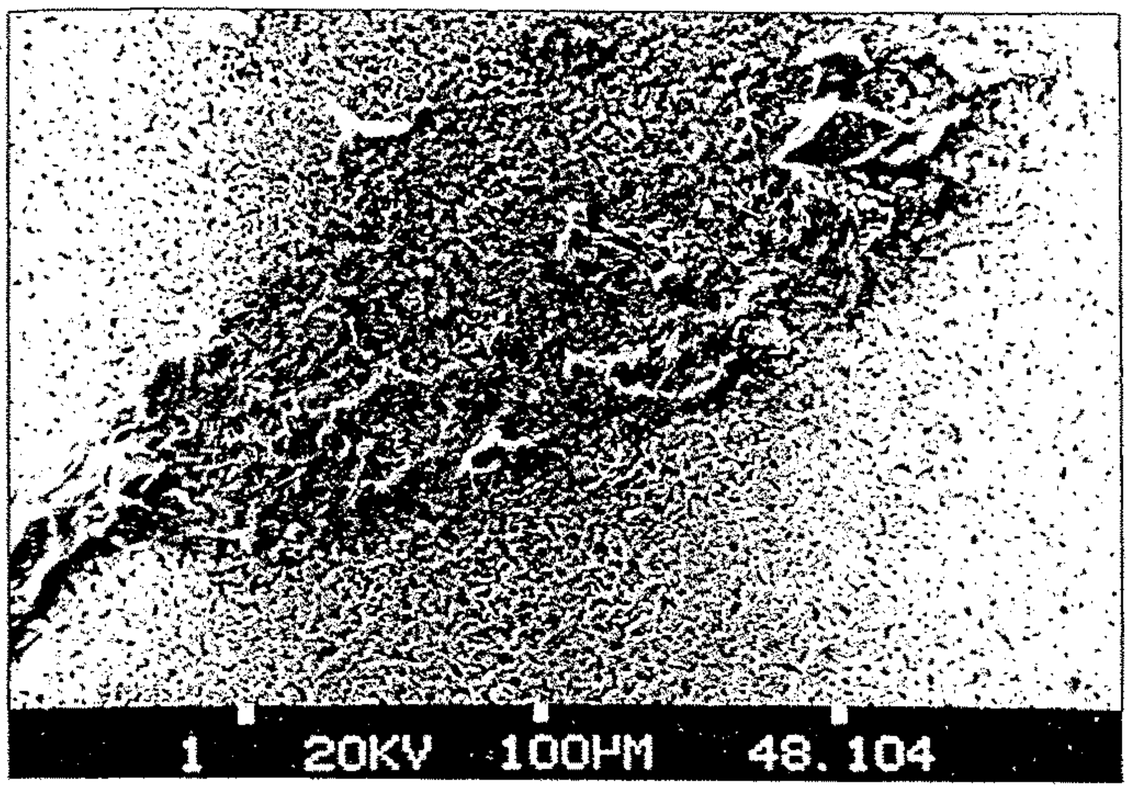

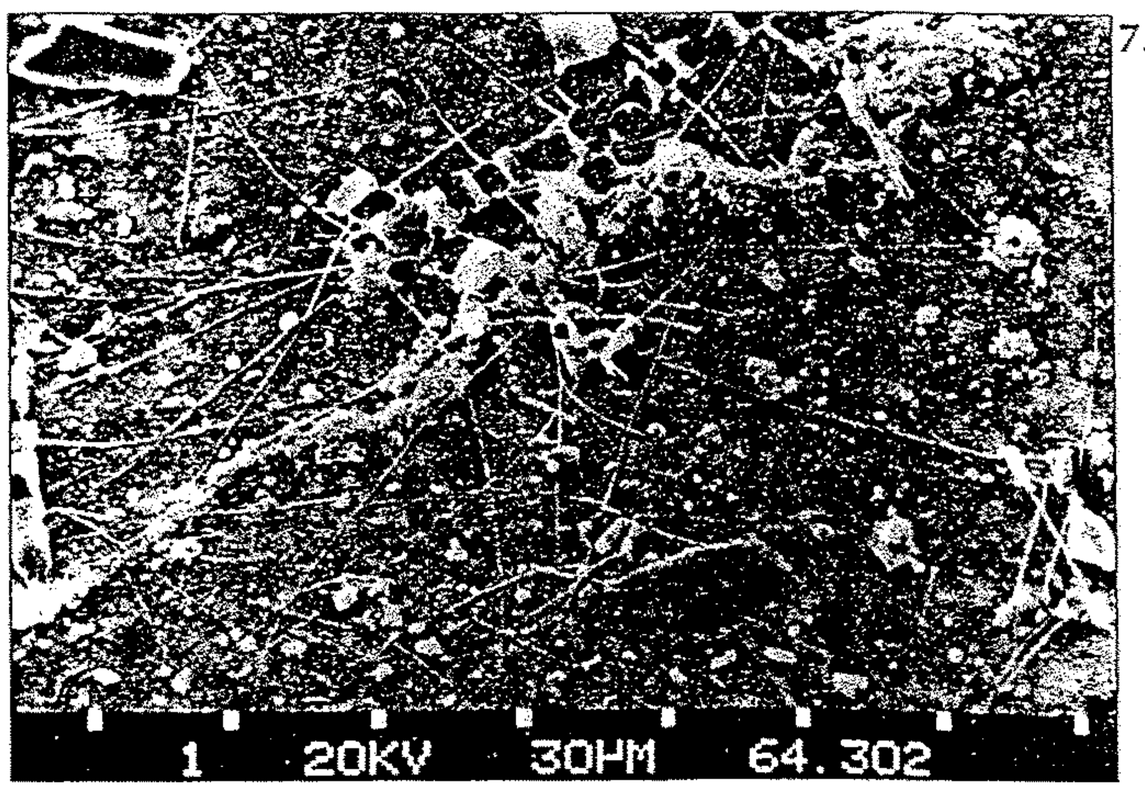

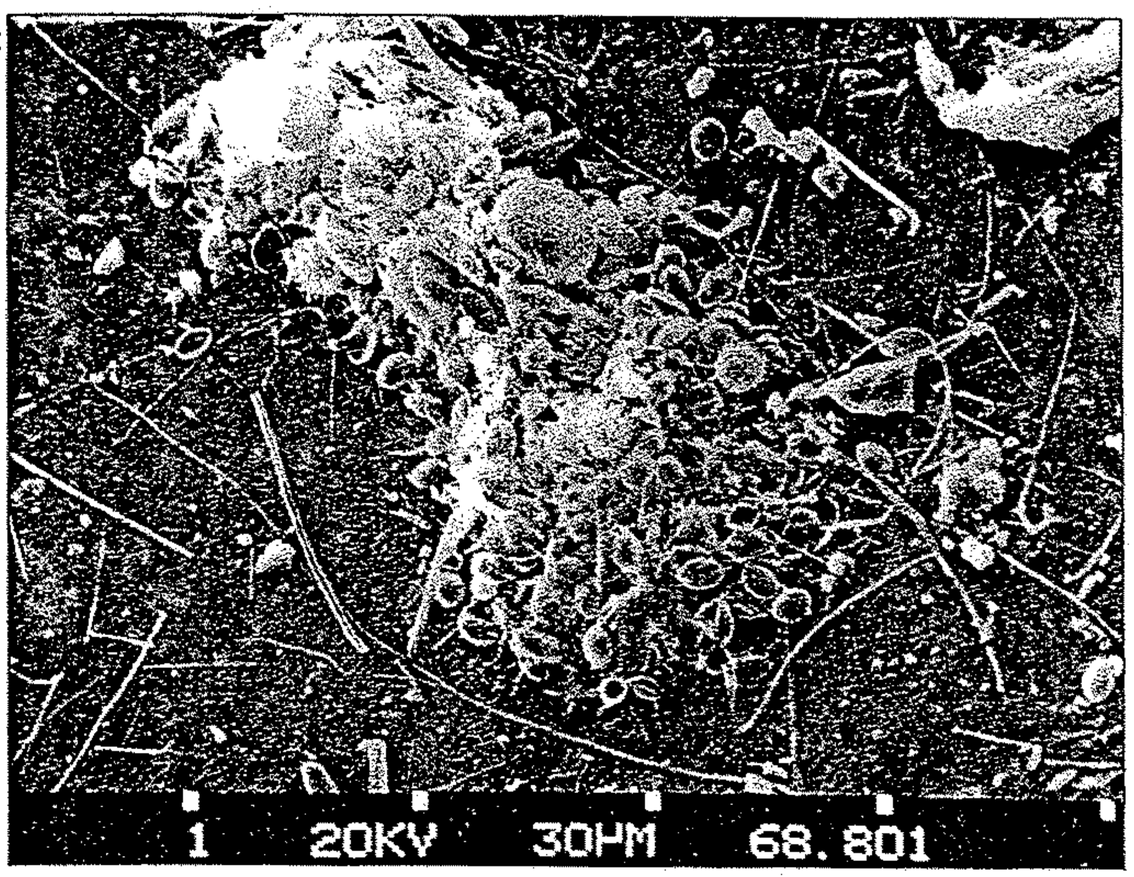

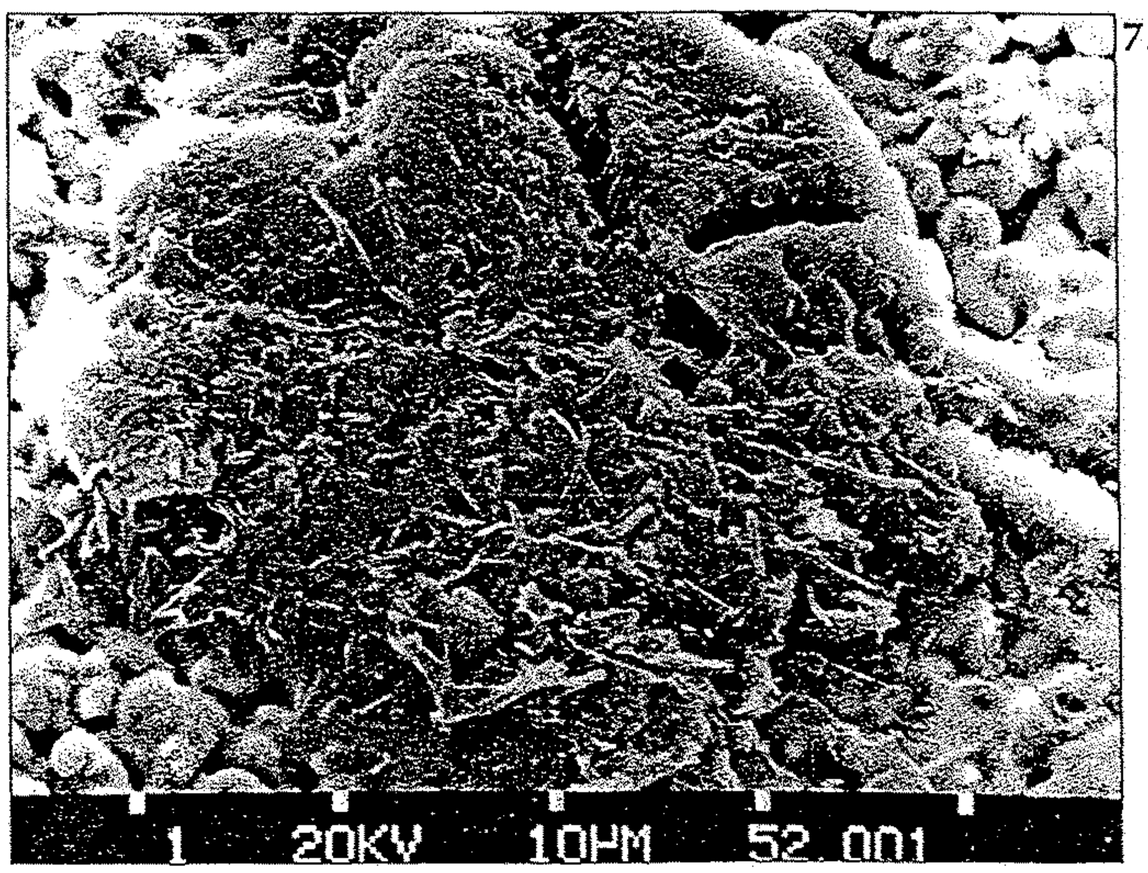

Figure 7.14 Scanning electron micrographs of marine snow particles collected off Baffin Island, showing a wide range of morphologies and composition. (a) Large mucoid aggregate collected at 30 m depth. (b) 'Stringer' collected at 1 m depth. (c) Mixed agglomerate dominated by biogenic material collected at 100 m depth. (d) Aggregate dominated by mineral matter collected at 5 m depth. (Courtesy of Dr Azetzu-Scott, Bedford Institute of Oceanography.)

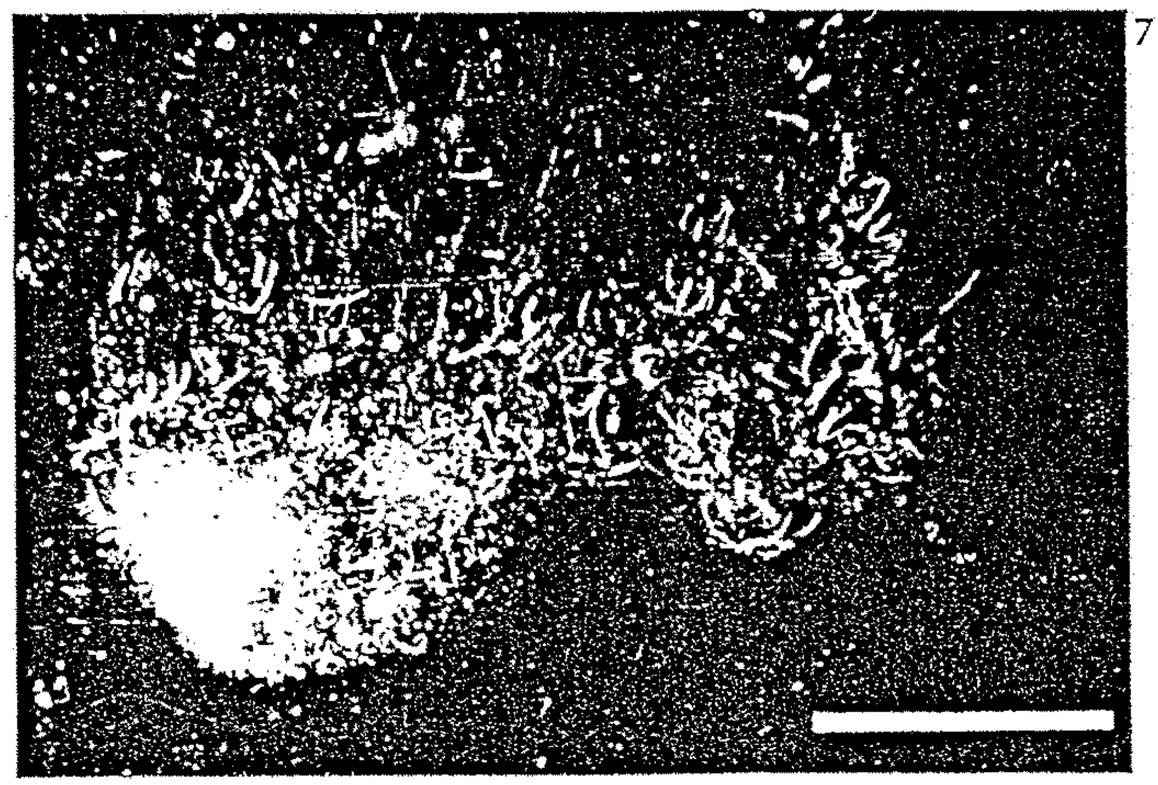

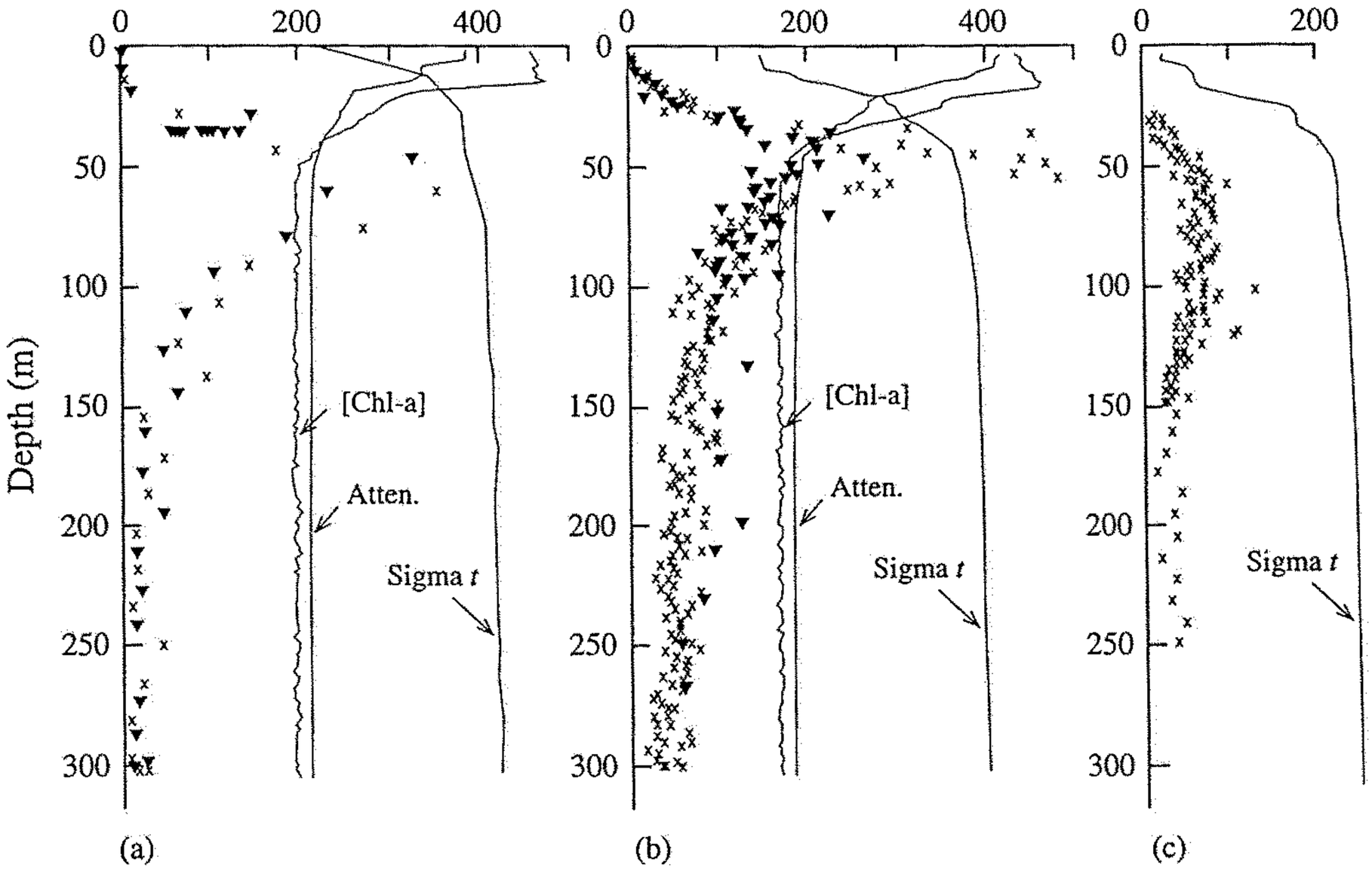

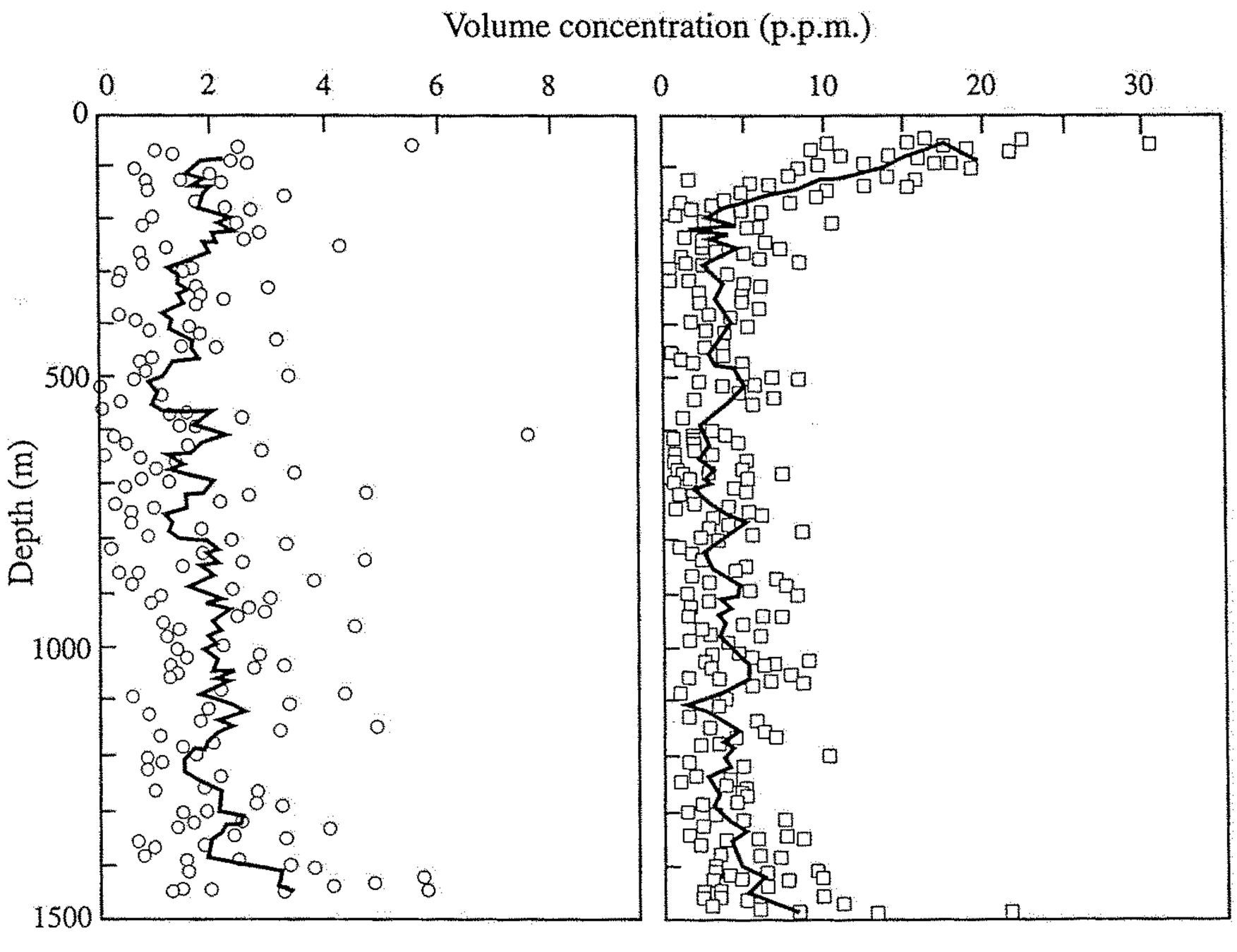

Figure 7.2 Examples of the distribution of marine snow particles greater than 0.6 mm diameter, expressed as volume concentration (p.p.m.). (a) 19 May 1990 (MSP 11), (b) 22 May 1990 (MSP 15), and (c) 26 May 1990 (MSP 19) from the Northeast Atlantic at a water depth of 4800 m (Lampitt *et al.*[12]). Sigma *t* is a measurement of water density, [Chl a] (Chlorophyll a) is the concentration of phytoplankton pigment, and Atten (attenuation) is a measure of the concentration of the smaller particles as determined by their effect on light transmission through the water. In terms of abundance, the maximum concentration of particles at around 50 m depth is about 200/l, decreasing to a deep-water minimum of approximately 30/l. (d) 22 November 1987 and (e) 28 January 1988 from Northwestern Gulf of Mexico at a water depth of 1500 m on two occasions; the lines are 9-point running means[26]. In most instances there is a peak in concentration near the surface, but not necessarily at the surface. Near the sea bed there are also elevated levels. There appears to be a very wide range in concentrations and, although some of this may be related to differences in technique, there can be considerable temporal variability at any one site (*Figure 7.6*); there are also likely to be large regional differences reflecting the structure and dynamics of the biological communities in the different environments.

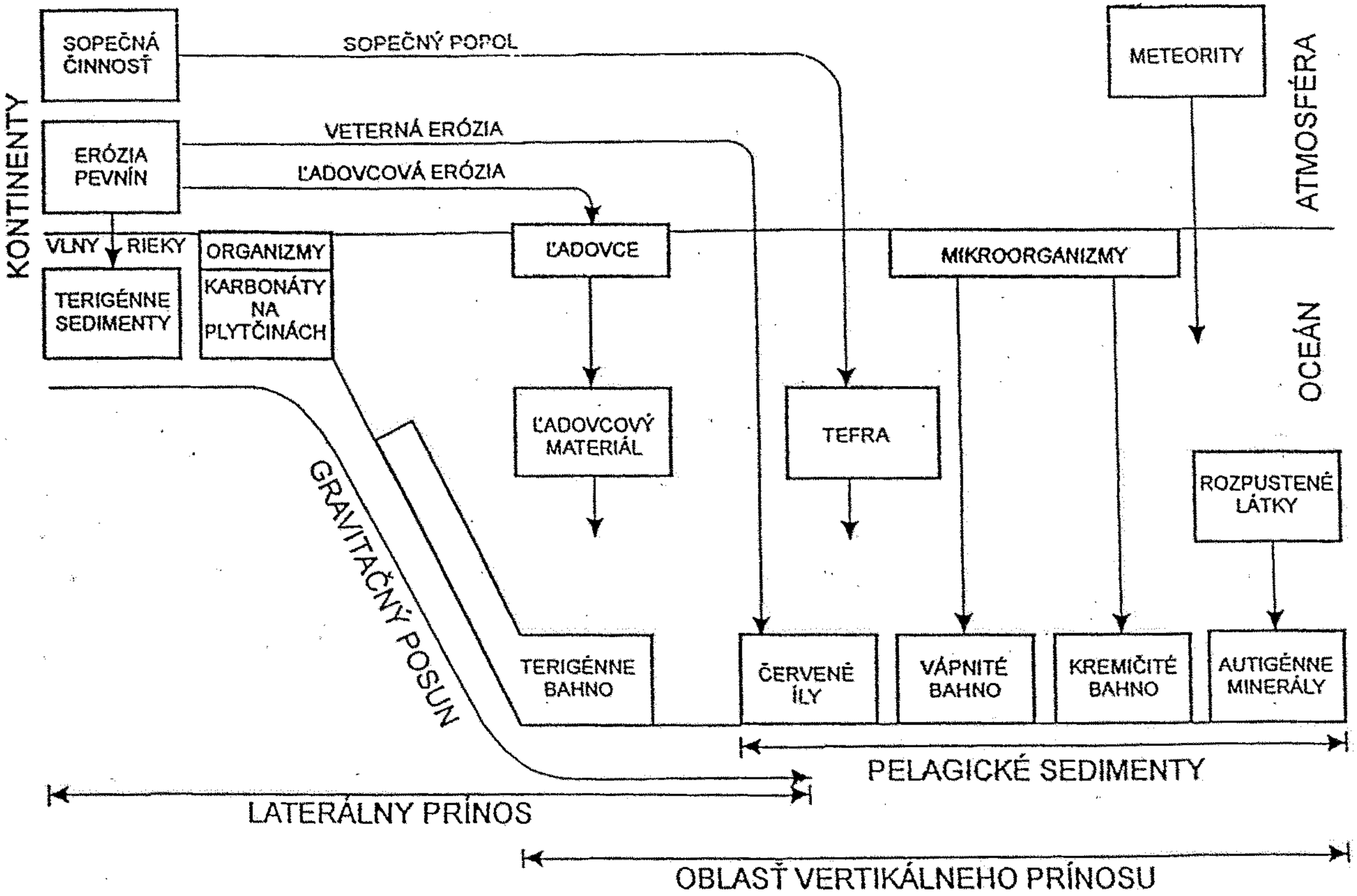

obr. 18.1. Základné typy morských (oceánskych) sedimentov a ich pôvod.

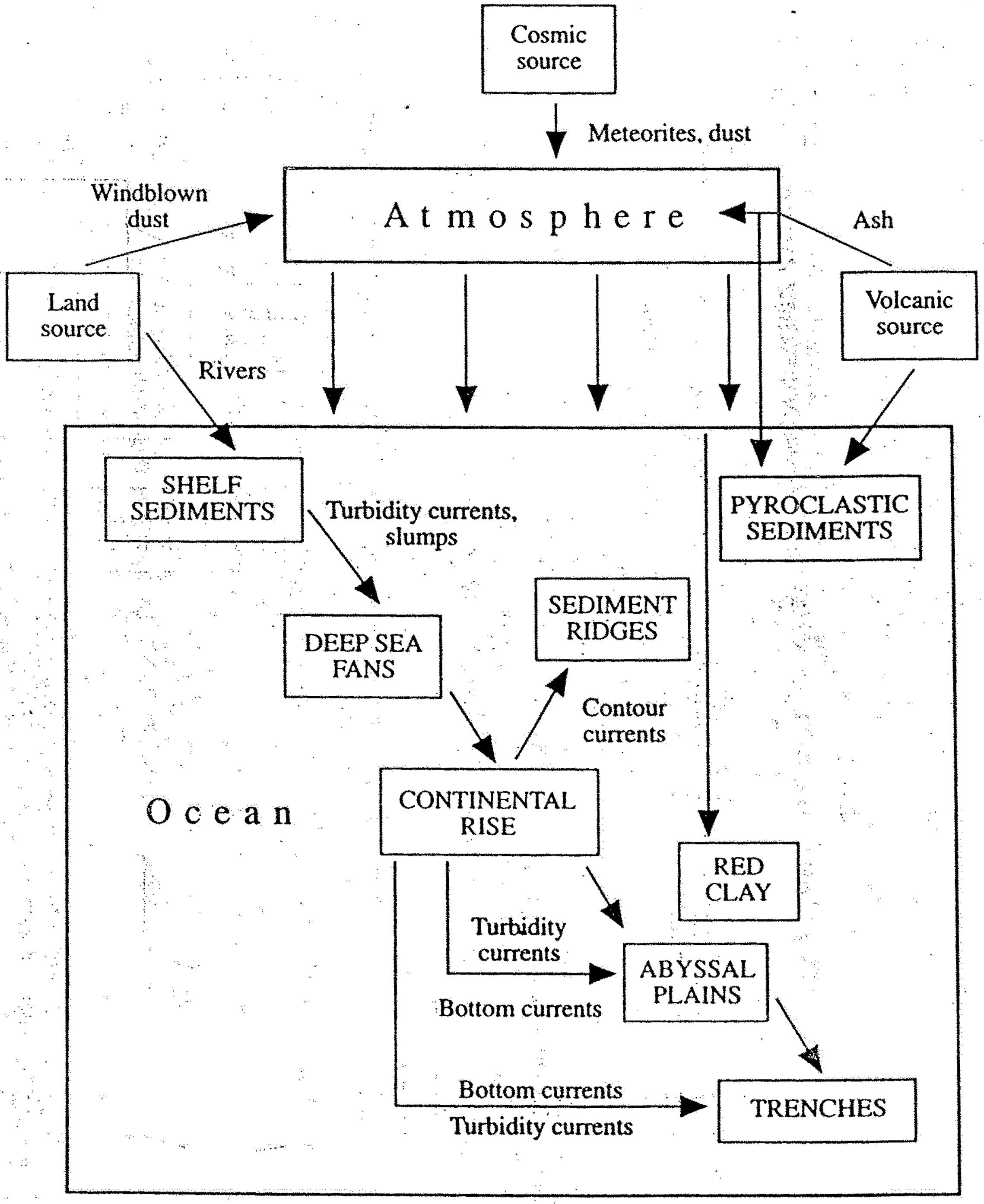

Figure 8.25 Processes of clastic sedimentation in the oceans (after Hay[17]).

Volcanic source

Ash

Cosmic source

Meteorites, dust

Windblown dust

Land source

Ice-rafting

Atmosphere

Ocean

$CaCO_3$

SiO_2

Pteropods | Foraminifera | Coccolithophores | Radiolaria | Diatoms

TROPICAL | TEMPERATE | TROPICAL HIGH PRODUCTIVITY | BOREAL

PTEROPOD OOZE

Aragonite compensation depth

GLOBIGERINA OOZE

'Lysocline'

COCCOLITH OOZE

Calcite compensation depth

RADIOLARIAN OOZE

DIATOM OOZE

GLACIAL MARINE SEDIMENTS

RED CLAY

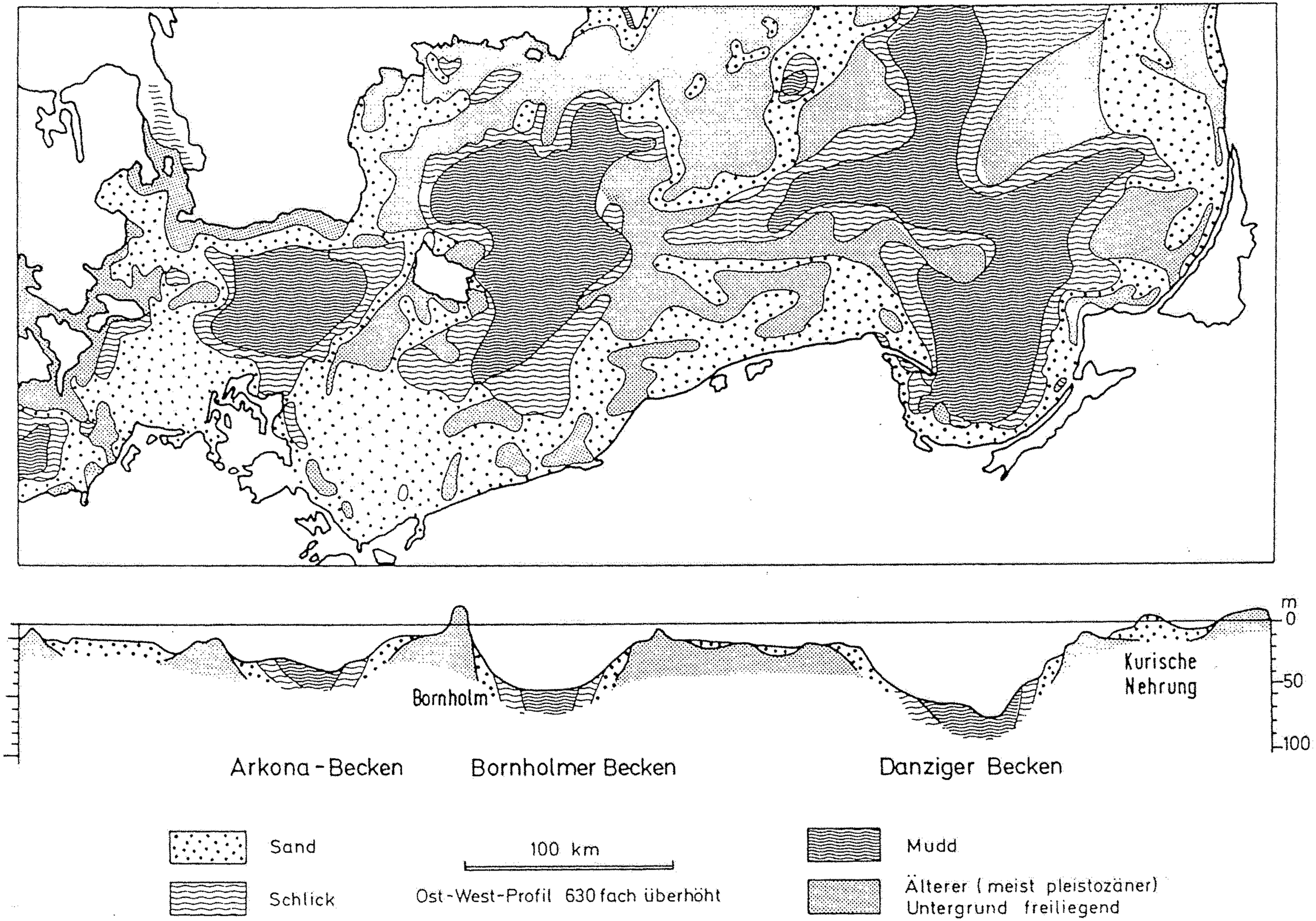

Abb. 6.22
Morphologie und Sedimente des Ostseebodens (aus ZEIL, 1990).

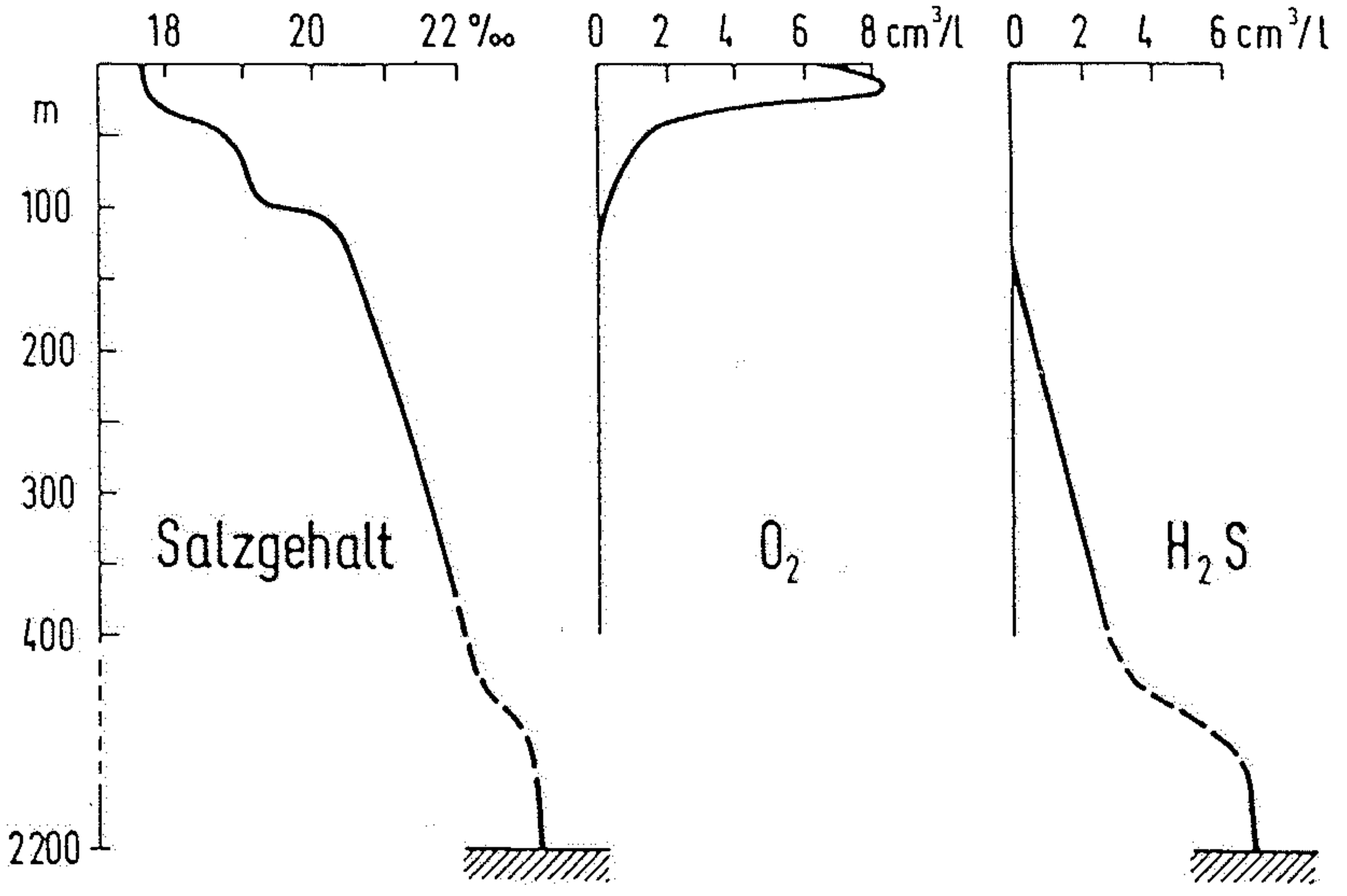

Abb. 6.23

a) Gehalte von Salz, Sauerstoff und Schwefelwasserstoff im Schwarzen Meer.

b) Strömungen und Sedimente im Schwarzen Meer (aus ZEIL, 1990):

Links oben: Meerestiefen; 1 = 0–200 m, 2 = 200–500 m, 3 = 500–1000 m, 4 = 1000–2000 m, 5 = >2000 m. Strömungen: Schwarze Pfeile.

Rechts oben: Heutige Sedimente: 1 = Sand und Schill, 2 = Muschelschlick, 3 = Tonschlamm, 4 = Übergang von Ton- zu Kalkschlamm, 5 = Kalkschlamm, 6 = sedimentfreie Fläche.

Links unten: Menge der während der letzten 2500 Jahre abgelagerten terrigenen Sedimente in g cm $^{-2}$, 1 = 0–20, 2 = 20–50, 3 = 50–100, 4 = 100–200, 5 = > 200, 6 = sedimentfreie Fläche.

Rechts unten: Kalkgehalt der heutigen Sedimente in %, 1 = 0–20, 2 = 20–30, 3 = 30–40, 4 = 40–50, 5 = > 50.

A Explanation:
A, B, C and D – Inferred response of the sediment cover to the shelf hydraulic regime as it responds to different tidal and storm conditions.
1-6 – Hypothetical depositional zones along a tidal current transport path. Length of depositional zone ca. several tens to hundreds of kilometres.

1. FAIR WEATHER CONDITIONS:-
Normal tidal currents dominant process

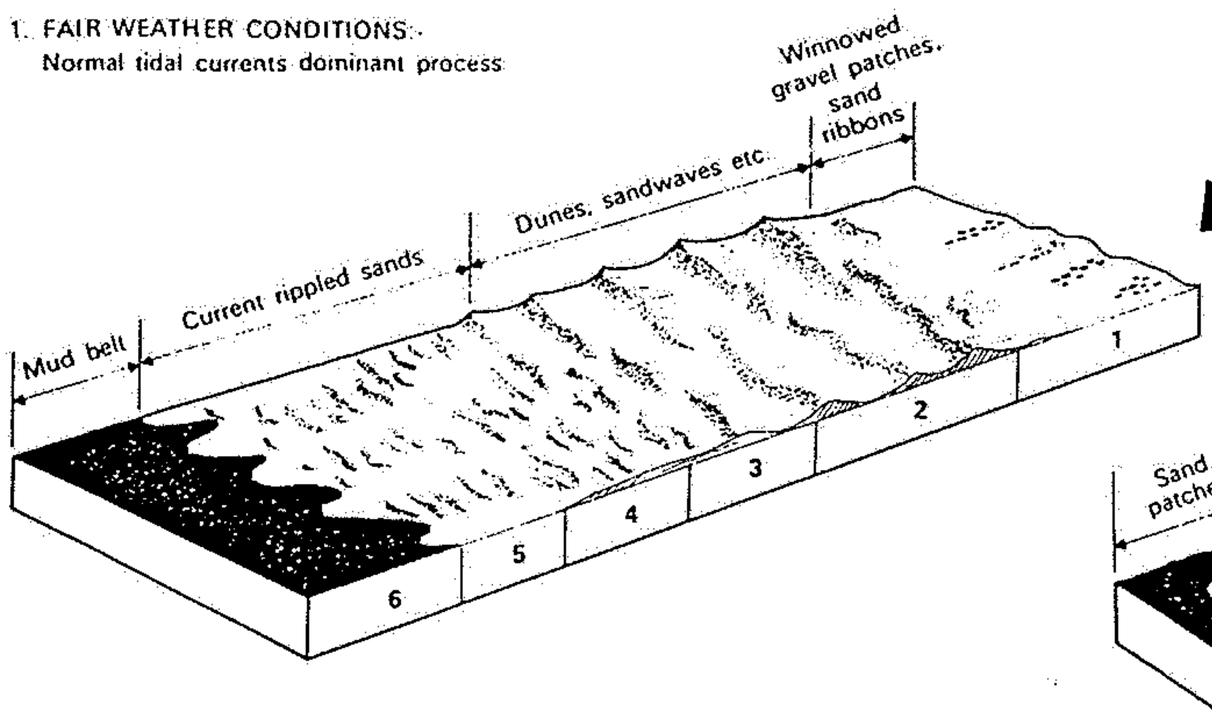

2. MODERATE STORM CONDITIONS:-
Tidal currents enhanced by storm processes

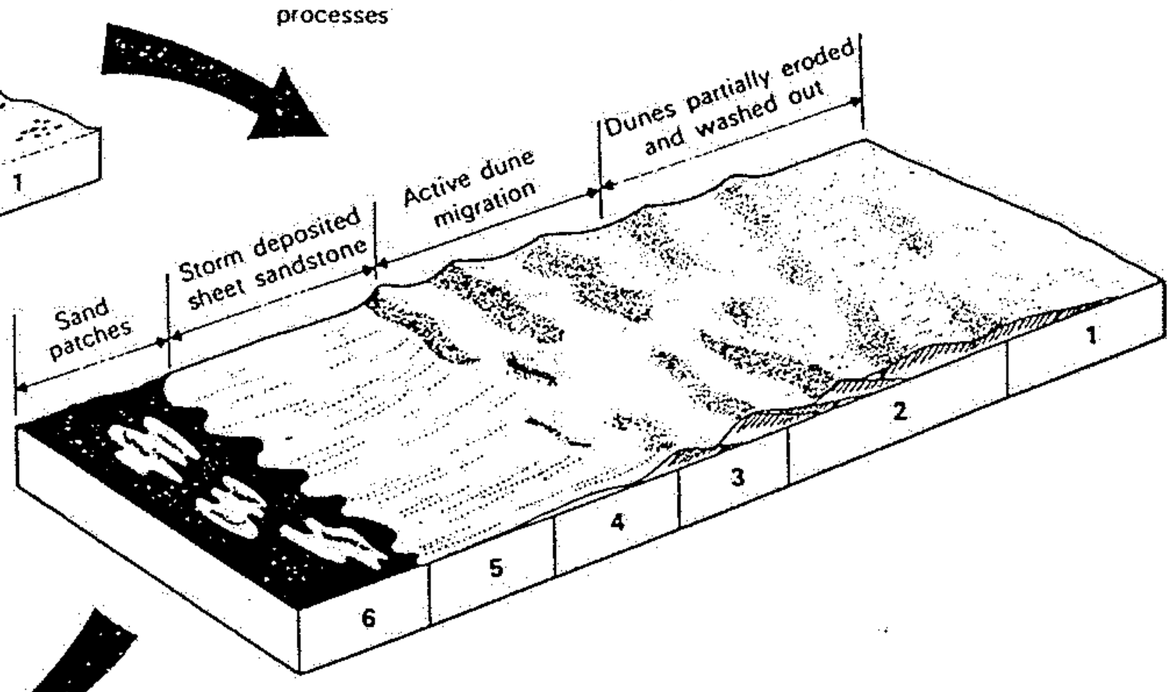

3. INTENSE STORM SURGE CONDITIONS:-
Tidal currents with maximum enhancement by storm surge flows

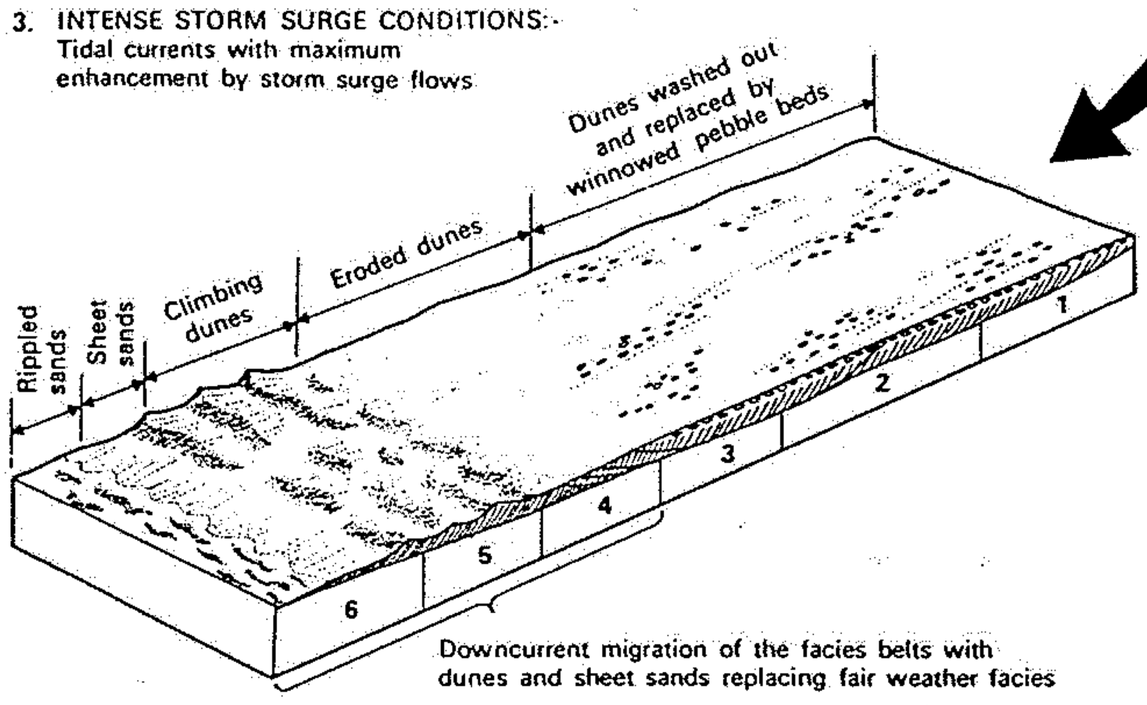

Downcurrent migration of the facies belts with dunes and sheet sands replacing fair weather facies

4. POST STORM/RETURN TO FAIR WEATHER CONDITIONS:-
Normal tidal currents

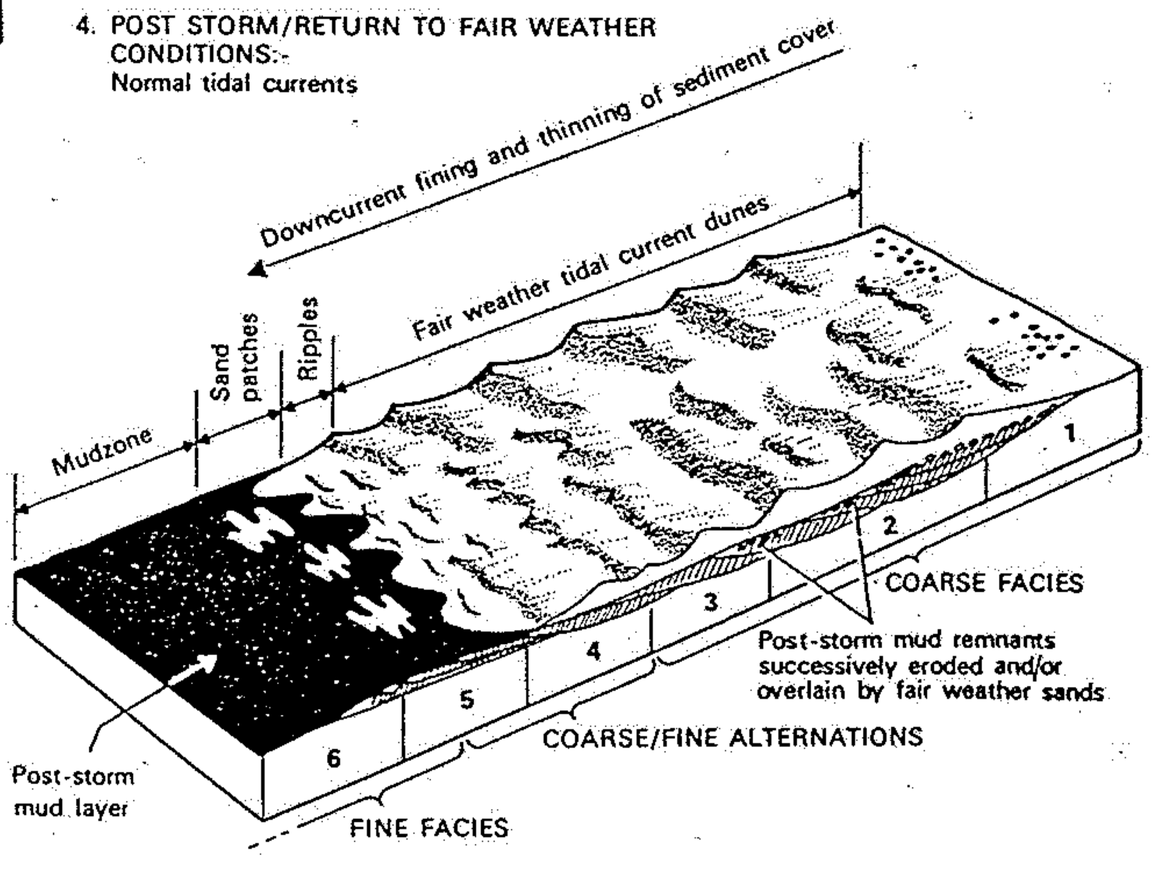

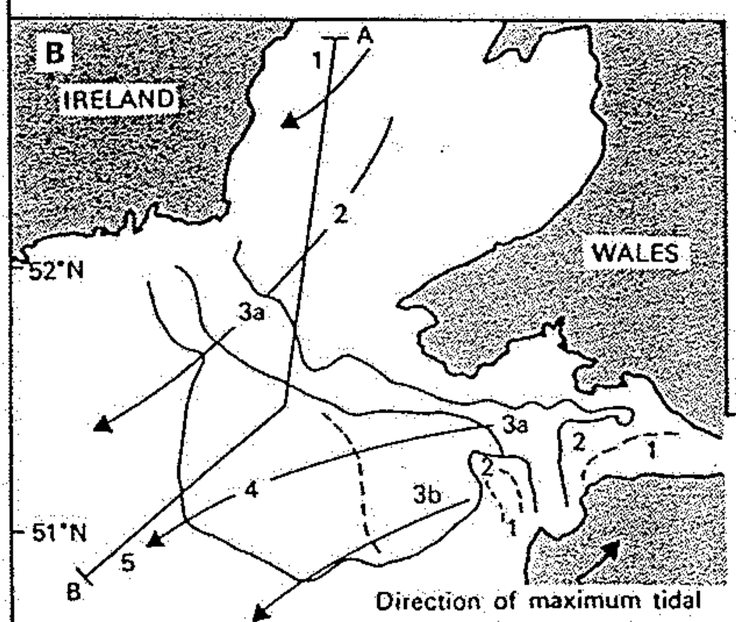

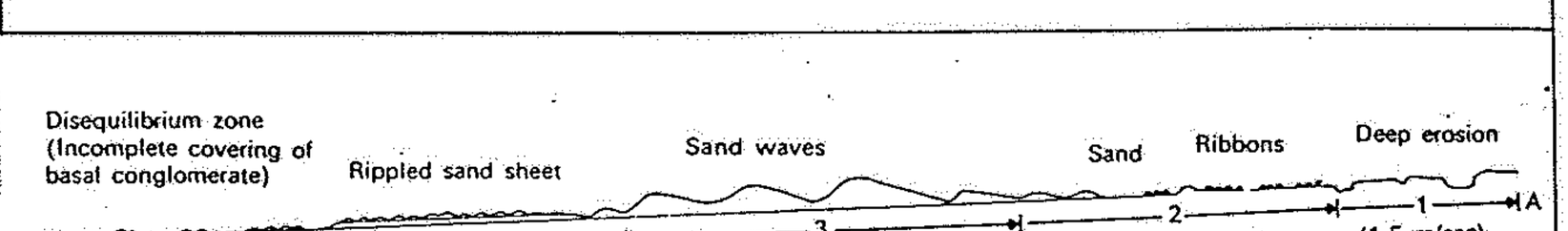

Fig. 9.34. A. Hypothetical reconstruction of the Jura Quartzite shelf sea as developed under different tidal and storm conditions. See text for explanation (after Anderton, 1976); and B. Possible modern analogue as exemplified by the tidal current transport paths in the Celtic Sea (from Belderson and Stride, 1966).

Fig. 9.42. Reconstruction of the Oxfordian sublittoral environmen during progradation of the linear tidal sand bars (after Brenner an Davies, 1973, 1974).